Performance Simulation of Planar Solid Oxide Fuel Cells

by

Siamak Farhad

A thesis
presented to the University of Waterloo
in fulfillment of the
thesis requirement for the degree of
Doctor of Philosophy
in
Mechanical Engineering

Waterloo, Ontario, Canada, 2011

Author's Declaration

I hereby declare that I am the sole author of this thesis. This is a true copy of the thesis, including any required final revisions, as accepted by my examiners.

I understand that my thesis may be made electronically available to the public.

Siamak Farhad

Abstract

The performance of solid oxide fuel cells (SOFCs) at the cell and system levels is studied using computer simulation.

At the cell level, a new model combining the cell micro and macro models is developed. Using this model, the microstructural variables of porous composite electrodes can be linked to the cell performance. In this approach, the electrochemical performance of porous composite electrodes is predicted using a micro-model. In the micro-model, the random-packing sphere method is used to estimate the microstructural properties of porous composite electrodes from the independent microstructural variables. These variables are the electrode porosity, thickness, particle size ratio, and size and volume fraction of electron-conducting particles. Then, the complex interdependency among the multi-component mass transport, electron and ion transports, and the electrochemical and chemical reactions in the microstructure of electrodes is taken into account to predict the electrochemical performance of electrodes. The temperature distribution in the solid structure of the cell and the temperature and species partial pressure distributions in the bulk fuel and air streams are predicted using the cell macro-model. In the macro-model, the energy transport is considered for the cell solid structure and the mass and energy transports are considered for the fuel and air streams.

To demonstrate the application of the cell level model developed, entitled the combined micro- and micro-model, several anode-supported co-flow planar cells with a range of microstructures of porous composite electrodes are simulated. The mean total polarization resistance, the mean total power density, and the temperature distribution in the cells are predicted. The results of this study reveal that there is an optimum value for most of the microstructural variables of the electrodes at which the mean total polarization resistance of the cell is minimized. There is also an optimum value for most of the microstructural variables of the electrodes at which the mean total power density of the cell is maximized. The microstructure of porous composite electrodes also plays a significant role in the mean temperature, the temperature difference between the hottest and coldest spots, and the maximum temperature gradient in the solid structure of the cell. Overall, using the combined micro- and micro-model, an appropriate microstructure for porous composite electrodes to enhance the cell performance can be designed.

At the system level, the full load operation of two SOFC systems is studied. To model these systems, the basic cell model is used for SOFCs at the cell level, the repeated-cell stack model is used for SOFCs at the stack level, and the thermodynamic model is used for the balance of plant components of the system. In addition to these models, a carbon deposition model based on the thermodynamic equilibrium assumption is employed.

For the system level model, the first SOFC system considered is a combined heat and power (CHP) system that operates with biogas fuel. The performance of this system at three different configurations is evaluated. These configurations are different in the fuel processing method to prevent carbon deposition on the anode catalyst. The fuel processing methods considered in these configurations are the anode gas recirculation (AGR), steam reforming (SR), and partial oxidation reformer (POX) methods. The application of this system is studied for operation in a wastewater treatment plant (WWTP) and in single-family detached dwellings. The evaluation of this system for operation in a WWTP indicates that if the entire biogas produced in the WWTP is used in the system with AGR or SR fuel processors, the electric power and heat required to operate the plant can be completely supplied and the extra electric power generated can be sold to the electrical grid. The evaluation of this system for operation in single-family detached dwellings indicates that, depending on the size, location, and building type and design, this system with all configurations studied is suitable to provide the domestic hot water and electric power demands.

The second SOFC system is a novel portable electric power generation system that operates with liquid ammonia fuel. Size, simplicity, and high electrical efficiency are the main advantages of this environmentally friendly system. Using a sensitivity analysis, the effects of the cell voltage at several fuel utilization ratios on the number of cells required for the SOFC stack, system efficiency and voltage, and excess air required for thermal management of the SOFC stack are studied.

Acknowledgements

I wish to express profound gratitude to my supervisor, Prof. Feridun Hamdullahpur, for his advice, encouragement, support, and insight throughout this research thesis. I would like to express sincere thanks to Mr. Yeong Yoo, a senior research officer from NRC-ICPET, for his support. I would also like to thank all my committee members, Prof. Xiangue Li, Prof. Fue-Sang Lien, Prof. Michael Fowler, and Prof. Junjie Gu, for their valuable time in reading this thesis, and for their comments and constructive criticism.

I gratefully acknowledge the financial support provided by Natural Sciences and Engineering Research Council (NSERC) of Canada. I would also like to thank to Prof. Edgar A. Matida from Carleton University and my colleagues, especially Dr. Can Ozgur Colpan and Dr. Fahad Al-Sulaiman, for their technical and moral support.

Last, but not least, I thank my wife Maryam Younessi-Sinaki for her full support during this research thesis and my parents, Ali Farhad and Monir Faramarzi-Nia, for their moral support.

To My Family

Table of Contents

List of Tables

List of Figures

List of Symbols

A	Area, m^2 / Coefficient of reaction rate constant, $m\ s^{-1}\ K^{-1}$ or $mol\ m^{-2}\ s^{-1}\ K^{-1}$
A_{TPB}	Electrochemical Active area per unit volume of electrode, $m^2\ m^{-3}$
C	Concentration, $mol\ m^{-3}$ / Carbon atom ratio
$\dot{C}$	Rate of consumption, $mol\ s^{-1}$
$\dot{C}'''$	Rate of consumption per unit volume, $mol\ m^{-3}\ s^{-1}$
$\overline{c_p}$	Heat capacity at constant pressure, $J\ mol^{-1}\ K^{-1}$
d	Differential / Diameter, m
D_A^{eff}	Effective diffusivity of anode, $m^2\ s^{-1}$ (see Equation (3.46))
D_C^{eff}	Effective diffusivity of cathode, $m^2\ s^{-1}$ (see Equation (3.47))
D_h	Hydraulic diameter, m
D_K^{eff}	Knudsen effective diffusivity, $m^2\ s^{-1}$
D_{l-m}^{eff}	Ordinary effective diffusivity of l through m, $m^2\ s^{-1}$
E°	Standard voltage, V
EA	Excess air
E_{act}	Activation energy, $J\ mol^{-1}$
E_{rev}	Reversible voltage, V
$\overline{e_x}$	Molar specific exergy, $J\ mol^{-1}$
$\dot{E}_x$	Rate of exergy, W
f	Darcy friction factor
F	Faraday's constant, $C\ mol^{-1}$
g	Gravity, $m\ s^{-2}$

$\bar{g}$	Molar specific Gibbs free energy, J mol^{-1}
h	Heat transfer coefficient, W m^{-2} K^{-1}
H	Height, m / Hydrogen atom ratio
$\bar{h}$	Molar specific enthalpy, J mol^{-1}
i	Current density, A m^{-2}
I	Current, A
i_0	Exchange current density, A m^{-2}
i_n	Transfer current density per unit of electrochemical active area, A m^{-2}
ITD	Initial temperature difference, K
j	jth finite volume along the length of the cell
k	Reaction rate constant, m s^{-1} or mol m^{-2} s^{-1} / Thermal conductivity, W m^{-1} K^{-1}
K_p	Equilibrium constant
L	Length, m
$\overline{LHV}$	Lower heating value, J mol^{-1}
M^{FV}	Number of finite volume along the thickness of the cell
MW	Molecular weight, g mol^{-1}
n	Number fraction of electron- or ion-conducting particles
$\dot{n}$	Molar flow rate, mol s^{-1}
$\dot{n}''$	Rate of molar flux, mol s^{-1} m^{-2}
N_{Cell}	Number of cells in the stack
N_{ch}	Number of fuel or air channels in a cell
N^{FV}	Number of finite volume along the length of the cell
$N_{Parallel}$	Number of parallel connections of cells in the stack
N_{pores}	Number of pores in an electrode

N_{Series}	Number of series connections of cells in the stack
n_t	Total number of particles per unit volume of electrode, m^{-3}
Nu	Nusselt number
O	Oxygen atom ratio
p	Pressure, Pa
P	Cluster probability of ion- or electron-conducting particle
$\dot{P}$	Rate of production, mol s^{-1}
p_{atm}	Atmospheric pressure, Pa
Pe	Péclet number
Pr	Prandtl number
$\dot{Q}$	Rate of heat transfer, W
R	Polarization resistance, Ω m^{-2}
R'	Resistivity, Ω m
R^{eff}	Effective resistivity, Ω m
R_u	Universal gas constant, J mol^{-1} K^{-1}
Ra	Rayleigh number
Re	Reynolds number
T	Temperature, K
T_∞	Ambient temperature, K
TER	Thermal energy to electric power ratio
U_f	Fuel utilization ratio
V	Voltage, V / Velocity, m s^{-1} / Volume m^3
W	Width, m
$\dot{w}$	Electric power density, W m^{-2}

$\dot{W}$	Electric power, W
x	Mole fraction / Spatial coordinate along the thickness of the cell
x'	Mole fraction in absence of inert gases in a gaseous mixture
y	Spatial coordinate along the length of the cell
z	Spatial coordinate along the width of the cell
Z	Overall average number of contact to a particle
Z'_1	Defined parameter (see Equation (3.259))
$Z'_{15(I)}$	Defined parameter (see Equation (3.256))
Z_{el}	Average number of contacts of both electron- and ion-conducting particles to an electron-conducting particle
Z_{io}	Average number of contacts of both electron- and ion-conducting particles to an ion-conducting particle
$Z_{el\text{-}el}$	Average number of electron-conducting particles in contact with an electron-conducting particle
$Z_{el\text{-}io}$	Average number of ion-conducting particles in contact with an electron-conducting particle
$Z_{io\text{-}io}$	Average number of ion-conducting particles in contact with an ion-conducting particle

Greek letters

α	Particle size ratio, d_{io}/d_{el} / aspect ratio of channel / thermal diffusivity, $m^2 s^{-1}$
β	Transfer coefficient
β'	Defined parameter, J mol^{-1} (see Equation (3.24))
β_0	Flow permeability, m^2
β_{th}	Thermal volume expansion, K^{-1}
γ'	Defined parameter, J mol^{-1} (see Equation (3.25))
δ	Thickness, m

δ'	Defined parameter, J mol^{-1} (see Equation (3.26))
ε	Porosity / Emissivity
η	Polarization, V / Efficiency
θ_c	Contact angle between an electron and ion conducting particle, rad
ϑ	Rate of reaction, mol m^{-2} s^{-1}
ℓ_{Char}	Characteristic length, m
μ	Dynamic viscosity, kg m^{-1} s^{-1}
ν	Kinematic viscosity, m^{2} s^{-1}
σ	Stefan-Boltzmann constant, W m^{-2} K^{-4}
τ	Tortuosity
φ	Volume fraction of electron or ion conducting particle

Subscripts

0	Ambient or reference
a	Air
A	Anode
$A\|E$	Interface of the anode and electrolyte
B	Boudouard reaction
bwd	Backward reaction
C	Cathode
$C\|E$	Interface of the cathode and electrolyte
CD	Carbon decomposition reaction
CDB	Carbon deposition boundary
ch	Channel
COR	Carbon monoxide reduction reaction

dest	Destruction
dew	Dew point
E	Electrolyte
ent	Entrance
el	Electron-conducting particle
ext	Exit
f	Fuel
FL	Functional layer
fwd	Forward reaction
I	First law
ig	Inert gas
II	Second law
Int	Interconnect
io	Ion-conducting particle
j	j^{th} finite volume along the length of the cell
l	l^{th} component of fuel
l'	$l'^{\,th}$ component of air
l"	$l''^{\,th}$ component of flue gas
m	m^{th} component of fuel
max	Maximum
min	Minimum
n	Number of fuel components
N^{FV}	N^{th} finite volume along the length of the cell
PEN	Positive electrode-Electrolyte-Negative electrode

s	Solid structure
s→a	Solid structure to air
s→f	Solid structure to fuel
SL	Substrate layer
$SL \parallel FL$	Interface of the anode substrate and functional layers
SR	Steam reforming reaction
tot	Total
WGS	Water-gas shift reaction

Superscripts

0	Pure material
o	Standard pressure

Abbreviations

0-D	Zero-dimensional
1-D	One-dimensional
2-D	Two-dimensional
3-D	Three-dimensional
A	Anode
AFC	Alkaline fuel cell
AGR	Anode gas recirculation
BoP	Balance of plant
C	Cathode
CDB	Carbon deposition boundary
CGR	Cathode gas recirculation
CHP	Combine heat and power

DGM	Dusty gas model
E	Electrolyte
GDC	Gadolinia-doped Ceria
Int	Interconnect
LSM	Strontium-doped lanthanum manganite
MCFC	Molten carbonate fuel cell
mCV	Minimum cell voltage
PAFC	Phosphoric acid fuel cell
PEFC	Polymer electrolyte fuel cell
PEN	Positive electrode-Electrolyte-Negative electrode
POX	Partial oxidation
SOFC	Solid oxide fuel cell
SR	Steam reforming
TER	Thermal to electric ratio
WGS	Water-gas shift
WWTP	Wastewater treatment plant
YSZ	Yttria-stabilized zirconia

Chapter 1

Introduction

The consumption of fossil fuels is increasing in the world due to the improvement in the quality of life, the industrialization of developing countries, and the increase in the world population. The increase in fossil fuel consumption leads to an increase in the rate of depletion of the fossil fuel reserve and the resulting negative impact on the environment. Therefore, fundamental changes in energy systems are necessary to improve their efficiency and to employ renewable fuels. Fuel cells are one of the cleanest and most efficient devices for generating electric power that can be potentially employed in a wide variety of applications, such as on-site electric power for residential and commercial buildings, auxiliary power units, portable electric power generation, and dispersed and distributed power generation. In fuel cells, the chemical energy of a fuel is converted directly into electrical energy through electrochemical reactions; therefore, the efficiency of fuel cells is not limited by thermodynamic limitations of heat engines, namely, Carnot efficiency. In fuel cells, the intermediate steps of producing heat and mechanical work, which are characteristics of many conventional power generation systems, are eliminated. In addition, because combustion is eliminated, fuel cells generate power with minimal pollutants.

Fuel cells are classified according to the choice of electrolyte and fuel, which in turn determine the electrode reactions and the type of ions that carry the current across the electrolyte [1]. The most common types of fuel cells are the polymer electrolyte fuel cell (PEFC), alkaline fuel cell (AFC), phosphoric acid fuel cell (PAFC), molten carbonate fuel cell (MCFC), and solid oxide fuel cell (SOFC). Some of the characteristics of these fuel cells are summarized in Table 1.1. The focus of this study is on the SOFCs.

1.1 Background

The high efficiency and high fuel flexibility make SOFCs an ideal candidate for a better exploitation of fossil fuels. The electrolyte in SOFCs is a solid, nonporous metal oxide. Due to the limited ion conductivity of solid electrolytes, SOFCs operate at an elevated temperature that may be between 600 – 1000 °C. During the past century, considerable advances were made in the theory and experimentation of SOFCs. At present, the electrical efficiency of SOFCs has achieved almost 55%; however, this efficiency can reach around 70% if SOFCs are combined with a gas turbine [3].

Table 1.1: The operational characteristics of some of the most common types of fuel cells.

Item	**PEFC**	**AFC**	**PAFC**	**MCFC**	**SOFC**
Charge carrier	H^+	OH^-	H^+	CO_3^{2-}	O^{2-}
Operating temperature [1]	40–80 °C	65–220 °C	205 °C	650 °C	600–1000 °C
Electrical Efficiency [2]	45–60%	40–60%	55%	60–65%	55–65%
External reformer for hydrocarbon fuels	Yes	Yes	Yes	For some fuels	For some fuels
Heat management [1]	Process gas + Liquid cooling medium	Process gas + Electrolyte recirculation	Process gas + Liquid cooling medium	Process gas + Internal reforming	Process gas + Internal reforming
Applications	Portable, Mobile, Space, Stationary [2]	Space, Mobile [2]	Dispersed / distributed power generation [2]	Distributed power generation [2]	See Figure 1.1

The SOFC technology is being developed for a broad range of applications such as heat and power generation in residential and industrial sectors, portable electric power generation, and oxygen production. The applications of SOFCs and the corresponding range of the operating power are summarized in Figure 1.1. To commercialize SOFCs for these applications, many collaborative programs have been initiated in the world. Examples are the *SECA* program in the United States, the *Framework 6* program in the European Union, and the *NEDO* program in Japan. Considering the research that is being carried out in the field of SOFCs, it is expected that SOFCs would be one of the major power generation devices for the next decade [4].

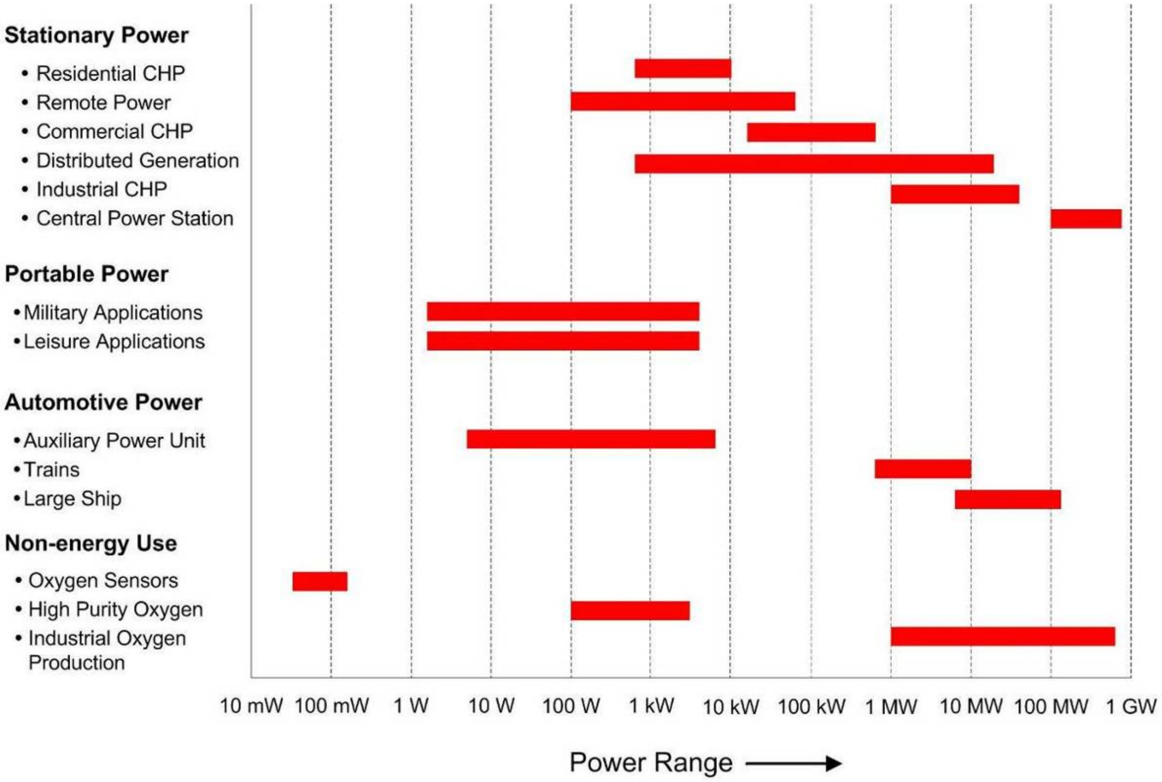

Figure 1.1: The applications of SOFCs [5].

As shown in Figure 1.2, a single cell of SOFC is made from solid layers of an anode (negative electrode), an electrolyte, and a cathode (positive electrode). The anode layer is made from particulate materials that are partially sintered to form porous conducting layer to allow fuel to flow toward the electrolyte. Nickel is the main material used in SOFC anodes because of its excellent catalytic properties for electrochemical reactions and reforming hydrocarbons, low reactivity with other components, and fairly low cost. To increase the adhesive ability of nickel to yttria-stabilized zirconia (YSZ) electrolytes and to improve the electrochemical performance of the anode, a mixture of Ni and YSZ powders (Ni-YSZ cermet) is usually used in anodes.

The cathode layer is also made from particulate materials that are partially sintered to form a porous conducting layer to allow air to flow toward the electrolyte. The cathodes operate in a highly oxidizing environment; hence, the base metals are not used in the structure of cathodes. Strontium-doped lanthanum manganite (LSM) gives a good electronic conductivity and thermal expansion coefficient for the cathode and is now commercially available for SOFCs. To increase the electrochemical reaction active sites of cathodes, a mixture of LSM and YSZ powders is usually used in cathodes.

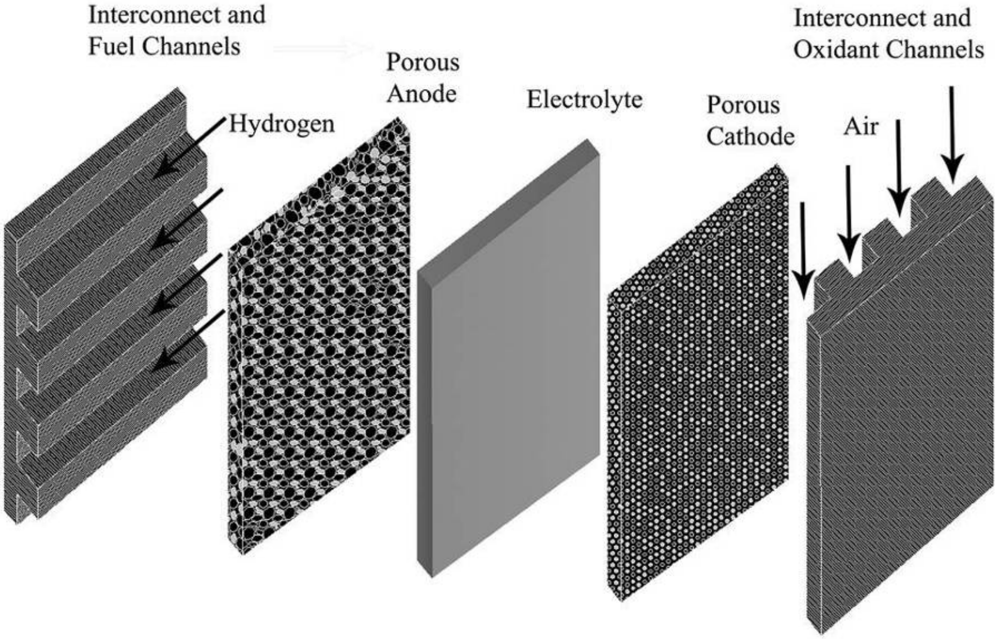

Figure 1.2: Structure of a cell of planar SOFC.

The electrolyte is a dense, gas-tight, and ion conductor layer in the cell that is sandwiched between the porous anode and cathode, and acts as a membrane to separate air and fuel from each other. The main electrolyte material used in SOFCs is YSZ. Although many other oxide materials conduct oxide ions better than YSZ, this material has the significant advantages of abundance, chemical stability, and non-toxicity in comparison to other oxide materials.

To use a cell for power generation, interconnect layers may be required. As shown in Figure 1.2, the interconnect layers are connected to the anode and cathode to collect the electric current generated and to supply fuel and air to the porous anode and cathode layers, respectively. The interconnect layer can be made from ceramic materials, e.g., magnesium-doped Lanthanum Chromite [4] or metallic alloys, e.g., Crofer® 22APU [6].

SOFCs may be classified according to the cell geometry, the arrangement of fuel and air flows, and the cell supporting layer. Because the electrolyte of SOFCs is solid, the cell can be fabricated with various geometries, such as tubular or planar. A planar cell is a flat plate, usually rectangular or circular. A tubular cell is like a tube. In most common designs of tubular cells, the tube is closed at one end and either air or fuel flows inside the tube and the other gas flows outside the tube. The sealing and separating fuel from air is easier for the tubular design of the cell; however, the efficiency and power density of the planar design is higher. The fuel and air may be co-flow (air and fuel flow parallel and in the same direction), counter-flow (air and fuel flow parallel but in opposite directions), or cross-flow (air and fuel flow perpendicular to each other). The flow arrangement may affect the distribution of several physical, chemical, and electrochemical variables in the cell. A cell may be self-supported or externally supported. In the self-supported cell, one of the electrolyte, anode, or cathode layers, often the thickest one, mechanically supports the cell structure. Thus, a self-supported cell can be electrolyte-supported, anode-supported, or cathode-supported. In the externally supported cell, the cell may be configured as thin layers on the interconnect.

To generate electric power in a cell, as shown schematically in Figure 1.3, air enters the air channel and O_2 molecules of air diffuse through the porous cathode toward the electrolyte. Then O_2 molecules are ionized by capturing electrons in the active sites of the cathode through the electroreduction reaction (2.R1). The O_2 ions produced then migrate through the electrolyte toward the anode. From the other side, fuel enters the fuel channel and the H_2 and/or CO contents of the fuel diffuse through the porous anode toward the electrolyte. The H_2 and/or CO molecules react with O_2 ions through electrooxidation reactions (2.R2) and/or (2.R3) in the active sites of the anode. This produces H_2O and/or CO_2 and the electrons are liberated. The liberated electrons flow to an external circuit and the electric power is generated.

$$O_2 + 4e^- \rightarrow 2O^{2-} \tag{2.R1}$$

$$H_2 + O^{2-} \rightarrow H_2O + 2e^- \tag{2.R2}$$

$$CO + O^{2-} \rightarrow CO_2 + 2e^- \tag{2.R3}$$

Because the electrochemical reactions to generate electric power take place at active sites of the anode and cathode, as electrodes of a cell, the improvement of the electrochemical performance of electrodes can play an important role in improving the performance of the cell. To improve the electrochemical performance of electrodes, in addition to the use of materials with a high catalytic activity, the electrodes can be fabricated with a composite structure that has extended active sites for electrochemical reactions [7-9]. The microstructure of a porous composite electrode is made of three phases: electron-conducting particles to transport electrons, ion-conducting particles to transport oxygen ions, and pores to transport reactant gases. The electrochemical reactions may take place throughout the microstructure of these electrodes where these three phases are present.

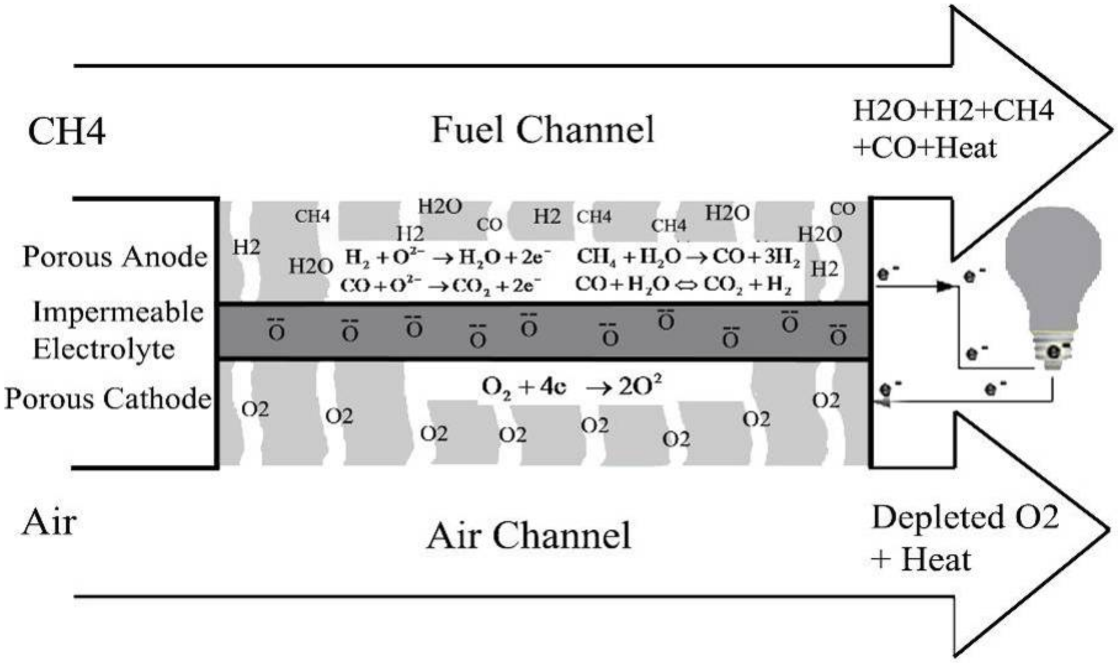

Figure 1.3: Electric power generation in SOFCs.

The use of hydrocarbon fuels always has the potential of carbon deposition on the anode catalyst. The carbon deposition leads to deactivation of the anode due to the reduction of electrochemical active sites. There are a number of methods for processing a hydrocarbon fuel. The three most popular methods are the anode gas recirculation (AGR), external steam reforming (SR), and external partial-oxidation (POX) methods. In the AGR method, a part of the outlet gas from the anode channels is mixed with the fuel stream to make a fuel suitable for SOFCs. Indeed, the water vapour and carbon dioxide in the outlet gas may react with hydrocarbon fuel to produce hydrogen and carbon monoxide before feeding the fuel to the cell. The SR is the most popular method of converting light hydrocarbons to hydrogen. This endothermic process provides the highest concentration of hydrogen. In this method, the fuel is heated and vaporized, then injected with superheated steam into a steam reformer reactor. Excess steam may be required to force the reaction to completion as well as to inhibit soot formation on the reactor catalyst. Most commercial steam reformers use Ni catalyst to enhance reaction rates at decreased temperatures. The reforming catalyst also promotes the exothermic water-gas shift (WGS) reaction in the steam reformer reactor. Because the combined SR and WGS reactions are endothermic, an external high temperature heat source is required to operate the reactor. The steam reforming is also a slow reaction and requires a large reactor; therefore, rapid start and transients cannot be achieved by SR method [1]. In the POX method, a substoichiometric amount of air or oxygen is used to partially combust the fuel. The POX is a fast process with a fast response and it uses a small reactor size. Non-catalytic POX fuel processors/reformers operate at temperatures of around 1400°C, but catalytic POX fuel processors/reformers may typically operate at temperatures of around 870°C. The POX reaction is highly exothermic; hence, the reformer does not need an external heat source [1].

The voltage that a single cell of SOFC can deliver is low for most practical applications. To reach a desired voltage, a number of cells should be connected in series. An SOFC stack consists of a group of cells that may be connected in series and fed by fuel and air in parallel. Of course, several SOFC stacks may be connected in parallel or in series to reach a desired electric power and voltage for an SOFC system.

In addition to the SOFC stack, an SOFC system requires several other sub-systems/components; the so-called balance of plant (BoP). In general, SOFC stacks need a steady supply of qualified fuel and air for continued generation of electric power. The temperature of the fuel and air should be close to the operating temperature of the cell. Therefore, the SOFC systems should be equipped with devices to increase the fuel and air temperatures. To prevent carbon deposition on the anode catalyst, a fuel processor may be required for systems that operate with hydrocarbon fuels. The pressure of fuel and air streams should also be increased to overcome pressure drops in the system. Since SOFC stacks generate DC electricity that is typically not directly usable for a load, electric power conditioning may be required to generate AC electricity. These are the minimum number of BoP components that are usually required for an SOFC system. The need to use other components depends on the fuel choice, the requirements of the cell and stack, and the application of the system. It is noted that the BoP components represent a significant fraction of the weight, volume, and cost of most SOFC systems.

An SOFC system can be designed to operate with a broad range of fuels. However, the main fuels considered in this research thesis are biogas and ammonia.

Biogas is a renewable and alternative source of fuel that can assist in reducing the consumption of fossil fuel and the emission of greenhouse gases. This gas – which is mainly produced using anaerobic digestion or fermentation of biodegradable materials such as biomass, manure, sewage, and municipal waste – has been recognized by the United Nations development program as one of the important decentralized sources of energy [10]. Pressure from environmental legislation on solid waste disposal methods in developed countries has increased the application of the anaerobic digestion process in wastewater treatment plants (WWTPs) for reducing waste volume and generating useful by-products. One of the important by-products of this process is a biogas containing mainly methane and carbon dioxide. If biogas is fed directly to a cell, the anode catalyst may be deactivated due to carbon deposition issues. Therefore, the SOFC system should be equipped by devices to process biogas before it is fed to the SOFC stack. Of course, due to the high carbon dioxide content of biogas, the reforming agent required to process biogas is substantially lower than that to process natural gas. However, the electrical efficiency of an SOFC system may drop around 1.1% if biogas is used instead of natural gas [11].

Ammonia is a gas at atmospheric pressure and ambient temperature; however, the gaseous ammonia can be easily liquefied at ambient temperature and pressure of around 10 atm. In these conditions, the density of ammonia increases around 850 times, which makes it a cost-effective fuel for portable applications [12]. The volumetric energy density of liquid ammonia is comparable with that of gasoline or methanol [12]. Ammonia is safer than many fuels because it does not burn in air under common conditions and it is generally considered non-flammable when transported. If released into the atmosphere, due to its lower density in comparison with air, it dissipates rapidly. In addition, because of its smell characteristic it can be easily detected [13]. According to the fuel maps developed for SOFCs, ammonia is a suitable fuel for electric power generation with high maximum voltage and efficiency [14, 15]. Of course, ammonia is corrosive [16]. If it is fed directly to a cell, the anode catalyst may be rapidly destroyed. However, this problem can be solved by decomposing ammonia into its constituent elements, i.e., nitrogen and hydrogen, before it is fed to the cell. These characteristics make ammonia a proper substitute with hydrogen and hydrocarbon fuels for the portable application of SOFC systems [17, 18]. It should be noted, that the use of hydrocarbon fuels increases the size and cost of the portable system because a fuel processor and a gas clean up system may be required [19, 20].

1.2 Thesis Objectives and Outline

The main objectives of this research thesis are as follows:

- Developing a model for SOFCs at the cell level to link the microstructure of porous composite electrodes to the cell performance.
- Developing a model for SOFCs at the system level to study the effect of the inlet hydrocarbon fuel and the fuel processor on system performance.

To develop a cell level model to link the microstructure of porous composite electrodes to the cell performance, both micro-model and macro-model of the cell are required. In the micro-model, the complex interdependency among the multi-component mass transport, electron and ion transports, and the electrochemical and chemical reactions within the microstructure of electrodes should be taken into account to predict the electrochemical performance of porous composite electrodes. In the macro-model, the energy transport in the cell solid structure and the mass and energy transports in the fuel and air streams should be considered to predict the local temperature of the cell solid structure and the local temperature and species partial pressures of the bulk fuel and air streams. Because the transport equations of the micro-model and macro-model are coupled, these models should be combined. The combination of these two models establishes a new cell level model that we have titled the combined micro- and macro-model. The transport equations and the chemical and electrochemical reactions that are considered in this new model for an anode-supported co-flow planar cell with porous composite electrodes are demonstrated in Figure 1.4. This model is described in detail in Chapter 3.

The originality of the combined micro- and macro-model lies in the fact that this model considers the electrochemical reaction(s) at the active site of the microstructure of porous composite electrodes at the real operating conditions of the cell. For example, at the real operating conditions of a co-flow planar cell, the temperature of the electrode and the partial pressures of reactants and products vary along the cell length. The main application of this model is to design an appropriate microstructure for porous composite electrodes to enhance the cell performance.

To develop a system level model for SOFCs that can predict the effect of the inlet hydrocarbon fuel and the fuel processor on the system performance – in addition to the cell level, stack level, and BoP models – a carbon deposition model is required. Because the heat transfer from the outer surfaces of the SOFC stack may play an important role in performance prediction of SOFC systems, a model to predict this heat transfer should be used. The concept of this system level model is shown in Figure 1.5.

As seen in this figure, the carbon deposition model is connected to the cell level model and the fuel-processor model as one of the BoP components of the SOFC system. Indeed, the carbon deposition model is used to predict the composition of the processed hydrocarbon fuel at the entrance of the cell and the minimum flow rate of reforming agent required for the fuel processor. This system level model can be applied for parametric studies and performance prediction of SOFC systems operating at a full load. This model is described in detail in Chapter 3.

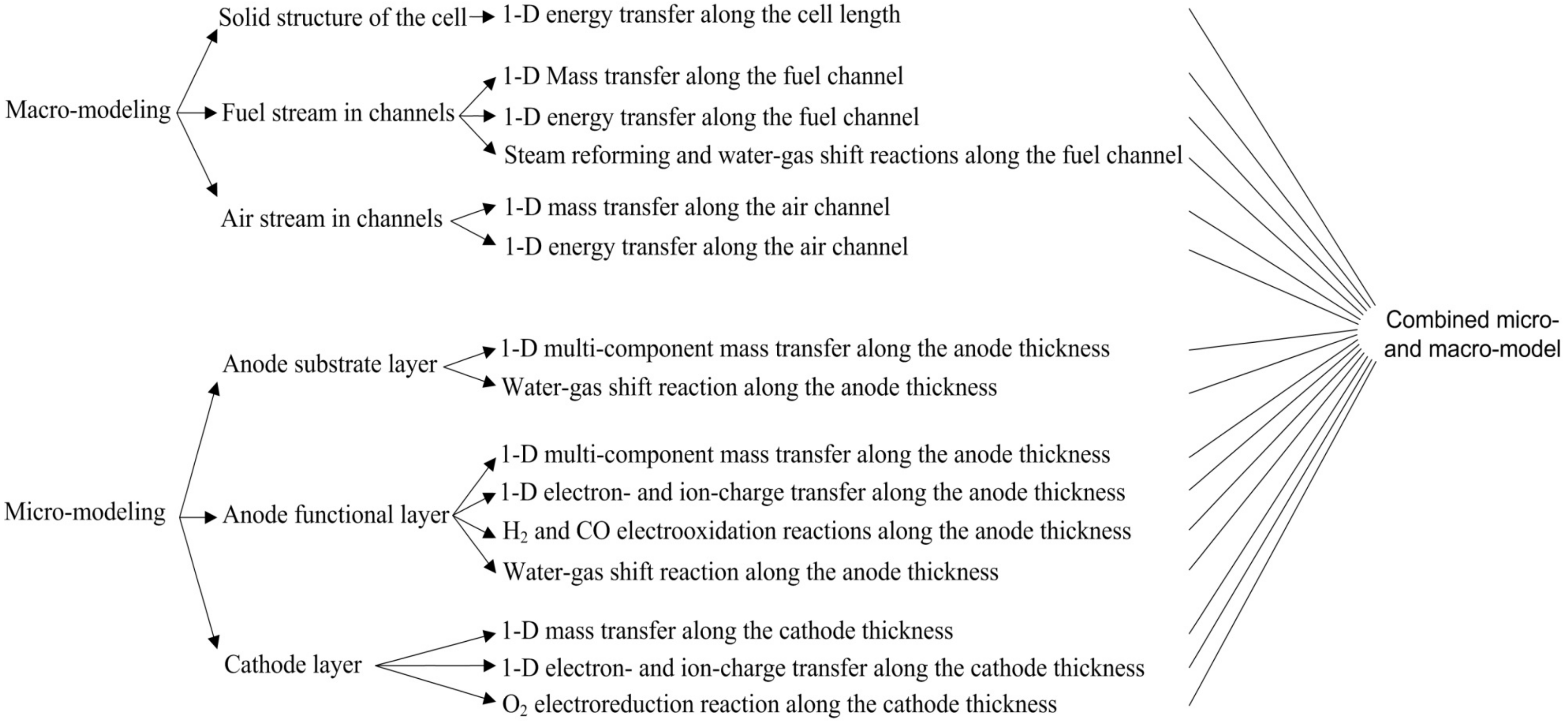

Figure 1.4: The combined micro- and macro-model for an anode-supported co-flow planar cell with porous composite anode and cathode.

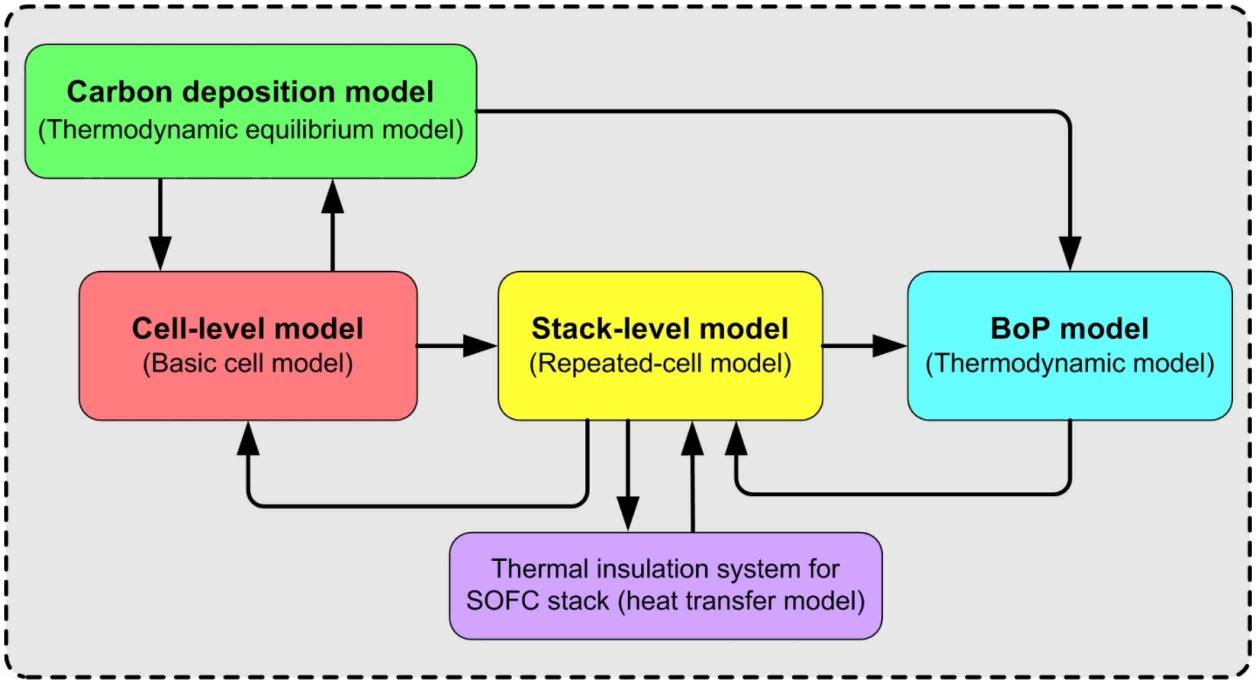

Figure 1.5: The suggested SOFC model at the system level.

This research thesis consists of five chapters. The SOFC models published in the literature that are important for the objectives of this research are reviewed in Chapter 2. Some of the results reported in the literature that are useful to effectively model SOFCs are also described in this chapter. In Chapter 3, the carbon deposition model and the cell, stack, and system level models of SOFCs in steady state operating conditions are presented. The validation and results of the models developed are presented in Chapter 4. Finally, some key conclusions and recommendations for future work are outlined in Chapter 5.

Chapter 2

Literature Survey

The activity in the field of SOFC modeling has been increased in the past two decades. Considerable progress in SOFC modeling has led to an improved understanding of relevant physical, chemical, and electrochemical phenomena in SOFCs. The SOFC models may be divided into the carbon deposition models and cell, stack, and system level models. These models are briefly described in this chapter.

2.1 Carbon Deposition Models

Several models have been developed to investigate the possibility of carbon deposition on the anode catalyst. In most of these models, the possibility of carbon deposition for different fuels is studied on the basis of thermodynamic equilibrium assumption. There are also a very few studies that take into account the detailed reaction mechanism and heterogeneous kinetics inside the porous anode catalyst [21] that are beyond the scope of this research thesis.

One of the earliest and fundamental studies that predicted carbon deposition was carried out by Cairns *et al.* [22] in 1964. They calculated the gas phase compositions in equilibrium with solid carbon for the full composition range of the CHO system and for temperatures in the range of 298 K to 1500 K at atmospheric pressure. Their calculation was based on the direct algebraic solution of a set of nonlinear equations, which were obtained from the material balance equations and the nonlinear form of the standard equilibrium constant equations. They introduced a very useful triangular representation of carbon deposition data in the C-H-O ternary diagram. They found that the species of major importance of a fuel in equilibrium are carbon in the solid phase and CO, CO_2, H_2, H_2O, and CH_4 in the gaseous phase. Sasaki *et al.* [23] also achieved the same results in 2003 through calculation of the chemical species of the equilibrium products of 300 different fuels including alkanes, alcohols, alkenes, alicyclic hydrocarbons, dimethyl ether, biogas, and coke oven gas.

In 1965, Broers *et al.* [24] established a simple method that was based on the findings of Cairns *et al.* [22] to obtain carbon deposition boundaries (CDBs) directly from three independent equations involving three equilibrium constants. No material balance equations and no trial and error procedures were needed in their method. However, they did not study the effect of the inert gas content of a fuel on the carbon deposition.

In the past two decades, the possibility of carbon deposition was studied through the Gibbs free energy minimization technique. For example, in 2005, Assabumrungrat *et al.* [25] employed this technique and analyzed the carbon formation in a methanol-fuelled SOFC. In their study, equilibrium calculations were performed to find the range of inlet steam to methanol ratio where carbon formation is thermodynamically unfavorable in the temperature range of 500 K to 1200 K. Singh *et al.* [26] also studied the risk of carbon deposition due to the tars present in the gasified biomass through the Gibbs free energy minimization technique. They studied the effect of various parameters such as current density, steam, and temperature on carbon deposition. Although the Gibbs free energy minimization technique can consider the effects of inert gases and the minor amount of heavy hydrocarbons in equilibrium composition of the fuel, the computational cost of this method is significantly higher than the method developed by Broers *et al.* [24].

In this research thesis, the method developed by Broers *et al.* [24] is modified to consider the effect of inert gases. It is then used to determine the minimum reforming agent required to process a hydrocarbon fuel to prevent carbon deposition on the anode catalyst.

2.2 SOFCs Models at Cell Level

There are several cell level models in the literature with a variety of complexities and accuracies to predict the performance of SOFCs. These models are included in, but not limited to, the zero-dimensional models, macro-models, and micro-models. These models are briefly described in the following sections.

2.2.1 Zero-dimensional Model

The zero-dimensional (0-D) model is the simplest approach to model SOFCs at the cell level. Using the principles of thermodynamics and electrochemistry, several performance parameters of a cell, such as the efficiency and output power, can be predicted. In this model, the electrochemical reactions are assumed to take place at the interface of electrodes and electrolyte and all physical, chemical, and electrochemical variables are assumed to be uniform throughout the cell. Of course, to calculate the concentration polarization, the partial pressure of the fuel and air species at the reaction sites are usually determined through a one-dimensional (1-D) mass transfer analysis along the thickness of electrodes. For this reason, we call this model the Basic Cell Model instead of the 0-D model. This modeling approach is broadly employed for evaluating SOFCs at the system level.

One of the earliest basic cell models was suggested by Kim *et al.* [27] in 1999. They considered humidified hydrogen as the fuel and modeled an anode-supported cell. They performed a simple 1-D mass transfer analysis based on Fick's law for estimating concentration polarization in electrodes. They considered both ordinary and Knudsen diffusions to make their mass transfer analysis accurate for different porous electrode designs. They also used Tafel equation to estimate the activation polarization; however, this equation is valid for large activation polarizations. In 2001, Chan *et al.* [28] replaced the Tafel equation with the Butler-Volmer equation for more precise prediction of the activation polarization. However, to calculate the activation polarization, the exchange current density was considered as constant. In 2002, Chan *et al.* [29] modified their model to include hydrocarbon fuels in addition to the humidified hydrogen. However, their model could not estimate the optimum composition of the processed fuel to prevent carbon deposition on the anode catalyst. Determination of the optimum composition of the processed fuel at different operating condition of the cell is necessary to precise evaluation of the system performance. In 2005, Chan *et al.* [30] used their cell level model to simulate an SOFC system fed by methane. To simulate the cell, they considered the exchange current density as a function of temperature. However, their model still could not predict the optimum composition of the processed fuel.

In this research thesis, the basic cell model is improved by adding a carbon deposition model to determine the optimum composition of the processed fuel. This modification increases the computational cost negligibly and makes this model stronger for a more precise evaluation of SOFC systems.

2.2.2 Macro-Models

In macro-models, in addition to the principles of thermodynamics and electrochemistry, the charge, mass, momentum, and energy transport equations in zero-dimension, one-dimension, two-dimension (2-D), or three-dimension (3-D) may be employed to predict the cell performance and distribution of several physical, chemical, and electrochemical variables in the cell. These variables may be included in, but not limited to the temperatures and species partial pressures of fuel and air streams, the temperature of the cell solid structure, and the current density. In macro-models, it is generally assumed that the electrochemical reactions take place at the interface of the electrodes and electrolyte. Therefore, the physical, chemical, and electrochemical processes inside the microstructure of porous composite electrodes are neglected in this model.

In macro-modeling of planar cells, a cell is divided into the solid structure and fluid flows. The solid structure may be divided into the anode, electrolyte, cathode, and interconnect. The fluid flows may be divided into the fuel stream passing through fuel channels, the air stream passing through air channels, the fuel flow inside the porous anode, and the air flow inside the porous cathode. The 0-D, 1-D, 2-D, or 3-D heat and charge transport equations may be used for the solid structure to determine the local temperature, voltage, current, and polarizations in the anode, electrolyte, cathode, and interconnect. The 0-D, 1-D, 2-D, or 3-D mass, momentum, and heat transport equations may be used to model the fluid flows to determine the local temperatures, species partial pressures, velocities, and flow rates of air and fuel.

The governing equations that model solid structure and fluid flows are strongly coupled and may be highly non-linear, which make it almost impossible to obtain analytically exact solutions. Therefore, the equations are usually solved numerically. The most commonly used numerical technique to solve governing equations developed for macro-modeling of a cell is the finite volume method (FVM) [31-34]; however, the finite difference method (FDM) [35-37] or even finite element method (FEM) [38-40] may be used. Depending on the objective of a study and the characteristics of a cell, a transport equation may be chosen in 0-D, 1-D, 2-D, or 3-D. For example, the 1-D heat transfer modeling of the solid structure may be used for co- and counter-flow cells; however, at least a 2-D heat transfer model is required for cross-flow cells. The 3-D modeling is usually used when a detailed knowledge of the behavior of SOFCs is needed. For 2-D and 3-D models, commercial computational fluid dynamics (CFD) software may be used. For instance, Yakabe *et al.* [41] and Recknagle *et al.* [42] used the commercial CFD software STAR-CD, Pasaogullari *et al.* [43] used the commercial software FLUENT, and Beale *et al.* [44] used the commercial software PHOENICS for 3-D modeling of a planar cell.

In early macro-models, the electrochemical principles have not been accurately established. For example, in 1994, Achenbach [45] developed a macro-model for co-, counter-, and cross-flow planar cells on the basis of the 1-D mass and heat transfer in fuel and air streams in channels and 3-D heat transfer in the solid structure. He considered the anode, electrolyte, cathode, and interconnect as a lumped homogenous structure in the heat transfer analysis. In his model, the fuel is a multi-component gas mixture, both H_2 and CO molecules participate in electrochemical reactions, the SR reaction is kinetically controlled, and the WGS reaction is in equilibrium. However, he assumed that the partial pressure of fuel and air species along the thickness of the anode and cathode are uniform and, consequently, neglected the concentration polarization. He also used preliminary correlations for the rate of H_2 and CO electrochemical reactions to prediction the activation polarization. Nevertheless, he reported several valuable results. He showed that the temperature of the solid structure is almost uniform along the width (z axis in Figure 3.1) of a co-flow planar cell. This statement is valid for a counter-flow cell if the methane content of fuel is low so that the cooling effect due to methane SR reaction is not significant. For a cross-flow planar cell, the heat transfer along the width of the cell should be considered. In 1996, Fergosen, *et al.* [31] improved the macro-model of co-, counter-, and cross-flow planar cells by taking into account the 3-D charge and heat transfer in anode, cathode, electrolyte, and interconnect. He also took into account the 3-D mass and heat transfer in fuel and air streams in channels, and the 3-D mass transfer of fuel and air species inside the electrodes. In their model, the fuel is a multi-component gas mixture, only the H_2 molecules participate in electrochemical reactions, the SR reaction is kinetically controlled, and the WGS reaction is in equilibrium. Furthermore, in the porous electrodes, Fick's law of diffusion was used. However, according to Krishna and Wesselingh [46] this is valid for binary or dilute mixtures. They reported that the efficiency of counter-flow planar cells is the highest, followed by the cross-flow and co-flow cells.

As macro-models developed, it became clear that the electrochemical models should be improved. In 2001, Yakabe, *et al.* [41] improved the macro-model of co- and counter-flow planar cells by taking into account the 3-D charge and heat transfer in anode, cathode, electrolyte, and interconnect; the 3-D mass, momentum and heat transfer in fuel and air streams in channels; and the 3-D mass, momentum, and energy transfer in fuel and air flows inside the porous electrodes. Their transport equations were coupled to a reliable electrochemical model. In their model, the fuel is a multi-component gas mixture; only H_2 molecules participate in electrochemical reactions; and SR and WGS reactions are kinetically controlled. Their results showed that the solid structure temperature in thickness and width directions of co- and counter-flow planar cells are almost uniform. Therefore, the heat transfer in the solid structure of these cells can be only modeled along the length of the cell. Moreover, because the temperature distribution in the thickness direction is uniform, the PEN (Positive electrode (cathode), Electrolyte, and Negative electrode (anode)) structure can be considered as a lumped homogenous structure in heat transfer modeling.

In 2003, Recknagle *et al.* [42] considered the PEN as a lumped structure in the heat transfer analysis and used almost the same 3-D model developed by Yakabe *et al.* [41] to model co-, counter-, and cross-flow planar cells. However, they did not consider methane in the multi-component fuel. Their results indicated that the temperature of the PEN structure, the current density, and the hydrogen partial pressure along the width of a co-flow cell are uniform. They also found that for a given fuel utilization ratio and average cell temperature, the co-flow cell has the most uniform temperature distribution and the smallest thermal gradients.

In 2004, Aguiar *et al.* [47] developed a successful macro-model for co- and counter-flow planar cells on the basis of the 1-D mass and heat transfer in fuel and air streams in channels, the 1-D heat transfer in the PEN structure and interconnect, and the 1-D mass transfer of fuel and air species inside the porous electrodes. In his model, the fuel is a multi-component gas mixture, only H_2 molecules participate in electrochemical reactions, the SR reaction is kinetically controlled, and the WGS reaction is in equilibrium. Their results showed that the temperatures of the PEN structure and interconnect are very close. Thus, the anode, electrolyte, cathode, and interconnect may be considered as a lumped homogenous structure in the heat transfer analysis.

In 2007, Nikooyeh *et al.* [48] developed a macro-model for internal reforming co-flow planar cells by taking into account the 3-D heat transfer in PEN and interconnect, the 3-D mass transfer in fuel stream passing through channels and inside the porous electrodes, and the 1-D heat transfer in fuel and air streams in channels. In their model, the fuel is a multi-component gas mixture, only H_2 molecules participate in electrochemical reactions, the SR reaction is kinetically controlled, and the WGS reaction is in equilibrium. The results of their studies showed that the solid structure temperature in the thickness direction of co-flow planar cells may not be completely uniform at the beginning of the cell length if the concentration of CH_4 in the inlet fuel is significantly high. For the worst scenario, a maximum temperature difference of <10°C was estimated in the thickness direction of the cell solid structure.

Overall, the behavior of a cell under several operating and design conditions has been adequately determined. This helps to effectively design a cell macro-model for a specific objective by choosing the dimension of each transport equation in each component of the cell.

2.2.3 Micro-Models

In macro-models, it is assumed that the electrochemical reactions take place at the interface of the electrodes and electrolyte. To remove this assumption, micro-modeling of porous composite electrodes is needed. A micro-model considers the microstructure of porous composite electrodes as a volume with extensive reaction sites. The objective of this model, which is based on the continuum mechanics assumptions, is to predict the local polarizations, current density, and rate of chemical and electrochemical reactions inside the microstructure of electrodes.

For micro-modeling, the microstructure of porous composite electrodes should be modeled to predict the microstructural properties of electrodes. For this purpose, the random-packing sphere method is usually used by researchers due to its simplicity and low computational cost, even for small-sized particles. In this method, the electrode is assumed to be random-packing of mono-size electron-conducting and mono-size ion-conducting spheres. The particle coordination number and percolation theories are used to estimate the electrode microstructural properties [49-54]. This method is applicable for electrodes in which their electron- and ion-conducting particles remain almost spherical during the sintering process; it loses its validity if the contact angle between the electron- and ion-conducting particles is large. Of course, several researchers reported that the average contact angle after sintering SOFC electrodes is almost 30° [55-57]. In a real electrode, there is a distribution of the size of particles that may affect the microstructural properties of the electrode. The effect of size distribution cannot be considered in the random-packing sphere method. In 2009, Kenney, *et al.* [58] developed a new method to determine the microstructural properties of a porous composite electrode with any size distribution of electron- and ion-conducting particles. In this method, a spherical electron- or ion-conducting particle is randomly dropped into a domain with specified dimensions. The particle rolls over other particles until it touches three other particles and its position is fixed. The desired volume fraction of electron- and ion-conductors is enforced by assigning a weighted probability to the particle selection before the particle is dropped. To consider the effect of sintering process, the minimum allowable distance between two contacting particles is varied until the desired structure is obtained. This varies the particle-particle contact angle. Using this structural generation technique, the coordinate, the particle size, and the contacting particles are known for each particle within the domain. It is possible to determine whether each particle in the structure belongs to a percolating network by tracking the connecting neighbors of each particle. Although this method can be implemented for any size distribution of electron- or ion-conducting particles, its computational cost is very high, especially for smaller sized particles.

One of the earliest micro-models that established a relation between the microstructure and the electrode performance was developed by Costamagna *et al.* [55] in 1998. They employed the random-packing sphere method to model the macrostructure of electrode. They also developed a 1-D model that takes into account the electron and ion transport through the electrode coupled with the electrochemical reaction at the active sites of the electrode. However, they ignored mass transport of fuel and air species through the pores. In fact, they assumed that the partial pressure of fuel and air species inside the electrodes is uniform and, consequently, ignored the effect of the concentration polarization on the electrode performance. Since the reactant is consumed at the reaction sites, the assumption of uniform concentration of species throughout the electrode may not be valid. They also assumed that the current density, temperature of the solid structure of the cell, and the temperature and partial pressures of the fuel and air species in the channels are uniform. They reported that the microstructure of porous composite electrodes significantly affects the electrode performance. They also emphasized that there is an optimum thickness for porous composite electrodes.

In 2001, Chan *et al.* [59] improved the model developed by Costamagna *et al.* [55] for porous composite anodes by taking into account the mass transport of humidified hydrogen fuel through the anode and considering the concentration polarization. They used Fick's law of diffusion to model the mass transfer. They assumed that the porosity, average pore size, and average tortuosity of the electrode are three independent microstructural variables. However, the average diameter of pores and tortuosity are dependent on the electrode microstructural variables of the porosity, particle size ratio, and size and volume fraction of electron-conducting particles. Moreover, the exchange current density in the Butler-Volmer equation was assumed as constant in their model. They showed that an overall polarization reaches a minimum at a certain particle size. In 2004, they modified their model by taking into account the exchange current density as a function of the partial pressure of hydrogen and water vapour in the fuel [60]. In 2004, they also used their modified model for a porous composite cathode [61, 62]. They considered a reaction mechanism for oxygen reduction at the LSM-YSZ interface. They found poor cathode performance for a very thin composite cathode due to the insufficient active sites for the oxygen reduction reaction. They also reported that the optimal cathode thickness increases with the increase of the particle size.

In 2006, Nam *et al.* [63] considered a micro-model of anode and cathode to model the performance of the PEN structure. They improved the mass transport model by considering the dusty gas model instead of Fick's law. They also established a relation between the average pore diameter and the independent microstructural variables of the electrode. They reported that the particle size, porosity, and thickness of electrodes significantly affect the PEN performance. They also found that at the particle size ratio of unity, the optimum volume fraction of electron-conducting particles is around 0.45 for both anode and cathode. In another study [57], they expanded their model to a PEN structure with two-layer electrodes, namely, the substrate and functional layers.

In 2007, Hussain *et al.* [64] improved the micro-model of the PEN structure with two-layer electrodes by taking into account the multi-component mass transport inside the anode. Their model is fuel-flexible and can consider any gas mixture with an arbitrary composition of CH_4, H_2O, H_2, CO, and CO_2. For such a multi-component gas mixture, the WGS and SR reactions are possible, and they considered these reactions in their model. However, they did not establish a relation between the average pore diameter and tortuosity and the independent microstructural variables of the electrode. They reported that the most significant contribution to cell potential loss is from the anode side of an anode-supported cell.

In 2009, Hussain *et al.* [65] improved the 1-D micro-model to the 2-D micro-model of the PEN structure with two-layer electrodes. However, their results indicated that the key performance parameters of the PEN structure are uniform along the width of the PEN. Therefore, the 2-D micro-model can be reduced to a 1-D micro-model.

Overall, much progress has been made in the micro-modeling of SOFCs. However, to link the microstructure of porous composite electrodes to the cell performance, this model should be significantly improved. For example, the transport equations to determine the local solid structure temperature, the local temperature and partial pressures of fuel and air species in the channel, and the local current density in the cell should be considered. For a hydrocarbon fuel, the electrochemical oxidation of CO in the anode functional layer should be taken into account. A relation between the microstructural variables of porous composite electrodes and the average diameter of pores and tortuosity should be established. The anode- and cathode- side interconnects should be included in the computational domain.

2.3 SOFC Models at Stack Level

The SOFC stack models can be divided into the repeated-cell stack models and the detailed stack models. In the repeated-cell stack model, the distribution of all physical, chemical, and electrochemical variables in all the cells of the stack are assumed to be identical. In this stack model, after prediction of the cell performance by a 0-D, 1-D, 2-D, or 3-D cell model, the stack performance can be easily predicted. For example, the stack power is obtained from multiplication of the cell power by the number of cells of the stack. The computational cost of this model is usually equal to the computational cost of a cell. This stack model is widely applied for the purpose of evaluation of the performance of SOFC systems. For example, in 2005, Chan *et al.* [66] developed a repeated-cell stack model on the basis of the cell 0-D model. They suggested a thermal insulation system for the stack and calculated the heat transfer from the outer surfaces of the stack to the ambient. They introduced this stack model as a suitable model for SOFC system level analyses. In 2006, Braun *et al.* [67] developed a repeated-cell stack model on the basis of the cell 1-D model. They did not calculate the heat transfer from the SOFC stack; however, they added a heat loss term (equal to 3% of the higher heating value of the input fuel) to the energy balance in the stack periphery. In 2010, Colpan *et al.* [68] developed a repeated-cell stack model on the basis of the cell 2-D model. However, the heat transfer from the SOFC stack and its effect on the cell performance was not calculated.

In the detailed stack models, all cells in the SOFC stack are modeled in two or three dimensions. The governing equations of each cell are coupled with governing equations of adjacent cells. The distribution of physical, chemical, and electrochemical variables in all the cells in the stack is determined simultaneously. This stack model is very useful to design a high performance and durable stack and generating the stack performance map. However, the computational cost of this model is very high, especially when the number of cells in the stack increases. Increasing the number of cells may progressively increase the computational cost. For this reason, this stack model is not usually used for evaluating the system performance. In 2008, Staxera Company in Germany [69] conducted an important study on a 30-cell stack. Their results indicated that the difference between the solid structure temperature of the top and bottom cells in the stack may be around 50°C. For such a temperature difference, a significant change in the performance of the cells of a stack may be expected. Therefore, the results of the repeated-cell stack model may not be accurate enough for making stack design decisions. In 2011, researchers in Pacific Northwest National Library (PNNL) in the United States successfully developed a quasi-two-dimensional stack model for co- and counter-flow cells [70]. They could significantly decrease the computational cost of the detailed stack model without notably decreasing the accuracy of the results. This new model can be applied for larger and more powerful stack towers.

Overall, new techniques to reduce the computational cost of the detailed stack model are under development. This model may be employed instead of the repeated-cell stack model for the purpose of the SOFC system level analyses in the future. In this research thesis, the repeated-cell stack model is chosen. Of course, to consider the effect of the difference in the performance of the cells of the stack, a correction term entitled “voltage drop due to stacking” is considered.

2.4 SOFC Models at System Level

Modeling SOFCs at the system level is strongly dependent on the system configuration and the objective of the study. Several SOFC systems with various configurations have been already developed. These systems are included in, but not limited to, the simple SOFC systems [11, 71], which have the simplest layout with minimum number of BoP components to generate only electric power, the SOFC combined heat and power (CHP) systems [72, 73], the SOFC-trigeneration systems [74, 75], the SOFC-gas turbine hybrid systems [76-78], the SOFC-gasifier integrated systems [68, 79], and the SOFC-Rankine cycle systems [80]. The objectives of the SOFC models at the system level are also included in, but not limited to, the performance prediction at full and partial load operations [81], the parametric study [82], the design of a reliable control system [83, 84], and the economic analysis [85] of the system. Among these system configurations and the objectives of the studies, the performance prediction at full load operation and the parametric study of the simple and CHP SOFC systems are the focus of this research thesis.

The SOFC system level models that cover the purposes of this thesis are usually based on the repeated-cell stack model and the thermodynamic model of BoP components of the system. In these models, the mass and energy equations are employed to predict the thermodynamic properties and flow rate of each stream of the system as well as the power and heat generated/required in each component of the system. The exergy analysis may be also employed to determine the exergy destruction in the system and optimization purposes. Some of these models are summarized in the following paragraphs.

In 2005, Yi *et al.* [11] modeled a 25 kW simple SOFC system operated by natural gas, biogas, coal syngas, and diesel reformate. Their model was based on the 0-D repeated-cell stack model and thermodynamic model of BoP components of the system. They have not considered the effect of the stack thermal insulation system on the thermal management of the stack. Their studies indicated that although the SOFC can tolerate a wide variety of fuel composition, the performance and operating conditions of the system significantly change with various fuels.

In 2005, Chan *et al.* [66] modeled the operation of a CHP SOFC system operated by methane fuel. Their model was based on the 0-D repeated-cell stack model and thermodynamic model of BoP components of the system. They considered the effect of the stack thermal insulation system on the thermal management of the stack; however, their model cannot predict the minimum flow rate of water required for the external steam reformer to prevent carbon deposition on the anode catalyst. Nevertheless, they showed that the system can achieve the 1^{st} and 2^{nd} law efficiency of 47% and 48.9%, respectively.

In 2006, Braun *et al.* [67] modeled a CHP SOFC system with five different configurations for application in residential dwellings. These five configurations are 1) hydrogen-fueled, 2) methane-fueled with external and internal catalytic steam reforming, 3) methane-fueled with cathode gas recirculation (CGR), 4) methane-fueled with AGR, and 5) integration of CGR, AGR, and internal reforming concepts. Their model was based on the 1-D repeated-cell stack model and thermodynamic model of BoP components of the system. However, they did not consider the effect of the stack thermal insulation system on the thermal management of the stack. Their model also cannot predict the minimum flow rate of reforming agent required to prevent carbon deposition on the anode catalyst. Using this model, they evaluated the system configurations in terms of their performance and suitability for meeting residential thermal-to-electric ratios (TERs). Their studies indicated that the maximum efficiency is achieved when cathode and anode gas recirculation is used along with internal reforming of methane. Furthermore, the results of sensitivity analysis revealed that the magnitude of the efficiency of methane-fuelled SOFC systems over hydrogen-fuelled ones can be as high as 6%.

In 2009, a simple biogas-fuelled SOFC system with two configurations, integrated with a membrane module, was modeled by Piroonlerkgul *et al.* [86]. In the first and second system configurations, CO_2 is captured from the inlet biogas and the reformed gas, respectively. Their model was based on the 0-D repeated-cell stack model and thermodynamic model of BoP components of the system. They have not considered the effect of the stack thermal insulation system on the thermal management of the stack. Their model also cannot predict the minimum flow rate of reforming agent required to prevent carbon deposition on the anode catalyst. Their studies indicated that both systems offer higher power density but lower electrical efficiency than those of the SOFC system without CO_2 capturing equipment.

Overall, the SOFC system level model based on the repeated-cell stack model and thermodynamic model of BoP components is an appropriate model for performance prediction at full load operation and parametric study of the simple and CHP SOFC systems. However, this model can be improved by considering the thermal management of the stack and determination of the minimum flow rate of the reforming agent to prevent carbon deposition on the anode catalyst.

2.5 Summary

The key findings of the literature review are summarized as follows:

- The method of obtaining carbon deposition boundary curves by three independent equations of equilibrium constants is an appropriate method to predict the potential of carbon deposition on the anode catalyst.
- The basic cell model is the simplest approach to model SOFCs at the cell level. This model has been well developed and broadly employed to evaluate SOFCs at the system level. Of course, connecting a carbon deposition model to this model can establish a more appropriate model to evaluate SOFC systems.
- The macro-model of SOFCs at the cell level has been well developed and the behaviour of a cell under several operating and design conditions has been adequately determined. This helps to effectively design a cell model for a specific objective by choosing the dimension of each transport equation in each component of the cell.
- In macro-models, it is generally assumed that the electrochemical reactions take place at the interface of the electrodes and electrolyte. Therefore, the physical, chemical, and electrochemical

processes inside the microstructure of porous composite electrodes are ignored in this modeling approach.

- The results of the macro-modeling of SOFCs at cell level indicated that for the co- and counter-flow planar cells, the solid structure temperature in thickness and width directions of the cell are almost uniform, especially if the methane content of the fuel at the entrance of the anode channels is not significantly high. Therefore, the heat transfer in solid structure of these cells can be modeled only along the length of the cell (1-D). The anode, electrode, cathode, and interconnect may also be considered as a lumped homogenous structure in the heat transfer analysis. The current density and hydrogen partial pressure along the width of a co-flow cell are almost uniform.
- The micro-modeling of SOFCs at the cell level is in progress. A more precise microstructure model and a model to link the microstructure of porous composite electrodes to the cell performance are under development.
- The random-packing sphere method to model the microstructure of porous composite electrodes and the 1-D model of electron, ion, and mass transport through two-layer electrodes coupled with electrochemical reaction(s) are somewhat established in micro-models. However, the current density, temperature of the solid structure of the cell, and the temperature and partial pressures of the fuel and air species in the channels are generally assumed to be uniform. Furthermore, a relation between the average pore diameter and tortuosity and the independent microstructural variables of the electrode has not been appropriately established. For a hydrocarbon fuel, the electrochemical oxidation of CO in the anode functional layer has not been considered. The anode- and cathode- side interconnects have not been included in the micro-models.
- The results of the 2-D micro-model for a co-flow cell indicated that the key performance parameters of the PEN structure are uniform along the width of the PEN. Therefore, the 2-D micro-model can be reduced to a 1-D micro-model.
- The repeated-cell stack model is broadly employed for the purpose of evaluation of the performance of SOFC stacks. However, the difference between the solid structure temperature of the top and bottom cells in the stack may be around 50°C and that may significantly affect the performance of the cells within the stack.
- The SOFC system level model based on the repeated-cell stack model and thermodynamic model of BoP components of the system is usually employed for performance prediction at full load operation and parametric study of the simple and CHP SOFC systems.

Chapter 3

Modeling

3.1 Carbon Deposition Model

Before feeding a fuel to a cell, it is necessary to investigate the possibility of carbon deposition on the anode catalyst. For this purpose, a simple model on the basis of the thermodynamic equilibrium assumption is presented to obtain the CDB curve in the C-H-O ternary diagram. Using this model, the possibility of carbon deposition at the given fuel composition, temperature, and pressure can be studied.

At the operating temperatures and pressures of SOFCs, the species of primary importance of the equilibrium products of a fuel, located in the C-H-O ternary diagram, are carbon, C, in the solid phase and a mixture of H_2, CO, CH_4, H_2O, and CO_2 in the gaseous phase. The species of secondary importance, which are present in minor amounts, are C_2H_6, C_2H_4, and C_2H_2. However, species such as CH_3OH, HCHO, C_2H_5OH, and $C_{10}H_{22}$ are present in amounts of several orders of magnitude smaller than the species of secondary importance [22, 23]. In this modeling, only the important species of H_2, CO, CH_4, H_2O, and CO_2 are taken into account for the gaseous phase of the equilibrium product of a fuel. Inert gases such as nitrogen may be present in this phase that we consider it in the equilibrium product. Neglecting the amounts of the minor constituents does not affect the results within the accuracy of the equilibrium constant data [22].

The mole fraction of species in the gaseous phase of the equilibrium product of a fuel (hereafter called just fuel) is obtained by dividing the partial pressures of H_2, CO, CH_4, H_2O, and CO_2 by the difference of the total gas pressure and the partial pressure of inert gases as follows:

$$x'_{f,l} = \frac{p_{f,l}}{p_{f,tot} - p_{f,ig}}, l \in \{CH_4, H_2, CO, H_2O, CO_2\} \tag{3.1}$$

Using Dalton's law:

$$x'_{f,H_2} + x'_{f,CO} + x'_{f,CH_4} + x'_{f,H_2O} + x'_{f,CO_2} = 1 \tag{3.2}$$

The location of a gaseous fuel in the C-H-O ternary diagram is found by determining two out of three atom ratios of carbon, hydrogen, and oxygen from the following equations [24]:

$$C = \frac{x'_{f,CO_2} + x'_{f,CO} + x'_{f,CH_4}}{2x'_{f,H_2} + 3x'_{f,CO_2} + 2x'_{f,CO} + 3x'_{f,H_2O} + 5x'_{f,CH_4}} \tag{3.3}$$

$$H = \frac{2x'_{f,H_2} + 2x'_{f,H_2O} + 4x'_{f,CH_4}}{2x'_{f,H_2} + 3x'_{f,CO_2} + 2x'_{f,CO} + 3x'_{f,H_2O} + 5x'_{f,CH_4}} \tag{3.4}$$

$$O = \frac{2x'_{f,CO_2} + x'_{f,CO} + x'_{f,H_2O}}{2x'_{f,H_2} + 3x'_{f,CO_2} + 2x'_{f,CO} + 3x'_{f,H_2O} + 5x'_{f,CH_4}} \tag{3.5}$$

In thermodynamic equilibrium, the CDB curve can be determined considering that the solid carbon can be formed by the three reactions of the carbon decomposition (3.R1), CO reduction (3.R2), and Boudouard reaction (3.R3) [87]. It is noted that for the fuels located on the CDB curve the net amount of solid carbon production and consumption by these reactions is zero [88].

$$CH_4 \xleftrightarrow{K_{p,CD}} C + 2H_2 \tag{3.R1}$$

$$H_2 + CO \xleftrightarrow{K_{p,COR}} C + H_2O \tag{3.R2}$$

$$2CO \xleftrightarrow{K_{p,B}} C + CO_2 \tag{3.R3}$$

Therefore, the mole fractions of CH_4, H_2O, and CO_2 of the fuels located on the CDB curve at the given fuel temperature, pressure, and partial pressure of inert gases can be determined from the equilibrium-constant relations of reactions (3.R1)-(3.R3) as follows:

$$x'_{f,CH_4,CDB} = x'^2_{f,H_2,CDB} \left(p_{f,tot} - p_{f,ig}\right)/K_{P,CD}\left(T_f\right) \tag{3.6}$$

$$x'_{f,H_2O,CDB} = K_{p,COR}\left(T_f\right) x'_{f,H_2,CDB}\, x'_{f,CO,CDB} \left(p_{f,tot} - p_{f,ig}\right) \tag{3.7}$$

$$x'_{f,CO_2,CDB} = K_{p,B}\left(T_f\right) x'^2_{f,CO,CDB} \left(p_{f,tot} - p_{f,ig}\right) \tag{3.8}$$

By placing Equations (3.6)-(3.8) into Equation (3.2), the mole fraction of H_2 of fuels located on the CDB curve can be determined as a function of the mole fraction of CO:

$$
\begin{aligned}
&x'_{f,H_2,CDB} \\
&= 0.5K_{P,CD}(T_f)\left(\frac{1}{(p_{f,tot}-p_{f,ig})}\right. \\
&\left.+ K_{p,COR}(T_f)x'_{f,CO,CDB}\right)\left(\sqrt{1+\frac{4\left(\frac{1-x'_{f,CO,CDB}}{(p_{f,tot}-p_{f,ig})}-K_{p,B}(T_f)x'^{2}_{f,CO,CDB}\right)}{K_{P,CD}(T_f)\left(\frac{1}{(p_{f,tot}-p_{f,ig})}+K_{p,COR}(T_f)x'_{f,CO,CDB}\right)^2}}-1\right)
\end{aligned}
\tag{3.9}
$$

The composition of fuels that makes the CDB curve in the C-H-O ternary diagram is determined using Equations (3.6)-(3.9) by varying the mole fraction of carbon monoxide from 0 to $x'_{CO,CDB,max}$.

$$
0 \le x'_{f,CO,CDB} \le x'_{f,CO,CDB,max} = \frac{\sqrt{1+4K_{p,B}(T_f)(p_{f,tot}-p_{f,ig})}-1}{2K_{p,B}(T_f)(p_{f,tot}-p_{f,ig})}
\tag{3.10}
$$

After determination of the CDB curve at the given temperature and pressure, the carbon deposition region in the C-H-O ternary diagram that is above the CDB curve and the safe region that is below the CDB curve can be determined. For any fuel located above the CDB curve, the carbon deposition is probable and that fuel should be processed to transfer its location to the safe region before feeding to the cell.

3.2 Cell Level Model

Modeling an SOFC at the cell level involves a large and complex number of phenomena occurring at the same time. When representing such a complex system with mathematical equations, the details of the model to describe the cell should be goal-driven. In fact, the complexity of the model should be connected to the main goal of the analysis. For example, when the main goal of the cell model is to provide the cell performance to analyze the performance of an SOFC system, the distribution of several physical, chemical, and electrochemical variables inside the cell may not be significant. In contrast, when the main purpose of the model is to design an appropriate microstructure for a porous composite electrode, it is important that the model is capable of providing detailed information for distribution of several physical, chemical, and electrochemical variables. In this section, the basic cell model that is suitable for performance evaluation of SOFC systems is presented. Then a cell level model entitled the "Combined Micro- and Macro-model" suitable to study the effect of the microstructure of porous composite electrodes on several performance-related variables of the cell is developed.

3.2.1 Basic Cell Model

The objective of the basic cell model presented in this thesis is to determine the voltage, power, flow rate of the inlet fuel and air, and flow rate and composition of the outlet fuel and air streams from the cell. This cell may operate at the given current density, fuel utilization ratio, pressure, temperature of the solid structure, composition of the inlet fuel and air, and temperature of the inlet and outlet fuel and air streams. The inlet fuel to the anode channel can have an arbitrary composition of CH_4, H_2, CO, H_2O, CO_2, and N_2. The cell design parameters required for this model are the thicknesses of the anode, cathode, electrolyte, and interconnect; the anode and cathode porosity and tortuosity; and the active length and width of the cell. The model developed in this section is employed to model the SOFC stack for the purpose of the performance evaluation of SOFC systems. The main assumptions of this model are:

- The temperature of the solid structure of the cell is uniform [29].
- The pressure of the fuel and air streams is identical and uniform throughout the cell [28].
- The composition of the fuel and air streams along the channels is uniform and equal to the average of the composition of the fuel and air streams at the inlet and outlet of the cell.
- The current density generated in the cell is uniform [28].
- The SR reaction (3.R4) and WGS (3.R5) are in equilibrium in the inlet and outlet fuel [132].
- Only H_2 participates in the direct electrooxidation reaction in the anode [30, 132].
- The CH_4 and CO contribute to electric power generation in the cell after participating in the SR and WGS reactions to produce H_2 for electrooxidation reaction (2.R2) [132].
- The electrochemical reactions take place at the interface of the electrode and electrolyte [28].
- The voltage is uniform over the surface of the cell [28].
- The fuel and air are treated as ideal gas mixtures [28].
- The electron conductivity of the electrolyte is negligible [28].

- The change in kinetic and potential energies of the fuel and air streams is negligible [28].
- There is no contact resistance between the cell components [28].

$$CH_4 + H_2O \overset{K_{p,SR}}{\longleftrightarrow} CO + 3H_2 \tag{3.R4}$$

$$CO + H_2O \overset{K_{p,WGS}}{\longleftrightarrow} CO_2 + H_2 \tag{3.R5}$$

First, the flow rate of fuel at the entrance and the flow rate and composition of fuel at the exit of the cell are determined. For this purpose, the mass balance equation is employed to establish a relation between the molar flow rate of each species of fuel at the entrance and exit of the cell:

$$\dot{n}_{f,CH_4,ext} = \dot{n}_{f,CH_4,ent} - \dot{C}_{CH_4} \tag{3.11}$$

$$\dot{n}_{f,H_2,ext} = \dot{n}_{f,H_2,ent} + 3\dot{C}_{CH_4} + \dot{P}_{CO_2} - \dot{C}_{H_2} \tag{3.12}$$

$$\dot{n}_{f,CO,ext} = \dot{n}_{f,CO,ent} + \dot{C}_{CH_4} - \dot{P}_{CO_2} \tag{3.13}$$

$$\dot{n}_{f,H_2O,ext} = \dot{n}_{f,H_2O,ent} - \dot{C}_{CH_4} - \dot{P}_{CO_2} + \dot{C}_{H_2} \tag{3.14}$$

$$\dot{n}_{f,CO_2,ext} = \dot{n}_{f,CO_2,ent} + \dot{P}_{CO_2} \tag{3.15}$$

$$\dot{n}_{f,N_2,ext} = \dot{n}_{f,N_2,ent} \tag{3.16}$$

The summation of both sides of these equations establishes a relation between the inlet and outlet flow rate of fuel from the cell:

$$\dot{n}_{f,ext} = \dot{n}_{f,ent} + 2\dot{C}_{CH_4} \tag{3.17}$$

The rates of hydrogen consumption through the electrooxidation reaction (2.R2), $\dot{C}_{\mathrm{H}_2}$, can be calculated from Faraday's electrochemical law:

$$\dot{C}_{H2} = \frac{i_{Cell} L_{Cell} W_{Cell}}{2F} \tag{3.18}$$

The rates of methane consumption through SR reaction (3.R4), $\dot{C}_{CH_4}$, and carbon dioxide production through WGS reaction (3.R5), $\dot{P}_{CO_2}$, can be predicted from the equilibrium-constant relations developed for the outlet fuel from the cell:

$$K_{p,SR}\left(T_{f,ext}\right) = p_{Cell}^2 \frac{x_{f,CO,ext}\, x_{f,H_2,ext}^3}{x_{f,CH_4,ext}\, x_{f,H_2O,ext}} = \frac{p_{Cell}^2}{\dot{n}_{f,ext}^2} \frac{\dot{n}_{f,CO,ext}\, \dot{n}_{f,H_2,ext}^3}{\dot{n}_{f,CH_4,ext}\, \dot{n}_{f,H_2O,ext}} \tag{3.19}$$

$$K_{p,WGS}\left(T_{f,ext}\right) = \frac{x_{f,CO_2,ext}\, x_{f,H_2,ext}}{x_{f,CO,ext}\, x_{f,H_2O,ext}} = \frac{\dot{n}_{f,CO_2,ext}\, \dot{n}_{f,H_2,ext}}{\dot{n}_{f,CO,ext}\, \dot{n}_{f,H_2O,ext}} \tag{3.20}$$

By placing Equations (3.11)–(3.15) into Equations (3.19) and (3.20), these equations can be expressed as follows:

$$\begin{aligned} &K_{p,SR}\left(T_{f,ext}\right) \\ &= \frac{p_{Cell}^2}{\left(\dot{n}_{f,ent} + 2\dot{C}_{CH_4}\right)^2} \frac{\left(\dot{n}_{f,ent}\, x_{f,CO,ent} + \dot{C}_{CH_4} - \dot{P}_{CO_2}\right)\left(\dot{n}_{f,ent}\, x_{f,H_2,ent} + 3\dot{C}_{CH_4} + \dot{P}_{CO_2} - \dot{C}_{H_2}\right)^3}{\left(\dot{n}_{f,ent}\, x_{f,CH_4,ent} - \dot{C}_{CH_4}\right)\left(\dot{n}_{f,ent}\, x_{f,H_2O,ent} - \dot{C}_{CH_4} - \dot{P}_{CO_2} + \dot{C}_{H_2}\right)} \end{aligned} \tag{3.21}$$

$$K_{p,WGS}\left(T_{f,ext}\right) = \frac{\left(\dot{n}_{f,ent}\, x_{f,CO_2,ent} + \dot{P}_{CO_2}\right)\left(\dot{n}_{f,ent}\, x_{f,H_2,ent} + 3\dot{C}_{CH_4} + \dot{P}_{CO_2} - \dot{C}_{H_2}\right)}{\left(\dot{n}_{f,ent}\, x_{f,CO,ent} + \dot{C}_{CH_4} - \dot{P}_{CO_2}\right)\left(\dot{n}_{f,ent}\, x_{f,H_2O,ent} - \dot{C}_{CH_4} - \dot{P}_{CO_2} + \dot{C}_{H_2}\right)} \tag{3.22}$$

Before solving Equations (3.21) and (3.22) for $\dot{C}_{CH_4}$ and $\dot{P}_{CO_2}$, the flow rate of the inlet fuel to the cell should be determined. For this purpose, the relation of fuel utilization ratio is used [89]:

$$U_f = \frac{\left(\dot{n}_{f,H_2,ent} - \dot{n}_{f,H_2,ext}\right)\beta' + \left(\dot{n}_{f,CO,ent} - \dot{n}_{f,CO,ext}\right)\gamma' + \left(\dot{n}_{f,CH_4,ent} - \dot{n}_{f,CH_4,ext}\right)\delta'}{\dot{n}_{f,ent}\left(x_{f,H_2,ent}\,\beta' + x_{f,CO,ent}\,\gamma' + x_{f,CH_4,ent}\,\delta'\right)} \tag{3.23}$$

Where,

$$\beta' = \overline{h}_{H_2O}(T_{f,ent}) - \overline{h}_{H_2}(T_{f,ent}) - 0.5\,\overline{h}_{O_2}(T_{f,ent}) \tag{3.24}$$

$$\gamma' = \overline{h}_{CO_2}(T_{f,ent}) - \overline{h}_{CO}(T_{f,ent}) - 0.5\,\overline{h}_{O_2}(T_{f,ent}) \tag{3.25}$$

$$\delta' = \overline{h}_{CO_2}(T_{f,ent}) + 2\overline{h}_{H_2O}(T_{f,ent}) - \overline{h}_{CH_4}(T_{f,ent}) - 2\overline{h}_{O_2}(T_{f,ent}) \tag{3.26}$$

By placing Equations (3.11)–(3.15) into Equation (3.23), this equation can be written as follows:

$$\dot{n}_{f,ent} = \frac{(\dot{C}_{H_2} - 3\dot{C}_{CH_4} - \dot{P}_{CO_2})\beta' + (\dot{P}_{CO_2} - \dot{C}_{CH_4})\gamma' + \dot{C}_{CH_4}\delta'}{U_f(x_{f,H_2,ent}\,\beta' + x_{f,CO,ent}\,\gamma' + x_{f,CH_4,ent}\,\delta')} \tag{3.27}$$

This equation is a function of the rates of methane consumption and carbon dioxide production in the cell; therefore, to determine these rates and the flow rate of the inlet fuel, Equations (3.21), (3.22), and (3.27) should be solved simultaneously. After solving these equations, the mole fraction and partial pressure of each species of the outlet fuel can be determined:

$$x_{f,l,ext} = \frac{\dot{n}_{f,l,ext}}{\dot{n}_{f,ext}}, l \in \{CH_4, H_2, CO, H_2O, CO_2, N_2\} \tag{3.28}$$

$$p_{f,l,ext} = x_{f,l,ext}\, p_{Cell}, l \in \{CH_4, H_2, CO, H_2O, CO_2, N_2\} \tag{3.29}$$

The average partial pressures of hydrogen and water vapour in the bulk fuel stream are estimated from the following equations:

$$p_{f,H_2,Bulk} = (p_{f,H_2,ent} + p_{f,H_2,ext})/2 \tag{3.30}$$

$$p_{f,H_2O,Bulk} = (p_{f,H_2O,ent} + p_{f,H_2O,ext})/2 \tag{3.31}$$

After determination of the flow rate of fuel at the entrance and the flow rate and composition of fuel at the exit of the cell, the cell voltage can be obtained:

$$V_{Cell} = E_{rev,cell} - \eta_{tot} \tag{3.32}$$

Where, the reversible voltage of the cell can be expressed as follows:

$$E_{rev,cell} = \frac{1}{2F}\left(\bar{g}^{\circ}_{H_2}(T_s) + 0.5\bar{g}^{\circ}_{O_2}(T_s) - \bar{g}^{\circ}_{H_2O}(T_s)\right) + \frac{R_u T_s}{2F}\ln\left(\frac{p_{f,H_2,Bulk}\, p^{0.5}_{a,O_2,Bulk}}{p_{f,H_2O,Bulk}}\right) \tag{3.33}$$

The Gibbs free energy of different species as a function of temperature required in this equation can be estimated from the thermodynamic properties data reported by NASA [90].

The main polarizations in SOFCs are the activation, ohmic, and concentration polarizations. Therefore, the total polarization of the cell is obtained as:

$$\eta_{tot} = \eta_{Activation,A} + \eta_{Activation,C} + \eta_{Ohmic,tot} + \eta_{Concentration,A} + \eta_{Concentration,C} \tag{3.34}$$

The activation polarization is caused by the activation energy required to start the anode and cathode electrochemical reactions. This polarization can be estimated from the Butler-Volmer equation [91]:

$$i_{Cell} = i_0\left[exp\left(\beta\frac{2F\eta_{Activation}}{R_u T_s}\right) - exp\left((1-\beta)\frac{-2F\eta_{Activation}}{R_u T_s}\right)\right] \tag{3.35}$$

If the transfer coefficient, β, is assumed to be 0.5 [28], the anode and cathode activation polarizations can be estimated from the following equations:

$$\eta_{Activation,A} = \frac{R_u T_s}{F}\sinh^{-1}\left(\frac{i_{Cell}}{2i_{0,A}}\right) \tag{3.36}$$

$$\eta_{Activation,C} = \frac{R_u T_s}{F}\sinh^{-1}\left(\frac{i_{Cell}}{2i_{0,C}}\right) \tag{3.37}$$

The exchange current density is the forward and backward electrochemical reaction rate at the equilibrium voltage, and it is a function of the cell temperature and partial pressures of the fuel and air [92]. The anode and cathode exchange current densities, $i_{0,A}$ and $i_{0,C}$, can be expressed as follows:

$$i_{0,A} = \gamma_A p_{f,H_2,Bulk}^{m_1} \, p_{f,H_2O,Bulk}^{m_2} exp\left(\frac{-E_{act,A}}{R_u T_s}\right) \tag{3.38}$$

$$i_{0,C} = \gamma_C p_{a,O_2,Bulk}^{m_3} exp\left(\frac{-\mathrm{E_{act,C}}}{R_u T_s}\right) \tag{3.39}$$

The constant values of γ_A, γ_C, m_1, m_2, m_3, $E_{act,A}$, and $E_{act,C}$ are usually obtained from experiment.

The ohmic polarization is due to the electronic resistance to flow electrons through the anode, cathode, and interconnect and the ionic resistance to flow ions through the electrolyte. If these resistances obey Ohm's law, the total ohmic polarization can be expressed as follows:

$$\begin{aligned} \eta_{Ohmic,tot} &= \eta_{Ohmic,A} + \eta_{Ohmic,C} + \eta_{Ohmic,Int} + \eta_{Ohmic,E} \\ &= i_{Cell}\delta_A R'_A(T_s) + i_{Cell}\delta_C R'_C(T_s) + i_{Cell}\delta_{Int} R'_{Int}(T_s) + i_{Cell}\delta_E R'_E(T_s) \end{aligned} \tag{3.40}$$

The concentration polarization is due to the reduction of the partial pressures of the fuel or air species at the reaction sites, and it is significant when the electrochemical reaction is faster than the gas diffusion to the reaction sites. Gas diffusion through the porous electrodes in SOFCs is usually described by the ordinary and Knudsen diffusions. In the ordinary diffusion, different components of the gaseous mixture move in relation to each other under the influence of concentration gradients. In the Knudsen diffusion, the mean free path of molecules of different components of the gaseous mixture is in the order of the pore size and the gas molecules collide frequently with the pore walls. The concentration polarizations for the anode and cathode can be calculated from the following equations:

$$\eta_{Concentration,A} = \frac{-R_u T_s}{2F} ln\left(\frac{p_{f,H_2,A|E}/p_{f,H_2,Bulk}}{p_{f,H_2O,A|E}/p_{f,H_2O,Bulk}}\right) \tag{3.41}$$

$$\eta_{Concentration,C} = \frac{-R_u T_s}{4F} ln\left(p_{a,O_2,C|E}/p_{a,O_2,Bulk}\right) \tag{3.42}$$

Where, the partial pressures of H_2 and H_2O at the interface of the anode and electrolyte ($p_{f,H_2,A|E}$ and $p_{f,H_2O,A|E}$) and the partial pressure of O_2 at the interface of the cathode and electrolyte ($p_{a,O_2,C|E}$) can be estimated from 1-D mass transfer equation developed by Chan *et al.* [28]:

$$p_{f,H_2,A|E} = p_{f,H_2,Bulk} - \frac{R_u T_s \delta_A}{2F D_A^{eff}} i_{Cell} \tag{3.43}$$

$$p_{f,H_2O,A|E} = p_{f,H_2O,Bulk} - \frac{R_u T_s \delta_A}{2F D_A^{eff}} i_{Cell} \tag{3.44}$$

$$p_{a,O_2,C|E} = \frac{D_{O_2-N_2}^{eff}}{D_C^{eff}} p_{Cell} - \left(\frac{D_{O_2-N_2}^{eff}}{D_C^{eff}} p_{Cell} - p_{a,O_2,Bulk}\right) exp\left(\frac{R_u T_s \delta_C}{4F D_C^{eff} p_{Cell}} i_{Cell}\right) \tag{3.45}$$

Where,

$$D_A^{eff} = \left(\frac{p_{f,H_2O,Bulk}}{p_{Cell}}\right)\left(\frac{1}{D_{K,H_2}^{eff}} + \frac{1}{D_{H_2-H_2O}^{eff}}\right)^{-1} + \left(\frac{p_{f,H_2,Bulk}}{p_{Cell}}\right)\left(\frac{1}{D_{K,H_2O}^{eff}} + \frac{1}{D_{H_2-H_2O}^{eff}}\right)^{-1} \tag{3.46}$$

$$D_C^{eff} = \left(\frac{1}{D_{K,O_2}^{eff}} + \frac{1}{D_{O_2-N_2}^{eff}}\right)^{-1} \tag{3.47}$$

The effective ordinary and Knudsen diffusion coefficients can be estimated from Equations (3.48) [93] and (3.49) [28], respectively.

$$D_{l-m}^{eff} = \frac{0.0101325}{\left(V_{a,l}^{1/3} + V_{a,m}^{1/3}\right)^2}\left(\frac{1}{MW_l} + \frac{1}{MW_m}\right)^{0.5} \frac{{T_s}^{1.75}}{p_{Cell}}\left(\frac{\varepsilon}{\tau}\right) \tag{3.48}$$

$$D_{K,l}^{eff} = 48.5\, d_{pores} \sqrt{\frac{T_s}{MW_l}} \left(\frac{\varepsilon}{\tau}\right) \tag{3.49}$$

After prediction of the cell polarizations and determination of the cell voltage, the total electric power generated in the cell can be calculated:

$$\dot{W}_{Cell} = V_{Cell} i_{Cell} L_{Cell} W_{Cell} \tag{3.50}$$

After determination of the power, the flow rate of air required to control the temperature of the cell is determined from the energy balance equation:

$$\dot{n}_{f,ent}\bar{h}_{f,ent} + \dot{n}_{a,ent}\bar{h}_{a,ent} = \dot{n}_{f,ext}\bar{h}_{f,ext} + \dot{n}_{a,ext}\bar{h}_{a,ext} + \dot{W}_{Cell} + \dot{Q}_{Cell} \tag{3.51}$$

From the mass balance equation and Faraday's electrochemical law, a relation between the air flow rate at the entrance and exit of the cell can be established:

$$\dot{n}_{a,ext} = \dot{n}_{a,ent} - \frac{i_{Cell} L_{Cell} W_{Cell}}{4F} \tag{3.52}$$

By placing Equation (3.52) into Equation (3.51), the air flow rate at the entrance of the cell can be determined:

$$\dot{n}_{a,ent} = \frac{\dot{n}_{f,ent}\bar{h}_{f,ent} - \dot{n}_{f,ext}\bar{h}_{f,ext} + \bar{h}_{a,ext}\, i_{Cell} L_{Cell} W_{Cell}/4F - \dot{W}_{Cell} - \dot{Q}_{Cell}}{\bar{h}_{a,ext} - \bar{h}_{a,ent}} \tag{3.53}$$

It is noted that the heat transfer from the cell is dependent on the design of the insulation system in the SOFC stack. The method of estimating this heat transfer is described in section 3.3.

After determination of the inlet air flow rate, the mole fraction and partial pressure of nitrogen and oxygen in the outlet air can be obtained:

$$\dot{n}_{a,N_2,ext} = x_{a,N_2,ent}\dot{n}_{a,ent} \tag{3.54}$$

$$\dot{n}_{a,O_2,ext} = x_{a,O_2,ent}\dot{n}_{a,ent} - i_{Cell}L_{Cell}W_{Cell}/4F \tag{3.55}$$

$$x_{a,l',ext} = \frac{\dot{n}_{a,l',ext}}{\dot{n}_{a,ext}}, l' \in \{O_2, N_2\} \tag{3.56}$$

$$p_{a,l',ext} = x_{a,l',ext}\, p_{Cell}, l' \in \{O_2, N_2\} \tag{3.57}$$

The excess air can be also calculated from the following equation:

$$EA = \frac{\dot{n}_{a,ent}}{\dot{n}_{a,Stoichiometric}} = \frac{\dot{n}_{a,ent}}{\left(2\dot{n}_{f,CH_4,ent} + 0.5\dot{n}_{f,H_2,ent} + 0.5\dot{n}_{f,CO,ent}\right)/x_{a,O_2,ent}} \tag{3.58}$$

The partial pressure of oxygen in the bulk air stream is also estimated as follows:

$$p_{a,O_2,Bulk} = \left(p_{a,O_2,ent} + p_{a,O_2,ext}\right)/2 \tag{3.59}$$

It is noted that the partial pressure of oxygen in the bulk air is usually close to the partial pressure of oxygen in the inlet air. Therefore, $p_{a,O_2,Bulk} \approx p_{a,O_2,ent}$ can be used in Equations (3.33), (3.39), (3.42), and (3.45). Of course, for more precise estimation of the air flow rate at the entrance of the cell, the partial pressure of oxygen in the bulk air stream should be corrected by the value obtained from Equation (3.59) and the calculations are repeated.

Finally, the first law efficiency of the cell is obtained:

$$\eta_{I,Cell} = \frac{\dot{W}_{Cell}}{\dot{n}_{f,ent}\overline{LHV}(T_{f,ent})} \tag{3.60}$$

Where,

$$\overline{LHV}\left(T_{f,ent}\right) = -\left(x_{f,H_2,ent}\,\beta' + x_{f,CO,ent}\,\gamma' + x_{f,CH_4,ent}\,\delta'\right) \tag{3.61}$$

3.2.2 Combined Micro- and Macro-model of Cell

In the combined micro- and macro-model of planar cells, the cell is divided into the solid structure that includes the anode, cathode, electrolyte, and interconnect; the fuel stream with an arbitrary composition of CH_4, H_2, CO, H_2O, CO_2, and N_2 in the fuel channel; the air stream in the air channel; the fuel flow inside the anode; and the air flow inside the cathode. It is assumed that the cell is adiabatic, it operates at steady state conditions, and that the fuel and air streams passing through the channels are parallel and in front of each other with a co-flow arrangement. The porous composite cathode considered for this cell contains LSM particles with the chemical composition of $(La_{0.8}Sr_{0.2})_{0.98}MnO_3$, as the electron conductor, and YSZ particles with the chemical composition of $(ZrO_2)_{0.92}(Y_2O_3)_{0.08}$, as the ion conductor. The porous composite anode of the cell is made of a thick substrate layer, which is a mechanical support of the cell structure, and a thin functional layer for H_2 and CO electrooxidation reactions. These two layers are fabricated with Ni particles that conduct the electron and YSZ particles with the same chemical composition of the YSZ particles in the cathode that conduct the ion. The electrolyte and interconnect of the cell are also made from the dense YSZ and stainless steel, respectively.

As illustrated in Figure 3.1, the fuel and air streams and the solid structure located at the middle of the stack are selected as the region of the modeling, and it is assumed that the results obtained in this region can be generalized for the entire cell. In this region, the temperature of the solid structure and the properties and composition of the fuel and air streams passing through the channels are assumed to be uniform along the width (z axis) and thickness (x axis) of the cell. This assumption was made on the basis of the results obtained from the macro-modeling of multi-dimensional co-flow planar cells that has been reported by several researchers. For more explanations, refer to section 2.2.2.

The WGS reaction (3.R5) is assumed to be locally in equilibrium throughout the modeling region. The SR reaction takes place in the fuel stream passing through the fuel channel. In addition to H_2 molecules, CO molecules participate in the electrooxidation reaction in the microstructure of the anode. The effect of the electrooxidation of methane is assumed to be negligible.

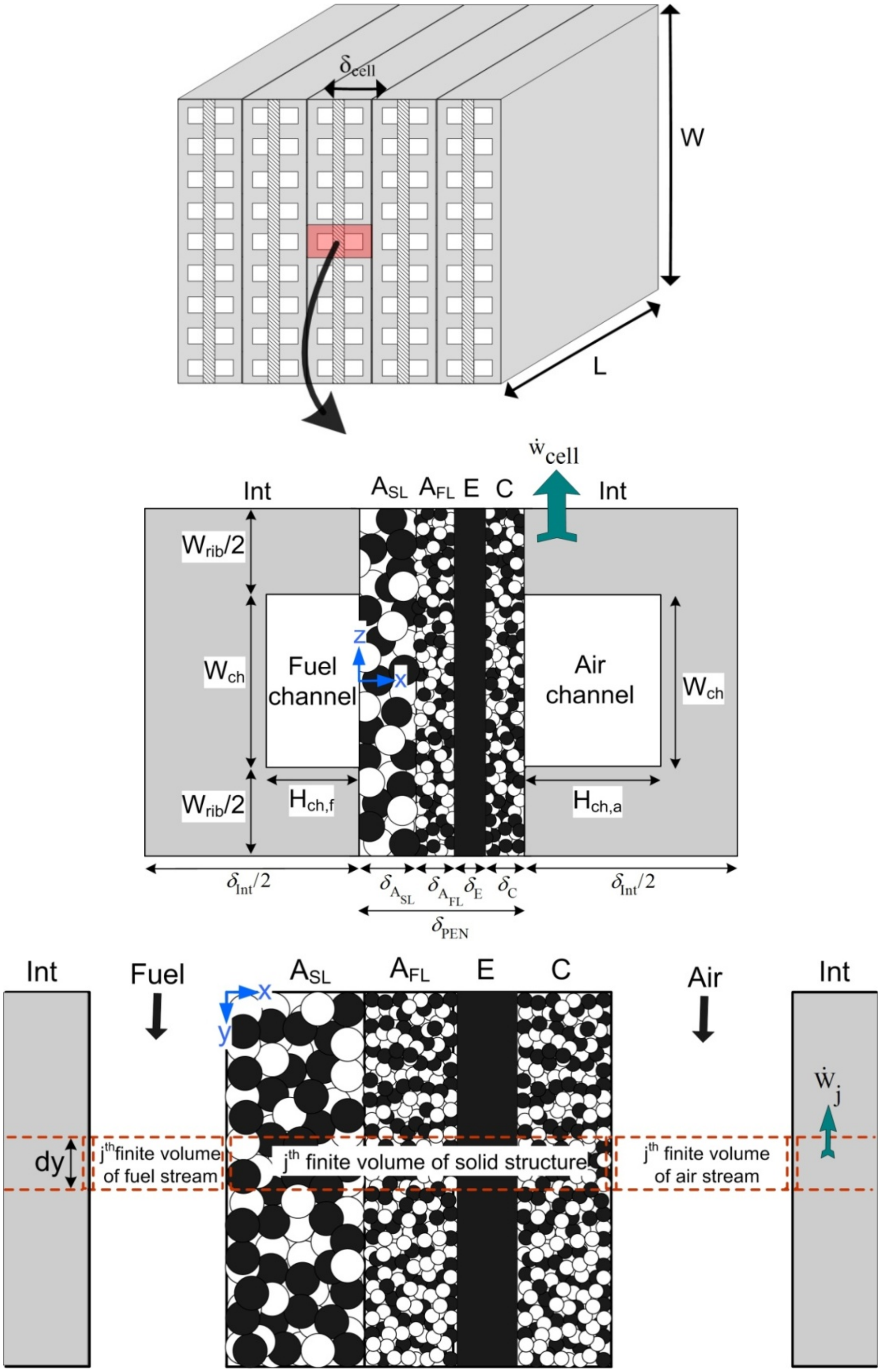

Figure 3.1: Schematic of the modeling region.

For the macro-modeling, the solid structure, fuel stream passing through the fuel channel, and air stream passing through the air channel are divided into N^{FV} uniform finite volumes along the length of the cell (y axis). In each finite volume of the fuel stream, H_2 and CO molecules are transferred from the fuel stream to the anode. H_2O and CO_2 molecules produced from the electrooxidation reactions in the anode functional layer are transferred from the anode to the fuel channel and mixed with the fuel stream. The methane SR reaction may take place in each finite volume due to the catalytic effect of Ni particles in the anode substrate layer. The conversion of CO to H_2 or vice versa may also occur through the WGS reaction. In each finite volume of the air stream, O_2 molecules required for the electroreduction reaction are transferred to the cathode and no chemical reaction takes place in the finite volume. In each finite volume of the solid structure, heat may be generated due to the polarizations, the WGS reaction, and the difference between the enthalpy and Gibbs free energy of the electrochemical reactions. This heat is dissipated to the fuel and air streams passing through the channels by convection. Additionally, a part of this heat may be diffused through the solid structure to the adjacent finite volumes.

It is assumed that the cell voltage along the length of the cell is uniform and the electric current generated in each finite volume of the solid structure does not transfer to the adjacent finite volumes in y direction. In these conditions, the equivalent electrical circuit of the solid structure can be demonstrated, as in Figure 3.2. Furthermore, the voltage difference between the anode and cathode side interconnects of each finite volume will be identical. Since the WGS reaction is in equilibrium, the reversible voltages due to the H_2 and CO electrooxidation reactions are identical in each finite volume:

$$\begin{aligned}
E_{rev,H_2,j} &= E^{\circ}_{H_2,j} + \frac{R_u T_{s,j}}{2F} \ln \frac{p_{f,H_2}(0,j)}{p_{f,H_2O}(0,j)} = \frac{\bar{g}^{\circ}_{H_2}(T_{s,j}) - \bar{g}^{\circ}_{H_2O}(T_{s,j})}{2F} \\
&+ \frac{R_u T_{s,j}}{2F} \ln \left(K_{p,WGS}(T_{s,j}) \frac{p_{f,CO}(0,j)}{p_{CO_2}(0,j)} \right) = \frac{\bar{g}^{\circ}_{H_2}(T_{s,j}) - \bar{g}^{\circ}_{H_2O}(T_{s,j})}{2F} \\
&+ \frac{R_u T_{s,j}}{2F} \ln \left(exp \left(- \frac{\bar{g}^{\circ}_{CO_2}(T_{s,j}) + \bar{g}^{\circ}_{H_2}(T_{s,j}) - \bar{g}^{\circ}_{CO}(T_{s,j}) - \bar{g}^{\circ}_{H_2O}(T_{s,j})}{R_u T_{s,j}} \right) \right) \\
&+ \frac{R_u T_{s,j}}{2F} \ln \left(\frac{p_{f,CO}(0,j)}{p_{f,CO_2}(0,j)} \right) = \frac{\bar{g}^{\circ}_{CO}(T_{s,j}) - \bar{g}^{\circ}_{CO_2}(T_{s,j})}{2F} + \frac{R_u T_{s,j}}{2F} \ln \left(\frac{p_{f,CO}(0,j)}{p_{f,CO_2}(0,j)} \right) \\
&= E^{\circ}_{CO,j} + \frac{R_u T_{s,j}}{2F} \ln \left(\frac{p_{f,CO}(0,j)}{p_{f,CO_2}(0,j)} \right) = E_{rev,CO,j}
\end{aligned} \tag{3.62}$$

As a consequence, the total polarization due to the H_2 and CO electrooxidation reactions is identical (see Figure 3.2):

$$\eta_{A,H_2,tot,j} = \eta_{A,CO,tot,j} = \eta_{A,tot,j} \tag{3.63}$$

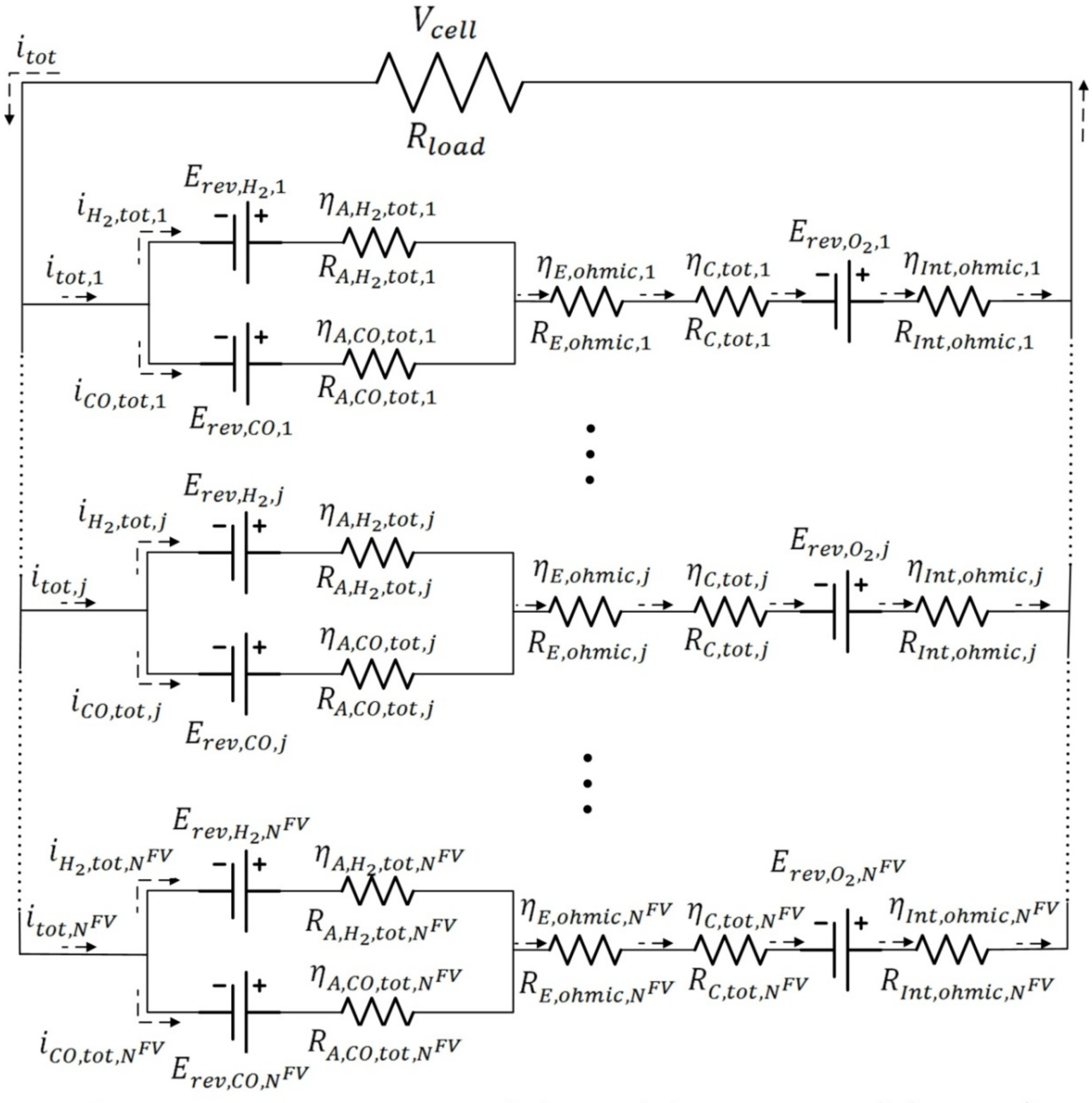

Figure 3.2: The equivalent electrical circuit of the cell.

Therefore, the total current generated in each finite volume, $i_{tot,j}$, at a given cell voltage, temperature of the solid structure, and species partial pressure of the fuel and air streams can be implicitly obtained from Equation (3.64).

$$\begin{aligned}\eta_{tot,j} &= E_{rev,H_2,j} + E_{rev,O_2,j} - V_{cell} \\ &= \frac{1}{2F}\left(-\Delta\bar{g}^{0}_{H_2+0.5O_2\rightarrow H_2O}\left(T_{s,j}\right) + R_u T_{s,j}\ ln\left(\frac{p_{f,H_2}(0,j)\ p^{0.5}_{a,O_2}(\delta_{PEN},j)}{p_{f,H_2O}(0,j)\ p^{0\ 0.5}}\right)\right) \\ &\quad - V_{cell}\end{aligned} \tag{3.64}$$

If the contact resistance between the cell components is neglected, the total polarization in the jth finite volume will be the sum of the total polarizations (activation+ohmic+concentration) in the anode, $\eta_{A,tot,j}$, and cathode, $\eta_{C,tot,j}$, and the ohmic polarizations in electrolyte, $\eta_{E,ohmic,j}$, and interconnect, $\eta_{Int,ohmic,j}$.

$$\eta_{tot,j} = \eta_{A,tot,j} + \eta_{C,tot,j} + \eta_{E,ohmic,j} + \eta_{Int,ohmic,j} \tag{3.65}$$

The ohmic polarization of the dense YSZ electrolyte and Crofer® 22APU metal interconnect [6] in the jth finite volume are estimated on the basis of Ohm's law, as follows:

$$\eta_{E,ohmic,j} = \frac{\delta_E T_{s,j}}{7.92\times 10^{8} exp\left(-111000/\left(R_u T_{s,j}\right)\right)} i_{tot,j} \tag{3.66}$$

$$\eta_{Int,ohmic,j} = \delta_{Int}\left(-6.25\times 10^{-5} T_{s,j}^{2} + 0.172 T_{s,j} + 2.77\right)\times 10^{-8}\ i_{tot,j} \tag{3.67}$$

The total polarizations of the porous composite cathode and anode in the jth finite volume are determined from Equations (3.68) and (3.69), respectively [61]. Of course, to use these equations, the local polarization of the cathode at $x=\delta_{PEN}$ and $x=\delta_{PEN}-\delta_C$ and the local polarization of the anode at $x=\delta_{A,SL}$ and $x=\delta_A$ should be determined from the cathode and anode micro-modeling.

$$\eta_{C,tot,j} = \frac{R^{eff}_{LSM,C,j} R^{eff}_{YSZ,C,j}}{R^{eff}_{LSM,C,j} + R^{eff}_{YSZ,C,j}}\left(\frac{\eta_C(\delta_{PEN},j)}{R^{eff}_{YSZ,C,j}} + i_{tot,j}\delta_C + \frac{\eta_C\left((\delta_{PEN}-\delta_C),j\right)}{R^{eff}_{LSM,C,j}}\right) \tag{3.68}$$

$$\eta_{A,tot,j} = \frac{R^{eff}_{Ni,A,j} R^{eff}_{YSZ,A,j}}{R^{eff}_{Ni,A,j} + R^{eff}_{YSZ,A,j}}\left(\frac{\eta_A\left(\delta_{A,SL},j\right)}{R^{eff}_{YSZ,A,j}} + i_{tot,j}\delta_{A,FL} + \frac{\eta_A(\delta_A,j)}{R^{eff}_{Ni,A,j}}\right) \tag{3.69}$$

3.2.2.1 Micro-Modeling

For the micro-modeling, the anode functional layer, anode substrate layer, and cathode of each finite volume of the solid structure with the fluid flow inside them are divided into $M_{A,FL}^{FV}$, $M_{A,SL}^{FV}$, and M_{C}^{FV} finite volumes, respectively, along the thickness of the cell. In the anode functional layer O_2 ions are transferred from the electrolyte to the anode reaction sites through the percolated YSZ particles, and the H_2 and CO molecules are transferred from the anode substrate layer to the reaction sites through pores. The H_2 and CO electrooxidation reactions take place at the reaction sites, the electrons produced are transferred to the anode substrate layer through the percolated Ni particles, and the H_2O and CO_2 molecules produced are transferred to the anode substrate layer through the pores. In the anode substrate layer, H_2 and CO molecules are transferred from the fuel channel to the anode functional layer and H_2O and CO_2 molecules are transferred from the anode functional layer to the fuel channel through pores. The electrons produced in the anode functional layer are also transferred to the anode side interconnect through the percolated Ni particles in the substrate layer. The electrons are transferred through the anode-side interconnect to the external circuit and then to the cathode side interconnect. Since the partial pressure of the fuel components varies along the thickness of anode substrate and functional layers and the WGS reaction is locally in equilibrium, a conversion of CO to H_2, or vice versa, through the WGS reaction may occur in these two layers. In the cathode, the electrons are transferred from the cathode-side interconnect to the reaction sites through the percolated LSM particles, the O_2 molecules are transferred from the air channel to the reaction sites through the pores, the O_2 electroreduction reaction takes place at the reaction sites, and the O_2 ions produced are transferred to the electrolyte through the percolated YSZ particles. Therefore, in micro-modeling the complex interdependency among the multi-component mass transport, electron and ion transports, and electrochemical and chemical reactions in the microstructure of the porous composite electrodes should be considered.

The micro-model starts with the microstructure modeling of the porous composite electrodes through which the electrode's microstructural properties, including the electrochemical active area per unit volume, A_{TPB}; permeability, β_0; average diameter of pores, d_{pores}; average tortuosity, τ; and the Ni, LSM, and YSZ effective resistivities, R_{Ni}^{eff} , R_{LSM}^{eff}, and R_{YSZ}^{eff}, are determined.

3.2.2.1.1 Modeling Microstructure of Porous Composite Electrodes

The random-packing sphere method is used to estimate the microstructural properties of porous composite electrodes. Before starting the microstructure modeling, three clusters of A, B, and C for ion-and electron-conducting particles are introduced. These clusters for the ion-conducting particles are schematically demonstrated in Figure 3.3. For cluster A, the ion-conducting particles are stretched from the electrolyte to the current collector. Therefore, oxygen ions can flow along the electrode and participate in the electrochemical reaction from the electrolyte to the current collector. For cluster B, the ion-conducting particles are connected to the electrolyte, but not stretched to the current collector; therefore, oxygen ions can flow along the electrode and participate in the electrochemical reaction from the electrolyte to the last ion-conducting particle of the chain. For cluster C, the ion-conducting particles are not connected to the electrolyte and are completely insulated with electron-conducting particles. It is, therefore, impossible for oxygen ions to flow along these particles and participate in the electrochemical reactions. There is a threshold in the volume fraction of both electron and ion-conducting particles at which the particles form only clusters B and C in an electrode. Cluster A is formed above this threshold, which is called the percolation threshold for cluster A. Indeed, clusters B and C turn into cluster A and their numbers are reduced when the volume fraction of the electron- and ion-conducting particles exceeds the percolation threshold. It is assumed that the volume fraction of both electron- and ion-conducting particles are beyond the percolation thresholds, thus the effect of cluster B on the microstructural properties of the electrode is assumed to be negligible.

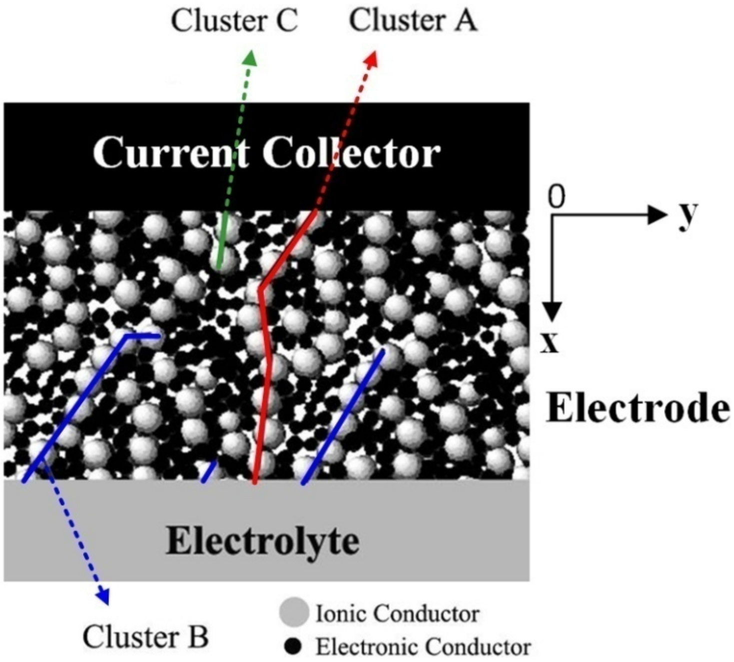

Figure 3.3: Schematic of a porous composite electrode.

To determine the electrochemical active area per unit volume of the porous composite electrode after the sintering process, A_{TPB}, it is assumed that the electron- and ion-conducting particles are distributed uniformly in the electrode. The electrochemical active area per unit volume is obtained using the statistical analysis of binary powder mixtures based on the theory of particle coordination number in the random-packing of spheres and the percolation theory [55]:

$$A_{TPB} = \left(\frac{\pi}{4} sin^2\left(\frac{\theta_c}{2}\right) d_i^2\right)(n_t n_{el}) Z_{el-io} P_{el} P_{io} \qquad d_i = mi\,n(d_{el}, d_{io}) \tag{3.70}$$

The number fraction of electron-conducting particles, n_{el}, the total number of particles per unit volume of the electrode, n_t, and the average number of ion-conducting particles in contact with an electron-conducting particle, Z_{el-io}, are determined from Equations (3.71)–(3.73), respectively [53].

$$n_{el} = \frac{\varphi_{el}\alpha^3}{1-\varphi_{el}+\varphi_{el}\alpha^3} \qquad \left(\alpha = \frac{d_{io}}{d_{el}}\right) \tag{3.71}$$

$$n_t = \frac{1-\varepsilon}{\frac{1}{6}\pi d_{el}^3 (n_{el} + (1-n_{el})\alpha^3)} \tag{3.72}$$

$$Z_{el-io} = Z_{el}\frac{(1-n_{el})Z_{io}}{Z} \tag{3.73}$$

Bouvard *et al.* [53] found that the overall average number of contacts per particle, Z, is exactly 6 for the binary random-packing of spheres. They also obtained the following equations for Z_{el}, and Z_{io}:

$$Z_{el} = 3 + \frac{Z-3}{n_{el} + (1-n_{el})\alpha^2} \tag{3.74}$$

$$Z_{io} = 3 + \frac{(Z-3)\alpha^2}{n_{el} + (1-n_{el})\alpha^2} \tag{3.75}$$

In Equation (3.70), the probability of cluster A of ion- and electron-conducting particles, P_{el} and P_{io}, is estimated from Equations (3.76) and (3.77), respectively [62].

$$P_{el} = \left[1 - \left(\frac{4.236 - Z_{el-el}}{2.472}\right)^{2.5}\right]^{0.4} \qquad (0.154 < \alpha < 6.464) \tag{3.76}$$

$$P_{io} = \left[1 - \left(\frac{4.236 - Z_{io-io}}{2.472}\right)^{2.5}\right]^{0.4} \qquad (0.154 < \alpha < 6.464) \tag{3.77}$$

where, $Z_{el\text{-}el}$, and $Z_{io\text{-}io}$, are determined as follows [59]:

$$Z_{el-el} = \frac{Z\, n_{el}}{n_{el} + (1 - n_{el})\alpha^2} \tag{3.78}$$

$$Z_{io-io} = \frac{Z(1 - n_{el})\alpha^2}{n_{el} + (1 - n_{el})\alpha^2} \tag{3.79}$$

To form cluster A for both electron- and ion-conducting particles, the volume fraction of electron-conducting particles, φ_{el}, should be limited to the percolation threshold of the electron- ($P_{el}=0$) and ion- ($P_{io}=0$) conducting particles. By solving Equation (3.76) for $P_{el}=0$ and Equation (3.77) for $P_{io}=0$, the range of the volume fraction of electron-conducting particles to form cluster A can be obtained:

$$\frac{1}{2.4\alpha + 1} < \varphi_{el} < \frac{1}{\frac{\alpha}{2.4} + 1} \qquad (0.154 < \alpha < 6.464) \tag{3.80}$$

After determination of the electrochemical active area per unit volume, the average diameter of pores, d_{pores}, and the average tortuosity, τ, of the porous composite electrodes are estimated. To estimate the average diameter of pores, it is assumed that the pores are cylindrical and are stretched from the current collector to the electrolyte with an average tortuosity of τ. Kenney *et al.* [58] showed in their computer modeling that more than 99% of the pores of an electrode are open from the current collector to the electrolyte. Therefore, all pores can be assumed to be open and the average diameter of the pores can be estimated as follows:

$$4 \times \frac{V_{pores}}{A_{pores}} = 4 \times \frac{\frac{\pi}{4} d_{pores}^2 \tau \delta N_{pores}}{\pi d_{pores} \tau \delta N_{pores}} = d_{pores} \tag{3.81}$$

Assuming that the surface area of the solid part of a porous electrode does not change significantly in the sintering process, the left side of Equation (3.81) can be developed as follows:

$$\begin{aligned} 4 \times \frac{V_{pores}}{A_{pores}} &= 4 \times \frac{V_{pores}}{V_{solid}} \times \frac{V_{solid}}{A_{pores}} \approx 4 \times \frac{\varepsilon}{1-\varepsilon} \times \frac{V_{solid}}{A_{solid}} \approx 4 \times \frac{\varepsilon}{1-\varepsilon} \times \frac{\frac{\pi}{6} d_{el}^3 n_{el} + \frac{\pi}{6} d_{io}^3 n_{io}}{\pi d_{el}^2 n_{el} + \pi d_{io}^2 n_{io}} \\ &= \frac{2}{3}\left(\frac{\varepsilon}{1-\varepsilon}\right) \frac{d_{el}}{\left(\varphi_{el} + \frac{1-\varphi_{el}}{\alpha}\right)} \end{aligned} \tag{3.82}$$

Therefore:

$$d_{pores} \approx \frac{2}{3}\left(\frac{\varepsilon}{1-\varepsilon}\right) \frac{d_{el}}{\left(\varphi_{el} + \frac{1-\varphi_{el}}{\alpha}\right)} \tag{3.83}$$

The average tortuosity is also estimated from the following equation:

$$\varepsilon = \frac{V_{pores}}{V_{pores} + V_{solid}} = \frac{\frac{\pi}{4} d_{pores}^2 \tau \delta N_{pores}}{W_{Cell} L_{Cell} \delta} \tag{3.84}$$

or:

$$\tau = \frac{\varepsilon}{\frac{\pi}{4} d_{pores}^2 \frac{N_{pores}}{W_{Cell} L_{Cell}}} \tag{3.85}$$

In Equation (3.85), $N_{pores}/W_{Cell}L_{Cell}$ is the number of pores per unit area of the porous electrode and may be roughly estimated with the number of solid particles per unit area as follows:

$$\frac{N_{pores}}{W_{Cell}L_{Cell}} \approx {n_t}^{2/3} \tag{3.86}$$

By placing Equation (3.86) into Equation (3.85), the average tortuosity for a porous composite electrode is obtained as follows:

$$\tau \approx \frac{\varepsilon}{\frac{\pi}{4} d_{pores}^2 n_t^{2/3}} \tag{3.87}$$

The effective resistivities of the Ni, LSM, and YSZ particles in a porous composite electrode for the particle contact angles usual for SOFCs can be estimated on the basis of the characteristics of the pure material and percolation theory from the following equation [63]:

$$R_i^{eff} = \frac{R'^0_i}{[(1-\varepsilon)\varphi_i P_i]^{1.5}}\,, \qquad i \in \{Ni, LSM, or\ YSZ\} \tag{3.88}$$

The pure electronic resistivity of Ni and LSM ($La_{0.8}Sr_{0.2}MnO_3$) and the pure ionic resistivity of YSZ ($(ZrO_2)_{0.92}(Y_2O_3)_{0.08}$) as a function of temperature can be estimated from Equations (3.89) [63], (3.90) [94], and (3.91) [94], respectively.

$$R'^0_{Ni} = (3.27 \times 10^6 - 1065.3T_s)^{-1} \tag{3.89}$$

$$R'^0_{LSM} = 5.618 \times 10^{-9}\, T_s\, exp\left(\frac{16{,}600}{R_u T_s}\right) \tag{3.90}$$

$$R'^0_{YSZ} = 1.263 \times 10^{-9}\, T_s\, exp\left(\frac{111{,}000}{R_u T_s}\right) \tag{3.91}$$

The permeability of porous electrodes, β_0, can be estimated from the Carman-Kozeny correlation for a porous medium made of spherical particles. We modified this correlation for the random mixture of binary spherical particles as follows:

$$\beta_0 = \frac{1}{180}\frac{\varepsilon^3}{(1-\varepsilon)^2}\left(\frac{\varphi_{el}}{d_{el}}+\frac{1-\varphi_{el}}{d_{io}}\right)^{-2} \tag{3.92}$$

From the model developed for microstructure of porous composite electrodes, the microstructural properties of these electrodes are dependent on the microstructural variables of the porosity, particle size ratio, and size and volume fraction of electron-conducting particles. It should be noted that for a random-packing of spherical particles with a given size, the porosity would be within a certain range. However, the porosity can increase if a pore former is used to fabricate the electrode or the porosity can decrease if the duration or temperature of the sintering process increases. In these conditions, the porosity will be an independent microstructural variable.

3.2.2.1.2 Micro-modeling of Porous LSM-YSZ Composite Cathodes

The micro-model of the porous composite cathode developed is a 1-D model along the thickness direction of the cathode (δ_{PEN}-δ_C<x<δ_{PEN}). It is assumed that the ionic conductivity of LSM and electronic conductivity of YSZ particles are negligible. The cathode layer considered is a functional layer and the effect of the current collector layer is not taken into account.

On the basis of Kirchhoff's circuit law, the electronic and ionic local current densities along the LSM and YSZ conductors in cathode are obtained from Equations (3.93) and (3.94), respectively [55].

$$\frac{di_{LSM,C}(x,j)}{dx} = A_{TPB,C}\,i_{n,C}(x,j) \qquad i_{LSM,C}(\delta_{PEN},j) = i_{tot,j} \tag{3.93}$$

$$\frac{di_{YSZ,C}(x,j)}{dx} = -A_{TPB,C}\,i_{n,C}(x,j) \qquad i_{YSZ,C}(\delta_{PEN},j) = 0 \tag{3.94}$$

To solve these differential equations, the transfer current density per unit of electrochemical active area, $i_{n,C}(x,j)$, should be determined for the oxygen electroreduction reaction. For this purpose, the charge transfer between the electron and ion conductors is assumed to be the rate determining step of reaction (2.R1), and the effect of the adsorption and dissociation of oxygen molecules on the electrocatalytic surface of the cathode is assumed to be negligible [55]. The reaction order of unity is also assumed for this reaction.

The local rate of the forward and backward reactions can be expressed as follows:

$$\vartheta_{fwd,(2.R1)}(x,j) = k_{fwd,(2.R1)}(x,j)C_{O_2}(x,j) \tag{3.95}$$

$$\vartheta_{bwd,(2.R1)}(x,j) = k_{bwd,(2.R1)}(x,j) \tag{3.96}$$

Where, $k_{fwd,(2.R1)}(x,j)$ and $k_{bwd,(2.R1)}(x,j)$ denote the forward and backward reaction rate constants, respectively, and can be estimated from the transition state theory [2] as follows:

$$k_{fwd,(2.R1)}(x,j) = A_{fwd,(2.R1),j}\, T_{s,j} \exp\left(\frac{-\Delta\bar{g}_{fwd,(2.R1)}(x,j)}{R_u T_{s,j}}\right) \tag{3.97}$$

$$k_{bwd,(2.R1)}(x,j) = A_{bwd,(2.R1),j}\, T_{s,j} \exp\left(\frac{-\Delta\bar{g}_{bwd,(2.R1)}(x,j)}{R_u T_{s,j}}\right) \tag{3.98}$$

In these equations, $\Delta\bar{g}_{fwd,(2.R1)}(x,j)$, and $\Delta\bar{g}_{bwd,(2.R1)}(x,j)$ are the actual standard Gibbs function of activation for the forward and backward reactions, respectively. These two parameters can be expressed in terms of the equilibrium standard Gibbs function of activation and the energy change of electron for the cathode polarized from the equilibrium to a desired voltage [95] (the absolute value of the voltages are considered):

$$k_{fwd,(2.R1)}(x,j) = A_{fwd,(2.R1)}T_{s,j} \exp\left(\frac{-\Delta\bar{g}^{\circ}_{fwd,(2.R1)} + 4F\beta_{(2.R1)}\left(E^{\circ}_{O_2,j} - V_C(x,j)\right)}{R_u T_{s,j}}\right) \tag{3.99}$$

$$k_{bwd,(2.R1)}(x,j) = A_{bwd,(2.R1)}T_{s,j} \exp\left(\frac{-\Delta\bar{g}^{\circ}_{bwd,(2.R1)} - 4F\left(1-\beta_{(2.R1)}\right)\left(E^{\circ}_{O_2,j} - V_C(x,j)\right)}{R_u T_{s,j}}\right) \tag{3.100}$$

The transfer current density per unit of electrochemical active area is then obtained from the transfer current densities of the forward and backward reactions [95]:

$$\begin{aligned}
&i_{n,C}(x,j) = 4Fk_{fwd,(2.R1)}(x,j)C_{O_2}(x,j) - 4Fk_{bwd,(2.R1)}(x,j) \\
&= 4FC_{O_2}(x,j)A_{fwd,(2.R1)}\, T_{s,j} \exp\left(\frac{-\Delta\bar{g}^{\circ}_{fwd,(2.R1)}}{R_uT_{s,j}}\right)\exp\left(\frac{4F\beta_{(2.R1)}\left(E^{\circ}_{O_2,j} - V_C(x,j)\right)}{R_uT_{s,j}}\right) \\
&- 4FA_{bwd,(2.R1)}T_{s,j} \exp\left(\frac{-\Delta\bar{g}^{\circ}_{bwd,(2.R1)}}{R_uT_{s,j}}\right)\exp\left(\frac{-4F\left(1-\beta_{(2.R1)}\right)\left(E^{\circ}_{O_2,j} - V_C(x,j)\right)}{R_uT_{s,j}}\right)
\end{aligned} \tag{3.101}$$

At equilibrium, $i_{n,C}(x,j)=0$, $V_C(x,j)=E_{rev,j}$, and $C_{O_2}(x,j) = C_{O_2}(\delta_{PEN},j)$. Therefore, the exchange current density of cathode, $i_{0,C,j}$, can be determined from Equation (3.101) as follows:

$$\begin{aligned}
&i_{0,C,j} \\
&= 4FC_{O_2}(\delta_{PEN},j)A_{fwd,(2.R1)}\, T_{s,j} \exp\left(\frac{-\Delta\bar{g}^{\circ}_{fwd,(2.R1)}}{R_uT_{s,j}}\right)\exp\left(\frac{4F\beta_{(2.R1)}\left(E^{\circ}_{O_2,j} - E_{rev,O_2,j}\right)}{R_uT_{s,j}}\right) \\
&= 4FA_{bwd,(2.R1)}T_{s,j} \exp\,(\frac{-\Delta\bar{g}^{\circ}_{bwd,(2.R1)}}{R_uT_{s,j}})\exp\left(\frac{-4F\left(1-\beta_{(2.R1)}\right)(E^{\circ}_{O_2,j} - E_{rev,O_2,j})}{R_uT_{s,j}}\right)
\end{aligned} \tag{3.102}$$

After determining the cathode exchange current density, Equation (3.101) can be simplified to:

$$\frac{i_{n,C}(x,j)}{i_{0,C,j}} = \left[\frac{C_{O_2}(x,j)}{C_{O_2}(\delta_{PEN},j)}exp\left(\frac{4F\beta_{(2.R1)}\eta_C(x,j)}{R_uT_{s,j}}\right) - exp\left(\frac{-4F\left(1-\beta_{(2.R1)}\right)\eta_C(x,j)}{R_uT_{s,j}}\right)\right] \tag{3.103}$$

In Equation (3.103), $\eta_C(x,j) = E_{rev,O_2,j} - V_C(x,j)$ is the local cathode polarization corresponding to the jth finite volume. The reversible voltage, $E_{rev,O_2,j}$, is obtained from the Nernst relation for reaction (2.R1):

$$E_{rev,O_2,j} = E^{\circ}_{O_2,j} + \frac{R_uT_{s,j}}{4F}\ln\frac{C_{O_2}(\delta_{PEN},j)}{C_a(\delta_{PEN},j)} \tag{3.104}$$

After placing Equation (3.104) into Equation (3.102), the cathode exchange current density corresponding to the jth finite volume is simplified as:

$$i_{0,C,j} = 4FA_{fwd,(2.R1)}\, T_{s,j}\, C_a(\delta_{PEN},j) \left(\frac{C_{O_2}(\delta_{PEN},j)}{C_a(\delta_{PEN},j)}\right)^{1-\beta_{(2.R1)}} \exp\left(\frac{-\Delta \mathring{\bar{g}}_{fwd,(2.R1)}}{R_u T_{s,j}}\right) \tag{3.105}$$

If it is assumed that the transfer coefficient, $\beta_{(2.R1)}$, is equal to 0.5 [95] and air is treated as an ideal gas, $C_{O_2}(x,j) = p_{O_2}(x,j)/\left(R_u T_{s,j}\right)$, Equations (3.103) and (3.105) can be expressed as follows:

$$i_{n,C}(x,j) = i_{0,C,j} \left[\frac{p_{O_2}(x,j)}{p_{O_2}(\delta_{PEN},j)} exp\left(\frac{2F\eta_C(x,j)}{R_u T_{s,j}}\right) - exp\left(\frac{-2F\eta_C(x,j)}{R_u T_{s,j}}\right)\right] \tag{3.106}$$

$$i_{0,C,j} = \frac{4FA_{fwd,(2.R1)}\, p_a(\delta_{PEN},j)}{R_u} \left(\frac{p_{O_2}(\delta_{PEN},j)}{p_a(\delta_{PEN},j)}\right)^{0.5} \exp\left(\frac{-\Delta \mathring{\bar{g}}_{fwd,(2.R1)}}{R_u T_{s,j}}\right) \tag{3.107}$$

Several values for the equilibrium standard Gibbs function of activation, $\Delta \mathring{\bar{g}}_{fwd,(2.R1)}$, for LSM-YSZ cathodes, ranging from 100 to 200 kJ/mol, are reported in the literature [96]. This wide range may be related to the different LSM chemical compositions employed to fabricate the cathodes by various researchers. In this study, the value of 120 kJ/mol, reported by Co, *et al.* [96], for $\Delta \mathring{\bar{g}}_f$, and the value of 3×10^8 for $4FA_{fwd,(2.R1)}\, p_a(\delta_{PEN},j)/R_u$ are chosen for the $(La_{0.8}Sr_{0.2})_{0.98}MnO_3$-$(ZrO_2)_{0.92}(Y_2O_3)_{0.08}$ cathode operated close to the atmospheric pressure.

According to Equations (106) and (107), the exchange current density is constant at a given temperature of the solid structure and bulk oxygen partial pressure in air channel; however, the local transfer current density is a function of the cathode local polarization, $\eta_C(x,j)$, and the local oxygen partial pressure, $p_{O_2}(x,j)$. The following equation is used to determine the cathode local polarization [55]:

$$\eta_C(x,j) = E_{rev,O_2,j} - V_C(x,j) = E_{rev,O_2,j} - \left(V_{C,YSZ}(x,j) - V_{C,LSM}(x,j)\right) \tag{3.108}$$

Using Ohm's law in Equations (3.109) and (3.110) [55], the first derivative of $\eta_C(x,j)$ is expressed as Equation (3.111):

$$\frac{dV_{C,LSM}(x,j)}{dx} = R_{LSM,C,j}^{eff} i_{LSM,C}(x,j) \tag{3.109}$$

$$\frac{dV_{C,YSZ}(x,j)}{dx} = R_{YSZ,C,j}^{eff} i_{YSZ,C}(x,j) \tag{3.110}$$

$$\frac{d\eta_C(x,j)}{dx} = -\left(\frac{V_{C,YSZ}(x,j)}{dx} - \frac{V_{C,LSM}(x,j)}{dx}\right) = -R_{YSZ,C,j}^{eff} i_{YSZ,C}(x,j) + R_{LSM,C,j}^{eff} i_{LSM,C}(x,j) \tag{3.111}$$

Using Kirchhoff's circuit law in Equations (3.93) and (3.94), the second derivative of *$\eta_C(x,j)$* establishes a relation between the local cathode polarization and the local transfer current density:

$$\begin{aligned} \frac{d^2\eta_C(x,j)}{dx^2} &= -R_{YSZ,C,j}^{eff} \frac{di_{YSZ,C}(x,j)}{dx} + R_{LSM,C,j}^{eff} \frac{di_{LSM,C}(x,j)}{dx} \\ &= \left(R_{YSZ,C,j}^{eff} + R_{LSM,C,j}^{eff}\right) A_{TPB,C} i_{n,C}(x,j) \end{aligned} \tag{3.112}$$

To obtain the local oxygen partial pressure, the dusty gas model (DGM) is used [97, 98]. The DGM includes the Stefan-Maxwell diffusion equation and takes into account the Knudsen diffusion. Using the DGM and considering that only oxygen is consumed in the cathode, the following equation is obtained for the local partial pressure of oxygen:

$$\frac{dp_{a,O_2}(x,j)}{dx} = -R_u T_{s,j} \left(\frac{1}{D_{K,O_2,j}^{eff}} + \frac{1}{D_{O_2-N_2,j}^{eff}}\right) \left(1 - \frac{p_{a,O_2}(x,j)}{p_a(\delta_{PEN},j)}\right) \dot{n}''_{a,O_2}(x,j) \tag{3.113}$$

Where, the effective ordinary and Knudsen diffusion coefficients are obtained from Equations (3.48) and (3.49), respectively. It is noted that the atomic diffusion volume, V_a, of O_2 and N_2 in Equation (3.48) is 16.3 and 18.5 cm^3, respectively [93].

In Equation (3.113), the rate of the oxygen flux in x direction, $\dot{n}''_{a,O_2}(x)$, is determined from the mass transfer equation as follows:

$$\frac{d\dot{n}''_{a,O_2}(x)}{dx} = \frac{1}{4F}\frac{di_{LSM,C}(x,j)}{dx} = -\frac{A_{TPB,C}\,i_{n,C}(x,j)}{4F} \tag{3.114}$$

According to Equations (3.112)–(3.114), the local cathode polarization and oxygen partial pressure are both function of the local transfer current density. Therefore, these equations along with Equation (3.106) form the System of Equation (3.115) that should be solved from $x=\delta_{PEN}-\delta_C$ to $x=\delta_{PEN}$ to determine the local transfer current density, cathode polarization, partial pressure of oxygen, and rate of oxygen flux corresponding to the jth finite volume.

$$\left\{\begin{array}{l} \dfrac{d^2\eta_C(x,j)}{dx^2} = \left(R^{eff}_{YSZ,C,j} + R^{eff}_{LSM,C,j}\right)A_{TPB,C}\; i_{n,C}(x,j) \\ \dfrac{dp_{a,O_2}(x,j)}{dx} = R_u T_{s,j}\left(\dfrac{1}{D^{eff}_{K,O_2,j}} + \dfrac{1}{D^{eff}_{O_2-N_2,j}}\right)\left(1 - \dfrac{p_{a,O_2}(x,j)}{p_a(\delta_{PEN},j)}\right)\dot{n}''_{a,O_2}(x,j) \\ \dfrac{d\dot{n}''_{a,O_2}(x,j)}{dx} = \dfrac{A_{TPB,C}\; i_{n,C}(x,j)}{4F} \\ i_{n,C}(x,j) = i_{0,C,j}\left[\dfrac{p_{a,O_2}(x,j)}{p_{a,O_2}(\delta_{PEN},j)} exp\left(\dfrac{2F\eta_C(x,j)}{R_u T_{s,j}}\right) - exp\left(\dfrac{-2F\eta_C(x,j)}{R_u T_{s,j}}\right)\right] \end{array}\right. \tag{3.115}$$

At x= δ_{PEN}: $d\eta_C(\delta_{PEN},j)/dx = R^{eff}_{LSM,C,j} i_{tot,j}$; $p_{a,O_2}(\delta_{PEN},j) = p_{a,O_2,j}$; $\dot{n}''_{a,O_2}(\delta_{PEN},j) = i_{tot,j}/4F$

At x= δ_{PEN}- δ_C: $d\eta_C(\delta_{PEN} - \delta_C,j)/dx = -R^{eff}_{YSZ,C,j} i_{tot,j}$

After solving this system of equation, the local current densities along the LSM and YSZ particles in x direction are determined from Kirchhoff's circuit law in Equations (3.93) and (3.94), respectively. The cathode total polarization resistance corresponding to the jth finite volume is determined from Equation (3.116).

$$R_{C,tot,j} = \frac{\eta_{C,tot,j}}{i_{tot,j}} \tag{3.116}$$

3.2.2.1.3 Micro-modeling of Porous Ni-YSZ Composite Anodes

The micro-model of the porous composite anode is a 1-D model along the thickness direction of the anode ($0<x<\delta_A$). It is assumed that the ionic conductivity of Ni and the electronic conductivity of YSZ particles are negligible. The anode studied is made of a thick substrate layer with a thickness of $\delta_{A,SL}$, as a mechanical support of the cell structure, and a thin functional layer with a thickness of $\delta_{A,FL}$ for H_2 and CO electrooxidation reactions. Since these two layers are different operationally, we model them separately.

3.2.2.1.3.1 Micro-modeling of the Anode Substrate Layer

The micro-model of the substrate layer ($0 \leq x \leq \delta_{A,SL}$) is required to determine the partial pressure of the fuel species at the interface of the substrate and functional layers ($x = \delta_{A,SL}$). For this purpose, the DGM is used to establish a relation between the local partial pressures and the rate of fluxes of the fuel species.

In the absence of thermal, forced, and surface diffusions, the gas transport through the porous anode can be described by three mechanisms of the ordinary diffusion, in which the different species of the fuel move relative to each other under the influence of concentration gradients; Knudsen diffusion, in which the mean free path of molecules of different species of the fuel is in the order of the pore size and the gas molecules collide frequently with the pore walls; and viscous flow, in which the fuel acts as a continuum fluid driven by a pressure gradient through pores of the anode. The electrical analogy for combined mechanisms of the ordinary diffusion, Knudsen diffusion, and viscous flow is shown in Figure 3.4. As seen, to determine the total flux, Knudsen and ordinary diffusive flows are combined like resistors in series and the total diffusive flow is combined with the viscous flow like resistors in parallel:

$$\dot{n}''_{f,l}(x,j) = \dot{n}''_{f,l,diffusion}(x,j) + \dot{n}''_{f,l,viscous}(x,j),\ \ l \in \{CH_4, H_2, CO, H_2O, CO_2, N_2\} \tag{3.117}$$

The DGM for the total diffusive flow, including the Maxwell-Stefan equation for the multi-component ordinary and Knudsen diffusions, is expressed as [97]:

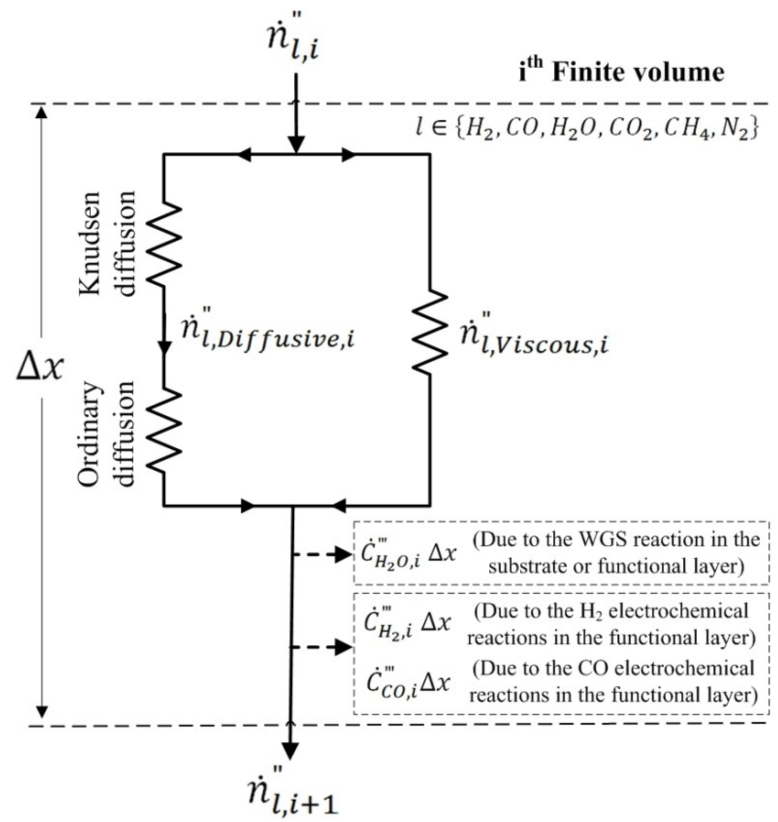

Figure 3.4: The electrical analogy for combined mechanisms of gas transport in the porous composite anode.

$$\frac{dp_{f,l}(x,j)}{dx} = -\frac{R_u T_{s,j}}{p_f(x,j)} \sum_{m=1}^{n} \frac{p_{f,m}(x,j)\,\dot{n}''_{f,l,diffusion}(x,j) - p_{f,l}(x,j)\,\dot{n}''_{f,m,diffusion}(x,j)}{D_{l-m,j}^{eff}} - R_u T_{s,j}\,\frac{\dot{n}''_{f,l,diffusion}(x,j)}{D_{K,l,j}^{eff}} \tag{3.118}$$

The effective ordinary and Knudsen diffusion coefficients are estimated from Equations (3.48) and (3.49), respectively. It is noted that the atomic diffusion volume, V_a, of H_2, CO, H_2O, CO_2, CH_4, and N_2 in Equation (3.48) is 6.12, 18.0, 13.1, 26.7, 25.14, and 18.5 cm^3, respectively [93].

The behavior of viscous flow in the porous anode is mathematically described as the creeping flow at which the Reynolds number is small that the inertia effects can be ignored in comparison to the viscous effects. If the gas mixture is not accelerating, the net force on any finite volume of the anode in x direction is zero, so the viscous-drag force just balances the force due to the pressure difference across the finite volume. In this condition, the rate of flux corresponding to viscous flow through the porous anode can be described by Darcy's law as follows [97]:

$$\dot{n}^{"}_{f,l,viscous}(x,j) = -\frac{p_{f,l}(x,j)}{R_u T_{s,j}} \frac{\beta_{0,A}}{\mu_f(x,j)} \frac{dp_f(x,j)}{dx} \tag{3.119}$$

The dynamic viscosity of fuel, as an n-component gas mixture, can be estimated by the Reichenberg method from the dynamic viscosity of the pure components [99].

If the rate of flux corresponding to viscous flow in Equation (3.119) is placed into Equation (3.117) and the rate of flux corresponding to the diffusive flow is obtained from Equation (3.117) and placed into Equation (3.118), the multi-component gas transport in the porous anode on the basis of the DGM for the combined mechanisms of the ordinary diffusion, Knudsen diffusion, and viscous flow is obtained as follows:

$$\begin{aligned}\frac{dp_{f,l}(x,j)}{dx} = &-\frac{R_u T_{s,j}}{p_f(x,j)} \sum_{m=1}^{n} \frac{p_{f,m}(x,j)\,\dot{n}^{"}_{f,l}(x,j) - p_{f,l}(x,j)\,\dot{n}^{"}_{f,m}(x,j)}{D^{eff}_{l-m,j}} - R_u T_{s,j} \frac{\dot{n}^{"}_{f,l}(x,j)}{D^{eff}_{K,l,j}} \\ &- \frac{\beta_{0,A}\, p_{f,l}(x,j)}{D^{eff}_{K,l,j}\, \mu_f(x,j)} \frac{dp_f(x,j)}{dx}\end{aligned} \tag{3.120}$$

If this equation is developed for all species of the fuel, the summation of both sides of the equations obtained yields the change of the fuel pressure along the anode thickness:

$$\frac{dp_f(x,j)}{dx} = -R_u T_{s,j} \frac{\sum_{m=1}^{n} \dot{n}^{"}_{f,m}(x,j)/D^{eff}_{K,m,j}}{\left(1 + \frac{\beta_{0,A}}{\mu_f(x,j)} \sum_{m=1}^{n} \frac{p_{f,m}(x,j)}{D^{eff}_{K,m,j}}\right)} \tag{3.121}$$

Placing Equation (3.121) into Equation (3.120) yields:

$$\begin{aligned}\frac{dp_{f,l}(x,j)}{dx} &= -\frac{R_u T_{s,j}}{\sum_{m=1}^{n} p_{f,m}(x,j)} \sum_{m=1}^{n} \frac{p_{f,m}(x,j)\,\dot{n}''_{f,l}(x,j) - p_{f,l}(x,j)\dot{n}''_{f,m}(x,j)}{D_{l-m,j}^{eff}} \\ &\quad - R_u T_{s,j}\frac{\dot{n}''_{f,l}(x,j)}{D_{K,l,j}^{eff}} + R_u T_{s,j}\frac{\beta_{0,A}\,p_{f,l}(x,j)}{D_{K,l,j}^{eff}\,\mu_f(x,j)} \\ &\quad \times \frac{\sum_{m=1}^{n} \dot{n}''_{f,m}(x,j)/D_{K,m,j}^{eff}}{\left(1+\frac{\beta_{0,A}}{\mu_f(x,j)}\sum_{m=1}^{n}\frac{p_{f,m}(x,j)}{D_{K,m,j}^{eff}}\right)}, l \in \{H_2, CO, H_2O, CO_2, CH_4, N_2\}\end{aligned} \tag{3.122}$$

In this equation, the gradient of the local partial pressure is dependent on the local rate of flux of the fuel components. The rate of flux of nitrogen and methane is zero in the anode microstructure; the local rate of flux of water and carbon dioxide is equal in magnitude and opposite in direction to that of hydrogen and carbon monoxide, respectively; and the local rate of flux of hydrogen and carbon monoxide can be obtained from the mass conservation equation as follows:

$$\frac{d\dot{n}''_{f,H_2}(x,j)}{dx} = \dot{C}'''_{H_2O,WGS}(x,j) \tag{3.123}$$

$$\dot{n}''_{f,CO}(x,j) = \frac{i_{tot,j}}{2F} - \dot{n}''_{f,H_2}(x,j) \tag{3.124}$$

$$\dot{n}''_{f,H_2O}(x,j) = -\dot{n}''_{f,H_2}(x,j) \tag{3.125}$$

$$\dot{n}''_{f,CO_2}(x,j) = -\dot{n}''_{f,CO}(x,j) \tag{3.126}$$

The change in the rate of flux of hydrogen in Equation (3.123) is dependent on the rate of water consumption through WGS reaction, $\dot{C}'''_{H_2O,WGS}(x,j)$, in the anode substrate layer. The rate of water consumption through WGS reaction can be determined from the relation of the equilibrium-constant of the WGS reaction with partial pressures of H_2, CO, H_2O, and CO_2.

$$K_{p,WGS}(T_{s,j}) = \frac{p_{f,H_2}(x,j)p_{f,CO_2}(x,j)}{p_{f,H_2O}(x,j)\,p_{f,CO}(x,j)} \tag{3.127}$$

Therefore, the partial pressure and rate of flux of the fuel components are coupled and the System of Equation (3.128) with the corresponding boundary conditions should be solved to determine these variables along the anode substrate layer.

$$\left\{\begin{aligned}
&\frac{dp_{f,l}(x,j)}{dx}=\frac{-R_uT_{s,j}}{\sum_{m=1}^{n}p_{f,m}(x,j)}\sum_{m=1}^{n}\frac{p_{f,m}(x,j)\dot{n}''_{f,l}(x,j)-p_{f,l}(x,j)\dot{n}''_{f,m}(x,j)}{D^{eff}_{l-m,j}}-R_uT_{s,j}\frac{\dot{n}''_{f,l}(x,j)}{D^{eff}_{K,l,j}}\\
&\quad+R_uT_{s,j}\frac{\beta_{0,A}p_{f,l}(x,j)}{D^{eff}_{K,l,j}\,\mu_f(x,j)}\frac{\sum_{m=1}^{n}\dot{n}''_{f,m}(x,j)/D^{eff}_{K,m,j}}{\left(1+\frac{\beta_{0,A}}{\mu_f(x,j)}\sum_{m=1}^{n}\frac{p_{f,m}(x,j)}{D^{eff}_{K,m,j}}\right)},\ l\in\{H_2,CO,H_2O,CO_2,CH_4,N_2\}\\
&\frac{d\dot{n}''_{f,H_2}(x,j)}{dx}=\dot{C}'''_{H_2O,WGS}(x,j)\\
&\dot{n}''_{f,CO}(x,j)=\frac{i_{tot,j}}{2F}-\dot{n}''_{f,H_2}(x,j)\\
&\dot{n}''_{f,H_2O}(x,j)=-\dot{n}''_{f,H_2}(x,j)\\
&\dot{n}''_{f,CO_2}(x,j)=-\dot{n}''_{f,CO}(x,j)\\
&\dot{n}''_{f,CH_4}(x,j)=\dot{n}''_{f,N_2}(x,j)=0\\
&K_{p,WGS}(T_{s,j})=\frac{p_{f,H_2}(x,j)p_{f,CO_2}(x,j)}{p_{f,H_2O}(x,j)\,p_{f,CO}(x,j)}
\end{aligned}\right.\tag{3.128}$$

At x=0: $p_{f,l}(0,j)=p_{f,l,j},\ l\in\{H_2,CO,H_2O,CO_2,CH_4,N_2\}$

3.2.2.1.3.2 Micro-modeling of the Anode Functional Layer

Since the ion conductivity of Ni and the electron conductivity of YSZ are negligible, the electron and ion local current densities generated/consumed by the electrooxidation reactions (2.R2) and (2.R3) can be obtained on the basis of Kirchhoff's circuit law from the following equations [59]:

$$\frac{di_{Ni,A}(x,j)}{dx}=-A_{TPB,A}i_{n,A}(x,j)\qquad i_{Ni,A}(\delta_{A,SL})=i_{tot,j}\tag{3.129}$$

$$\frac{di_{YSZ,A}(x,j)}{dx}=A_{TPB,A}i_{n,A}(x,j)\qquad i_{YSZ,A}(\delta_{A,SL})=0\tag{3.130}$$

Where, $\delta_{A,SL}\leq x\leq\delta_A$.

To solve these differential equations, the anode total transfer current density per unit of the electrochemical active area, $i_{n,A}(x,j)$, due to the electrochemical reactions in the anode functional layer, should be determined.

To determine the contribution of the hydrogen electrooxidation reaction in the anode total transfer current density, the charge transfer between the electron and ion conductors is assumed to be the rate determining step of reaction (2.R2), and the effect of the adsorption and dissociation of hydrogen molecules on the electrocatalytic surface of the anode is neglected. The reaction order of unity is also assumed for this reaction. Therefore, the local rate of the forward and backward reactions corresponding to reaction (2.R2), $\vartheta_{fwd,(2.R2)}(x,j)$ and $\vartheta_{bwd,(2.R2)}(x,j)$, can be expressed as follows:

$$\vartheta_{fwd,(2.R2)}(x,j) = k_{fwd,(2.R2)}(x,j) C_{f,H_2}(x,j) \tag{3.131}$$

$$\vartheta_{bwd,(2.R2)}(x,j) = k_{bwd,(2.R2)}(x,j) C_{f,H_2O}(x,j) \tag{3.132}$$

Where, $k_{fwd,(2.R2)}(x,j)$ and $k_{bwd,(2.R2)}(x,j)$ denote the reaction rate constants for the forward and backward reactions, respectively, and can be estimated from the transition state theory [2]:

$$k_{fwd,(2.R2)}(x,j) = A_{fwd,(2.R2)}\, T_{s,j}\, exp\left(\frac{-\Delta\bar{g}_{fwd,(2.R2)}(x,j)}{R_u T_{s,j}}\right) \tag{3.133}$$

$$k_{bwd,(2.R2)}(x,j) = A_{bwd,(2.R2)}\, T_{s,j}\, exp\left(\frac{-\Delta\bar{g}_{bwd,(2.R2)}(x,j)}{R_u T_{s,j}}\right) \tag{3.134}$$

In these equations, $\Delta\bar{g}_{fwd,(2.R2)}(x,j)$ and $\Delta\bar{g}_{bwd,(2.R2)}(x,j)$, are the actual standard Gibbs function of activation for the forward and backward reactions, respectively. These two parameters can be expressed in terms of the equilibrium standard Gibbs function of activation and the electron energy change for the anode polarized from the equilibrium state to a desired voltage [95]:

$$k_{fwd,(2.R2)}(x,j) = A_{fwd,(2.R2)} T_{s,j}\, exp\left(\frac{-\Delta\bar{g}^{\circ}_{fwd,(2.R2)} + 2F\beta_{(2.R2)}\left(E^{\circ}_{H_2,j} - V_A(x,j)\right)}{R_u T_{s,j}}\right) \tag{3.135}$$

$$k_{bwd,(2.R2)}(x,j) = A_{bwd,(2.R2)} T_{s,j}\, exp\left(\frac{-\Delta\bar{g}^{\circ}_{bwd,(2.R2)} - 2F\left(1-\beta_{(2.R2)}\right)\left(E^{\circ}_{H_2,j} - V_A(x,j)\right)}{R_u T_{s,j}}\right) \quad (3.136)$$

Therefore, the contribution of the hydrogen electrochemical reaction in the anode total transfer current density can be found as follows:

$$\begin{aligned} i_{n,A,H_2}(x,j) &= 2Fk_{fwd,(2.R2)}(x,j)C_{f,H_2}(x,j) - 2Fk_{bwd,(2.R2)}(x,j)C_{f,H_2O}(x,j) \\ &= 2FC_{f,H_2}(x,j)A_{fwd,(2.R2)}\, T_{s,j}\, exp\left(\frac{-\Delta\bar{g}^{\circ}_{fwd,(2.R2)}}{R_u T_{s,j}}\right) exp\left(\frac{2F\beta_{(2.R2)}\left(E^{\circ}_{H_2,j} - V_A(x,j)\right)}{R_u T_s}\right) \\ &\quad - 2FC_{f,H_2O}(x,j)A_{bwd,(2.R2)}\, T_{s,j}\, exp\left(\frac{-\Delta\bar{g}^{\circ}_{bwd,(2.R2)}}{R_u T_{s,j}}\right) exp\left(\frac{-2F\left(1-\beta_{(2.R2)}\right)\left(E^{\circ}_{H_2,j} - V_A(x,j)\right)}{R_u T_{s,j}}\right) \end{aligned} \quad (3.137)$$

At equilibrium, $i_{n,A,H_2}(x,j)$=0, $V_A(x,j) = E_{rev,H_2,j}$, $C_{f,H_2}(x,j) = C_{f,H_2}(0,j)$, and $C_{f,H_2O}(x,j) = C_{f,H_2O}(0,j)$. Therefore, the exchange current density corresponding to the hydrogen electrochemical reaction, $i_{0,A,H_2,j}$, can be determined from Equation (3.138):

$$\begin{aligned} i_{0,A,H_2,j} &= 2FC_{f,H_2}(0,j)A_{fwd,(2.R2)}\, T_{s,j}\, exp\left(\frac{-\Delta\bar{g}^{\circ}_{fwd,(2.R2)}}{R_u T_{s,j}}\right) exp\left(\frac{2F\beta_{(2.R2)}\left(E^{\circ}_{H_2,j} - E_{rev,H_2,j}\right)}{R_u T_{s,j}}\right) \\ &= 2FC_{f,H_2O}(0,j)A_{bwd,(2.R2)}\, T_{s,j}\, exp\left(\frac{-\Delta\bar{g}^{\circ}_{bwd,(2.R2)}}{R_u T_{s,j}}\right) exp\left(\frac{-2F\left(1-\beta_{(2.R2)}\right)\left(E^{\circ}_{H_2,j} - E_{rev,H_2,j}\right)}{R_u T_{s,j}}\right) \end{aligned} \quad (3.138)$$

And Equation (3.137) can be simplified to:

$$\begin{aligned} \frac{i_{n,A,H_2}(x,j)}{i_{0,A,H_2,j}} &= \frac{C_{f,H_2}(x,j)}{C_{f,H_2}(0,j)} exp\left(\frac{2F\beta_{(2.R2)}\left(E_{rev,H_2,j} - V_A(x,j)\right)}{R_u T_{s,j}}\right) \\ &\quad - \frac{C_{f,H_2O}(x,j)}{C_{f,H_2O}(0,j)} exp\left(\frac{-2F\left(1-\beta_{(2.R2)}\right)\left(E_{rev,H_2,j} - V_A(x,j)\right)}{R_u T_{s,j}}\right) \end{aligned} \quad (3.139)$$

If the reversible voltage of the hydrogen electrochemical reaction, $E_{rev,H_2,j}$, is obtained from the Nernst relation in Equation (3.140) and is placed into Equation (3.138), $i_{0,A,H_2,j}$ can be written as Equation (3.141):

$$E_{rev,H_2,j} = \overset{\circ}{E}_{H_2,j} + \frac{R_u T_{s,j}}{2F} \ln \frac{C_{f,H_2}(0,j)}{C_{f,H_2O}(0,j)} \tag{3.140}$$

$$i_{0,A,H_2,j} = 2FA_{fwd,(2.R2)}\, T_{s,j}\, C_{f,H_2}(0,j)^{1-\beta_{(2.R2)}}\, C_{f,H_2O}(0,j)^{\beta_{(2.R2)}} \exp\left(\frac{-\Delta \overset{\circ}{\bar{g}}_{fwd,(2.R2)}}{R_u T_{s,j}}\right) \tag{3.141}$$

Since the WGS reaction is in equilibrium, the reversible voltage of the hydrogen and carbon monoxide electrooxidation reactions are identical (see Equation (3.62)); consequently, the local anode polarizations for both hydrogen and carbon monoxide electrooxidation reactions are identical:

$$\eta_{A,H_2}(x,j) = E_{rev,H_2,j} - V_A(x,j) = E_{rev,CO,j} - V_A(x,j) = \eta_{A,CO}(x,j) = \eta_A(x,j) \tag{3.142}$$

Because the gaseous fuel is treated as an ideal gas, $C_{f,l,j} = p_{f,l,j}/(R_u T_{s,j})$. If the transfer coefficient, $\beta_{(2.R2)}$, is assumed to be 0.5 [95], Equations (3.139) and (3.141) can be expressed as:

$$i_{n,A,H_2}(x,j) = i_{0,A,H_2,j}\left[\frac{p_{f,H_2}(x,j)}{p_{f,H_2}(0,j)} exp\left(\frac{F\eta_A(x,j)}{R_u T_{s,j}}\right) - \frac{p_{f,H_2O}(x,j)}{p_{f,H_2O}(0,j)} exp\left(\frac{-F\eta_A(x,j)}{R_u T_{s,j}}\right)\right] \tag{3.143}$$

$$i_{0,A,H_2,j} = \frac{2FA_{fwd,(2.R2)}}{R_u} p_{f,H_2}^{0.5}(0,j)\, p_{f,H_2O}^{0.5}(0,j)\, exp\left(\frac{-\Delta \overset{\circ}{\bar{g}}_{fwd,(2.R2)}}{R_u T_{s,j}}\right) \tag{3.144}$$

With the same method and assumptions, the transfer and exchange current densities due to the CO electrooxidation reaction (2.R3) can be determined:

$$i_{n,A,CO}(x,j) = i_{0,A,CO,j}\left[\frac{p_{f,CO}(x,j)}{p_{f,CO}(0,j)} exp\left(\frac{F\eta_A(x,j)}{R_u T_{s,j}}\right) - \frac{p_{f,CO_2}(x,j)}{p_{f,CO_2}(0,j)} exp\left(\frac{-F\eta_A(x,j)}{R_u T_{s,j}}\right)\right] \tag{3.145}$$

$$i_{0,A,CO,j} = \frac{2FA_{fwd,(2.R3)}}{R_u}\, p_{f,CO}^{0.5}(0,j) p_{f,CO_2}^{0.5}(0,j)\, exp\left(\frac{-\Delta \bar{g}^{\circ}_{fwd,(2.R3)}}{R_u T_{s,j}}\right) \tag{3.146}$$

After determination of the transfer current densities of H_2 and CO electrochemical reactions, the anode total transfer current density yields as:

$$\begin{aligned} i_{n,A}(x,j) &= i_{n,A,H_2}(x,j) + i_{n,A,CO}(x,j) \\ &= i_{0,A,H_2,j}\frac{p_{f,H_2}(x,j)}{p_{f,H_2}(0,j)}\left(1 + \frac{i_{0,A,CO,j}}{i_{0,A,H_2,j}} \times \frac{p_{f,H_2}(0,j)p_{f,CO}(x,j)}{p_{f,H_2}(x,j)p_{f,CO}(0,j)}\right) exp\left(\frac{F\eta_A(x,j)}{R_u T_{s,j}}\right) \\ &- i_{0,A,H_2,j}\frac{p_{f,H_2O}(x,j)}{p_{f,H_2O}(0,j)}\left(1 + \frac{i_{0,A,CO,j}}{i_{0,A,H_2,j}}\right. \\ &\left.\times \frac{p_{f,H_2O}(0,j)p_{f,CO_2}(x,j)}{p_{f,H_2O}(x,j)p_{f,CO_2}(0,j)}\right) exp\left(\frac{-F\eta_A(x,j)}{R_u T_{s,j}}\right) \end{aligned} \tag{3.147}$$

Since the WGS reaction is locally in equilibrium,

$$\begin{aligned} K_{p,WGS}(T_{s,j}) &= \frac{p_{f,H_2}(0,j)\, p_{f,CO_2}(0,j)}{p_{f,H_2O}(0,j)\, p_{f,CO}(0,j)} = \frac{p_{f,H_2}(x,j)\, p_{f,CO_2}(x,j)}{p_{f,H_2O}(x,j)\, p_{f,CO}(x,j)} \quad or \quad \frac{p_{f,H_2}(0,j)p_{f,CO}(x,j)}{p_{f,H_2}(x,j)\, p_{f,CO}(0,j)} \\ &= \frac{p_{f,H_2O}(0,j)p_{f,CO_2}(x,j)}{p_{f,H_2O}(x,j)p_{f,CO_2}(0,j)} \end{aligned} \tag{3.148}$$

Therefore, Equation (3.147) is simplified to:

$$\begin{aligned} i_{n,A}(x,j) &= i_{0,A,H_2,j}\left[\frac{p_{f,H_2}(x,j)}{p_{f,H_2}(0,j)} exp\left(\frac{F\eta_A(x,j)}{R_u T_{s,j}}\right) - \frac{p_{f,H_2O}(x,j)}{p_{f,H_2O}(0,j)} exp\left(\frac{-F\eta_A(x,j)}{R_u T_{s,j}}\right)\right]\left(1\right. \\ &\left.+ \frac{i_{0,A,CO,j}}{i_{0,A,H_2,j}} \times \frac{p_{f,H_2}(0,j)\, p_{f,CO}(x,j)}{p_{f,H_2}(x,j)\, p_{f,CO}(0,j)}\right) \end{aligned} \tag{3.149}$$

It should be noted that the effect of the last parentheses on the right hand side of Equation (3.149) on the anode local transfer current density is not taken into account if just hydrogen is assumed to be involved in the electrooxidation reaction in the anode functional layer.

For the exchange current densities of H_2 and CO electrooxidation reactions, we developed the following equations from the experimental results reported by Habibzadeh [100].

$$i_{0,A,H_2,j} = 86.71\, p_{f,H_2}^{0.5}(0,j)\, p_{f,H_2O}^{0.5}(0,j)\, exp\left(\frac{-76{,}500}{R_u T_{s,j}}\right) \tag{3.150}$$

$$i_{0,A,CO,j} = 438.7\, p_{f,CO}^{0.5}(0,j)\, p_{f,CO_2}^{0.5}(0,j)\, exp\left(\frac{-102{,}750}{R_u T_{s,j}}\right) \tag{3.151}$$

According to Equation (3.149), to determine the anode local transfer current density, the anode local polarization and the local partial pressures of the fuel species should be obtained. The following equation is used to determine the anode local polarization [59]:

$$\eta_A(x,j) = E_{rev,H_2,j} - V_A(x,j) = E_{rev,H_2 j} - \left(V_{Ni}(x,j) - V_{YSZ}(x,j)\right) \tag{3.152}$$

Using Ohm's law in Equations (3.153) and (3.154), the first derivative of $\eta_A(x,j)$ is expressed as Equation (3.155):

$$\frac{dV_{Ni}(x,j)}{dx} = R_{Ni,j}^{eff} i_{Ni}(x,j) \tag{3.153}$$

$$\frac{dV_{YSZ}(x,j)}{dx} = R_{YSZ,j}^{eff} i_{YSZ}(x,j) \tag{3.154}$$

$$\frac{d\eta_A(x,j)}{dx} = -\left(\frac{V_{Ni}(x,j)}{dx} - \frac{V_{YSZ}(x,j)}{dx}\right) = R_{YSZ,j}^{eff} i_{YSZ}(x,j) - R_{Ni,j}^{eff} i_{Ni}(x,j) \tag{3.155}$$

Using Kirchhoff's circuit law in Equations (3.129) and (3.130), the second derivative of $\eta_A(x,j)$ establishes a relation between the anode local polarization and the local transfer current density:

$$\frac{d^2\eta_A(x,j)}{dx^2} = R^{eff}_{YSZ,j}\frac{di_{YSZ}(x,j)}{dx} - R^{eff}_{Ni,j}\frac{di_{Ni}(x,j)}{dx} = \left(R^{eff}_{YSZ,j} + R^{eff}_{Ni,j}\right)A_{TPB,A}i_{n,A}(x,j) \tag{3.156}$$

The local partial pressure of the fuel components in the anode functional layer is determined using the similar model and assumptions considered for the anode substrate layer. The only difference is the effect of the H_2 and CO electrooxidation reactions that should be taken into account in the mass conservation equation (see Figure 3.4). The rate of flux of H_2 and CO along the x axis is determined as Equations (3.157) and (3.158), respectively.

$$\frac{d\dot{n}^{"}_{f,H_2}(x,j)}{dx} = -\dot{C}^{'''}_{H_2}(x,j) + \dot{C}^{'''}_{H_2O,WGS}(x,j) \tag{3.157}$$

$$\frac{d\dot{n}^{"}_{f,CO}(x,j)}{dx} = -\dot{C}^{'''}_{CO}(x,j) - \dot{C}^{'''}_{H_2O,WGS}(x,j) \tag{3.158}$$

Where, the rate of hydrogen and carbon monoxide consumptions, $\dot{C}^{'''}_{H_2}(x,j)$ and $\dot{C}^{'''}_{CO}(x,j)$, are dependent on the transfer current density corresponding to the H_2 and CO electrochemical reactions:

$$\dot{C}^{'''}_{H_2}(x,j) = \frac{A_{TPB,A}}{2F}i_{n,A,H_2}(x,j) \tag{3.159}$$

$$\dot{C}^{'''}_{CO}(x,j) = \frac{A_{TPB,A}}{2F}i_{n,A,CO}(x,j) \tag{3.160}$$

Therefore, the anode local transfer current density, local polarization, and local partial pressures of the fuel species are coupled and the System of Equation (3.161) should be solved with the corresponding boundary conditions to determine the distribution of these variables along the anode functional layer.

$$
\begin{cases}
\dfrac{d^2\eta_A(x,j)}{dx^2} = \left(R_{YSZ,A,j}^{eff} + R_{Ni,A,j}^{eff}\right)A_{TPB,A}i_{n,A}(x,j) \\
i_{n,A}(x,j) = i_{0,A,H_2,j}\left[\dfrac{p_{f,H_2}(x,j)}{p_{f,H_2}(0,j)}exp\left(\dfrac{F\eta_A(x,j)}{R_uT_{s,j}}\right) - \dfrac{p_{f,H_2O}(x,j)}{p_{f,H_2O}(0,j)}exp\left(\dfrac{-F\eta_A(x,j)}{R_uT_{s,j}}\right)\right]\times \\
\qquad\qquad\qquad \left(1 + \dfrac{i_{0,A,CO,j}}{i_{0,A,H_2,j}}\times\dfrac{p_{f,H_2}(0,j)p_{f,CO}(x,j)}{p_{f,H_2}(x,j)p_{f,CO}(0,j)}\right) \\
\dfrac{dp_{f,l}(x,j)}{dx} = -\dfrac{R_uT_{s,j}}{\sum_{m=1}^{n}p_{f,m}(x,j)}\sum_{m=1}^{n}\dfrac{p_{f,m}(x,j)\dot{n}_{f,l}''(x,j) - p_{f,l}(x,j)\dot{n}_{f,m}''(x,j)}{D_{l-m,j}^{eff}} - R_uT_{s,j}\dfrac{\dot{n}_{f,l}''(x,j)}{D_{K,l,j}^{eff}} \\
\qquad +R_uT_{s,j}\dfrac{\beta_0 p_{f,l}(x,j)}{D_{K,l,j}^{eff}\,\mu(x,j)}\dfrac{\sum_{m=1}^{n}\dfrac{\dot{n}_{f,m}''(x,j)}{D_{K,m,j}^{eff}}}{\left(1 + \dfrac{\beta_0}{\mu(x,j)}\sum_{m=1}^{n}\dfrac{p_{f,m}(x,j)}{D_{K,m,j}^{eff}}\right)} \quad l \in \{H_2, CO, H_2O, CO_2, CH_4, N_2\} \\
\dfrac{d\dot{n}_{f,H_2}''(x,j)}{dx} = -\dfrac{A_{TPB,A}}{2F}i_{0,A,H_2,j}\times \\
\qquad \left[\dfrac{p_{f,H_2}(x,j)}{p_{f,H_2}(0,j)}exp\left(\dfrac{F\eta_A(x,j)}{R_uT_{s,j}}\right) - \dfrac{p_{f,H_2O}(x,j)}{p_{f,H_2O}(0,j)}exp\left(\dfrac{-F\eta_A(x,j)}{R_uT_{s,j}}\right)\right] + \dot{C}_{H_2O,WGS}'''(x,j) \\
\dfrac{d\dot{n}_{f,CO}''(x,j)}{dx} = -\dfrac{A_{TPB,A}}{2F}i_{0,A,CO,j}\times \\
\qquad \left[\dfrac{p_{f,CO}(x,j)}{p_{f,CO}(0,j)}exp\left(\dfrac{F\eta_A(x,j)}{R_uT_{s,j}}\right) - \dfrac{p_{f,CO_2}(x,j)}{p_{f,CO_2}(0,j)}exp\left(\dfrac{-F\eta_A(x,j)}{R_uT_{s,j}}\right)\right] - \dot{C}_{H_2O,WGS}'''(x,j) \\
\dot{n}_{f,H_2O}''(x,j) = -\dot{n}_{f,H_2}''(x,j) \\
\dot{n}_{f,CO_2}''(x,j) = -\dot{n}_{f,CO}''(x,j) \\
\dot{n}_{f,CH_4}''(x,j) = \dot{n}_{f,N_2}''(x,j) = 0 \\
K_{p,WGS}\left(T_{s,j}\right) = \dfrac{p_{f,H_2}(x,j)p_{f,CO_2}(x,j)}{p_{f,H_2O}(x,j)p_{f,CO}(x,j)}
\end{cases}
\tag{3.161}
$$

At x=$\delta_{A,SL}$: $d\eta_A(\delta_{SL},j)/dx = -R_{Ni,A,j}^{eff}i_{tot,j}$; $p_{f,l}(\delta_{SL},j) = p_{f,l,j,SL\|FL}$, $l \in \{H_2, CO, H_2O, CO_2, CH_4, N_2\}$

At x= δ_A: $d\eta_A(\delta_A,j)/dx = R_{YSZ,A,j}^{eff}i_{tot,j}$; $\dot{n}_{f,H_2}''(\delta_A,j) = 0$; $\dot{n}_{f,CO}''(\delta_A,j) = 0$

After solving this system of equation, the distribution of current densities corresponding to the H$_2$ and CO electrochemical reactions can be determined from the following differential equations:

$$di_{Ni,H_2}(x,j) = -A_{TPB,A}i_{n,A,H_2}(x,j) \tag{3.162}$$

$$di_{Ni,CO}(x,j) = -A_{TPB,A}i_{n,A,CO}(x,j) \tag{3.163}$$

Finally, the total polarization resistance of anode is determined:

$$R_{A,tot,j} = \frac{\eta_{A,tot,j}}{i_{tot,j}} \tag{3.164}$$

Since the ohmic polarization in the substrate layer is usually negligible, the effect of this polarization has not been considered to determine the total polarization resistance of the anode.

It is noted that to solve the System of Equation (3.161), the species partial pressure of the fuel at the interface of the anode substrate and functional layers ($x=\delta_{A,SL}$) should be obtained. For this purpose, the System of Equation (3.128), obtained from the micro-modeling of the anode substrate layer, should be solved along the thickness of the anode from $x=0$ to $x=\delta_{A,SL}$.

To determine the total current density generated in the j^{th} finite volume from Equation (3.64), the use of iterative methods is required. Indeed, for a given total current density, the distributions of the total polarization in electrodes are obtained from the System of Equations (3.115), (3.128), (3.161), and the total polarization of the cell is calculated from Equation (3.65). For a new total current density, a new value for the cell total polarization is obtained from Equation (3.65). The total current density may change until the total polarization obtained from Equation (3.65) satisfies Equation (3.64). However, before determination of the total current density the temperature of the solid structure and species partial pressure of the fuel and air streams in the j^{th} finite volume should be obtained from the cell macro-modeling.

3.2.2.2 Macro-modeling

The macro-model of the co-flow planar cell is a 1-D model of the fuel and air streams passing through the channels and the cell solid structure along the length of the cell ($0<y<L_{Cell}$).

3.2.2.2.1 Macro-modeling of the Fuel and Air Streams

The objective of the macro-modeling of the fuel and air streams passing through the channels is to determine the distribution of the temperature and species partial pressure of the fuel and air along the length of the cell. For this purpose, it is assumed that the heat and mass diffusions in the air and fuel streams along the length of the cell are negligible. In such a situation, the dependency of the air and fuel streams upon downstream locations is diminished and the computational cost is reduced significantly.

The mass and energy flows in the jth finite volume of the fuel and air streams passing through the channels are shown in Figures 3.5 and 3.6, respectively. From the mass balance in the jth finite volume of the fuel stream, the change in the molar flow rate of each species of fuel can be determined:

$$\Delta\dot{n}_{f,CH_4,j} = -\dot{C}_{CH_4,SR,j} \tag{3.165}$$

$$\Delta\dot{n}_{f,H_2,j} = 3\dot{C}_{CH_4,SR,j} + \dot{P}_{CO_2,WGS,j} - \dot{n}_{H_2}(0,j) \tag{3.166}$$

$$\Delta\dot{n}_{f,CO,j} = \dot{C}_{CH_4,SR,j} - \dot{P}_{CO_2,WGS,j} - \dot{n}_{CO}(0,j) \tag{3.167}$$

$$\Delta\dot{n}_{f,H_2O,j} = -\dot{C}_{CH_4,SR,j} - \dot{P}_{CO_2,WGS,j} + \dot{n}_{H_2O}(0,j) \tag{3.168}$$

$$\Delta\dot{n}_{f,CO_2,j} = \dot{P}_{CO_2,WGS,j} + \dot{n}_{CO_2}(0,j) \tag{3.169}$$

$$\Delta\dot{n}_{f,N_2,j} = 0 \tag{3.170}$$

At y=0: $\dot{n}_{f,l}(0,0) = \dot{n}_{f,l,ent}$, $l \in \{H_2, CO, H_2O, CO_2, CH_4, N_2\}$

The molar flow rate of H$_2$, $\dot{n}_{H_2}(0,j)$, and CO, $\dot{n}_{CO}(0,j)$ transferred to the anode, is equal to the molar flow rate of H$_2$O, $\dot{n}_{H_2O}(0,j)$, and CO$_2$, $\dot{n}_{CO_2}(0,j)$ transferred to the fuel stream, respectively, and can be determined from Faraday's electrochemical law:

$$\dot{n}_{H_2}(0,j) = \frac{i_{tot,H_2,j}}{2F}(W_{ch} + W_{rib})\,\Delta y \tag{3.171}$$

$$\dot{n}_{CO}(0,j) = \frac{i_{tot,CO,j}}{2F}(W_{ch} + W_{rib})\,\Delta y \tag{3.172}$$

Several correlations for the rate of CH$_4$ steam reforming reaction, $\dot{C}_{CH_4,SR,j}$ at the presence of the anode catalyst are reported in the literature [33, 45, 101-104]; however, the effect of the microstructure of the anode catalyst on the reaction rate has been considered in one of these correlations developed by Ǿdegard *et al.* [104]. This correlation for the jth finite volume of the fuel stream can be expressed as follows:

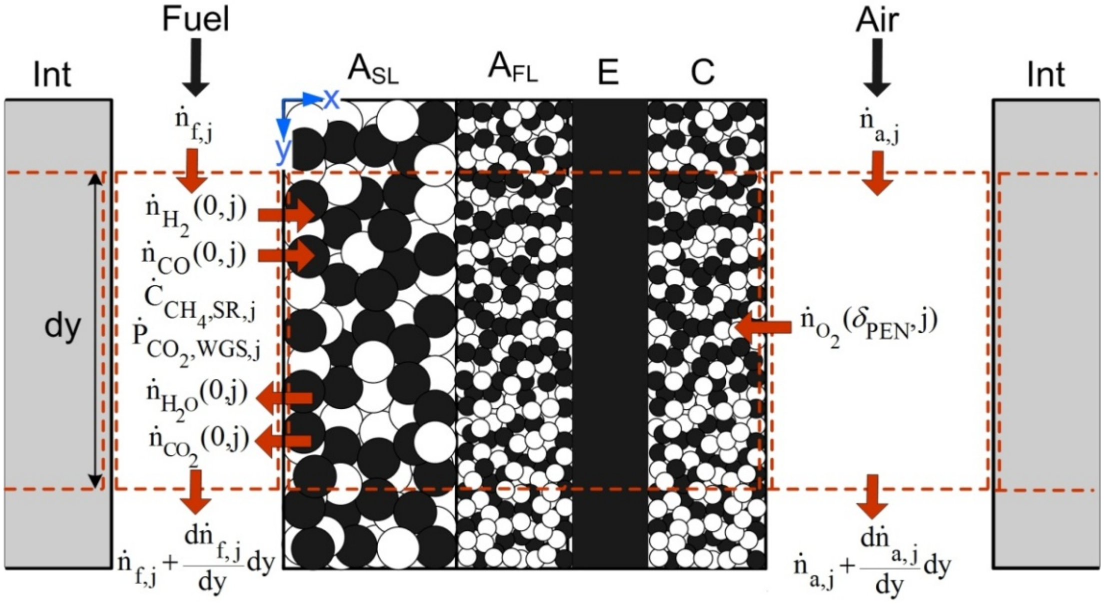

Figure 3.5: The mass flow in the j^{th} finite volume of the fuel and air streams.

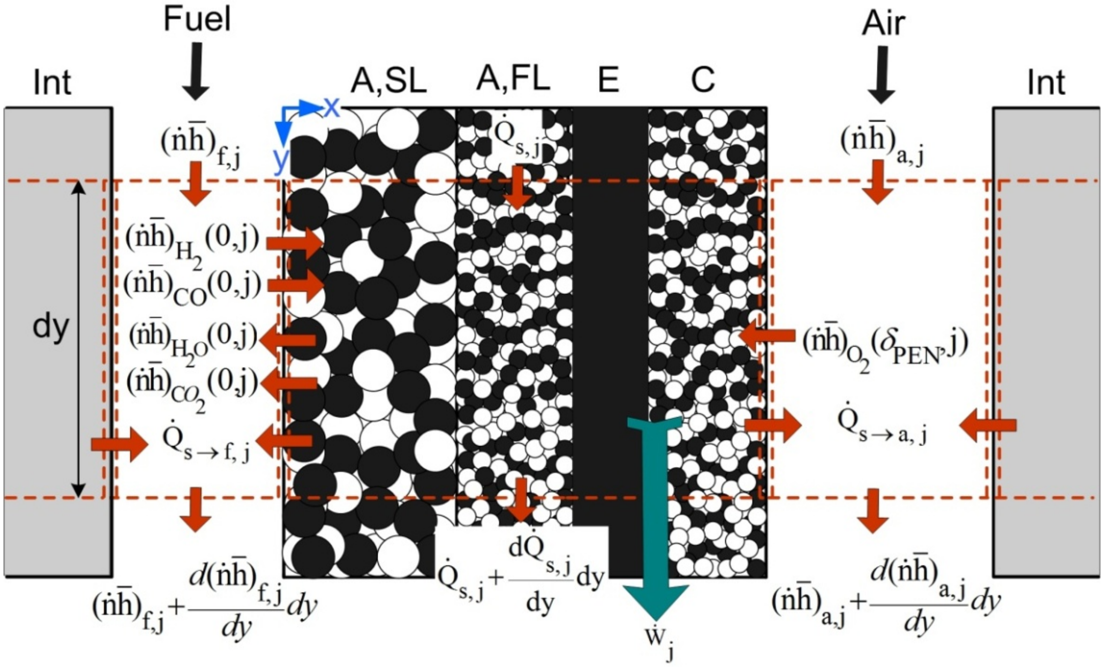

Figure 3.6: The energy flow in the j^{th} finite volume of the fuel and air streams and solid structure.

$$\dot{C}_{CH_4,SR,j} = 5.19 \times 10^6 (1 - \varepsilon_{A,SL}) \varphi_{Ni,A,SL} \left(\frac{p_{f,CH_4,j}}{p_{atm}}\right)^{1.2} ex\,p \left(\frac{-57{,}840}{R_u T_{s,j}}\right) W_{ch} \delta_{A,SL}\, \Delta y \qquad (3.173)$$

The rate of CO$_2$ production through the WGS reaction in the jth finite volume of the fuel stream, $\dot{P}_{CO_{2,WGS,j}}$, is also determined from the equilibrium-constant equation of this reaction:

$$K_{p,WGS}(T_{f,j+1}) = \frac{p_{CO_2,j+1}\; p_{H_2,j+1}}{p_{CO,j+1}\; p_{H_2O,j+1}} \qquad (3.174)$$

To solve Equation (3.174), the temperature of fuel at the exit of the jth finite volume should be determined. To determine this temperature, the energy equation for the fuel stream should be solved. From the energy balance in the jth finite volume of the fuel stream shown in Figure 3.6:

$$\Delta(\dot{n}\bar{h})_{f,j} = (\dot{n}\bar{h})_{H_2O}(0,j) + (\dot{n}\bar{h})_{CO_2}(0,j) - (\dot{n}\bar{h})_{H_2}(0,j) - (\dot{n}\bar{h})_{CO}(0,j) + \dot{Q}_{s\to f,j}$$

$$\text{At y=0: } T_f = T_{f,ent} \qquad (3.175)$$

Where, $\dot{Q}_{s\to f,j}$ is the heat transfer from the solid structure of the jth finite volume to the fuel stream by convection:

$$\dot{Q}_{s\to f,j} = 2h_{f,j}\; (W_{ch} + H_{ch,f})(T_{s,j} - T_{f,j})\, \Delta y \qquad (3.176)$$

To solve Equation (3.175), the molar flow rate of each species of the fuel at the exit of the jth finite volume should be determined. Therefore, the mass and energy equations for the fuel stream passing through the fuel channel are coupled and should be solved simultaneously.

For the air stream passing through the air channel, the molar flow rate of each species of air at the exit of the jth finite volume can be determined from the mass balance in this finite volume of the air stream shown in Figure 3.5:

$$\Delta \dot{n}_{a,O_2,j} = -\dot{n}_{O_2}(\delta_{PEN}, j) \tag{3.177}$$

$$\Delta \dot{n}_{a,N_2,j} = 0 \tag{3.178}$$

$$\text{At y=0: } \dot{n}_{a,l'}(0,0) = \dot{n}_{a,l',ent} \quad l' \in \{O_2, N_2\}$$

According to Faraday's electrochemical law, the molar flow rate of O_2, $\dot{n}_{O_2}(\delta_{PEN}, j)$, transferred from the air channel to the cathode, can be determined as:

$$\dot{n}_{O_2}(\delta_{PEN}, j) = \frac{i_{tot,j}}{4F}(W_{ch} + W_{rib})\,\Delta y \tag{3.179}$$

The air temperature at the exit of the jth finite volume is determined from the energy balance in this finite volume, as shown in Figure 3.6:

$$\begin{gathered}\Delta\left(\dot{n}\bar{h}\right)_{a,j} = -\left(\dot{n}\bar{h}\right)_{O_2}(\delta_{PEN}, j) + \dot{Q}_{s\to a,j} \\ \text{At y=0: } T_a = T_{a,ent}\end{gathered} \tag{3.180}$$

Where, $\dot{Q}_{s\to a,j}$ is the heat transfer from the solid structure of the jth finite volume to the air stream by convection:

$$\dot{Q}_{s\to a,j} = 2h_{a,j}\left(W_{ch} + H_{ch,a}\right)\left(T_{s,j} - T_{a,j}\right)\Delta y \tag{3.181}$$

In contrast to the fuel stream, the mass and energy balance equations are not coupled for the air stream passing through the air channel and can be solved individually to determine the temperature and species partial pressure of air at the exit of the finite volume.

The convective heat transfer coefficient of the fuel, $h_{f,j}$, and air, $h_{a,j}$, in Equations (3.176) and (3.181) are estimated from the Nusselt number correlation for the hydrodynamically and thermally developed and the laminar flow in rectangular ducts for the case of uniform heat transfer at four walls of the channel

[105]:

$$Nu = \frac{h_j D_{h,ch}}{k_{fluid,j}} = 8.235(1 - 2.0421\alpha + 3.0853\alpha^2 - 2.4765\alpha^3 + 1.0578\alpha^4 - 0.1861\alpha^5) \tag{3.182}$$

Where, the hydroalic diameter, $D_{h,ch}$, and the aspect ratio, α, of channels are defined as:

$$D_{h,ch} = \frac{2H_{ch}\,W_{ch}}{H_{ch} + W_{ch}} \tag{3.183}$$

$$\alpha = \frac{H_{ch}}{W_{ch}}\ H_{ch} < W_{ch} \quad or \quad \alpha = \frac{W_{ch}}{H_{ch}}\ H_{ch} > W_{ch} \tag{3.184}$$

In Equation (3.182), the thermal conductivity of air or fuel, $k_{fluid,j}$, as a multi-component gas mixture can be approximated from Wassiljewa's expression with the Mason-Saxena modification [99] using the thermal conductivity of the pure components [106].

The change in pressures of the air and fuel streams along the length of the cell is predicted from the Darcy-Weisbach equation:

$$\Delta p_j = (fRe)\frac{\mu_j V_j}{2D_{h,ch}^2}\Delta y \tag{3.185}$$

At y=L $p_f = p_a = p_{ext}$

The Darcy friction factor of the hydrodynamically developed laminar flow in rectangular ducts can be estimated from the correlation suggested by Shah and London [105].

$$fRe = 24(1 - 1.3553\alpha + 1.9467\alpha^2 - 1.7012\alpha^3 + 0.9564\alpha^4 - 0.2537\alpha^5) \tag{3.186}$$

3.2.2.2.2 Macro-Modeling of the Solid Structure

The objective is to determine the distribution of the temperature of solid structure along the length of the cell. The anode, electrolyte, cathode, and interconnect are assumed as a lumped homogenous structure in the heat transfer analysis. From the energy balance in the jth finite volume of the solid structure, as shown in Figure 3.6:

$$\Delta\dot{Q}_{s,j} = \left(\dot{n}\bar{h}\right)_{H_2}(0,j) + \left(\dot{n}\bar{h}\right)_{CO}(0,j) + \left(\dot{n}\bar{h}\right)_{O_2}(\delta_{PEN},j) - \left(\dot{n}\bar{h}\right)_{H_2O}(0,j) - \left(\dot{n}\bar{h}\right)_{CO_2}(0,j) \\ - \dot{Q}_{s\rightarrow f,j} - \dot{Q}_{s\rightarrow a,j} - \dot{W}_j \tag{3.187}$$

The electric power generated in the finite volume is:

$$\dot{W}_j = i_{tot,j} V_{cell} (W_{ch} + W_{rib})\,\Delta y \tag{3.188}$$

Using the Fourier law of conductive heat transfer:

$$\frac{\Delta\dot{Q}_{s,j}}{\mathrm{d}y} = -k_s A_s \frac{T_{s,j+1} - 2T_{s,j} + T_{s,j-1}}{\mathrm{d}y^2} \tag{3.189}$$

Where, the thermal conductivity of the solid structure, k_s, is approximated from the weight average of the thermal conductivities of the anode, cathode, electrolyte, and interconnect as follows:

$$k_s = \left(k_A \times \delta_A + k_C \times \delta_C + k_E \times \delta_E + k_{Int} \times \delta_{Int} - k_{Int} \times W_{ch} \frac{h_{ch,f} + h_{ch,a}}{W_{ch} + W_{rib}}\right) \\ \Big/ \left(\delta_A + \delta_C + \delta_E + \delta_{Int} - W_{ch} \frac{h_{ch,f} + h_{ch,a}}{W_{ch} + W_{rib}}\right) \tag{3.190}$$

By placing Equations (3.188) and (3.189) into Equation (3.187), the energy balance equation in the jth finite volume of the solid structure can be written as:

$$T_{s,j+1} - 2T_{s,j} + T_{s,j-1} \\ = \left(-\left(\dot{n}\bar{h}\right)_{H_2}(0,j) - \left(\dot{n}\bar{h}\right)_{CO}(0,j) - \left(\dot{n}\bar{h}\right)_{O_2}(\delta_{PEN},j) + \left(\dot{n}\bar{h}\right)_{H_2O}(0,j) \\ + \left(\dot{n}\bar{h}\right)_{CO_2}(0,j) + \dot{Q}_{s\rightarrow f,j} + \dot{Q}_{s\rightarrow a,j} + i_{tot,j} V_{cell}(W_{ch} + W_{rib})\,\Delta y\right) \frac{\Delta y}{k_s A_s} \tag{3.191}$$

At y=0 and y=L: $\Delta T_s / \Delta y = 0$

According to Equation (3.191), the temperature of the solid structure can be determined at the given temperatures of the fuel and air streams. However, the fuel and air temperatures are dependent on the temperature of the solid structure. Therefore, the equations obtained from mass and energy balance relations in the macro-modeling are coupled and should be solved simultaneously. The System of Equation (3.192) is obtained from the macro-modeling of the cell.

$$\left\{\begin{array}{l} T_{s,j+1} - 2T_{s,j} + T_{s,j-1} = \left(\Delta\left(\dot{n}\bar{h}\right)_{f,j} + \Delta\left(\dot{n}\bar{h}\right)_{a,j} + \dot{W}_j\right)\frac{\Delta y}{k_s A_s} \\ \Delta\left(\dot{n}\bar{h}\right)_{f,j} = \left(\dot{n}\bar{h}\right)_{f,H_2O}(0,j) + \left(\dot{n}\bar{h}\right)_{f,CO_2}(0,j) - \left(\dot{n}\bar{h}\right)_{f,H_2}(0,j) - \left(\dot{n}\bar{h}\right)_{f,CO}(0,j) + \\ \qquad\qquad 2h_{f,j}\left(W_{ch}+H_{ch,f}\right)\left(T_{s,j} - T_{f,j}\right)\Delta y \\ \Delta\left(\dot{n}\bar{h}\right)_{a,j} = -\left(\dot{n}\bar{h}\right)_{a,O_2}(\delta_{PEN},j) + 2h_{a,j}\left(W_{ch}+H_{ch,a}\right)\left(T_{s,j} - T_{a,j}\right)\Delta y \\ \Delta\dot{n}_{f,CH_4,j} = -\dot{C}_{CH_4,SR,j} \\ \Delta\dot{n}_{f,H_2,j} = 3\dot{C}_{CH_4,SR,j} + \dot{P}_{CO_2,WGS,j} - \frac{i_{tot,H_2,j}}{2F}(W_{ch} + W_{rib})\Delta y \\ \Delta\dot{n}_{f,CO,j} = \dot{C}_{CH_4,SR,j} - \dot{P}_{CO_2,WGS,j} - \frac{i_{tot,CO,j}}{2F}(W_{ch} + W_{rib})\Delta y \\ \Delta\dot{n}_{f,H_2O,j} = -\dot{C}_{CH_4,SR,j} - \dot{P}_{CO_2,WGS,j} + \frac{i_{tot,H_2,j}}{2F}(W_{ch} + W_{rib})\Delta y \\ \Delta\dot{n}_{f,CO_2,j} = \dot{P}_{CO_2,WGS,j} + \frac{i_{tot,CO,j}}{2F}(W_{ch} + W_{rib})\Delta y \\ \Delta\dot{n}_{f,N_2,j} = \Delta\dot{n}_{a,N_2,j} = 0 \\ \Delta\dot{n}_{a,O_2,j} = -\frac{i_{tot,j}}{4F}(W_{ch} + W_{rib})\Delta y \\ \Delta p_{f,j} = (fRe)_f \frac{\mu_{f,j}V_{f,j}}{2D_{h,ch,f}^2}\Delta y \\ \Delta p_{a,j} = (fRe)_a \frac{\mu_{a,j}V_{a,j}}{2D_{h,ch,f}^2}\Delta y \\ \dot{C}_{CH_4,SR,j} = 5.19 \times 10^6\left(1 - \varepsilon_{A,SL}\right)\varphi_{Ni,A,SL}\left(\frac{p_{f,CH_4,j}}{p_{atm}}\right)^{1.2} exp\left(\frac{-57{,}840}{R_u T_{s,j}}\right) W_{ch}\delta_{A,SL}\,\Delta y \\ K_{p,WGS}(T_{f,j+1}) = \frac{p_{f,CO_2,j+1}p_{f,H_2,j+1}}{p_{f,CO,j+1}p_{f,H_2O,j+1}} \end{array}\right. \tag{3.192}$$

At y=0: $\dot{n}_{f,l}(0,0) = \dot{n}_{f,l,ent}$, $l \in \{H_2, CO, H_2O, CO_2, CH_4, N_2\}$; $T_f = T_{f,ent}$; $\dot{n}_{a,l'}(0,0) = \dot{n}_{a,l',ent}$, $l' \in \{O_2, N_2\}$; $T_a = T_{a,ent}$; $\Delta T_s/\Delta y = 0$

At y=L: $\Delta T_s/\Delta y = 0$; $p_f = p_a = p_{ext}$

According to the equations developed in the macro-modeling, the temperature of the solid structure and species partial pressures of the fuel and air streams in each finite volume are dependent on the total current generated in the finite volume. Thus, the equations developed in the macro-modeling are coupled with the equations developed in micro-modeling. The flowchart presented in Figure 3.7 suggests a method to determine the cell performance at a given cell voltage, fuel utilization ratio, and excess air using the combined micro- and macro-model.

After determination of the cell performance, the cell mean current density, power density, and reversible voltage can be obtained from Equations (3.193)–(3.195), respectively.

$$i_{cell} = \frac{1}{N^{FV}} \sum_{j=1}^{j=N^{FV}} i_{tot,j} \tag{3.193}$$

$$\dot{w}_{cell} = \frac{1}{N^{FV}} \sum_{j=1}^{j=N^{FV}} i_{tot,j} V_{cell} \tag{3.194}$$

$$E_{rev,cell} = \frac{\sum_{j=1}^{N^{FV}} i_{tot,j} E_{rev,j}}{\sum_{j=1}^{N^{FV}} i_{tot,j}} \tag{3.195}$$

The mean polarization of the anode, cathode, electrolyte, and interconnect, and the mean total polarization of the cell can be also determined from Equations (3.196)–(3.200), respectively.

$$\eta_{A,cell} = \frac{\sum_{j=1}^{N^{FV}} i_{tot,j} \eta_{A,j}}{\sum_{j=1}^{N^{FV}} i_{tot,j}} \tag{3.196}$$

$$\eta_{C,cell} = \frac{\sum_{j=1}^{N^{FV}} i_{tot,j} \eta_{C,j}}{\sum_{j=1}^{N^{FV}} i_{tot,j}} \tag{3.197}$$

$$\eta_{E,cell} = \frac{\sum_{j=1}^{N^{FV}} i_{tot,j} \eta_{E,j}}{\sum_{j=1}^{N^{FV}} i_{tot,j}} \tag{3.198}$$

$$\eta_{Int,cell} = \frac{\sum_{j=1}^{N^{FV}} i_{tot,j} \eta_{Int,j}}{\sum_{j=1}^{N^{FV}} i_{tot,j}} \tag{3.199}$$

$$\eta_{tot,cell} = \eta_{A,cell} + \eta_{C,cell} + \eta_{E,cell} + \eta_{Int,cell} \tag{3.200}$$

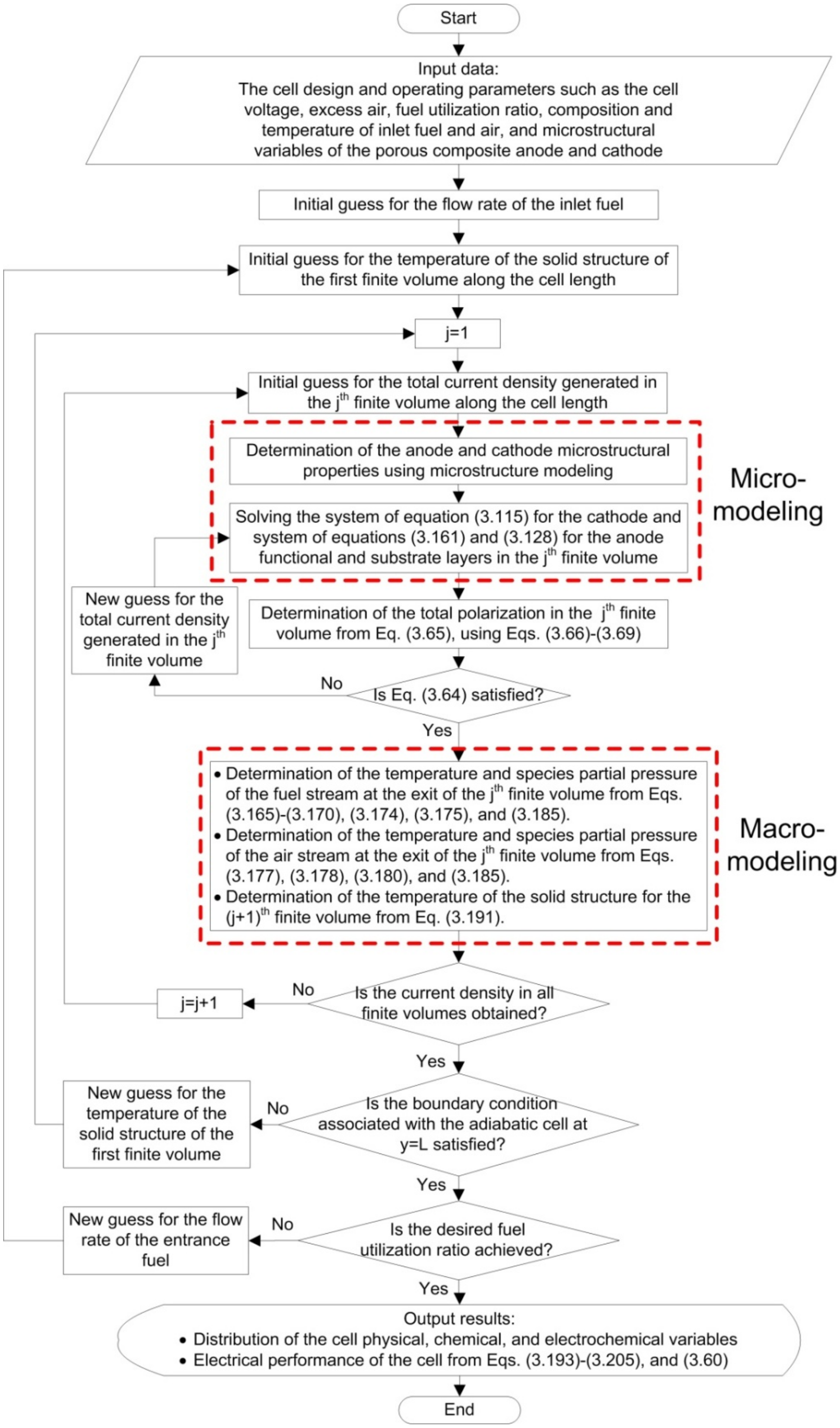

Figure 3.7: The flowchart of determination of the cell performance using the combined micro- and macro-model.

The mean polarization resistances of the anode, cathode, electrolyte, and interconnect, and the mean total polarization resistance of the cell are also determined from Equations (3.201)-(3.205), respectively.

$$R_{A,cell} = \frac{1}{i_{cell}} \frac{\sum_{j=1}^{N^{FV}} i_{tot,j}^2 R_{A,j}}{\sum_{j=1}^{N^{FV}} i_{tot,j}} \tag{3.201}$$

$$R_{C,cell} = \frac{1}{i_{cell}} \frac{\sum_{j=1}^{N^{FV}} i_{tot,j}^2 R_{C,j}}{\sum_{j=1}^{N^{FV}} i_{tot,j}} \tag{3.202}$$

$$R_{E,cell} = \frac{1}{i_{cell}} \frac{\sum_{j=1}^{N^{FV}} i_{tot,j}^2 R_{E,j}}{\sum_{j=1}^{N^{FV}} i_{tot,j}} \tag{3.203}$$

$$R_{Int,cell} = \frac{1}{i_{cell}} \frac{\sum_{j=1}^{N^{FV}} i_{tot,j}^2 R_{Int,j}}{\sum_{j=1}^{N^{FV}} i_{tot,j}} \tag{3.204}$$

$$R_{tot,cell} = R_{A,cell} + R_{C,cell} + R_{E,cell} + R_{Int,cell} \tag{3.205}$$

Finally, the first law efficiency of the cell can be obtained from Equation (3.60).

3.2.2.3 Exergy Analysis of the Cell

The minimization of the exergy destruction in SOFCs is important, especially when the exit gases from the SOFC are used to generate extra power in another power generation system. Since the microstructure of the porous composite electrodes significantly affects the exergy destruction in a cell, the combined micro- and macro-model is expanded to include the exergy analysis.

From the exergy balance in the jth finite volume of the solid structure, fuel stream, and air stream, shown in Figure 3.8, the exergy destruction in these finite volumes is obtained from Equations (3.206)–(3.208), respectively. It is noted that the parameters in the right side of these equations are determined from the results of the cell combined micro- and macro-modeling.

$$\begin{aligned}\dot{E}_{x_{dest},s,j} = {} & (\dot{n}\overline{e_x})_{H_2}(0,j) + (\dot{n}\overline{e_x})_{CO}(0,j) + (\dot{n}\overline{e_x})_{O_2}(\delta_{PEN},j) - (\dot{n}\overline{e_x})_{H_2O}(0,j) \\ & - (\dot{n}\overline{e_x})_{CO_2}(0,j) - \dot{E}_{x,\dot{Q}_{s\to f,j}} - \dot{E}_{x,\dot{Q}_{s\to a,j}} - \Delta\dot{E}_{x,\dot{Q}_{s,j}} - \dot{w}_j\,(W_{ch} + W_{rib})\Delta y\end{aligned} \tag{3.206}$$

$$\dot{E}_{x_{dest},f,j} = (\dot{n}\overline{e_x})_{H_2O}(0,j) + (\dot{n}\overline{e_x})_{CO_2}(0,j) - (\dot{n}\overline{e_x})_{H_2}(0,j) - (\dot{n}\overline{e_x})_{CO}(0,j) + \dot{E}_{x,\dot{Q}_{s\to f,j}} - \Delta(\dot{n}\overline{e_x})_{f,j} \tag{3.207}$$

$$\dot{E}_{x_{dest},a,j} = -(\dot{n}\overline{e_x})_{O_2}(\delta_{PEN},j) + \dot{E}_{x,\dot{Q}_{s\to a,j}} - \Delta(\dot{n}\overline{e_x})_{a,j} \tag{3.208}$$

The total exergy destruction in the jth finite volume is obtained from a summation of the exergy destructions in the solid structure, fuel stream, and air stream:

$$\begin{aligned}\dot{E}_{x_{dest},j} &= \dot{E}_{x_{dest},s,j} + \dot{E}_{x_{dest},a,j} + \dot{E}_{x_{dest},f,j} \\ &= -\Delta\dot{E}_{x,\dot{Q}_{s,j}} - \Delta(\dot{n}\overline{e_x})_{f,j} - \Delta(\dot{n}\overline{e_x})_{a,j} - \dot{w}_j\,(W_{ch} + W_{rib})\Delta y\end{aligned} \tag{3.209}$$

The total exergy destruction in the cell can be also obtained as:

$$\dot{E}_{x_{dest},cell} = \left(-\int_{y=0}^{L} d\dot{E}_{x,\dot{Q}_s} - \int_{y=0}^{L} d(\dot{n}\overline{e_x})_a - \int_{y=0}^{L} d(\dot{n}\overline{e_x})_f - \dot{w}_{cell}\,(W_{ch} + W_{rib})L_{Cell}\right)N_{ch} \tag{3.210}$$

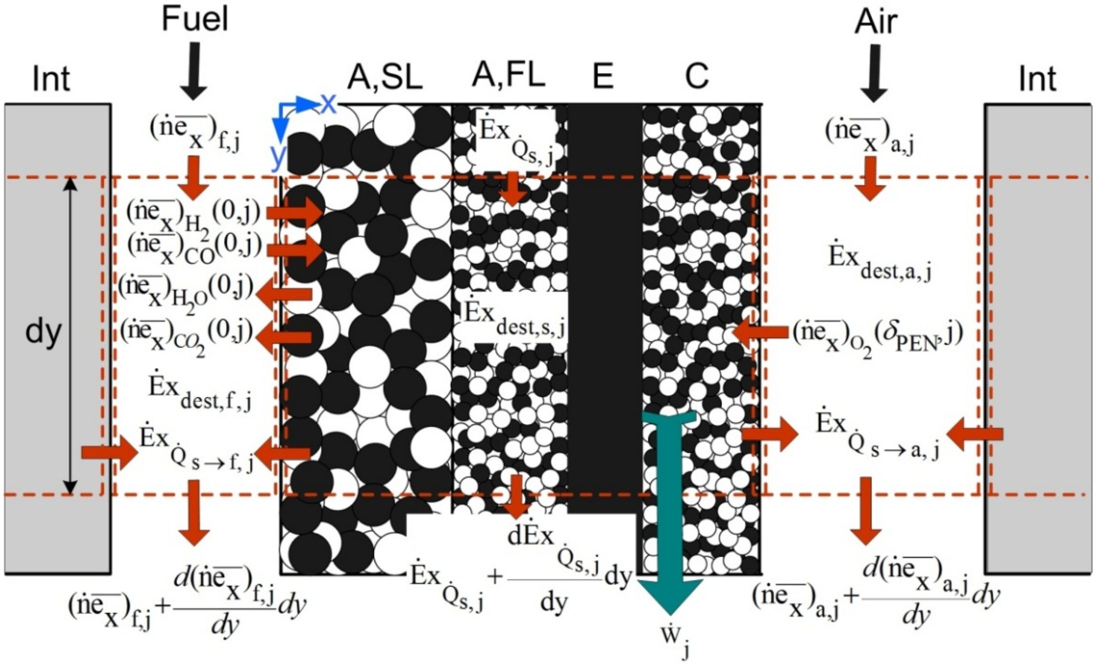

Figure 3.8: The exergy flow in the jth finite volume of the solid structure, fuel stream, and air stream.

Where,

$$\int_{y=0}^{L} d(\dot{n}\overline{e_x})_a = (\dot{n}\overline{e_x})_{a,ext} - (\dot{n}\overline{e_x})_{a,ent} \tag{3.211}$$

$$\int_{y=0}^{L} d(\dot{n}\overline{e_x})_f = (\dot{n}\overline{e_x})_{f,ext} - (\dot{n}\overline{e_x})_{f,ent} \tag{3.212}$$

Since the cell is assumed adiabatic:

$$\int_{y=0}^{L} d\dot{E}_{x,\dot{Q}_s} = 0 \tag{3.213}$$

Thus, the total exergy destruction in the cell can be simplified to:

$$\begin{aligned}\dot{E}_{x_{dest},cell} = \big((\dot{n}\overline{e_x})_{a,ent} - (\dot{n}\overline{e_x})_{a,ext} + (\dot{n}\overline{e_x})_{f,ent} - (\dot{n}\overline{e_x})_{f,ext} \\ - \dot{w}_{cell}\,(W_{ch} + W_{rib})L_{Cell}\big)N_{ch}\end{aligned} \tag{3.214}$$

The second law efficiency of the cell can be also determined from:

$$\eta_{II} = \frac{\dot{w}_{cell}\,(W_{ch} + W_{rib})L_{Cell}}{(\dot{n}\overline{e_x})_{f,ent} + (\dot{n}\overline{e_x})_{a,ent} - (\dot{n}\overline{e_x})_{f,ext} - (\dot{n}\overline{e_x})_{a,ext}} \tag{3.215}$$

3.3 Stack Level Model

The SOFC stack model is based on the basic cell model. It is assumed that all the cells in the stack have the same design and operating conditions with the same performance; however, the effect of the voltage drop due to stacking the cells can be considered as a correction term. At the given minimum voltage and power required for the stack and the voltage drop due to stacking the cells, the number of series and parallel cells can be determined:

$$N_{Series} = \left(\frac{V_{Stack,min}}{V_{Cell}\left(1 - \frac{V_{drop\ in\ Stacking}}{V_{Cell}N_{Series}}\right)} \right)_{Rounded\ up\ to\ the\ next\ integer\ value} \tag{3.216}$$

$$N_{\text{Parallel}} = \left(\frac{\frac{\dot{W}_{Stack,min}}{\dot{W}_{Cell}\left(1 - \frac{V_{drop\ in\ Stacking}}{V_{Cell}N_{Series}}\right)}}{N_{Series}} \right)_{Rounded\ up\ to\ the\ next\ integer\ value} \tag{3.217}$$

And the total number of cells would be:

$$N_{Cells} = N_{Series} \times N_{Parallel} \tag{3.218}$$

After determination of the number of series and parallel cells, the operating voltage and power of the stack can be determined:

$$V_{Stack} = V_{Cell}N_{Series}\left(1 - \frac{V_{drop\ in\ Stacking}}{V_{Cell}N_{Series}}\right) \tag{3.219}$$

$$\dot{W}_{Stack} = N_{Cells}\,\dot{W}_{Cell}\left(1 - \frac{V_{drop\ in\ Stacking}}{V_{Cell}N_{Series}}\right) \tag{3.220}$$

And the following equations can be employed to determine the flow rate and composition of fuel and air streams, current, and efficiency of the SOFC stack:

$$\dot{n}_{f,ent,Stack} = \dot{n}_{f,ent,Cell}N_{Cells} \tag{3.221}$$

$$\dot{n}_{f,ext,Stack} = \dot{n}_{f,ext,Cell}N_{Cells} \tag{3.222}$$

$$\dot{n}_{a,ent,Stack} = \dot{n}_{a,ent,Cell}N_{Cells} \tag{3.223}$$

$$\dot{n}_{a,ext,Stack} = \dot{n}_{a,ext,Cell}N_{Cells} \tag{3.224}$$

$$x_{f,l,ent,Stack} = x_{f,l,ent,Cell}, l \in \{CH_4, H_2, CO, H_2O, CO_2, N_2\} \tag{3.225}$$

$$x_{f,l,ext,Stack} = x_{f,l,ext,Cell}, l \in \{CH_4, H_2, CO, H_2O, CO_2, N_2\} \tag{3.226}$$

$$x_{a,l',ent,Stack} = x_{a,l',ent,Cell}, l' \in \{O_2, N_2\} \tag{3.227}$$

$$x_{a,l',ext,Stack} = x_{a,l',ext,Cell}, l' \in \{O_2, N_2\} \tag{3.228}$$

$$I_{Stack} = i_{Cell} W_{Cell} L_{Cell} N_{Parallel} \tag{3.229}$$

$$\eta_{I,Stack} = \eta_{I,Cell}\left(1 - \frac{V_{drop\ in\ Stacking}}{V_{Cell} N_{Series}}\right) \tag{3.230}$$

Since SOFCs operate at elevated temperatures, an appropriate thermal insulation system is required to reduce the rate of heat transfer from the SOFC stack to the ambient. If the heat transfer from the stack is not controlled appropriately, a significant change in distribution of temperature in the solid structure of cells occurs that may cause an unfavourable effect on the performance and durability of cells. Determination of the rate of heat transfer from the stack is also important in the SOFC system modeling to calculate the excess air required to control the temperature of the cells. For this purpose, two thermal insulation systems for SOFC stacks with cubic geometry are suggested, and the rate of heat transfer and the temperature of the outer walls of stack are determined. As demonstrated in Figure 3.9, these thermal insulation systems consist of a solid insulation layer or a vacuum layer that is mechanically supported by two metal layers. For thermal insulation system I with a solid insulation layer that is shown in Figure 3.9(a), the heat transfer mechanism is heat conduction through the solid insulation layer and radiation and natural convection through the outer walls of the stack. This thermal insulation system is suitable for large stacks for residential and industrial applications of SOFCs. For thermal insulation system II with the vacuum layer that is shown in Figure 3.9(b), the heat transfer mechanism through the vacuum layer is radiation that can be minimized by employing reflective coatings on the metal surfaces. The radiation and natural convection are also the mechanism of heat transfer from the outer walls of the stack. This thermal insulation system is suitable for small size stacks, especially for portable applications of SOFCs.

It is assumed that the temperature of each metal layer of the stack is uniform and the temperature of the interior metal layer is equal to the mean temperature of the solid structure of cells. Based on the equivalent thermal circuit of the thermal insulation system I in Figure 3.9(a), the heat transfer from the SOFC stack and the temperature of the outer walls can be determined as follows:

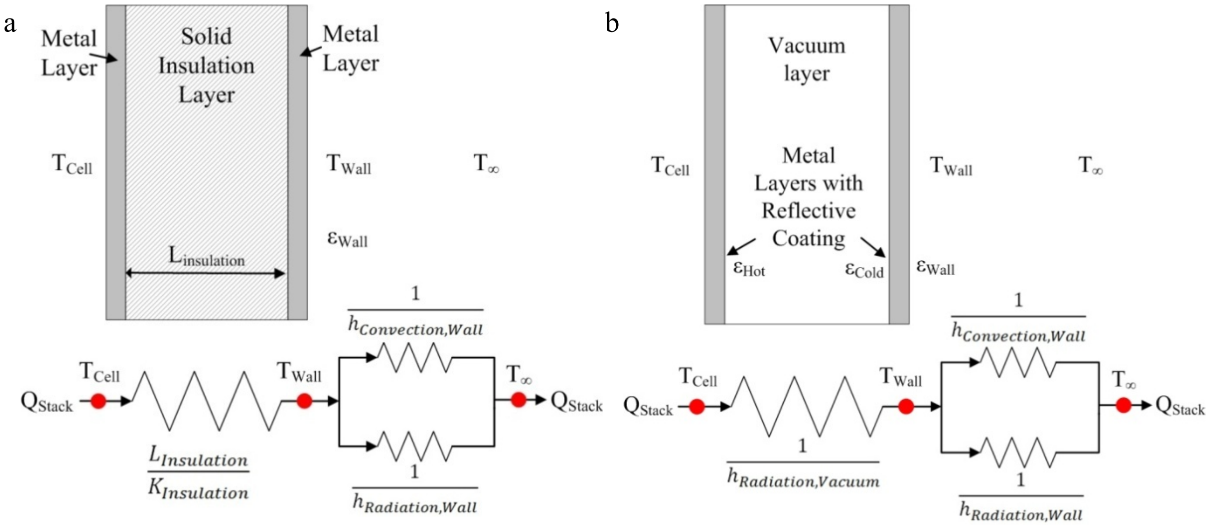

Figure 3.9: Schematic of the thermal insulation systems for SOFC stacks with (a) solid insulation layer and (b) vacuum layer.

$$\dot{Q}_{Stack} = \frac{A_{Stack}(T_{Cell} - T_{\infty})}{\frac{L_{Insulation}}{k_{Insulation}} + \frac{1}{h_{Radiation,Wall} + h_{Convection,Wall}}} \tag{3.231}$$

$$T_{Wall} = \frac{T_{Cell} + \frac{L_{Insulation}}{k_{Insulation}}\left(h_{Radiation,Wall} + h_{Convection,Wall}\right)T_{\infty}}{1 + \frac{L_{Insulation}}{k_{Insulation}}\left(h_{Radiation,Wall} + h_{Convection,Wall}\right)} \tag{3.232}$$

The heat transfer from the SOFC stack and the temperature of the outer walls of the stack with the thermal insulation system II can be obtained as follows:

$$\dot{Q}_{Stack} = \frac{A_{Stack}(T_{Cell} - T_{\infty})}{\frac{1}{h_{Radiation,Vacuum}} + \frac{1}{h_{Radiation,Wall} + h_{Convection,Wall}}} \tag{3.233}$$

$$T_{Wall} = \frac{T_{Cell} + \dfrac{h_{Radiation,Wall} + h_{Convection,Wall}}{h_{Radiation,Vacuum}} T_{\infty}}{1 + \dfrac{h_{Radiation,Wall} + h_{Convection,Wall}}{h_{Radiation,Vacuum}}} \tag{3.234}$$

The radiative heat transfer coefficient corresponding to the vacuum layer and outer walls [107] and the convective heat transfer coefficienct corresponding to the outer walls of the stack can be determined from the following equations:

$$h_{Radiation,Vacuum} = \frac{\sigma\left(T_{Cell}^2 + T_{Wall}^2\right)\left(T_{Cell} + T_{Wall}\right)}{\dfrac{1}{\varepsilon_{Hot}} + \dfrac{1}{\varepsilon_{Cold}} - 1} \tag{3.235}$$

$$h_{Radiation,Wall} = \varepsilon_{Wall}\sigma\left(T_{Wall}^2 + T_{\infty}^2\right)\left(T_{Wall} + T_{\infty}\right) \tag{3.236}$$

$$\begin{aligned} h_{Convection} = \big(&2L_{Stack}H_{Stack}h_{Vertical\,Wall} + 2W_{Stack}H_{Stack}h_{Vertical\,Wall} \\ &+ L_{Stack}W_{Stack}h_{Horizontal\,Wall,Top} + L_{Stack}W_{Stack}h_{Horizontal\,Wall,Bottom}\big) \\ &/A_{Stack} \end{aligned} \tag{3.237}$$

Where, the surface area of the stack is:

$$A_{Stack} = 2L_{Stack}H_{Stack} + 2W_{Stack}H_{Stack} + 2L_{Stack}W_{Stack} \tag{3.238}$$

The convective heat transfer coefficints for different orientation of the outer walls can be determined from Equations (3.239)–(3.241) on the basis of the Nusselt numbers in Equations (3.242)–(3.244) [108].

$$h_{Vertical\,Wall} = \frac{Nu_{Vertical\,Wall}\,k_a}{H_{Stack}} \tag{3.239}$$

$$h_{Horizontal\,Wall,Top} = \frac{Nu_{Horizontal\,Wall,Top}\,k_a}{\ell_{Char}} \tag{3.240}$$

$$h_{Horizontal\,Wall,Bottom} = \frac{Nu_{Horizontal\,Wall,Bottom}\,k_a}{\ell_{Char}} \tag{3.241}$$

$$Nu_{Vertical\,Wall} = \left(0.825 + \frac{0.387\,Ra_{Vertical\,Wall}^{\frac{1}{6}}}{\left(1 + (0.492/Pr_a)^{\frac{9}{16}}\right)^{\frac{8}{27}}}\right)^2 \tag{3.242}$$

$$\begin{cases} Nu_{Horizontal\,Wall,Top} = 0.54 Ra_{Horizontal\,Wall}^{\frac{1}{4}},\ (10^4 < Ra_{Horizontal\,Wall} < 10^7) \\ Nu_{Horizontal\,Wall,Top} = 0.15 Ra_{Horizontal\,Wall}^{\frac{1}{3}},\ (10^7 < Ra_{Horizontal\,Wall} < 10^{11}) \end{cases} \tag{3.243}$$

$$Nu_{Horizontal\,Wall,Bottom} = 0.27 Ra_{Horizontal\,Wall}^{\frac{1}{4}},\ (10^5 < Ra_{Horizontal\,Wall} < 10^{10}) \tag{3.244}$$

Where, Prandtl number and Rayleigh numbers associated with the vertical and horizontal walls are:

$$Pr_a = \frac{\nu_a}{\alpha_a} \tag{3.245}$$

$$Ra_{Vertical\,Wall} = \frac{g\beta_{th}(T_{Wall} - T_\infty)H_{Stack}^3}{\nu_a \alpha_a} \tag{3.246}$$

$$Ra_{Horizontal\,Wall} = \frac{g\beta_{th}(T_{Wall} - T_\infty)\ell_{Char}^3}{\nu_a \alpha_a} \tag{3.247}$$

And the thermal volume expansion, β_{th}, is:

$$\beta_{th} = \frac{1}{(T_{Wall} + T_\infty)/2} \tag{3.248}$$

After determination of the heat transfer from the stack, the heat transfer from each cell, required for Equation (3.51), can be calculated:

$$\dot{Q}_{Cell} = \frac{\dot{Q}_{Stack}}{N_{Cells}} - \frac{V_{drop\,in\,Stacking}}{V_{Cell}N_{Series}}\dot{W}_{Cell} \tag{3.249}$$

3.4 System Level Model

Two SOFC systems are modeled. The first system (system I) is a CHP system suitable for residential and industrial applications. The second system (system II) is an electric power generation system suitable for portable applications.

3.4.1 SOFC System I

3.4.1.1 System Configurations

The biogas is selected as the entrance fuel to this system and the AGR, SR, and POX are the methods employed to process the biogas. Depending on the fuel processing method employed, this system can have three different configurations. These configurations are shown in Figure 3.10-3.12. The SOFC system I is mainly composed of an SOFC stack used to generate DC electric power and heat; an air heater used to increase the air temperature before it enters the SOFC stack; an air blower used to overcome the pressure drop in the system; and a burner used to convert the chemical energy of the unutilized fuel in the SOFC stack to heat. Other essentials of the system are a boiler used to produce hot water for the hot water demand or space heating; a power conditioner used to invert the DC electric power generated in the SOFC stack to AC; and a reformer control volume that may contain a fuel clean-up system, heater(s), reformer(s), and a mixer to mix the anode exit gas for configuration I (Figure 3.10), water for configuration II (Figure 3.11), or air for configuration III (Figure 3.12) with the fuel stream. A boiler feedwater pump and a biogas blower may also be required in this system. However, their effects on the energy balance of the system may be negligible. Other sub-systems such as hot water storage tanks and electric storage batteries may also be required that are not considered in this study.

3.4.1.2 Process Description

In this system, biogas fuel enters a gas clean-up system where the contaminants in the biogas are reduced to levels that do not damage the anode and/or reformer catalysts. Depending on the operating temperature of the gas clean-up system, a heat exchanger may be required in the reformer control volume before cleaning the biogas. The most attractive and convenient method to remove hydrogen sulfide from biogas in the gas clean-up system is the use of an activated carbon bed. This method is highly effective at relatively low loadings of hydrogen sulfide ($H_2S<200$ ppm) [109]. In the case of high hydrogen sulfide content, additional removal technologies are required to reduce the hydrogen sulfide content to below 200 ppm. After cleaning, the biogas should be processed before entering the SOFC stack. For this purpose, the biogas is mixed with the anode exit gas stream 15(I) in configuration I of the system. In configuration II of the system, the entrance water stream 15(II) and biogas enter a steam reformer. In configuration III of the system, the biogas stream and the air stream 15(III) enter a partial oxidation reformer. After chemical reactions and increasing the temperature of the fuel to a certain value in the reforming control volume, the processed fuel enters the SOFC stack. The air also enters the SOFC stack after increasing its pressure and temperature in the blower and air heater to a certain value. Then the electric power is generated in the SOFC stack. The depleted fuel and air streams that have exited the stack enter the burner. For configuration I of the system, the required anode exit gas branches from the depleted fuel stream before entering the burner. The hot gas produced in the burner then passes through the reforming control volume and air heater to supply their required heat. Finally, the thermal energy of this stream is used to increase the temperature of the inlet cold water to the boiler to produce hot water.

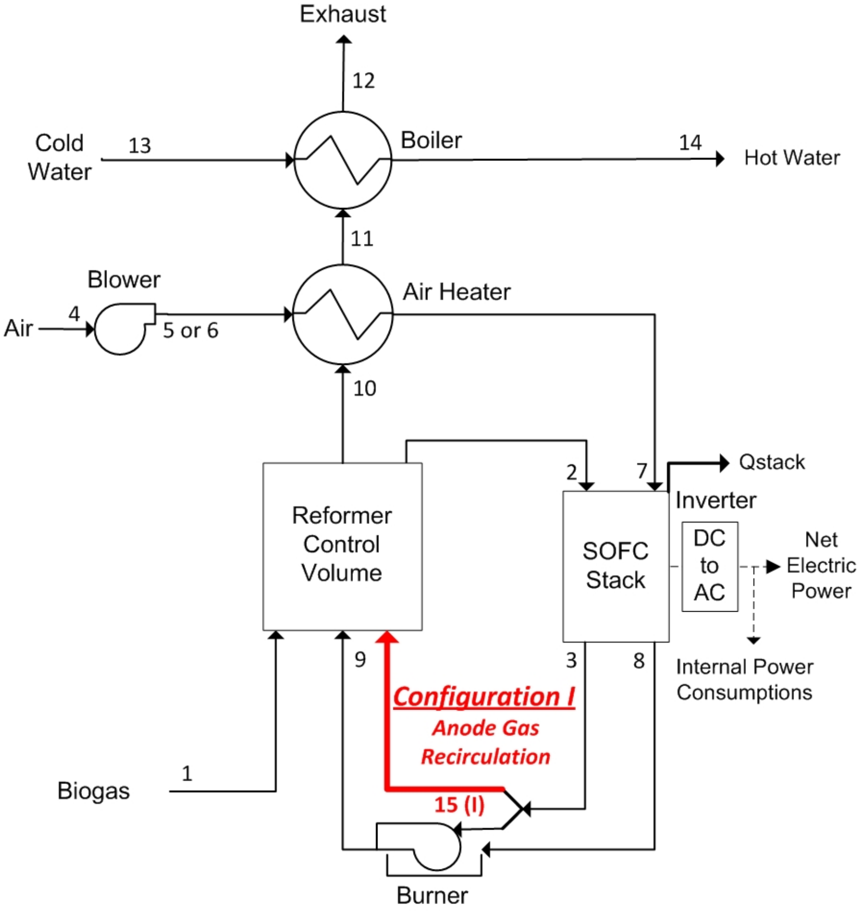

Figure 3.10: The SOFC system I with configuration I (anode gas recirculation).

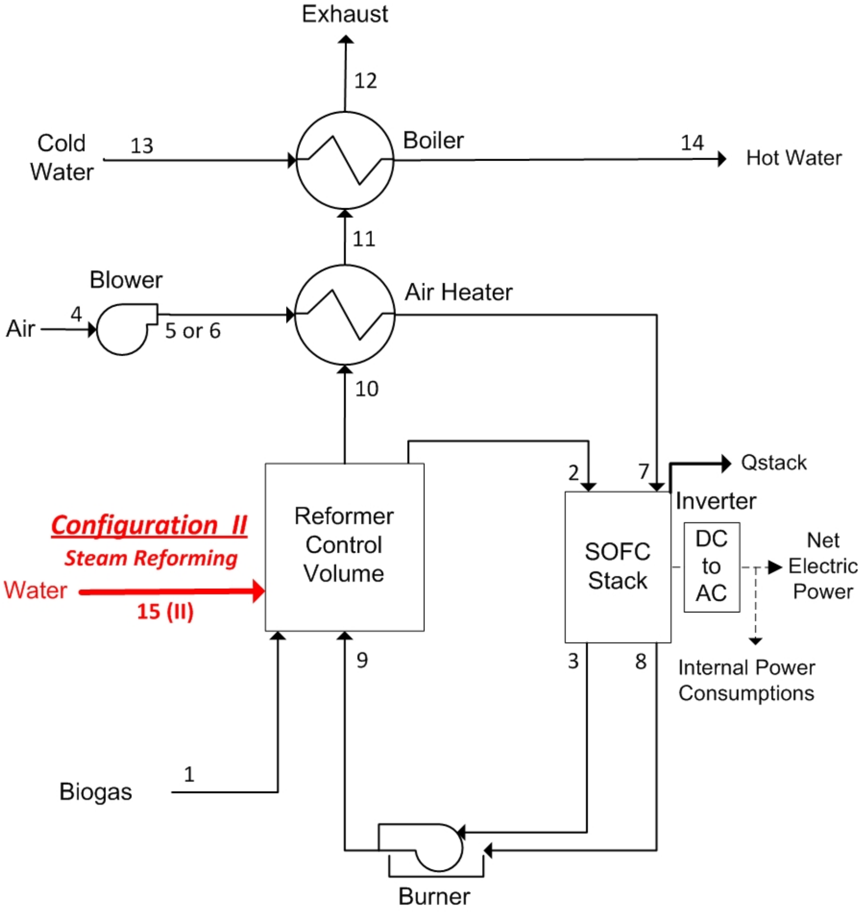

Figure 3.11: The SOFC system I with configuration II (steam reforming).

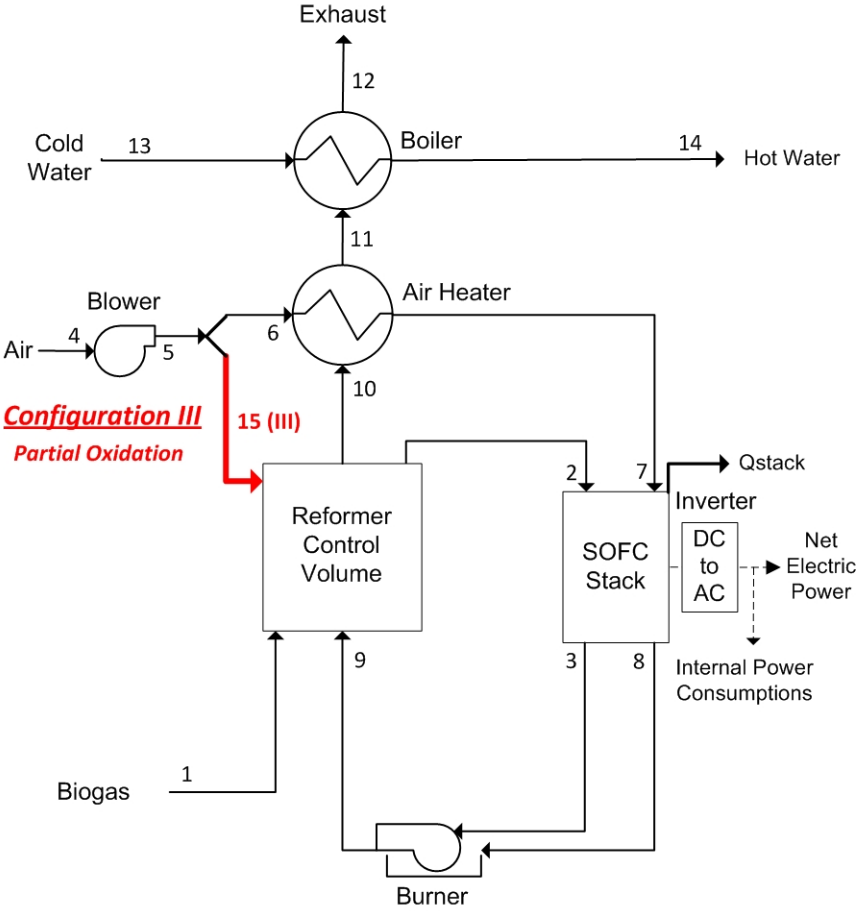

Figure 3.12: The SOFC system I with configuration III (partial oxidation).

3.4.1.3 Modeling the BoP Components

In the system modeling, it is assumed that all components of the system are adiabatic, except the SOFC stack, and all streams are treated as ideal gases, except the steam and water streams 13, 14, and 15(II). The inlet and outlet fuel streams from the SOFC stack are also assumed to be in thermodynamic equilibrium.

The system is modeling at the given system net AC electric power; ambient temperature and pressure; blower isentropic efficiency; outlet air pressure from the blower; inverter efficiency; fuel and air temperatures at the inlet and outlet of the SOFC stack; and the cold and hot water temperatures (T_{13} and T_{14}). The model used for the SOFC stack is based on the model described in section 3.3 and the thermal insulation system I is selected for the stack. The BoP components are thermodynamically modeled under steady state operating conditions to determine the properties, composition, and flow rate of all the streams in the system.

Before modeling the BoP components, the location of the inlet fuel to the system on the C-H-O ternary diagram is determined (e.g., point 1 in Figure 3.13). If the fuel is located below the CDB curve in the safe region, its equilibrium composition at T_2 is calculated and considered as the input fuel to the SOFC stack. In this case, the fuel reforming is not required and the flow rates of streams 15(I), 15(II), and 15(III) are zero. If the fuel is located above the CDB curve in the carbon deposition region, the equilibrium composition of the fuel located at the intersection of the CDB curve and line 1-15(I) for configuration I, 1-15(II) for configuration II, and 1-15(III) for configuration III (see Figure 3.13) at T_2 is obtained and considered as the inlet fuel to the SOFC stack. Of course, to prevent carbon deposition, the composition of a fuel that is a little below the intersection should be considered as the inlet fuel to the SOFC stack.

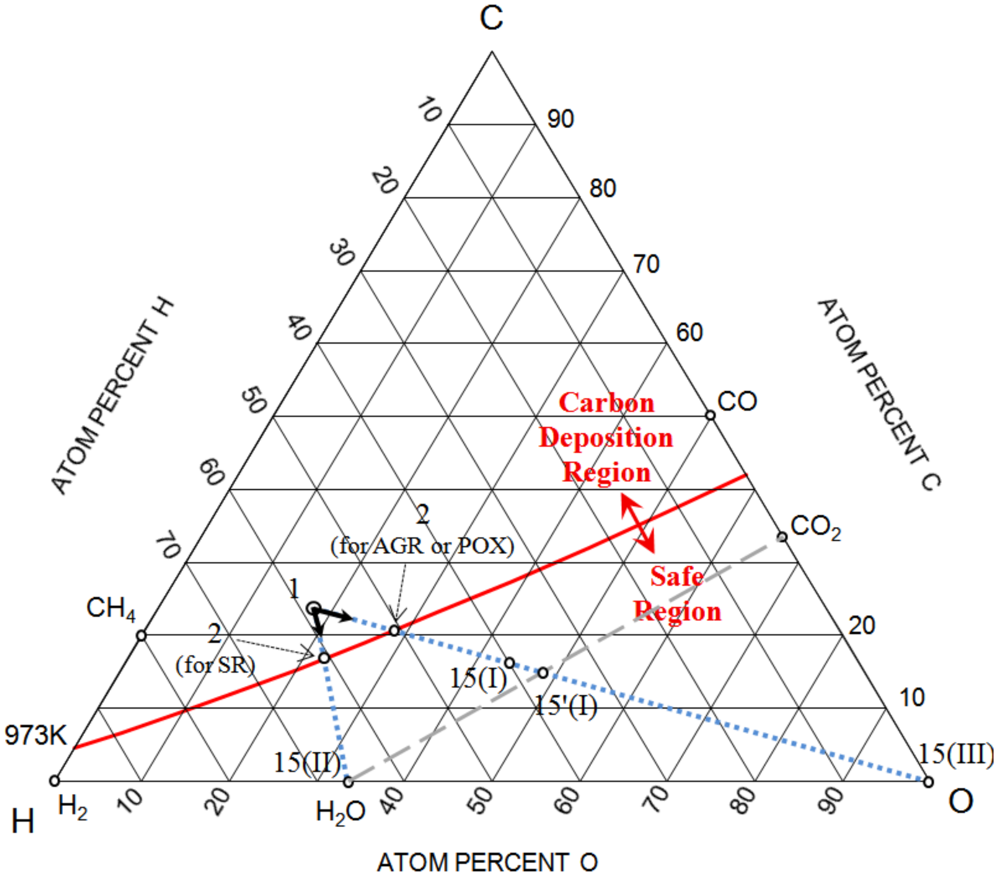

Figure 3.13: The location of an arbitrary fuel and carbon deposition boundary curves at atmospheric pressure and temperature of 973 K in the C-H-O ternary diagram.

3.4.1.3.1 Air Blower

From the energy balance equation, the electric power required for the air blower and the temperature of air at the exit of the blower are determined as follows:

$$\dot{W}_{Blower} = \dot{n}_4 \bar{C}_{p,a} T_4 \frac{\left(\left(\frac{p_5}{p_4} \right)^{\frac{R_u}{\bar{C}_{p,a}}} - 1 \right)}{\eta_{Blower}} \tag{3.250}$$

$$T_5 = T_4 \left(1 + \frac{\left(\frac{p_5}{p_4} \right)^{\frac{R_u}{\bar{C}_{p,a}}} - 1}{\eta_{Blower}} \right) \tag{3.251}$$

Where, $T_4 = T_0$ and $p_4 = p_0$.

After determination of the electric power of the air blower, the DC electric power generated in the SOFC stack can be obtained:

$$\dot{W}_{Stack} = \frac{\dot{W}_{System} + \dot{W}_{Blower}}{\eta_{Inverter}} \tag{3.252}$$

This power is considered as the minimum power required to be generated in the stack. At the given minimum voltage of the stack and the voltage drop due to stacking the cells, the number of series and parallel cells is obtained from Equations (3.216) and (3.217). Then, the operating voltage and power of the stack and the flow rate of the inlet and outlet fuel and air streams from the stack can be determined from Equations (3.219)–(3.224). The minimum flow rate of the reforming agent for the reformer control volume can be also calculated as follows:

$$\dot{n}_{15(I)} = \frac{\frac{Z'_1}{Z'_{15(I)}}\left(\frac{C_1 - C_2}{C_2 - C_{15(I)}}\right)\frac{MW_2}{MW_1}}{1 + \frac{Z'_1}{Z'_{15(I)}}\left(\frac{C_1 - C_2}{C_2 - C_{15(I)}}\right)\frac{MW_3}{MW_1}}\dot{n}_2 \tag{3.253}$$

$$\dot{n}_{15(II)} = \frac{\frac{Z'_1}{3}\left(\frac{C_1}{C_2} - 1\right)\frac{MW_2}{MW_1}}{1 + \frac{Z'_1}{3}\left(\frac{C_1}{C_2} - 1\right)\frac{MW_{H_2O}}{MW_1}}\dot{n}_2 \tag{3.254}$$

$$\dot{n}_{15(III)} = \frac{\frac{1}{0.21}\frac{Z'_1}{2}\left(\frac{C_1}{C_2} - 1\right)\frac{MW_2}{MW_1}}{1 + \frac{1}{0.21}\frac{Z'_1}{2}\left(\frac{C_1}{C_2} - 1\right)\frac{MW_a}{MW_1}}\dot{n}_2 \tag{3.255}$$

Where,

$$Z'_{15(I)} = 5x'_{CH_4,3} + 2x'_{H_2,3} + 2x'_{CO,3} + 3x'_{CO_2,3} + 3x'_{H_2O,3} \tag{3.256}$$

$$C_{15(I)} = \frac{x'_{CH_4,3} + x'_{CO,3} + x'_{CO_2,3}}{Z'_{15(I)}} \tag{3.257}$$

$$C_2 = \frac{x'_{CH_4,2} + x'_{CO,2} + x'_{CO_2,2}}{5x'_{CH_4,2} + 2x'_{H_2,2} + 2x'_{CO,2} + 3x'_{CO_2,2} + 3x'_{H_2O,2}} \tag{3.258}$$

For the inlet biogas fuel to the system,

$$Z'_1 = 5x'_{CH_4,1} + 3x'_{CO_2,1} + 2x'_{O_2,1} + 3x'_{H_2O,1} \tag{3.259}$$

$$C_1 = \frac{x'_{CH_4,1} + x'_{CO_2,1}}{Z'_1} \tag{3.260}$$

After determination of the flow rate of the reforming agent, the inlet biogas flow rate corresponding to the system with configurations I-III is determined from Equations (3.261)–(3.263), respectively.

$$\dot{n}_{1,Configuration\ I} = \frac{MW_2}{MW_1}\dot{n}_2 - \frac{MW_3}{MW_1}\dot{n}_{15(I)} \tag{3.261}$$

$$\dot{n}_{1,Configuration\ II} = \frac{MW_2}{MW_1}\dot{n}_2 - \frac{MW_{H_2O}}{MW_1}\dot{n}_{15(II)} \tag{3.262}$$

$$\dot{n}_{1,Configuration\ III} = \frac{MW_2}{MW_1}\dot{n}_2 - \frac{MW_a}{MW_1}\dot{n}_{15(III)} \tag{3.263}$$

The inlet air flow rate to the system can be also calculated:

$$\dot{n}_4 = \dot{n}_7 + \dot{n}_{15(III)} \tag{3.264}$$

Obviously, $\dot{n}_{15(III)}$ is zero for configurations I and II of the SOFC system.

To calculate the inlet air flow rate to the system, the power generated in the SOFC stack should be determined and, to determine this power, the power required for the air blower should be obtained. This power can be obtained if the inlet air flow rate to the system is specified. Therefore, the use of iterative methods to determine the inlet air flow rate to the system is required. After determination of the inlet air flow rate, the excess air and the composition of the air and fuel at the exit of the stack can be determined.

3.4.1.3.2 Burner

The objective is to determine the temperature and molar flow rate of each component of the flue gas at the exit of the burner. For the combustion reaction (3.R6) in the burner, the molar flow rate of each component of the flue gas is obtained from the mass balance equation:

$$\begin{aligned}&\left(\dot{n}_{CH_4,3}-\dot{n}_{CH_4,15(I)}\right) CH_4 + \left(\dot{n}_{CO_2,3}-\dot{n}_{CO_2,15(I)}\right) CO_2 + \left(\dot{n}_{CO,3}-\dot{n}_{CO,15(I)}\right) CO\\ &\quad + \left(\dot{n}_{H_2,3}-\dot{n}_{H_2,15(I)}\right) H_2 + \left(\dot{n}_{H_2O,3}-\dot{n}_{H_2O,15(I)}\right) H_2O\\ &\quad + \left(\dot{n}_{N_2,3}-\dot{n}_{N_2,15(I)}\right) N_2 + \left(\dot{n}_{N_2,8}\right) N_2 + \left(\dot{n}_{O_2,8}\right) O_2\\ &\quad \rightarrow \left(\dot{n}_{CO_2,9}\right) CO_2 + \left(\dot{n}_{H_2O,9}\right) H_2O + \left(\dot{n}_{O_2,9}\right) O_2 + \left(\dot{n}_{N_2,9}\right) N_2\end{aligned} \tag{3.R6}$$

$$\dot{n}_{CO_2,9} = \dot{n}_{CH_4,3}-\dot{n}_{CH_4,15(I)} + \dot{n}_{CO_2,3}-\dot{n}_{CO_2,15(I)} + \dot{n}_{CO,3}-\dot{n}_{CO,15(I)} \tag{3.265}$$

$$\dot{n}_{H_2O,9} = 2\dot{n}_{CH_4,3}-2\dot{n}_{CH_4,15(I)} + \dot{n}_{H_2,3}-\dot{n}_{H_2,15(I)} + \dot{n}_{H_2O,3}-\dot{n}_{H_2O,15(I)} \tag{3.266}$$

$$\dot{n}_{O_2,9} = \dot{n}_{O_2,8} - 2\dot{n}_{CH_4,3}+2\dot{n}_{CH_4,15(I)} - 0.5\,\dot{n}_{CO,3}+0.5\,\dot{n}_{CO,15(I)} - 0.5\,\dot{n}_{H_2,3}+0.5\dot{n}_{H_2,15(I)} \tag{3.267}$$

$$\dot{n}_{N_2,9} = \dot{n}_{N_2,3} - \dot{n}_{N_2,15(I)} + \dot{n}_{N_2,8} \tag{3.268}$$

$$\dot{n}_9 = \dot{n}_{CO_2,9} + \dot{n}_{H_2O,9} + \dot{n}_{O_2,9} + \dot{n}_{N_2,9} \tag{3.269}$$

The flue gas temperature at the exit of the burner, T$_9$, is obtained from the energy balance equation:

$$\bar{h}_9(T_9) = \frac{\dot{n}_3 - \dot{n}_{15(I)}}{\dot{n}_9}\bar{h}_3 + \frac{\dot{n}_8}{\dot{n}_9}\bar{h}_8 \tag{3.270}$$

Where, $\dot{n}_{l,15(I)}$, $l \in \{CH_4, H_2, H_2O, CO_2, CO, N_2\}$ is zero for configurations II and III of the system.

3.4.1.3.3 Reformer Control Volume

The objective is to determine the flow rate and temperature of flue gas at the exit of the reformer control volume. From the mass balance equation:

$$\dot{n}_{l",10} = \dot{n}_{l",9}, l" \in \{ H_2O, CO_2, N_2, O_2\} \tag{3.271}$$

Depending on the configuration of the system, the flue gas temperature at the exit of the reformer can be determined from one of the following equations:

$$\bar{h}_{10}\left(T_{10,Configuration\ I}\right) = \bar{h}_9 - \frac{\dot{n}_2\bar{h}_2 - \dot{n}_1\bar{h}_1 - \dot{n}_{15(I)}\bar{h}_3}{\dot{n}_9} \tag{3.272}$$

$$\bar{h}_{10}\left(T_{10,Configuration\ II}\right) = \bar{h}_9 - \frac{\dot{n}_2\bar{h}_2 - \dot{n}_1\bar{h}_1 - \dot{n}_{15(II)}\bar{h}_{15(II)}}{\dot{n}_9} \tag{3.273}$$

$$\bar{h}_{10}\left(T_{10,Configuration\ III}\right) = \bar{h}_9 - \frac{\dot{n}_2\bar{h}_2 - \dot{n}_1\bar{h}_1 - \dot{n}_{15(III)}\bar{h}_5}{\dot{n}_9} \tag{3.274}$$

Where,

$$\bar{h}_1 = \bar{h}_{Biogas}(T_0) \tag{3.275}$$

$$\bar{h}_{15(III)} = \bar{h}_{Water}(T_0) \tag{3.276}$$

3.4.1.3.4 Air Heater

The objective is to determine the flow rate and temperature of flue gas at the exit of the air heater. From the mass balance equation:

$$\dot{n}_{l",11} = \dot{n}_{l",10}, l" \in \{ H_2O, CO_2, N_2, O_2\} \tag{3.277}$$

From the energy balance equation, the flue gas temperature at the exit of the air heater can be determined from the following equation:

$$\bar{h}_{11}(T_{11}) = \bar{h}_{10} - \frac{\dot{n}_5 - \dot{n}_{15(III)}}{\dot{n}_{10}}\left(\bar{h}_7 - \bar{h}_5\right) \tag{3.278}$$

Where, $\dot{n}_{15(III)}$ is zero for configurations I and II of the SOFC system.

3.4.1.3.5 Boiler

The objective is to determine the flow rate of hot water produced in the boiler. For this purpose, the exhaust gas temperature from the system, T_{12}, should be determined. This temperature is set at the dew point temperature of the flue gas + ΔT or the sum of the cold water temperature and initial temperature difference of the boiler, whichever is higher.

$$T_{12} = max\left(\left(T_{dew,flue\ gas} + \Delta T\right), \left(T_{13} + ITD\right)\right) \tag{3.279}$$

After determination of this temperature, the flow rate of the hot water produced and the total heat generated in the system can be determined:

$$\dot{n}_{14} = \frac{\dot{n}_{11}\left(\bar{h}_{11} - \bar{h}_{12}\right)}{\left(\bar{h}_{14} - \bar{h}_{13}\right)} \tag{3.280}$$

$$\dot{Q}_{System} = \dot{n}_{14}\left(\bar{h}_{14} - \bar{h}_{13}\right) \tag{3.281}$$

3.4.1.4 Exergy Analysis

After determination of the properties, composition, and flow rate of all streams, the exergy destruction in each component of the system can be calculated. For the exergy analysis, the atmospheric air (Ar=0.912%, CO_2=0.0337%, H_2O=2.215, N_2=76.305%, and O_2=20.531 [110]) with a temperature of 298.15K and pressure of 1 atm are considered as the reference environmental condition. The exergy destruction in different components and the total exergy destruction in the SOFC system I with configurations considered can be calculated from the equations listed in Table 3.1.

3.4.1.5 Efficiency of the System

The first- and second-law electrical and CHP efficiencies and the thermal to electric power ratio (TER) of the SOFC system I with configurations considered are determined as follows:

$$\eta_I = \frac{\dot{W}_{System}}{\dot{n}_1 \overline{LHV}_{Biogas}} \tag{3.296}$$

$$\eta_{I,CHP} = \frac{\dot{W}_{System} + \dot{Q}_{System}}{\dot{n}_1 \overline{LHV}_{Biogas}} \tag{3.297}$$

$$\eta_{II} = \frac{\dot{W}_{System}}{\dot{E}x_{dest,total} + \dot{W}_{System}} \tag{3.298}$$

$$\eta_{II,CHP} = \frac{\dot{W}_{System} + \dot{n}_{14}\left(\bar{e}_{x,14} - \bar{e}_{x,13}\right)}{\dot{E}x_{dest,total} + \dot{W}_{System}} \tag{3.299}$$

$$TER = \frac{\dot{Q}_{System}}{\dot{W}_{System}} \tag{3.300}$$

Table 3.1: Exergy destructions in different components of the SOFC system I.

Item		Equation	
Blower		$\dot{E}x_{dest,Blower} = \dot{n}_4 T_0 \left(\bar{C}_{p,a} ln\left(\frac{T_5}{T_0}\right) - R_u ln\left(\frac{p_5}{p_0}\right) \right)$	(3.282)
SOFC stack		$\dot{E}x_{dest,SOFC\ Stack} = \dot{n}_2 \bar{e}_{x,2} + \dot{n}_7 \bar{e}_{x,7} - \dot{n}_3 \bar{e}_{x,3} - \dot{n}_8 \bar{e}_{x,8} - \dot{W}_{Stack}$	(3.283)
Burner	configuration I	$\dot{E}x_{dest,Burner} = \left(\dot{n}_3 - \dot{n}_{15(I)}\right) \bar{e}_{x,3} + \dot{n}_8 \bar{e}_{x,8} - \dot{n}_9 \bar{e}_{x,9}$	(3.284)
	configurations II or III	$\dot{E}x_{dest,Burner} = \dot{n}_3 \bar{e}_{x,3} + \dot{n}_8 \bar{e}_{x,8} - \dot{n}_9 \bar{e}_{x,9}$	(3.285)
Reformer control volume	configuration I	$\dot{E}x_{dest,Reformer} = \dot{n}_9 \left(\bar{e}_{x,9} - \bar{e}_{x,10}\right) - \left(\dot{n}_2 \bar{e}_{x,2} - \dot{n}_1 \bar{e}_{x,1} - \dot{n}_{15(I)} \bar{e}_{x,3}\right)$	(3.286)
	configuration II	$\dot{E}x_{dest,Reformer} = \dot{n}_9 \left(\bar{e}_{x,9} - \bar{e}_{x,10}\right) - \left(\dot{n}_2 \bar{e}_{x,2} - \dot{n}_1 \bar{e}_{x,1} - \dot{n}_{15(II)} \bar{e}_{x,Water}(T_0)\right)$	(3.287)
	configuration III	$\dot{E}x_{dest,Reformer} = \dot{n}_9 \left(\bar{e}_{x,9} - \bar{e}_{x,10}\right) - \left(\dot{n}_2 \bar{e}_{x,2} - \dot{n}_1 \bar{e}_{x,1} - \dot{n}_{15(III)} \bar{e}_{x,5}\right)$	(3.288)
Air heater	configurations I or II	$\dot{E}x_{dest,Air\ Heater} = \dot{n}_{10} \left(\bar{e}_{x,10} - \bar{e}_{x,11}\right) - \dot{n}_5 \left(\bar{e}_{x,7} - \bar{e}_{x,6}\right)$	(3.289)
	configuration III	$\dot{E}x_{dest,Air\ Heater} = \dot{n}_{10} \left(\bar{e}_{x,10} - \bar{e}_{x,11}\right) - \left(\dot{n}_5 - \dot{n}_{15(III)}\right)\left(\bar{e}_{x,7} - \bar{e}_{x,6}\right)$	(3.290)
Boiler		$\dot{E}x_{dest,Boiler} = \dot{n}_{11} \left(\bar{e}_{x,11} - \bar{e}_{x,12}\right) - \dot{n}_{14} \left(\bar{e}_{x,14} - \bar{e}_{x,13}\right)$	(3.291)
Exhaust		$\dot{E}x_{dest,Exhaust} = \dot{n}_{12} \left(\bar{e}_{x,12} - \bar{e}_{x,0}\right)$	(3.292)
Pressure drop		$\dot{E}x_{dest,Pressure\ drop} = \dot{n}_4 T_0 R_u ln\left(\frac{p_5}{p_0}\right)$	(3.293)
DC to AC inverter		$\dot{E}x_{dest,Inverter} = \dot{W}_{Stack}(1 - \eta_{Inverter})$	(3.294)
Total exergy destruction in the SOFC system I		$\dot{E}x_{dest,total} = \dot{E}x_{dest,Blower} + \dot{E}x_{dest,SOFC\ Stack} + \dot{E}x_{dest,Burner} + \dot{E}x_{dest,Reformer} + \dot{E}x_{dest,Air\ Heater} + \dot{E}x_{dest,Boiler} + \dot{E}x_{dest,Exhaust} + \dot{E}x_{dest,Pressure\ drop} + \dot{E}x_{dest,Inverter}$	(3.295)

3.4.2 SOFC System II

3.4.2.1 System Configuration

The ammonia is selected as a fuel for this system. As shown in Figure 3.14, this system is mainly comprised of an oxygen ion-conducting SOFC stack used to generate electric power, liquid ammonia and water cylinders enough for a specified-duration of operation of the system, and an air blower used to supply air to the SOFC stack and to overcome the pressure drop in the system. Other essential components of the system are a heat exchanger used to increase the temperature of air, water, and ammonia before they enter the SOFC stack, and a catalytic burner used to convert the chemical energy of the unutilized fuel in the SOFC stack to heat. In contrast to most of the hydrocarbon-fuelled SOFC systems, a clean-up system to remove sulfur compounds from the fuel is not required for this electric power generation system. Even if fossil fuels or biomass are used as a feedstock for the ammonia production, the sulfur compounds of the feedstock should be removed in the first step of the ammonia production process to prevent deactivation of catalysts used in ammonia production plants [111].

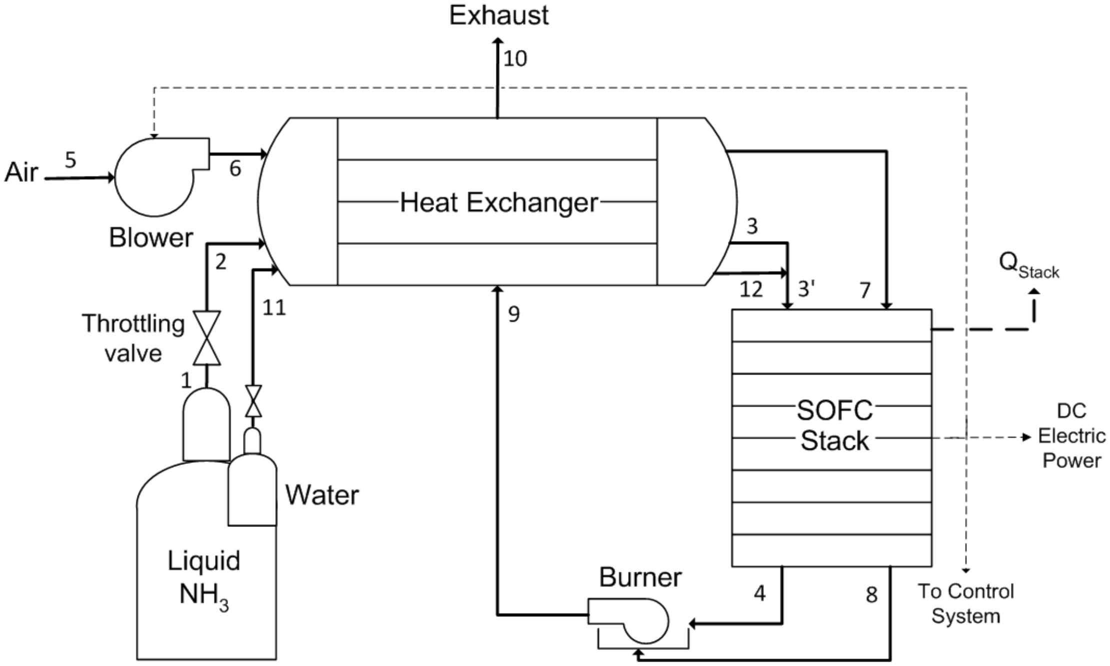

Figure 3.14: The SOFC system II proposed for portable electric power generation with ammonia fuel.

3.4.2.2 Process Description

The high pressure liquid ammonia in the small cylinder can be easily vaporized using a throttle valve. Although, the direct utilization of the vaporized ammonia in proton-conducting SOFCs is possible [112-114], the ammonia content of the inlet fuel to an oxygen ion-conducting SOFC should be kept as low as possible to prevent a corrosion problem. In the portable SOFC system illustrated in Figure 3.14, the vaporized ammonia enters a heat exchanger where its temperature increases to around 700°C. By increasing the temperature, ammonia starts to be decomposed to its constituent elements, i.e., hydrogen and nitrogen, through the following endothermic reaction [115]:

$$NH_3 + 46.5\ \text{kJ/mol} \leftrightarrow 1.5H_2 + 0.5N_2 \tag{3.R7}$$

To predict the composition of ammonia at the outlet of the heat exchanger, a thermodynamic, equilibrium-based study was performed; the result is shown in Figure 3.15. As seen in this figure, for temperatures higher than 450°C, more than 99% of the ammonia can be decomposed. However, the rate of the decomposition reaction may be slow at this temperature [116]. The amount of ammonia at the inlet of the SOFC stack can reach less than 250 ppm in equilibrium at the temperature of 700°C. It is assumed that the ammonia decomposition reaction is fast enough at this temperature compared to the residence time of ammonia in the heat exchanger. Because iron acts as a suitable catalyst for the ammonia decomposition reaction [117], an iron porous body can be inserted in the ammonia's paths in the heat exchanger to increase the rate of the reaction. In this condition, the outlet fuel from the heat exchanger can be considered to be close to thermodynamic equilibrium.

In addition to increasing the ammonia's temperature and decomposition to hydrogen and nitrogen, both the temperature of water after the exit from the water cylinder and air after the exit from the air blower increase to 700°C in the heat exchanger. The water vapour at 700°C is mixed with the decomposed ammonia before entering the SOFC stack. The fuel and air enter the stack where electricity, heat, and water vapour are generated due to the electrochemical reactions. Ma Q. *et al.* [118] investigated the possibility of nitric oxide formation in a variety of ammonia conversion rates and temperatures in SOFCs. They found that the amount of nitric oxide is not detectable even at 800°C. Therefore, nitric oxide is not expected to be formed in the stack. The outlet fuel and air from the stack enter a catalytic burner where the chemical energy of the unutilized fuel is converted to heat. A portion of the heat produced in the catalytic burner and SOFC stack is used for increasing the temperature of ammonia, air, and water to

700°C in the heat exchanger and for the decomposition of ammonia. The rest of the heat is vented to the atmosphere. The exhaust gas from this system is expected to be only water vapour, oxygen, and nitrogen.

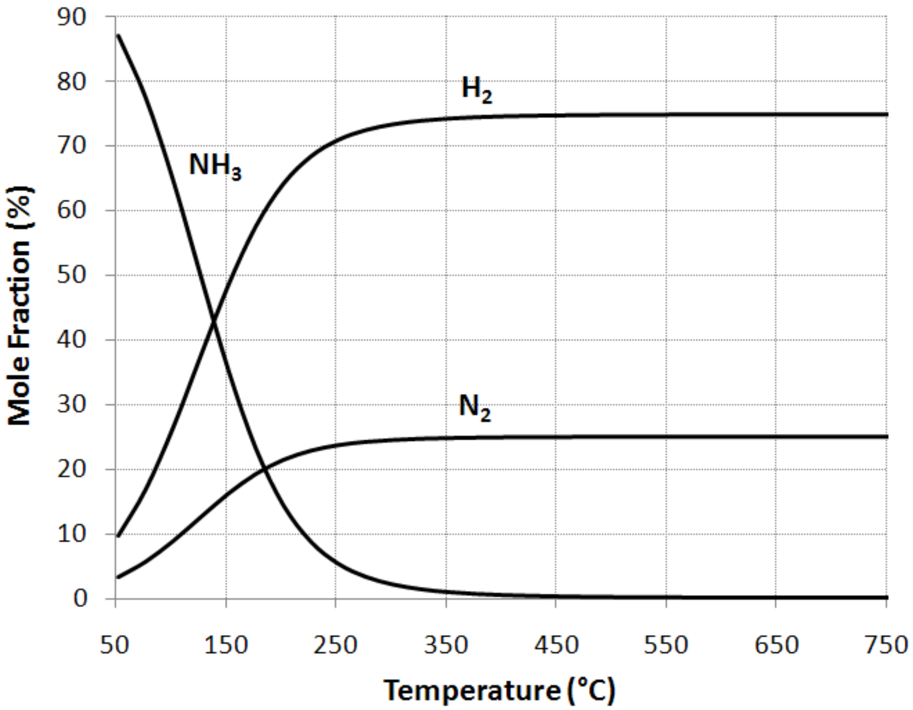

Figure 3.15: Mole fraction of ammonia, hydrogen, and nitrogen in thermodynamic equilibrium at different temperatures and pressure of 1 atm.

3.4.2.3 Modeling the BoP Components

To model this system, all components are assumed to be adiabatic, except the SOFC stack, and all streams are ideal gases, except streams 1 and 11. The inlet and outlet fuel streams from the SOFC stack are also assumed to be in equilibrium. The system is modeled at the given system net DC electric power, ambient temperature and pressure, isentropic efficiency of the blower, outlet air pressure from the blower, fuel and air temperatures at the inlet and outlet of the SOFC stack, the electric power required for control system (if required), and the mixing ratio of the ammonia and water ($\dot{n}_1/\dot{n}_{11}$). The model used for the SOFC stack is based on the model described in section 3.3. The thermal insulation system for the stack should be thin to reduce the size of the system. Therefore, the thermal insulation system II is selected for the SOFC stack. The BoP components are thermodynamically modeled under steady state operating conditions to determine the properties, composition, and flow rate of all streams in the system.

First, the composition of the inlet fuel to the SOFC stack at $T_{3'}$ should be determined. For a given mixing ratio of the ammonia and water, the mole fraction of water vapour in the inlet fuel to the stack, $x_{H_2O,3'}$, can be calculated from the following equation:

$$x_{H_2O,3'} = \frac{1}{2\left(\frac{\dot{n}_1}{\dot{n}_{11}}\right) + 1} \tag{3.301}$$

The composition of stream 3 at 700°C is approximately 0.25 N_2 + 0.75 H_2. Therefore, the mole fraction of N_2 and H_2 in stream 3' will be:

$$x_{N_2,3'} = 0.25\left(1 - x_{H_2O,3'}\right) \tag{3.302}$$

$$x_{H_2,3'} = 0.75\left(1 - x_{H_2O,3'}\right) \tag{3.303}$$

From the mass balance equation:

$$\dot{n}_1 = \dot{n}_2 = \frac{\dot{n}_3}{2} \tag{3.304}$$

$$\dot{n}_{11} = \dot{n}_{12} \tag{3.305}$$

$$\dot{n}_5 = \dot{n}_6 = \dot{n}_7 \tag{3.306}$$

$$\dot{n}_9 = \dot{n}_{10} \tag{3.307}$$

3.4.2.3.1 Air Blower

From the energy balance equation, the electric power required for the air blower and the temperature of air at the exit of the blower can be predicted:

$$\dot{W}_{Blower} = \dot{n}_5 \bar{C}_{p,a} T_5 \frac{\left(\left(\frac{p_6}{p_5}\right)^{\frac{R_u}{\bar{C}_{p,a}}} - 1\right)}{\eta_{Blower}} \tag{3.308}$$

$$T_6 = T_5 \left(1 + \frac{\left(\frac{p_6}{p_5}\right)^{\frac{R_u}{\bar{C}_{p,a}}} - 1}{\eta_{Blower}}\right) \tag{3.309}$$

Where, $T_5 = T_0$ and $p_5 = p_0$.

After determination of the power required for the air blower, the DC electric power generated in the SOFC stack can be calculated:

$$\dot{W}_{Stack} = \dot{W}_{System} + \dot{W}_{Control} + \dot{W}_{Blower} \tag{3.310}$$

This power is considered as the minimum power required for the SOFC stack. At the given voltage drop due to stacking the cells and considering that all cells are connected in series ($N_{Cells}=N_{Series}$), the number of cells can be determined from Equation (3.217). The voltage and power of the stack and the flow rate of the inlet and outlet fuel and air from the stack can be also obtained from Equations (3.219)–(3.224). Then the flow rate of ammonia in stream 1 and water in stream 11 can be calculated:

$$\dot{n}_1 = \frac{\left(1 - x_{H_2O,3'}\right)}{2} \dot{n}_{3'} \tag{3.311}$$

$$\dot{n}_{11} = x_{H_2O,3'} \dot{n}_{3'} \tag{3.312}$$

To determine the inlet air flow rate to the system, the power generated in the SOFC stack should be determined; to determine this power, the power required for the air blower should be calculated. This power can be calculated if the inlet air flow rate to the system is known. Therefore, to determine the inlet air flow rate, the use of iterative methods is required. After determination of the inlet air flow rate, the excess air and the composition of air and fuel at the exit of the stack can be determined.

3.4.2.3.2 Throttle Valve

In the throttling process, the enthalpy of the inlet and outlet streams to the throttling valve remains constant. Therefore, the temperature of stream 2 can be determined from the following equation:

$$\bar{h}_2(T_2) = \bar{h}_1 \tag{3.313}$$

Where,

$$\bar{h}_1 = \bar{h}_{Ammonia}(T_0) \tag{3.314}$$

3.4.2.3.3 Catalytic Burner

The objective is to determine the temperature and flow rate of each component of the flue gas at the exit of the catalytic burner. For the combustion reaction (3.R8) in the burner, the molar flow rate of each component is obtained from the mass balance equation:

$$\begin{aligned} &\dot{n}_{H_2,4}\, H_2 + \dot{n}_{H_2O,4}\, H_2O + \dot{n}_{N_2,4}\, N_2 + \dot{n}_{N_2,8}\, N_2 + \dot{n}_{O_2,8}\, O_2 \\ &\qquad \rightarrow \dot{n}_{H_2O,9}\, H_2O + \dot{n}_{O_2,9}\, O_2 + \dot{n}_{N_2,9}\, N_2 \end{aligned} \tag{3.R8}$$

$$\dot{n}_{H_2O,9} = \dot{n}_{H_2,4} + \dot{n}_{H_2O,4} \tag{3.315}$$

$$\dot{n}_{O_2,9} = \dot{n}_{O_2,8} - 0.5\, \dot{n}_{H_2,4} \tag{3.316}$$

$$\dot{n}_{N_2,9} = \dot{n}_{N_2,4} + \dot{n}_{N_2,8} \tag{3.317}$$

$$\dot{n}_9 = \dot{n}_{H_2O,9} + \dot{n}_{O_2,9} + \dot{n}_{N_2,9} \tag{3.318}$$

The flue gas temperature at the exit of the burner, T_9, is also obtained from the energy balance equation:

$$\bar{h}_9(T_9) = \frac{\dot{n}_4}{\dot{n}_9}\bar{h}_4 + \frac{\dot{n}_8}{\dot{n}_9}\bar{h}_8 \tag{3.319}$$

3.4.2.3.4 Heat Exchanger

The objective is to determine the temperature of flue gas at the exit of the system. It is assumed that mixing streams 3 and 12 are done inside the heat exchange. In this condition, the temperature of flue gas at the exit of the system can be determined from the following equation:

$$\bar{h}_{10}(T_{10}) = \bar{h}_9 - \frac{\dot{n}_6}{\dot{n}_9}\left(\bar{h}_7 - \bar{h}_6\right) - \frac{1}{\dot{n}_9}\left(\dot{n}_{3'}\bar{h}_{3'} - \dot{n}_2\bar{h}_2 - \dot{n}_{11}\bar{h}_{11}\right) \tag{3.320}$$

Where,

$$\bar{h}_{11} = \bar{h}_{Water}(T_0) \tag{3.321}$$

3.4.2.4 Exergy Analysis

After determination of the properties, composition, and flow rate of all streams, the exergy destruction in each component of the system can be calculated. For the exergy analysis, the atmospheric air (Ar=0.912%, CO_2=0.0337%, H_2O=2.215, N_2=76.305%, and O_2=20.531 [110]) with a temperature of 298.15K and pressure of 1 atm is considered as the reference environmental condition. The exergy destruction in different components and the total exergy destruction in the SOFC system II can be calculated from the equations listed in Table 3.2.

3.4.2.5 Efficiency of the System

The first- and second-law electrical efficiencies of the SOFC system II can be determined from Equations (3.330) and (3.331), respectively.

$$\eta_I = \frac{\dot{W}_{System}}{\dot{n}_1 \overline{LHV}_{Ammonia}} \tag{3.330}$$

$$\eta_{II} = \frac{\dot{W}_{System}}{\dot{E}x_{dest,total} + \dot{W}_{System} + \dot{W}_{Control}} \tag{3.331}$$

Table 3.2: Exergy destructions in different components of the SOFC system II.

Item	Equation	
Blower	$\dot{E}x_{dest,Blower} = \dot{n}_5 T_0 \left(\bar{C}_{p,a} ln\left(\frac{T_6}{T_0}\right) - R_u ln\left(\frac{p_6}{p_0}\right)\right)$	(3.322)
SOFC stack	$\dot{E}x_{dest,SOFC\ Stack} = \dot{n}_{3'}\bar{e}_{x,3'} + \dot{n}_7\bar{e}_{x,7} - \dot{n}_4\bar{e}_{x,4} - \dot{n}_8\bar{e}_{x,8} - \dot{W}_{Stack}$	(3.323)
Throttle valve	$\dot{E}x_{dest,Throttle\ Valve} = \dot{n}_1\left(\bar{e}_{x,1} - \bar{e}_{x,2}\right)$	(3.324)
Burner	$\dot{E}x_{dest,Burner} = \dot{n}_4\bar{e}_{x,4} + \dot{n}_8\bar{e}_{x,8} - \dot{n}_9\bar{e}_{x,9}$	(3.325)
Heat Exchanger	$\dot{E}x_{dest,Heat\ Exchanger} = \dot{n}_9\left(\bar{e}_{x,9} - \bar{e}_{x,10}\right) - \dot{n}_6\left(\bar{e}_{x,7} - \bar{e}_{x,6}\right) - \left(\dot{n}_{3'}\bar{e}_{x,3'} - \dot{n}_2\bar{e}_{x,2} - \dot{n}_{11}\bar{e}_{x,11}\right)$	(3.326)
Exhaust	$\dot{E}x_{dest,Exhaust} = \dot{n}_{10}\left(\bar{e}_{x,10} - \bar{e}_{x,0}\right)$	(3.327)
Pressure drop	$\dot{E}x_{dest,Pressure\ drop} = \dot{n}_5 T_0 R_u ln\left(\frac{p_6}{p_0}\right)$	(3.328)
Total exergy destruction in SOFC system II	$\dot{E}x_{dest,total} = \dot{E}x_{dest,Blower} + \dot{E}x_{dest,SOFC\ Stack} + \dot{E}x_{dest,Burner} + \dot{E}x_{dest,Throttle\ Valve} + \dot{E}x_{dest,Heat\ Exchanger} + \dot{E}x_{dest,Exhaust} + \dot{E}x_{dest,Pressure\ drop}$	(3.329)

3.5 Summary

A model based on thermodynamic equilibrium was presented to predict the possibility of carbon deposition on the anode catalyst. Using this model, the presence of solid carbon in the equilibrium composition of any hydrocarbon fuel in the CHO system at the operating temperatures and pressures of SOFCs can be predicted. If the carbon deposition for a fuel is possible, this model can be employed to calculate the minimum flow rate of reforming agent required to process the fuel before feeding to the cell.

The SOFC was modeled at the cell, stack, and system levels. Two models of the “basic model” and the “combined micro- and macro-model,” were presented for the SOFC at the cell level. The basic cell model is a simple model that is appropriate to evaluate the performance of SOFC systems. However, the combined micro- and macro-model considers the complex interdependency among the multi-component mass transport, energy transport, electron and ion transports, and electrochemical and chemical reactions in the cell. This model is suitable for detailed studies of the cell. Using this model, the effect of the microstructure of porous composite electrodes on the cell performance can be predicted before the cell is fabricated.

The stack level model considered in this study is the repeated-cell stack model. Two different insulation systems for SOFC stacks to predict the heat transfer from the stack were modeled. In the system level, two SOFC systems were modeled. The first system operates with biogas fuel to generate heat and electric power. This system is suitable for industrial and residential applications. The second system operates with liquid ammonia fuel. This system is suitable for portable power generation applications.

Chapter 4

Results and Discussion

4.1 Validation of the Models

The validation of the cell basic model and the combined micro- and macro-model were investigated through the experimental results reported in the literature.

4.1.1 The Basic Cell Model

To validate the cell basic model, the electrochemical performance of the ASC-3 anode-supported and ESC-4 electrolyte-supported cells produced by H.C. Starck Company [119] was simulated. This company reported the experimental i-V curves of these almost commercialized cells with the design and test conditions listed in Table 4.1.

Table 4.1: Design and test conditions of ASC-3 and ESC-4 cells produced by H.C. Starck Company.

Parameter		ACE-3 Cell	ESC-4 Cell
Operating temperature		700°C and 800 °C	850 °C
Operating pressure		1 atm	1 atm
Inlet air flow rate		40 l/hr	40 l/hr
Inlet fuel flow rate		20 l/hr	20 l/hr
Composition of the inlet fuel	H_2	40%	40%
	H_2O	5%	5%
	N_2	55%	55%
Anode	thickness	518 µm	40 µm
	porosity (assumed)	0.33 (–)	0.33 (–)
	tortuosity (assumed)	4 (–)	4 (–)
	pore size (assumed)	0.66 µm	0.66 µm
Cathode	thickness	45 µm	40 µm
	porosity (assumed)	0.33 (–)	0.33 (–)
	tortuosity (assumed)	4 (–)	4 (–)
	pore size (assumed)		
Electrolyte thickness		5 µm	90 µm
Cell active length		4 cm	4 cm
Cell active width		4 cm	4 cm

Both ASC-3 and ESC-4 cells are comprised of the dense YSZ electrolyte and LSM-YSZ cathode. The materials used for the anodes of the ASC-3 and ESC-4 cells are Ni-YSZ and Ni-GDC (Gadolinia-doped Ceria), respectively. Although the efficiency of the ASC-3 cell is higher than that of the ESC-4 cell, the Ni-GDC anode in the ESC-4 cell is more resistant to carbon deposition than the Ni-YSZ anode in the ASC-3 cell [120]. Therefore, less maintenance is required for the ESC-4 cell. This may make the ESC-4 cell suitable for residential applications rather than the ASC-3 cell, which is more appropriate for industrial applications of SOFCs where the system may be maintained by operators.

Figures 4.1 and 4.2 illustrate the performance of the ASC-3 and ESC-4 cells, respectively, obtained from the experiment conducted by H.C. Starck Company and predicted by the computer simulation on the basis of the cell basic model. As seen in these figures, the performance of both cells predicted by the computer simulation shows a satisfactory agreement with the experimental results.

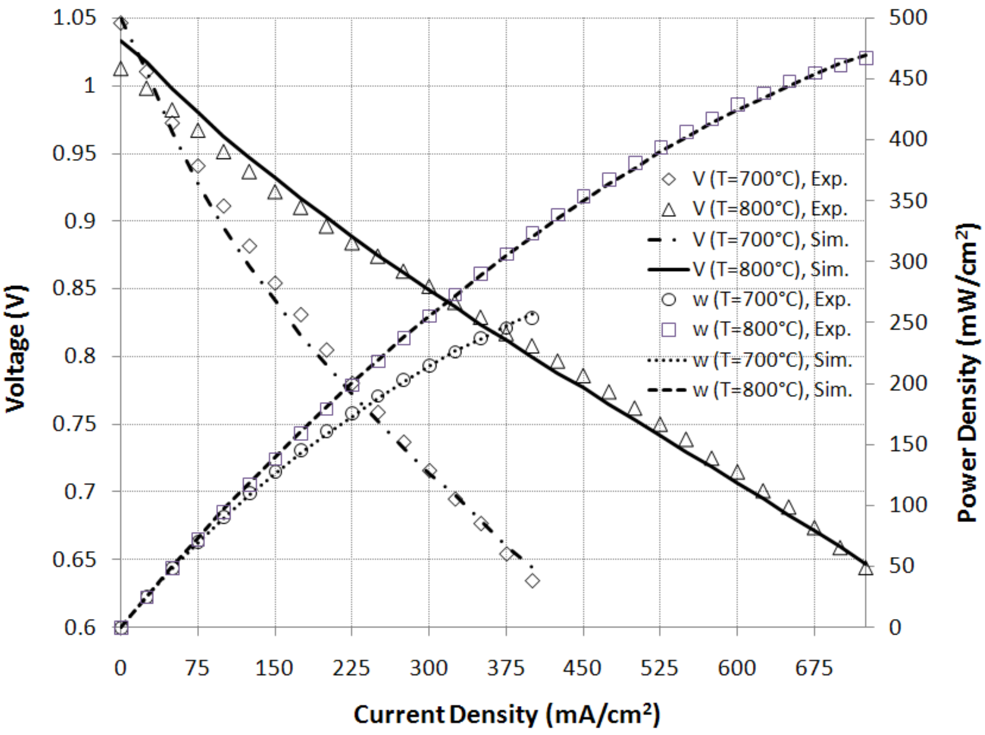

Figure 4.1: The performance of ASC-3 cells obtained from the experiment and the computer simulation.

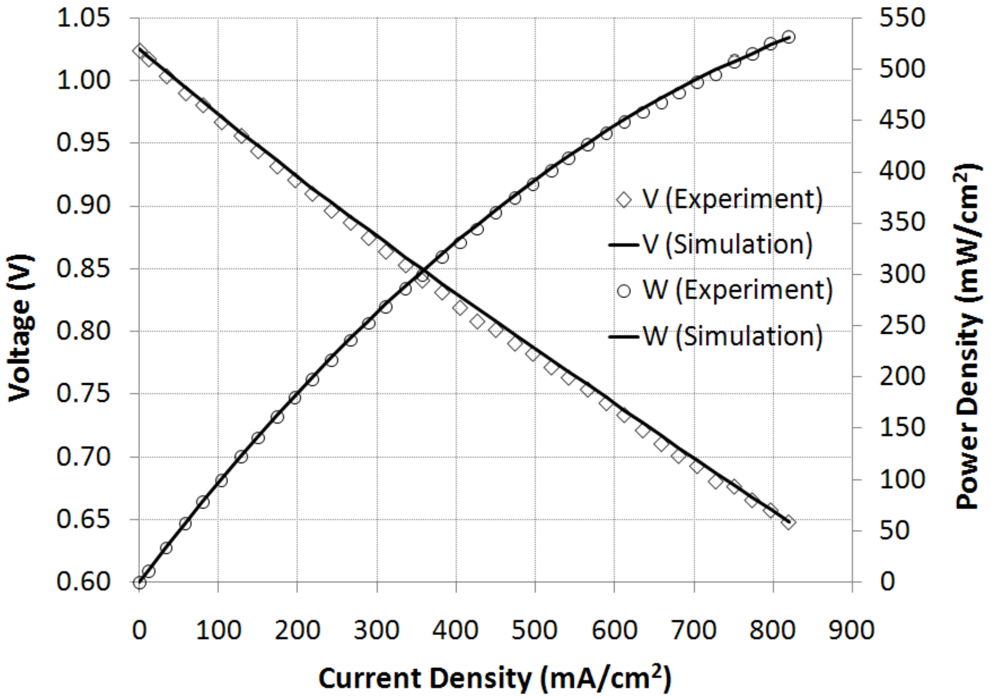

Figure 4.2: The performance of ESC-4 cells obtained from the experiment and the computer simulation.

4.1.2 The Cell Combined Micro- and Macro-model

A few experimental studies can be found in the open literature to link the microstructural variables of porous composite electrodes to the electrode performance. These experimental studies were usually conducted on small-sized, half-cell samples at a specified cell temperature and species partial pressures of the bulk fuel and air streams. We simulated these samples and compared the results of the computer simulation with the experimental results.

Kim *et al*. [121, 122] conducted valuable experiments to correlate the cathode total polarization resistance to the volume fraction of YSZ particles in the cathode. Their experiments were conducted on the porous LSM-YSZ composite cathode samples with a thickness of 40 μm, particle size ratio of 0.25, and an LSM particle size of 1 μm, operated at the mean cell temperature of 1223.15 K and bulk oxygen partial pressure of 0.2 atm. While they did not provide any value for the porosity and average contact angle between the LSM and YSZ particles, we used 0.33 following Smith *et al.* [123] and 30° from Chen *et al*. [62], respectively. As seen in Figure 4.3, the computer simulation could predict the total polarization resistance of their cathode samples with the LSM volume fraction of 0.69 and 0.79 with a relative error of

4.6% and 2.0%, respectively. However, a significant difference is seen for the cathode with the LSM volume fraction of 0.89 that is close to the percolation threshold of the YSZ particles.

Near the percolation threshold of YSZ, the effect of the cluster B of YSZ particles on the cathode microstructural properties becomes significant. Since we did not consider the effect of cluster B particles, the model developed would not be applicable when the volume fraction of electron- or ion-conducting particles is near or less than their percolation thresholds.

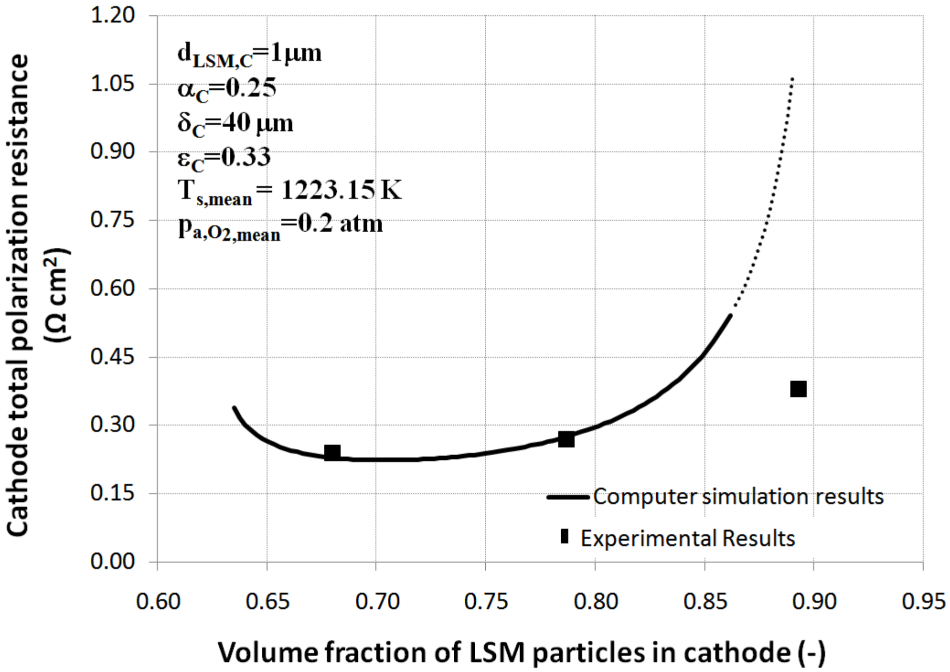

Figure 4.3: The results obtained from the computer simulation and experiment for the cathode samples fabricated by Kim *et al.* [121, 122].

Barbucci *et al.* [124] reported some experimental results to correlate the total polarization resistance of porous LSM-YSZ composite cathodes ($d_{LSM,C}$=0.3 μm, α_C=1 μm, $\varphi_{LSM,C}$=0.5, ε_C=0.4, $T_{s,mean}$=1073.15 K, $p_{a,O2,mean}$=0.21 atm) to the cathode thickness. As seen in Figure 4.4, a satisfactory agreement between the computer simulation and experimental results was obtained for the cathode thickness at which the minimum cathode total polarization resistance can be obtained (≈45-50 μm). A relative error of ≈15% was also obtained. This error may be due to the difference between the chemical composition of the LSM used to fabricate the cathodes samples, $(La_{0.75}Sr_{0.25})_{0.95}MnO_3$, and that used in the computer simulation, $(La_{0.8}Sr_{0.2})_{0.98}MnO_3$.

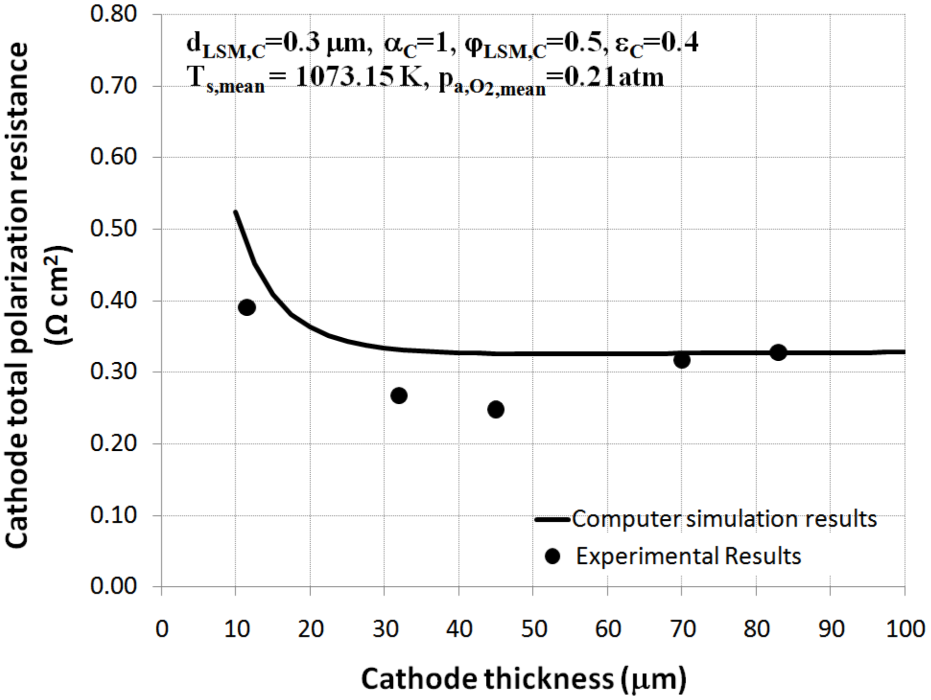

Figure 4.4: The results obtained from the computer simulation and experiment for the cathode samples fabricated by Barbucci *et al.* [124].

Brown *et al.* [125] have conducted several experiments on hydrogen-fuelled Ni-YSZ anode samples ($d_{Ni,A,FL}$≈0.8 µm, $\alpha_{A,FL}$≈0.94, $\varphi_{Ni,A,FL}$≈0.4, and $\varepsilon_{A,FL}$=0.5) to correlate the anode total polarization resistance with the anode thickness at the pressure of 1 atm and the cell mean temperature of 1273.15 K. As seen in Figure 4.5, the results of the computer simulation show reasonably good agreement with their experimental results with an average relative error of ≈5.6%.

Matsuzaki *et al.* [126] have also conducted several experiments on an anode sample ($d_{Ni,A,FL}$=0.9 µm, $\varphi_{Ni,A,FL}$≈0.8, $\delta_{A,FL}$=25 µm, and $\varepsilon_{A,FL}$=0.45) to correlate the anode total polarization with the current density at a pressure of 1 atm and mean cell temperature of 1023.15 K for the fuel group I (fuels No. 1 to 3) and a mean cell temperature of 1273.15 K for the fuel group II (fuels No. 4-6), as shown in Table 4.2. They did not report particle size ratio; however, if this ratio is assumed to be ≈0.17, the anode total polarization obtained from the computer simulation and reported for one of the experimental points corresponding to hydrogen fuel (x_{f,H_2}=78.5%, x_{f,H_2O}=21.5%, $T_{s,mean}$=1273.15 K, and $i_{tot,mean}$=0.3 A/m^2) are almost identical. Since the computer simulation could predict the experimental results reported by Brown *et al.* [125] for hydrogen fuel, we assumed the value of 0.17 for the particle size ratio of the anode sample tested by Matsuzaki *et al.* [126]. Considering this assumption, the validity of the model for the other experimental points for different fuels was investigated.

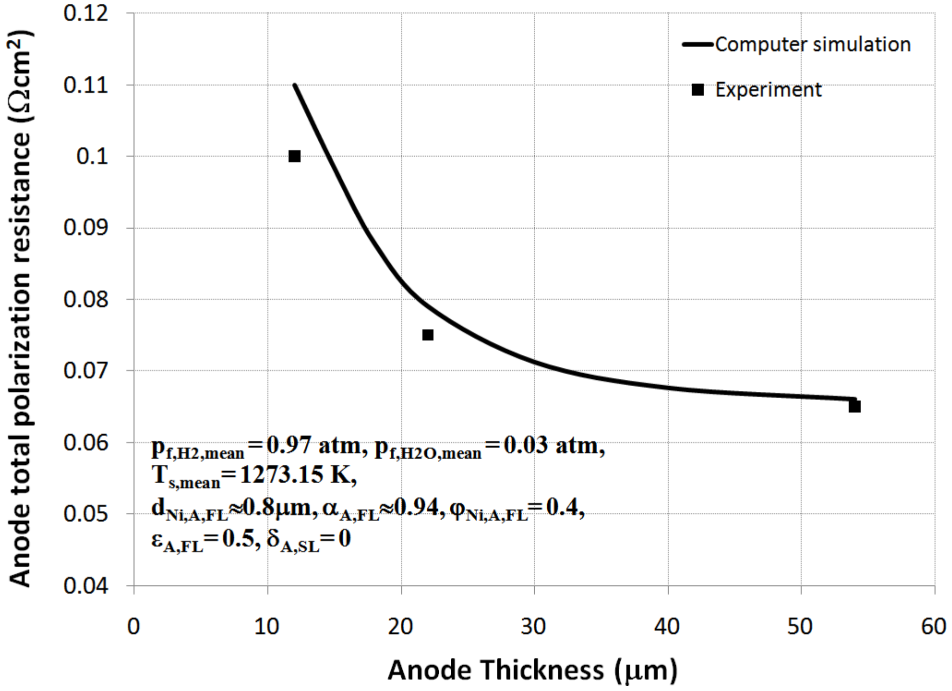

Figure 4.5: The results obtained from the computer simulation and experiment for the anode samples fabricated by Brown *et al.* [125].

Table 4.2: The composition of fuels in the experiments conducted by Matsuzaki *et al.* [126].

Fuel		H_2	CO	H_2O	CO_2	Cell temperature
Group	No.	(%)	(%)	(%)	(%)	(K)
I	1	64.2	14.9	16.0	4.9	1023.15
	2	38.8	38.8	9.7	12.6	1023.15
	3	18.8	57.8	4.7	18.8	1023.15
II	4	62.8	17.2	17.2	2.8	1273.15
	5	41.0	41.0	11.2	6.8	1273.15
	6	12.0	72.8	3.3	12.0	1273.15

As seen in Figure 4.6, the experimental results associated with the effect of the fuel composition on the anode total polarization can be predicted by computer simulation. The anode total polarization at several current densities and temperatures could be predicted with an average relative error of ≈8.8%.

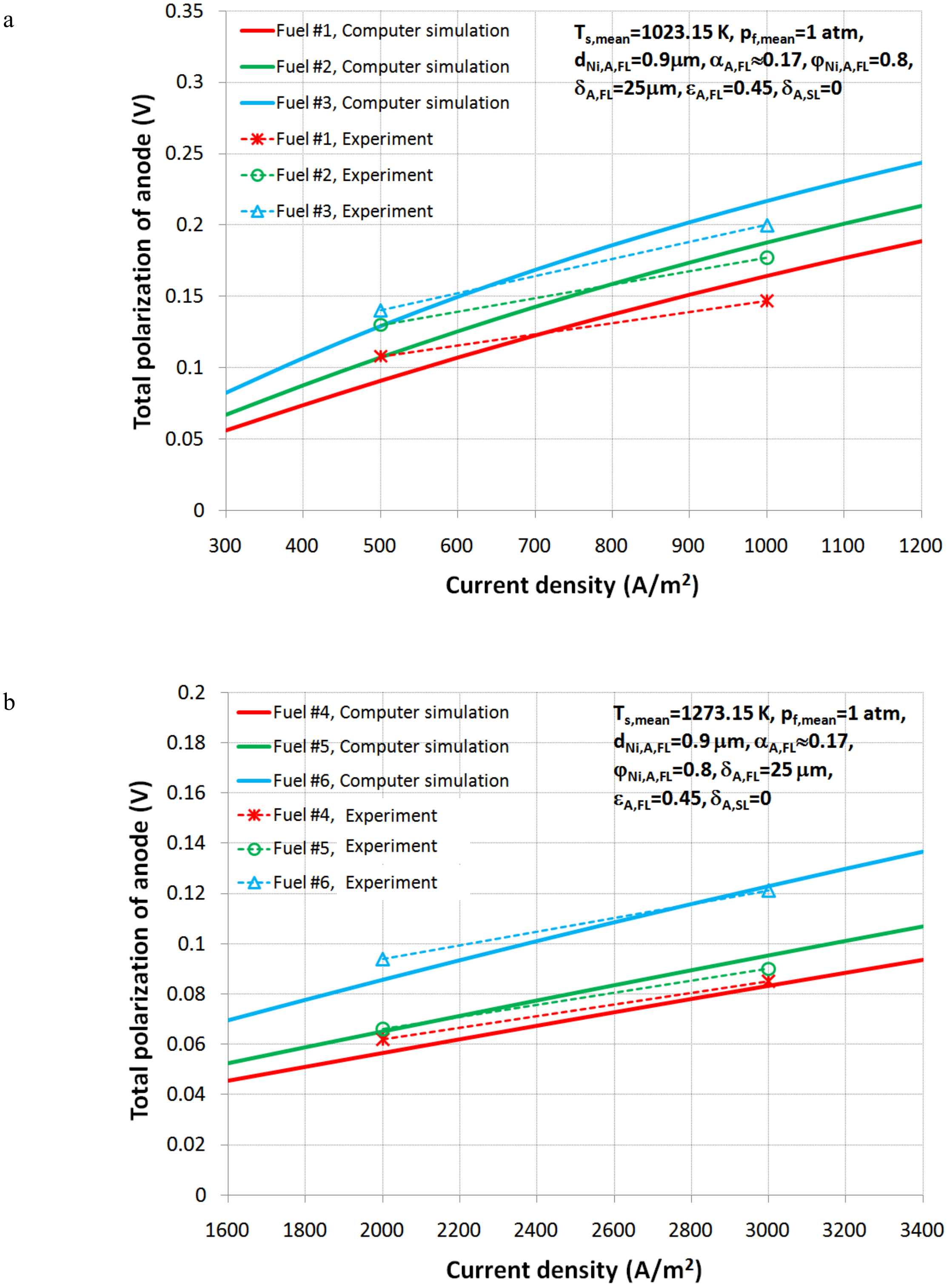

Figure 4.6: The results obtained from the computer simulation and experiment for the anode sample fabricated by Matsuzaki *et al.* [126], (a) $T_{s,mean}$=1023.15, (b) $T_{s,mean}$=1273.15K.

4.2 Carbon Deposition

The CDB curve at the temperature of 1100 K and pressure of 1 atm was obtained and is shown in the C-H-O ternary diagram in Figure 4.7. The locations of some typical fuels are also shown in this diagram. As seen, most of these fuels are located above the CDB curve in the carbon deposition region. This means that the carbon deposition on the anode catalyst is probable if these fuels are fed directly to the anode channel. However, each of these fuels can be mixed with a mixture located below the CDB curve to make a new mixture, located in the safe region, before feeding to the anode channel.

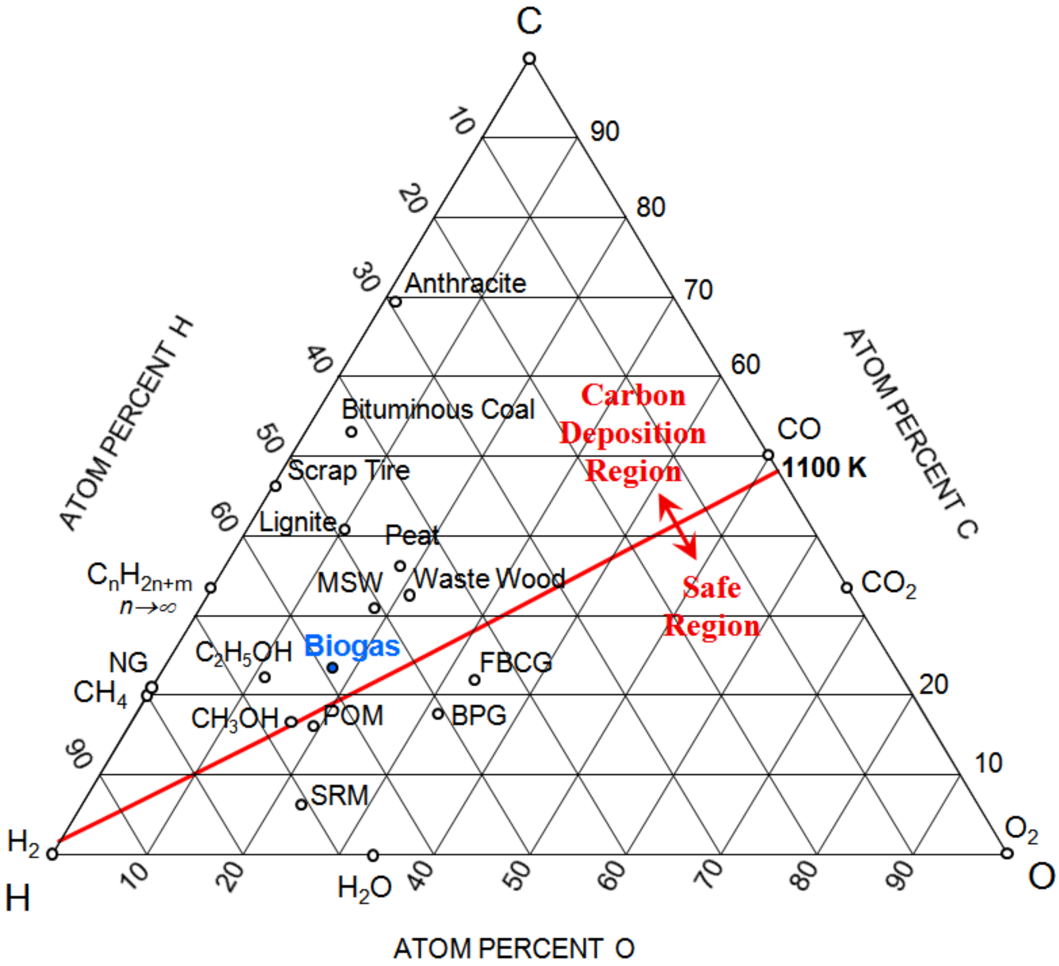

Figure 4.7: The location of some fuels in the C-H-O ternary diagram and the carbon deposition curve at the temperature of 1100 K and pressure of 1 atm[1].

---

[1] NG: Natural gas; SRM: Steam reforming of methane; POM: Partial oxidation of methane; FBCG: Fluidized bed coal gasifier; BPG: Biomass produced gas; MSW: Municipal solid waste.

The fuel considered in this study is the average composition of biogas produced in WWTPs in Ontario. The key chemical components of this gas are methane (61.1%), carbon dioxide (35.0%), nitrogen (2.4%), oxygen (1.5%), and water vapour (0.01%) [109]. The location of this gas in the C-H-O diagram in Figure 4.7 indicates that this fuel lies in the carbon deposition region. Three optional methods for processing biogas were considered in this study. These three methods were the AGR method through which the biogas is mixed with a part of the outlet fuel from the anode channel, the SR method through which the biogas is mixed with water, and the POX method through which the biogas is mixed with air. The equilibrium composition of the biogas processed by these methods at the pressure of 1 atm and temperatures of 973 K, 1023 K, 1073 K and 1123 K was calculated and listed in Table 4.3. Since the air is used as the reforming agent for the POX method, the nitrogen content of the fuel processed by this method is significantly higher than that processed by the AGR or SR methods. These processed gases were employed as the inlet fuel to cells studied in this thesis.

Table 4.3: Compositions of the biogas processed by AGR, SR, and POX methods at p=1 atm.

Composition	Biogas processing method											
	AGR				SR				POX			
	973 K	1023 K	1073 K	1123 K	973 K	1023 K	1073 K	1123 K	973 K	1023 K	1073 K	1123 K
CH_4 (mol%)	2.5	1.8	1.2	0.8	3.7	2.4	1.5	1.0	1.3	1.0	0.8	0.5
H_2 (mol%)	44.1	48.6	51.5	53.1	53.2	55.7	57.4	58.3	31.5	36.9	40.6	42.7
CO (mol%)	32.5	38.1	40.9	42.3	26.3	32.2	35.6	37.3	23.5	28.9	32.2	33.9
H_2O (mol%)	9.0	5.1	2.8	1.5	8.8	5.0	2.7	1.5	4.7	3.0	1.7	1.0
CO_2 (mol%)	10.7	5.2	2.4	1.1	7.0	3.7	1.8	0.9	5.6	3.0	1.5	0.7
N_2 (mol%)	1.2	1.2	1.2	1.1	1.0	1.0	1.0	1.0	33.4	27.2	23.2	21.2

4.2.1 Effect of the Temperature and Pressure on the CDB Curve

The location of the CDB curve and the areas of the carbon deposition and safe regions in the C-H-O diagram vary with the temperature and pressure. As shown in Figure 4.8(a), with an increase in the temperature, the carbon deposition region enlarges on the left side and shrinks on the right side of the C-H-O ternary diagram. Furthermore, the area of the carbon deposition region decreases with an increase in the temperature, which means that the number of fuels that fall in the carbon deposition region decreases.

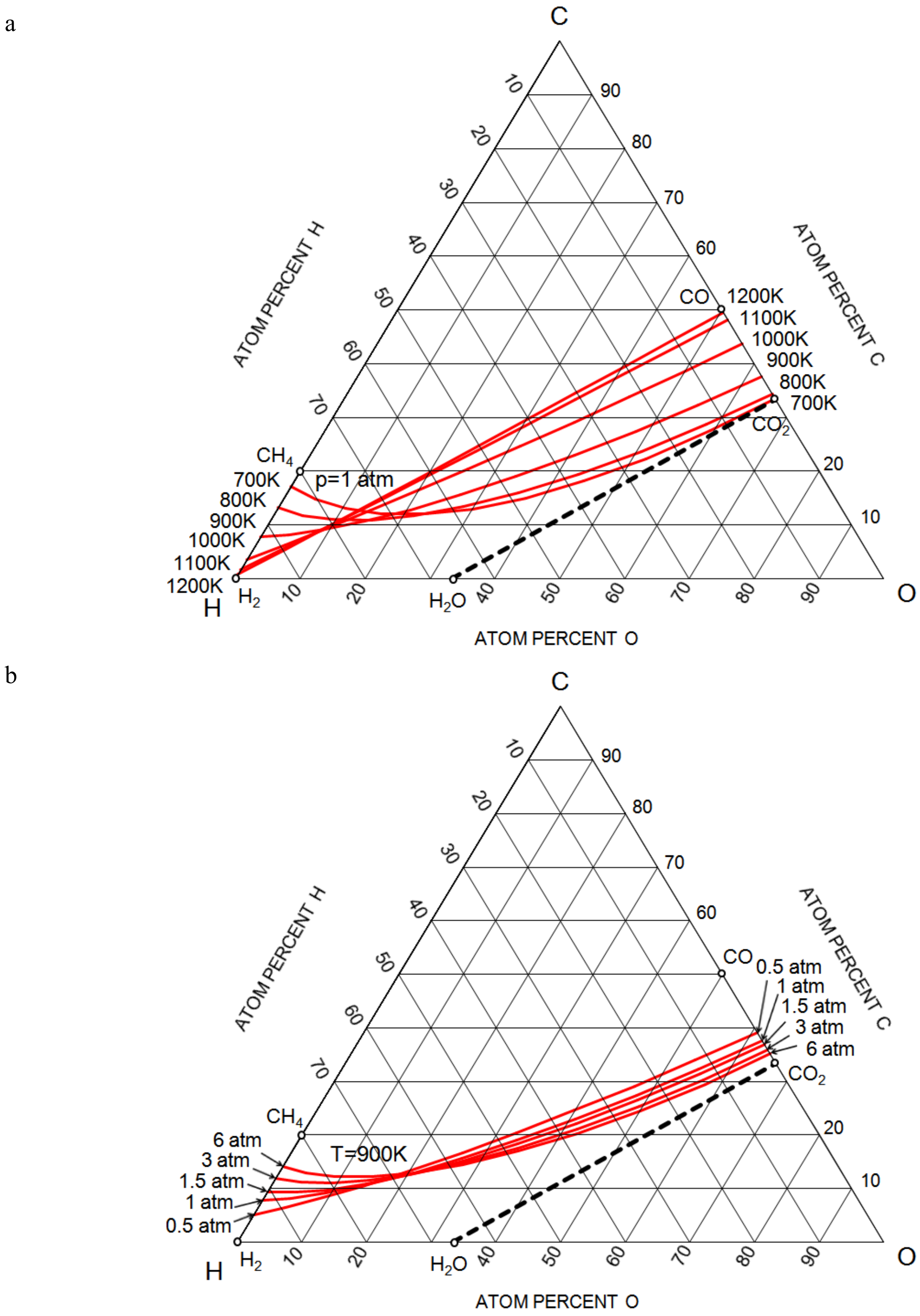

Figure 4.8: The CDB curve in the C-H-O ternary diagram, (a) effect of temperature (b) effect of pressure.

For temperatures greater than 1200 K, the CDB curve is almost a straight line joining points H_2 and CO together. In these conditions, the area of the carbon deposition and safe regions is identical. For temperatures of less than 1200 K, the area of the carbon deposition region is greater than that of the safe region. This means that if the temperature is less than 1200 K, the number of fuels that fall in the carbon deposition region is greater than those that fall in the safe region. As shown in Figure 4.8(b), the effect of the increase in the pressure on the CDB curve is similar to the effect of the decrease in the temperature. In fact, with an increase in the pressure, the safe region shrinks on the left side and enlarges on the right side. To determine the possibility of carbon deposition for a fuel containing an inert gas such as nitrogen, the CDB curve corresponding to the pressure obtained from the difference of the fuel pressure and partial pressure of inert gases should be considered. For example, if a gaseous fuel contains 20 mol% inert gases, the CDB curve for evaluating this fuel is equivalent to the fuel without any inert gas and a pressure of 20% less than the pressure of the fuel with inert gases. Therefore, the effect of the increase in the mole fraction of inert gases is equivalent to the effect of the decrease in the fuel pressure.

4.3 Microstructural Properties of Porous Composite Electrodes

On the basis of the microstructure modeling of porous composite electrodes presented, the effect of the size and volume fraction of electron-conducting particles and the particle size ratio on the microstructural properties of the electrochemical active area per unit volume, pore size, and effective resistivities of the electron- and ion-conductors were studied.

4.3.1 Electrochemical Active Area per Unit Volume

Figure 4.9 shows the effect of the volume fraction of electron-conducting particles at several particle size ratios and sizes of the electron-conducting particles on the electrochemical active area per unit volume of the porous composite electrode, A_{TPB}. The studies indicate that the electrochemical active area per unit volume is maximized at the average volume fraction of the electron- and ion-conducting particles at percolation thresholds, i.e. $\varphi_{el}=(3.38\alpha+2.4)/(2.4\alpha^2+6.76\alpha+2.4)$, and that it increases once the particle size ratio approaches unity ($\alpha=1$) or the size of the electron-conducting particles decreases. The electrochemical active area decreases considerably at the percolation threshold of the electron or ion-conducting particles; thus, it is expected that the activation polarization increases significantly at percolation thresholds. As a remarkable result, the maximum electrochemical active area is obtained when the size and volume fraction of electron- and ion-conducting particles is identical.

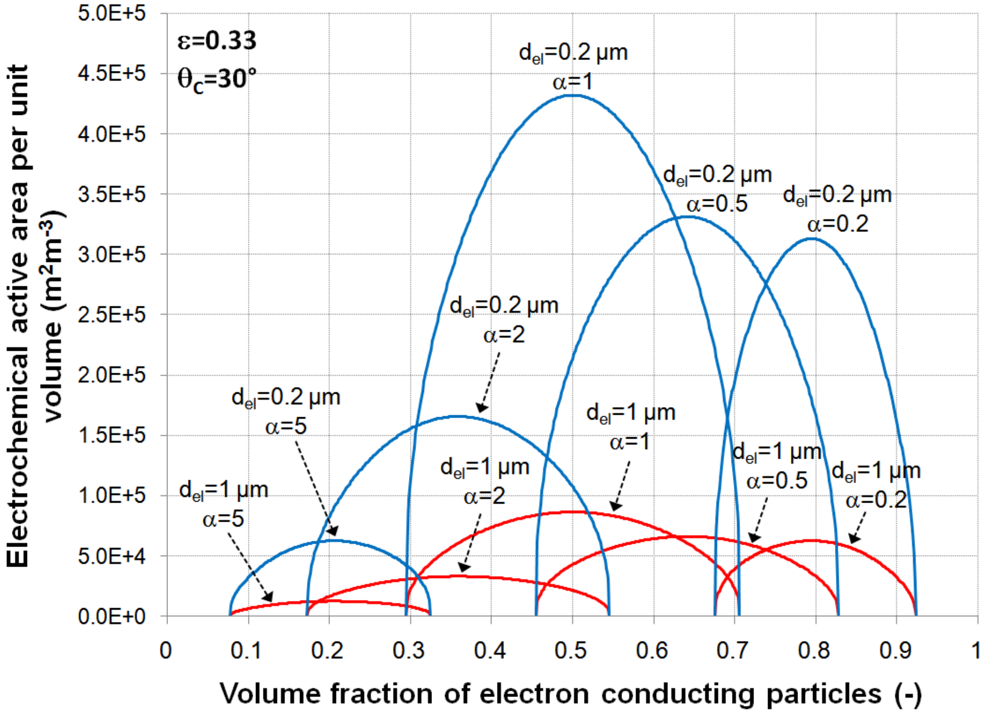

Figure 4.9: Effect of the volume fraction of electron-conducting particles at several particle size ratios and sizes of the electron-conducting particles on the electrochemical active area per unit volume.

4.3.2 Pore Size

The effect of the volume fraction of electron-conducting particles at several particle size ratios and electron-conducting particle sizes on the average pore size of electrode is shown in Figure 4.10. With an increase in the volume fraction of electron-conducting particles, the pore size decreases if the particle size ratio is greater than unity (α>1), and it increases if this ratio is smaller than unity (α<1). For the particle size ratio of unity (α=1), the average pore size remains constant throughout the entire range of the volume fraction of electron-conducting particles. This result is consistent with the computer modeling result reported by Kenney *et al.* [58]. For the particle size ratio of unity, the pore size decreases linearly with a decrease in the size of the electron-conducting particles. The decrease in the pore size may inhibit gas transport from the bulk to the active sites of the electrode, which can lead to an increase in the concentration polarization.

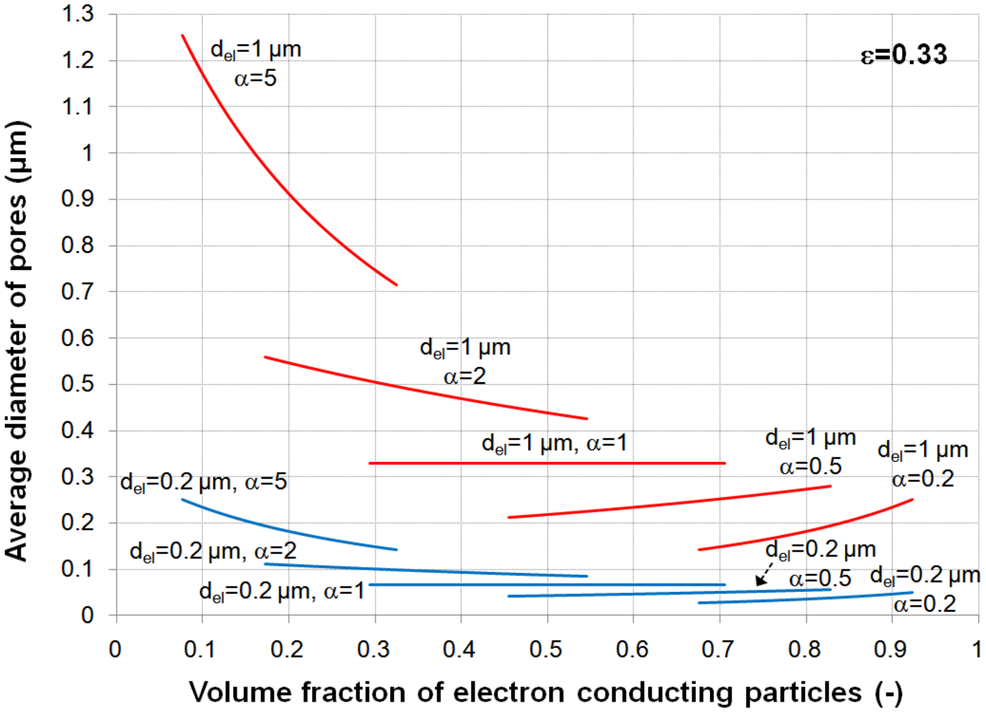

Figure 4.10: Effect of the volume fraction of electron-conducting particles at several particle size ratios and sizes of the electron-conducting particles on the average pore size.

4.3.3 Effective resistivities of the Electron and Ion Conductors

The effect of the volume fraction of electron-conducting particles at several particle size ratios and the temperature of 1073.15 K on the effective electronic resistivity of Ni and LSM ($La_{0.8}Sr_{0.2}MnO_3$) and the ionic resistivity of YSZ ($((ZrO_2)_{0.92}(Y_2O_3)_{0.08})$) is shown in Figure 4.11. For a given particle size ratio, the effective resistivities are independent of the size of the electron-conducting particles. A sudden jump in the effective resistivities of electron and ion conductors occurs near their percolation thresholds. This sudden jump is due to the assumption that the effect of cluster B particles in the microstructure modeling of electrodes has not been taken into account. As a remarkable result, the effective resistivity of YSZ is greater than that of Ni or LSM by several orders of magnitude if the Ni and LSM volume fractions are beyond their percolation thresholds. Hence, the effective resistivity of YSZ may play an important role in determining the optimum microstructure of the electrode rather than the effective resistivities of Ni or LSM. The effective resistivity of YSZ decreases with a decrease in the volume fraction of electron-conducting particles or an increase in the particle size ratio.

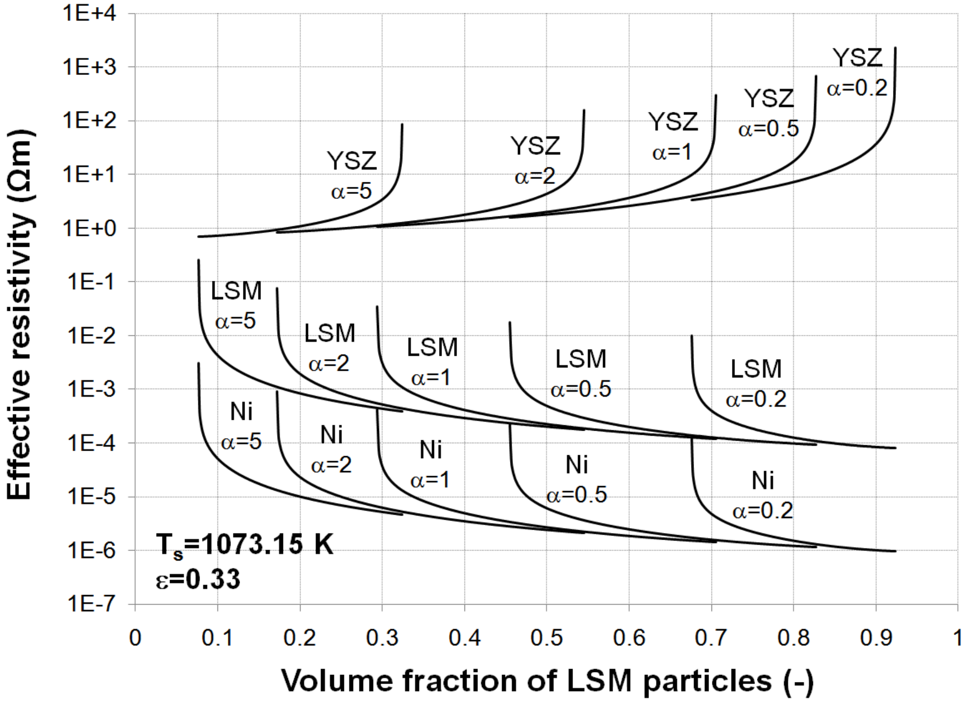

Figure 4.11: Effect of the volume fraction of electron-conducting particles at several particle size ratios on the effective Ni, LSM, and YSZ resistivities.

4.4 The Cell Combined Micro- and Macro-model

An anode-supported co-flow planar cell with design and operating parameters listed in Table 4.4 was simulated on the basis of the cell combined micro- and macro-model; and the electrical performance and distributions of several physical, chemical, and electrochemical variables along the thickness and length of the cell were predicted. The gas obtained from processing biogas by the AGR method at the temperature of 1073.15 K and pressure of 1 atm was used as the inlet fuel to the cell studied. The composition of this gas is listed in Table 4.3. The thermal conductivities of 3, 3, 2, and 27 W/m K were also considered for the anode, cathode, electrolyte, and interconnect of this cell, respectively [31].

The results of the computer simulation of this cell are listed in Table 4.5. For the microstructures of the porous composite anode and cathode of this cell, the first and second law efficiencies of 41.7% and 91.3%, respectively, were predicted. This cell generates ≈39.0 W, ≈28.4 W of which is due to the H_2 electrochemical reaction and ≈10.6 W due to the CO electrochemical reaction; only ≈3.63 W of the exergy of the processed biogas is destructed in the cell.

Table 4.4: The design and operating parameters required to simulate the anode-supported co-flow planar cell.

Parameter	Value
Temperature of the inlet fuel to the fuel channel	1073.15 K
Temperature of the inlet air to the air channel	1073.15 K
Mole fraction of O_2 / N_2 in the inlet air to the air channel	21% / 79%
Fuel utilization ratio	80%
Cell voltage	0.7 V
Excess air	10
Air/fuel pressure at the outlet of the cell	1 atm
Heat transfer from the cell	0
Arrangement of the fuel and air streams	Co-flow
Design parameters	
Thickness of electrolyte	5 μm
Thickness of interconnect	3500 μm
Height of fuel channels	0.5 mm
Height of air channels	1.5 mm
Width of fuel and air channels	1 mm
Width of ribs	1 mm
Active length of the cell	10 cm
Active width of the cell	10 cm
Number of fuel/air channels in a cell	50
Microstructure of cathode ($(La_{0.8}Sr_{0.2})_{0.98}MnO_3$–$(ZrO_2)_{0.92}(Y_2O_3)_{0.08}$)	
LSM particle size	1 μm
Particle size ratio	1
LSM volume fraction	0.41
Porosity	0.25
Thickness	60 μm
Microstructure of anode functional layer (Ni–$(ZrO_2)_{0.92}(Y_2O_3)_{0.08}$)	
Ni particle size	1 μm
Particle size ratio	1
Ni volume fraction	0.43
Porosity	0.33
Thickness	45 μm
Microstructure of anode substrate layer (Ni–$(ZrO_2)_{0.92}(Y_2O_3)_{0.08}$)	
Ni particle size	2.5 μm
Particle size ratio	1
Ni volume fraction	0.5
Porosity	0.4
Thickness	472.5 μm

Table 4.5: The results of the computer simulation of the anode-supported co-flow planar cell with the design and operating parameters listed in Table 4.4.

Parameter	Value
Outlet fuel from the fuel channel	
Flow rate	35.1 g/hr
Temperate	1192.8 K
CH_4	0 %
H_2	9.32 %
CO	9.31 %
H_2O	46.06 %
CO_2	34.21 %
N_2	1.09 %
Outlet air from the air channel	
Flow rate	849.3 g/hr
Temperate	1191.7 K
O_2	19.64 %
N_2	80.36 %
Inlet fuel to the fuel channel	
Flow rate	18.9 g/hr
Pressure	101723 Pa
Inlet air to the air channel	
Flow rate	865.5 g/hr
Pressure	102336 Pa
Mean parameters of the cell	
Pressure differences between the air and fuel streams	312 Pa
Reversible voltage	0.927 V
Power density	3900 W/m^2
Power density generated due to H_2 electrooxidation reaction	2840 W/m^2
Power density generated due to CO electrooxidation reaction	1060 W/m^2
Exergy destruction density	363 W/m^2
Temperature of the solid structure	1160.8 K
Total polarization resistance	0.416 Ω cm^2
polarization resistance of anode	0.241 Ω cm^2
polarization resistance of cathode	0.167 Ω cm^2
polarization resistance of electrolyte	0.008 Ω cm^2
polarization resistance of interconnect	4×10^{-5} Ω cm^2
Maximum/minimum local parameters in the cell	
Maximum pressure difference between the air and fuel streams	614 Pa
Minimum power density	4400 W/m^2
Maximum power density	2430 W/m^2
Minimum exergy destruction density	121 W/m^2
Maximum exergy destruction density	898 W/m^2
Maximum temperature of the solid structure	1192.8 K
Temperature difference between the hottest and coldest spots in the solid structure	79.1 K
Maximum temperature gradient in the solid structure	11.8 K/cm
1st law efficiency	41.7 %
2nd law efficiency	91.3 %

4.4.1 Distribution of Physical, Chemical, and Electrochemical Variables along the Cell Length

4.4.1.1 Reynolds and Péclet Numbers

The distribution of the Reynolds number ($Re=\rho VD_{h,ch}/\mu$) corresponding to the air and fuel streams passing through the channels along the length of the cell is shown in Figure 4.12. The Reynolds number of the fuel and air streams does not significantly change along the length of the cell. The maximum Reynolds number of the air stream is at the entrance of the air channel (y=0) with a value of less than 90, and the maximum Reynolds number of the fuel stream is at the exit of the fuel channel (y=L) with a value of less than 10. Therefore, the air and fuel streams passing through the channels are laminar.

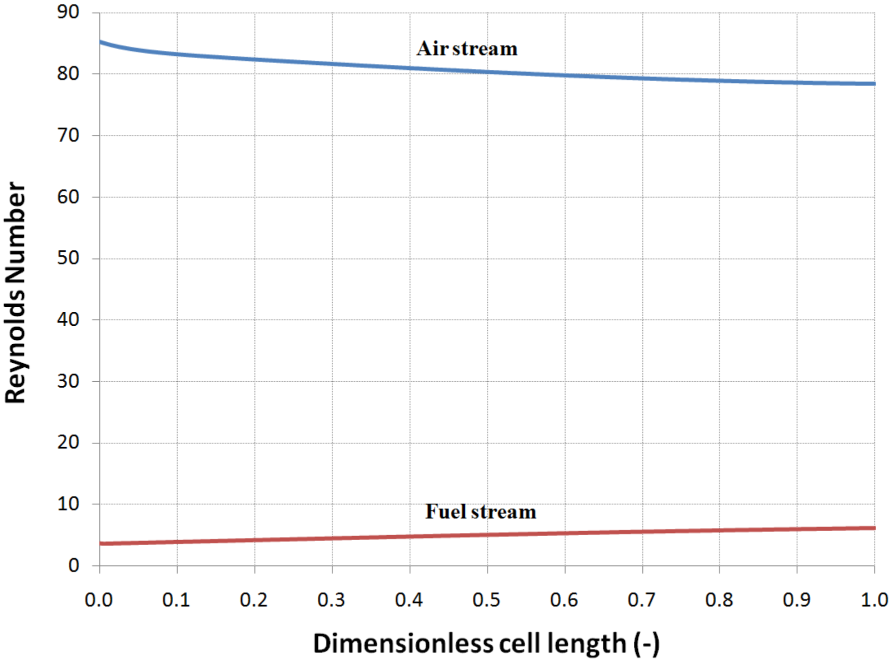

Figure 4.12: Distribution of Reynolds number of the air and fuel streams passing through the channels along the length of the cell.

Figures 4.13 and 4.14 show the distribution of the Péclet number associated with the mass ($Pe=VL/D$) and energy ($Pe=VL/\alpha$) transports in the air and fuel streams along the cell length. The minimum Péclet numbers associated with the mass and energy transports in the air stream are at the exit of the air channel (y=L) with a value greater than 4500 (see Figure 4.13).

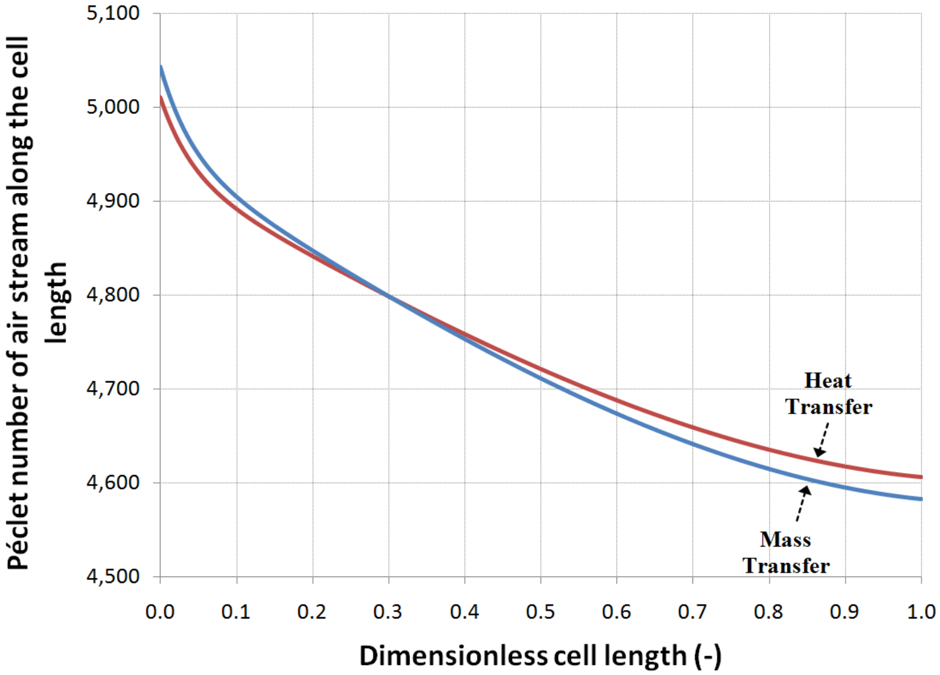

Figure 4.13: Distribution of Péclet number associated with the mass and energy transports in the air stream along the length of the cell.

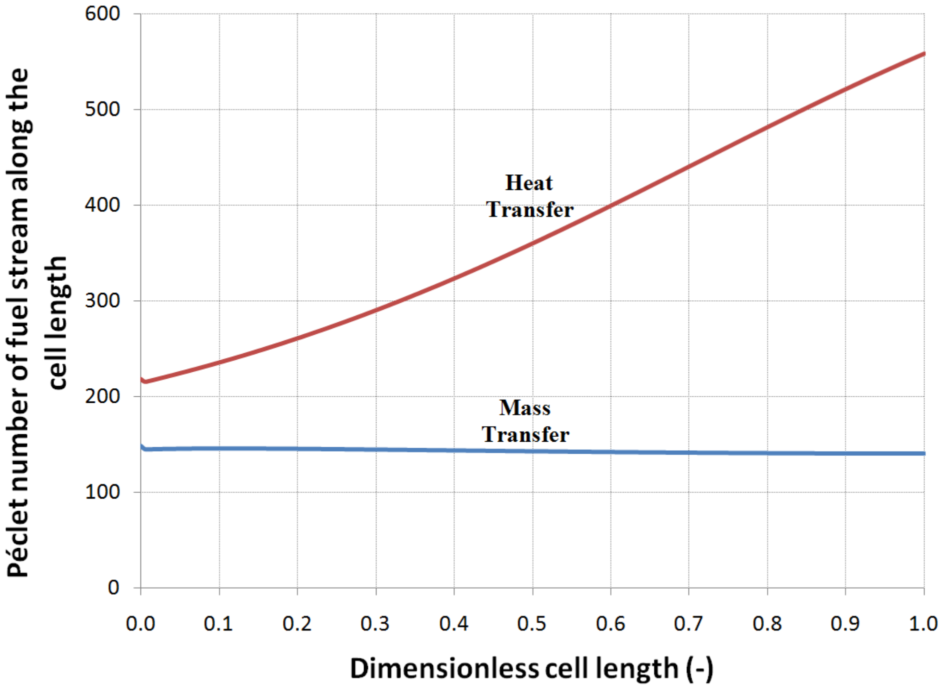

Figure 4.14: Distribution of Péclet number associated with the mass and energy transports in the fuel stream along the length of the cell.

The minimum Péclet number associated with the energy transport in the fuel stream is at the entrance of the fuel channel (y=0) with a value greater than 200 (see Figure 4.14). The lowest mass transport Péclet number in the fuel, which belongs to the diffusion of hydrogen through water vapour, is almost uniform throughout the length of the cell with a value of ≈140. Thus, the Péclet numbers associated with the mass and energy transports in the air and fuel streams are substantially greater than unity, and the heat and mass diffusions in the air and fuel streams along the cell length can be ignored.

4.4.1.2 Temperatures of Solid Structure, Fuel Stream, and Air Stream

The distribution of the temperatures of the solid structure, fuel stream, and air stream along the length of the cell is illustrated in Figure 4.15. The temperature of the fuel stream approaches the temperature of the solid structure before y≈0.1L, and there is an overlap between the temperatures of the fuel stream and the solid structure in the rest of the length of the cell. The temperature of the air stream slowly approaches the temperature of the solid structure, and the overlap between the temperatures of the air stream and solid structure occurs at the end of the length of the cell. The temperature of the solid structure increases from 1113.7 K at y=0 (as the coldest spot of the solid structure) to 1192.8 K at y=L (as the hottest spot of the solid structure) along the length of the cell. Therefore, the temperature difference between the hottest and coldest spots of the cell is ≈79.1 K. The mean temperature of the solid structure is predicted to be 1160.8 K. The maximum temperature gradient of the solid structure is also estimated to be ≈11.8 K/cm that occurs at y≈0.2L. It is noted that because the methane content of the inlet fuel to the cells studied is ≈1.2%, the effect of the cooling of the cell structure due to the methane steam reforming reaction is insignificant for the cells studied.

4.4.1.3 Pressure of the Fuel and Air Streams

As shown in Figure 4.16, the pressure of the air and fuel streams passing through the air and fuel channels varies linearly along the length of the cell. Although the cross section area of the air channel is three times larger than that of the fuel channel, the pressure drop in the air stream passing through the air channel is ≈2.5 times higher than that of the fuel stream passing through the fuel channel. This difference is due to the fact that the mass flow rate of the air stream is ≈45 times higher than that of the fuel stream at the excess air of 10. This leads to a mean pressure difference of 312 Pa between the air and fuel streams; however, the maximum pressure difference is 614 Pa and that occurs at y=0. Since the PEN structure that separates the fuel and air streams is very thin (≈600 μm for the cell studied), a change in the height of the air or fuel channels may be required to reduce the pressure difference between the air and fuel streams.

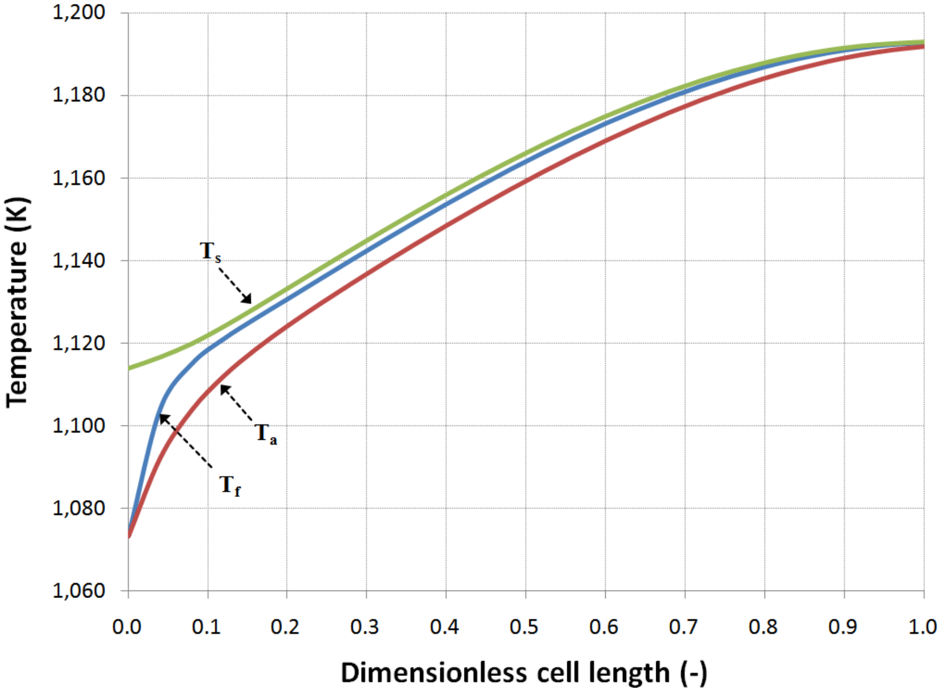

Figure 4.15: Distribution of the temperatures of the solid structure, fuel stream, and air stream along the length of the cell.

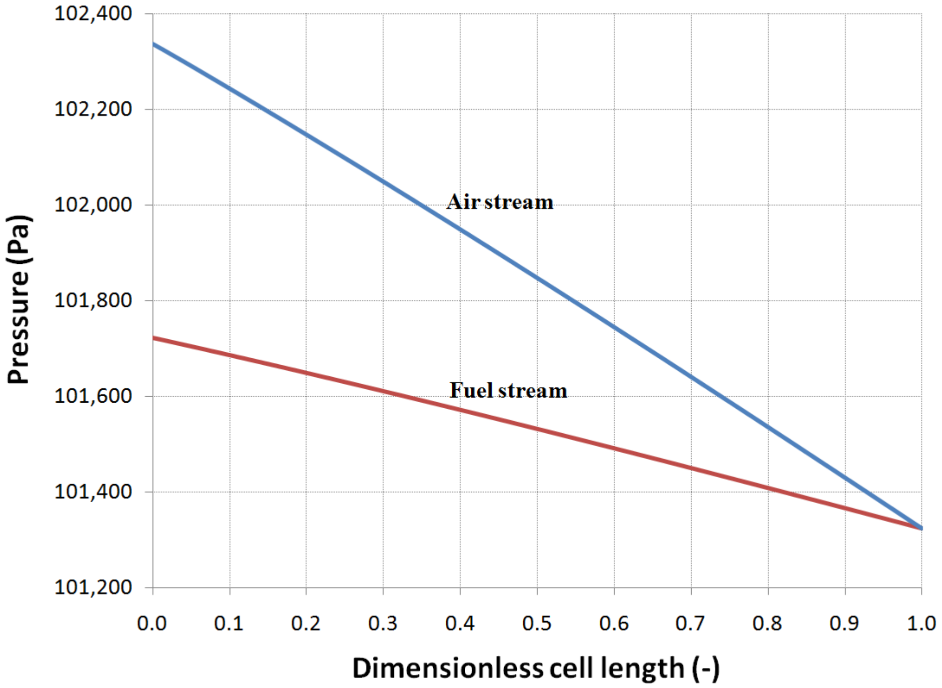

Figure 4.16: Distribution of the pressure of fuel and air streams along the length of the cell.

4.4.1.4 Mole Fraction of the Fuel and Air Species

Figure 4.17 shows the distribution of the mole fraction of the fuel species along the fuel channel. It is evident that the mole fraction of CH_4 decreases and approaches zero before y≈0.2L. Therefore, the steam reforming reaction occurs mainly at the entrance of the fuel channel where y<0.2L. At the fuel utilization ratio of 80%, the mole fraction of H_2 and CO decreases to 9.32% and 9.31%, respectively, and the mole fraction of H_2O and CO_2 increases to 46.06% and 34.21%, respectively. The mole fraction of N_2 is almost uniform throughout the fuel channel.

The distribution of the mole fractions of O_2 and N_2 along the air channel is shown in Figure 4.18. The mole fraction of O_2 decreases almost linearly with a slight slope along the length of the cell, and its value reaches ≈19.64% at the exit of the air channel (y=L). This negligible change in the mole fraction of O_2 is due to the high value of the excess air required to control the temperature of the cell.

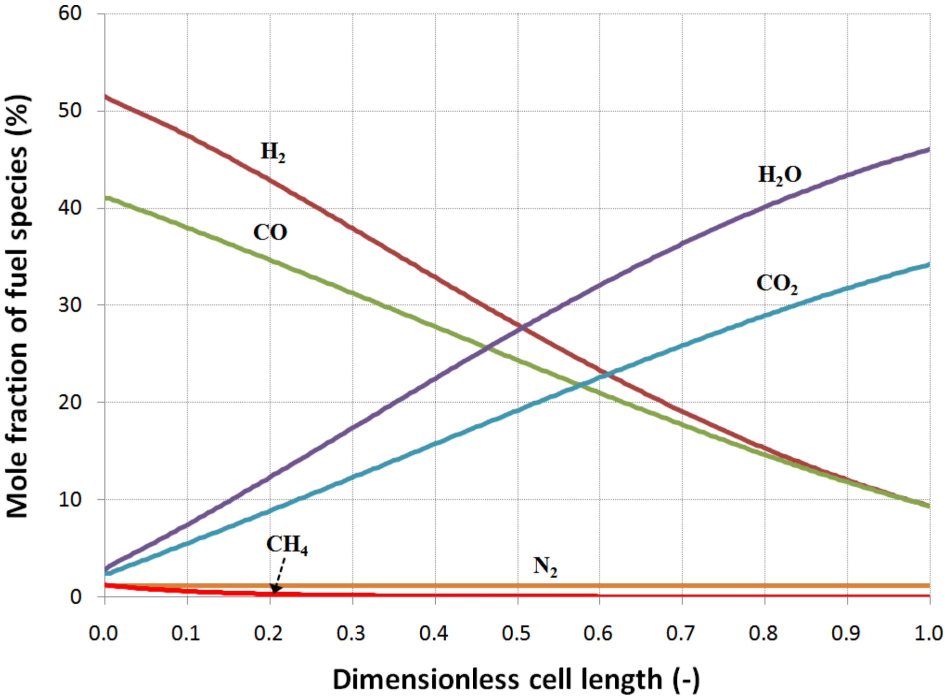

Figure 4.17: Distribution of the mole fraction of the fuel species along the length of the cell.

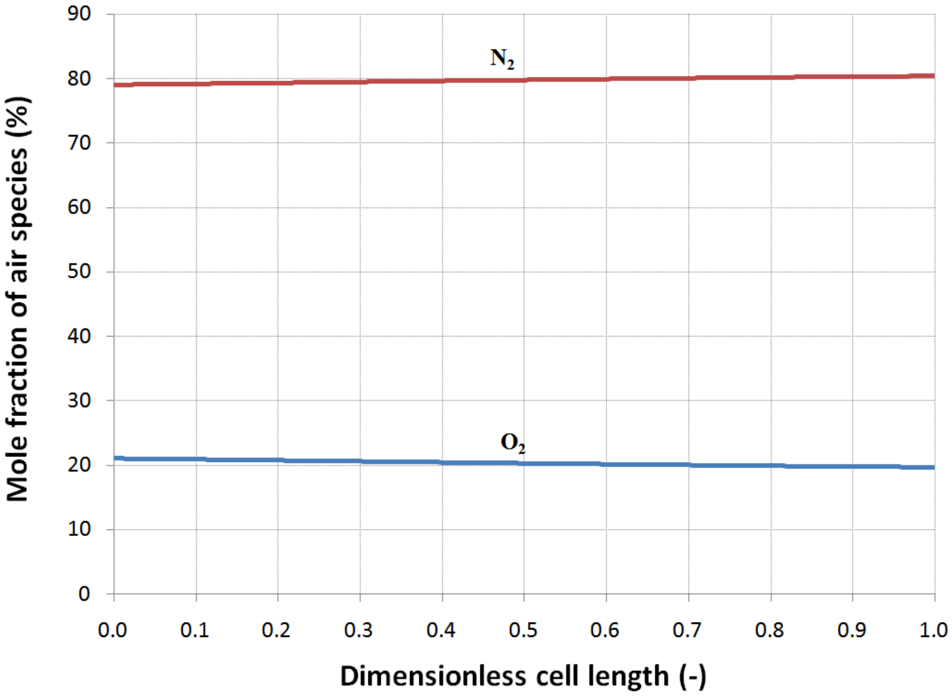

Figure 4.18: Distribution of the mole fraction of air species along the length of the cell.

4.4.1.5 Mass Flow Rate and Velocity of the Fuel and Air Streams

Figure 4.19 shows the distribution of the mass flow rate and velocity of the air and fuel streams along the length of the cell. The mass flow rate of the air stream decreases linearly with a slight slope along the air channel so that its value at the exit of the air channel is only 1.9% less than that at the entrance of the air channel. The mass flow rate of the fuel stream increases linearly along the fuel channel, and it has the same slope at which the flow rate of the air stream decreases. Of course, the fuel flow rate at the exit of the fuel channel is ≈86% higher than that at the entrance of the fuel channel. The mean velocities of the fuel and air streams increase along the length of the cell so that their values at the exit of the channels increase ≈15% and ≈10%, respectively, compared to the fuel and air velocities at the entrance of the channels.

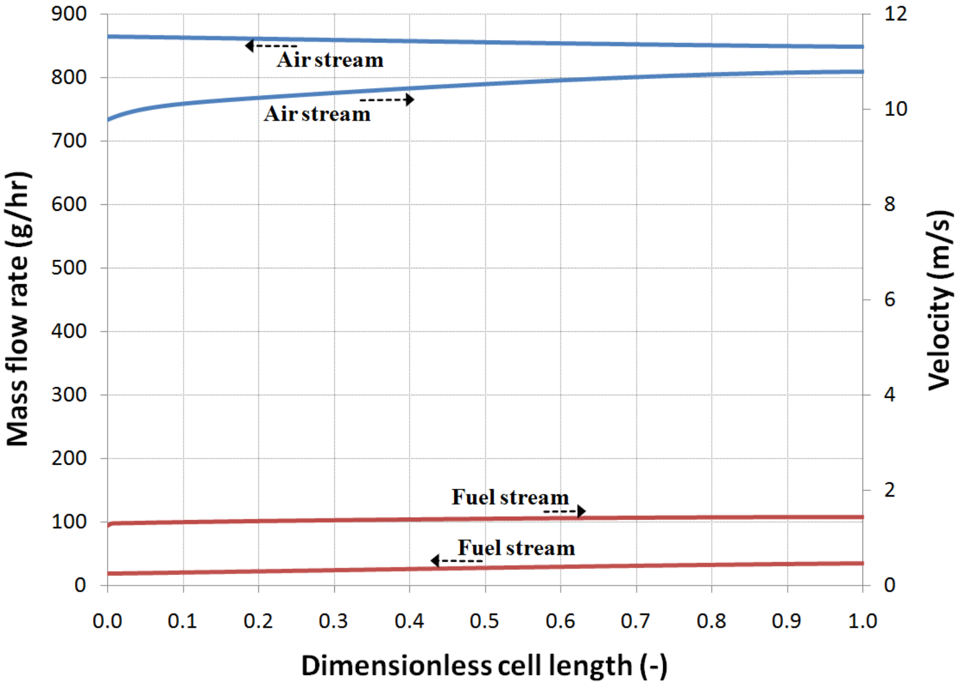

Figure 4.19: Distribution of the mass flow rate and velocity of the fuel and air streams along the length of the cell.

4.4.1.6 Power Densities

Figure 4.20 illustrates the distribution of the total power density, $W"_{local,tot} = W"_{local,H_2} + W"_{local,CO}$, and the power densities generated due to H_2, $W"_{local,H_2}$, and CO, $W"_{local,CO}$, electrochemical reactions along the length of the cell. The results indicate that the minimum local total power density with the value of 0.243 W/cm^2 and the minimum power densities corresponding to the H_2 and CO electrochemical reactions with values of 0.185 W/cm^2 and 0.058 W/cm^2, respectively, occur at y=L. The maximum local total power density with the value of 0.44 W/cm^2 also occurs at y≈0.28L; however, the maximum local power densities corresponding to the H_2 and CO electrochemical reactions with values of 0.318 W/cm^2 and 0.14 W/cm^2 occur at y≈0.36L and y=0, respectively. As a remarkable result, the ratio of the local power densities generated due to the H_2 and CO electrochemical reactions ($W"_{loccal,H_2}/W"_{local,CO}$) increases along the length of the cell. Indeed, the contribution of the H_2 electrochemical reaction in the local total power density reaches from 68% at y=0 to 76% at y=L. The mean total power density generated in the cell is predicted to be 0.39 W/cm^2, 73% of which is contributed from H_2 and the remaining is from the CO electrochemical reaction.

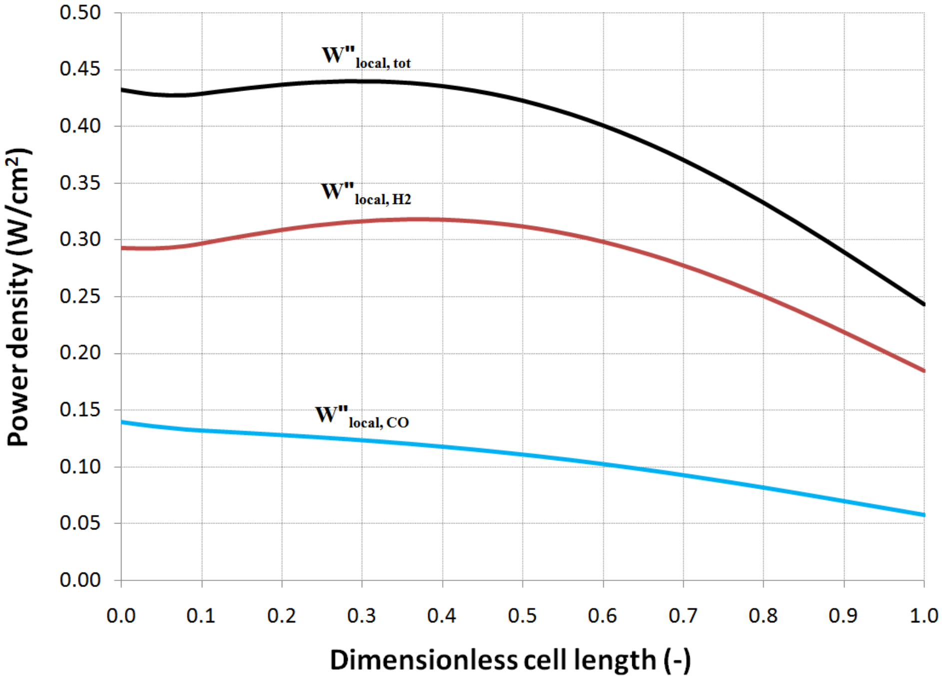

Figure 4.20: Distribution of the total power density and power densities due to H_2 and CO electrochemical reactions along the length of the cell.

4.4.1.7 Polarization Resistances

Figure 4.21 illustrates the distribution of the total cell polarization resistance along the length of the cell. The total cell polarization resistance varies approximately as a concave upward parabolic curve along the length of the cell with the maximum value of ≈0.617 Ω cm^2 that occurs at y=0 and the minimum value of ≈0.329 Ω cm^2 that occurs at y≈0.76L. The value of ≈0.416 Ω cm^2 can be also predicted for the mean total cell polarization resistance. The contributions of the anode, cathode, electrolyte, and interconnect in the total local polarization resistance are also shown in Figure 4.21. The anode has the highest contribution with a mean value of ≈0.241 Ω cm^2, followed by the cathode with a mean value of ≈0.167 Ω cm^2, the electrolyte with a mean value of ≈0.008 Ω cm^2, and the interconnect with a negligible value. The local anode polarization resistance varies approximately as a concave upward parabolic curve along the length of the cell with the maximum value of ≈0.396 Ω cm^2 that occurs at y=0 and the minimum value of ≈0.188 Ω cm^2 that occurs at y≈0.72L. The local cathode polarization resistance decreases from ≈0.210 Ω cm^2 at y=0 to ≈0.131 Ω cm^2 at y≈0.92L and then increases slightly. The local polarization resistance of the electrolyte also decreases along the length of the cell; however, its value is negligible where y>0.6L.

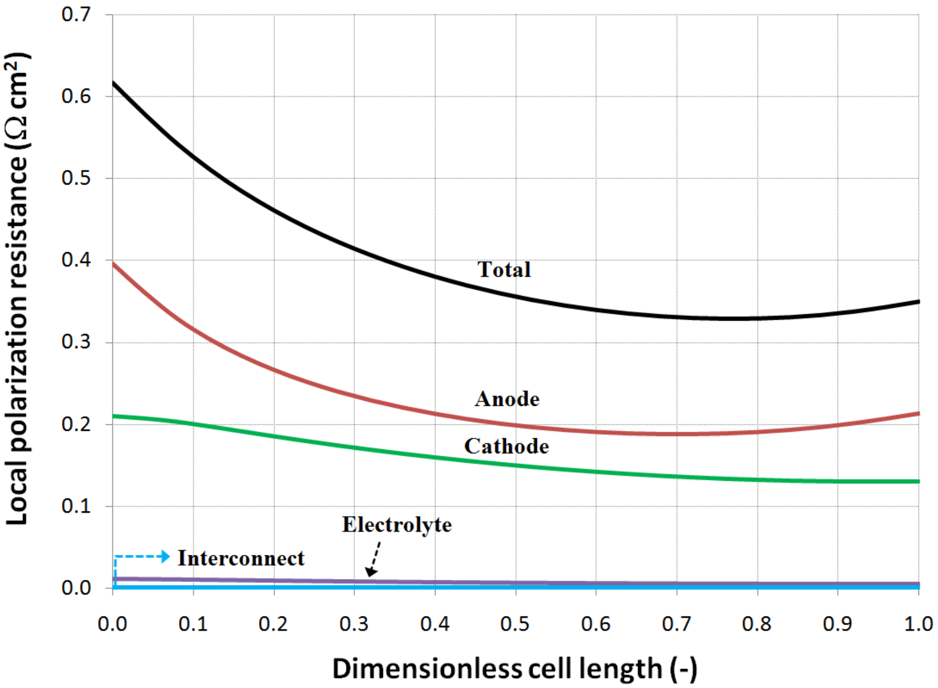

Figure 4.21: Distribution of the total polarization resistance and polarization resistances of the anode, cathode, electrolyte, and interconnect along the length of the cell.

4.4.1.8 Exergy Destruction Densities

The distribution of the total exergy destruction density along the length of the cell is shown in Figure 4.22. From a maximum value of 898 W/m^2 at y=0, the value of the total exergy destruction decreases sharply where y<0.1L. This is due to the relatively high temperature difference between the air stream and the solid structure. This value then decreases almost linearly along the length of the cell and achieves a minimum value of 121 W/m^2 at y=L. A value of ≈363 W/m^2 is predicted for the mean total exergy destruction density of the cell. Also revealed in Figure 4.22 is the exergy destruction in the solid structure, air stream, and fuel stream. The exergy destruction in the solid structure decreases almost linearly along the length of the cell. However, the exergy destruction in the air and fuel streams reduces sharply where y<0.1L and y<0.03L, respectively; and then remains constant along the length of the cell. The solid structure has the main contribution to the total exergy destruction with a mean value of 331 W/m^2; it is followed by the air stream with a mean value of 29 W/m^2 and by the fuel stream with a mean value of 3 W/m^2.

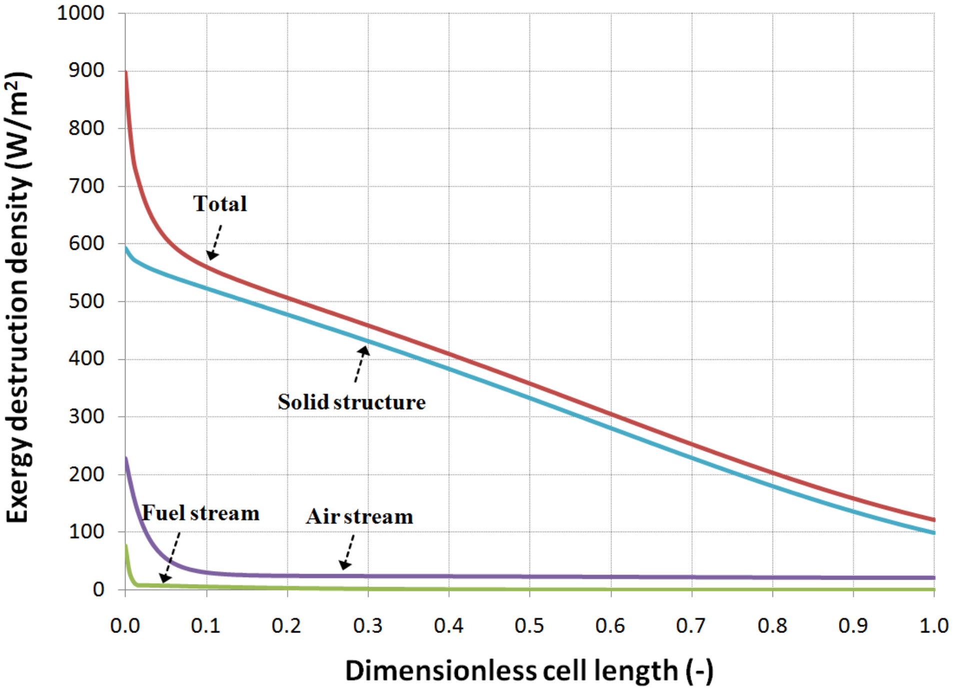

Figure 4.22: Distribution of the total exergy destruction density and the exergy destruction densities in the solid structure, air stream, and fuel stream along the length of the cell.

4.4.2 Distribution of Physical, Chemical, and Electrochemical Variables along the Cell Thickness

4.4.2.1 Partial Pressure of Oxygen in Cathode

Figure 4.23 shows the distribution of the local partial pressure of oxygen along the thickness of the cathode at the beginning, middle, and end of the cell length. The results indicate that the local partial pressure of oxygen decreases with a slight slope along the cathode thickness from the cathode and interconnect interface to the cathode and electrolyte interface. At the beginning, middle, and end of the air channel, the partial pressure of oxygen in the bulk air stream decreases only about 9.6%, 9.4%, and 5.3%, respectively, at the interface of the cathode and electrolyte.

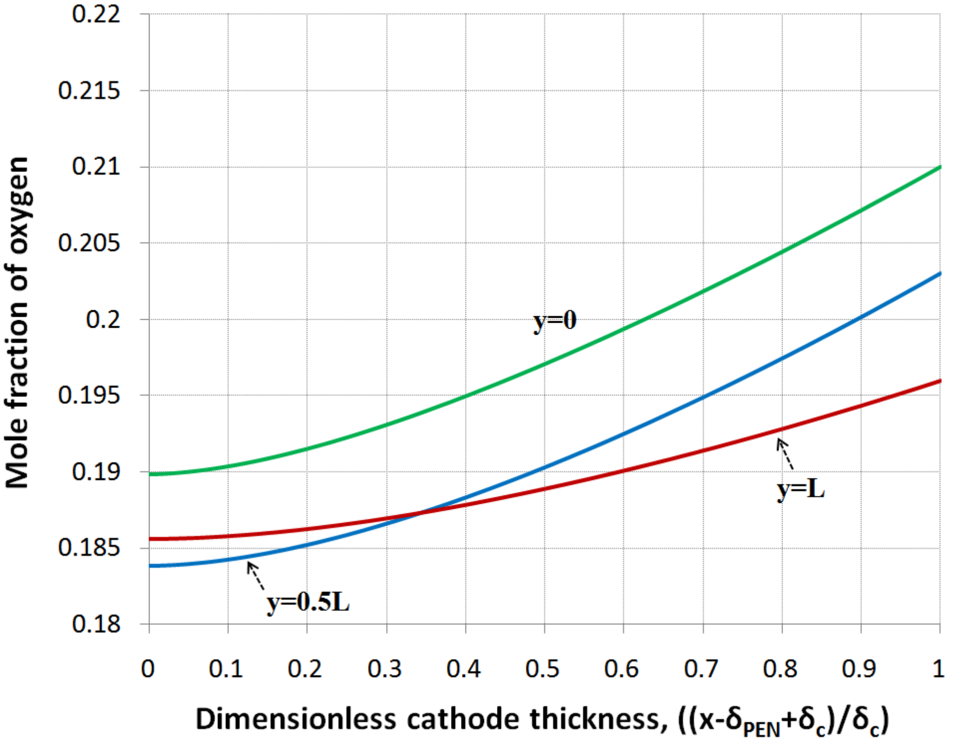

Figure 4.23: Distribution of the local oxygen partial pressure along the thickness of the cathode, $((\delta_{PEN}-\delta_C)<x<\delta_{PEN})$.

4.4.2.2 Current Density in Cathode

Figure 4.24 shows the distribution of the local current density along the thickness of the cathode at the beginning, middle, and end of the cell length. The consumption of electric current increases along the cathode thickness from the interface of the cathode and interconnect to the interface of the cathode and electrolyte. At the beginning of the cell length, more than 45% of the electric current is consumed within 20% of the cathode thickness near the cathode and electrolyte interface. This means that more than 45% of the oxygen electroreduction reaction takes place within 20% of the cathode near the interface of the cathode and electrolyte. Moreover, less than 10% of the electric current is consumed within 20% of the cathode thickness near the interface of the cathode and interconnect. At the end of the cell length, less than 35% and more than 12% of the electric current is consumed within 20% of the cathode thickness near the interfaces of the cathode and electrolyte and the cathode and interconnect, respectively.

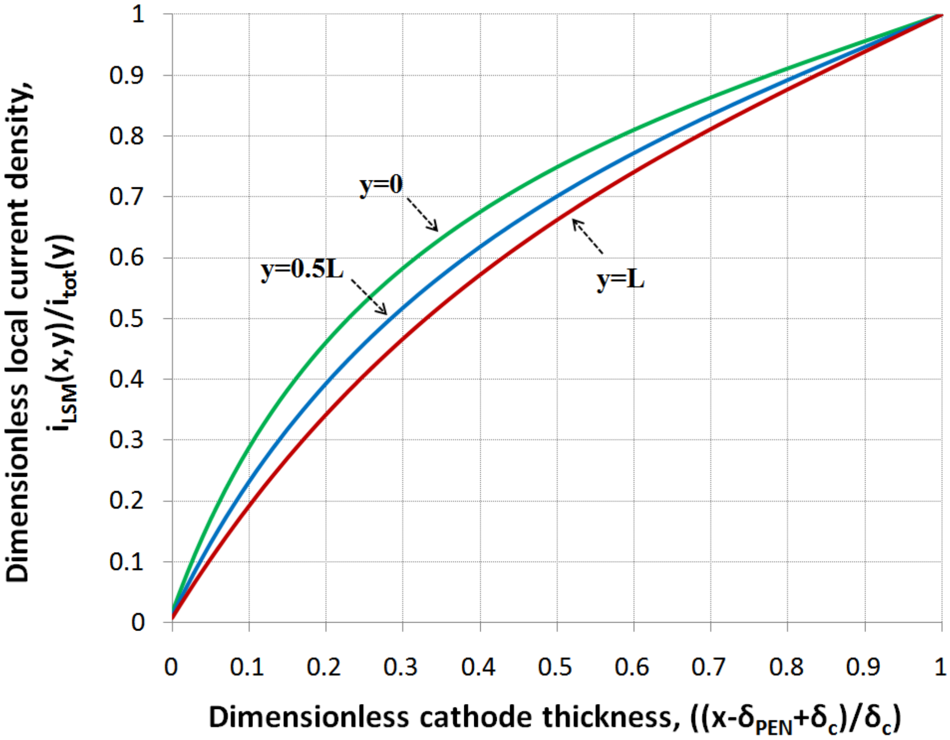

Figure 4.24: Distribution of the local current density along the thickness of the cathode, $((\delta_{PEN}-\delta_C)<x<\delta_{PEN})$.

4.4.2.3 Polarization in Cathode

Figure 4.25 shows the distribution of the local cathode polarization along the thickness of the cathode at the beginning, middle, and end of the cell length. The local cathode polarization increases along the cathode thickness from the interface of the cathode and interconnect to the interface of the cathode and electrolyte. The increase in the local polarization is negligible at the interface of the cathode and interconnect, and it reaches the maximum value at the interface of the cathode and electrolyte.

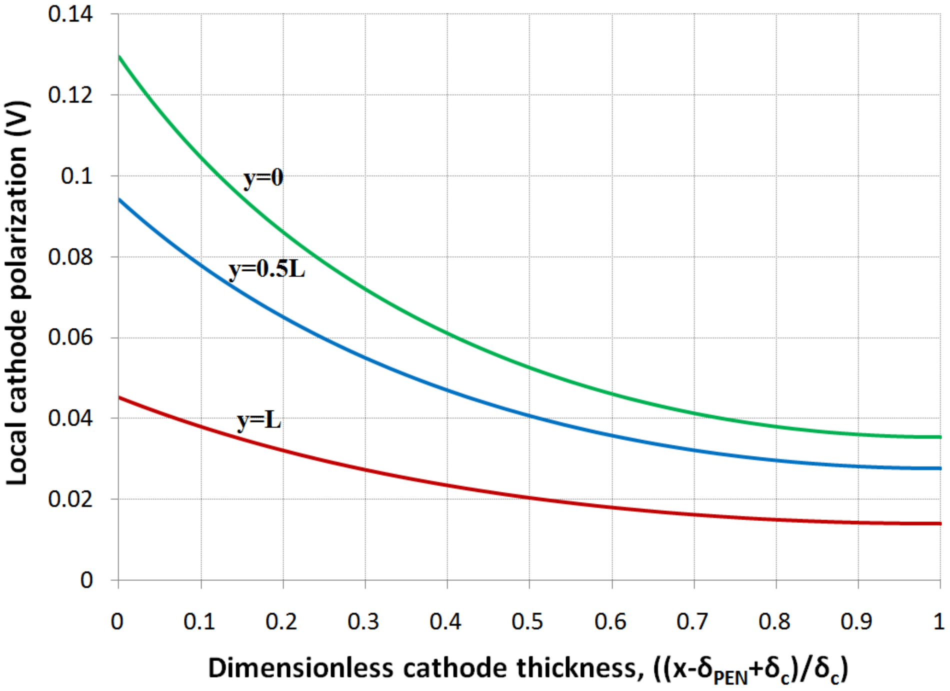

Figure 4.25: Distribution of the local cathode polarization along the thickness of the cathode, ((δ_{PEN}-δ_C)<x<δ_{PEN}).

4.4.2.4 Mole Fraction of H_2, CO, H_2O, and CO_2 in Anode

Figure 4.26 shows the distribution of the mole fraction of H_2 and CO along the thickness of the anode at the beginning, middle, and end of the cell length. The mole fraction of H_2 and CO decreases linearly with a slight slope along the thickness of the anode substrate layer and decreases approximately as a concave upward parabolic curve along the thickness of the anode functional layer. The minimum mole fraction of H_2 and CO occurs at the interface of the anode and electrolyte. At the beginning, middle, and end of the fuel channel, the mole fraction of H_2 in the bulk fuel stream decreases about 4.0%, 6.3%, and 9.6% and the mole fraction of CO decreases about 7.5%, 10.3%, and 11.8% respectively, at the interface of the anode and electrolyte.

Figure 4.27 shows the distribution of the mole fraction of H_2O and CO_2 along the thickness of the anode at the beginning, middle, and end of the cell length. The mole fraction of H_2O and CO_2 increases in both the substrate and functional layers. At the beginning, middle, and end of the fuel channel, the mole fraction of H_2O in the bulk fuel stream increases about 116.1%, 10.8%, and 3.5% and the mole fraction of CO_2 increases about 81.5%, 7.0%, and 1.1% respectively, at the interface of the anode and electrolyte.

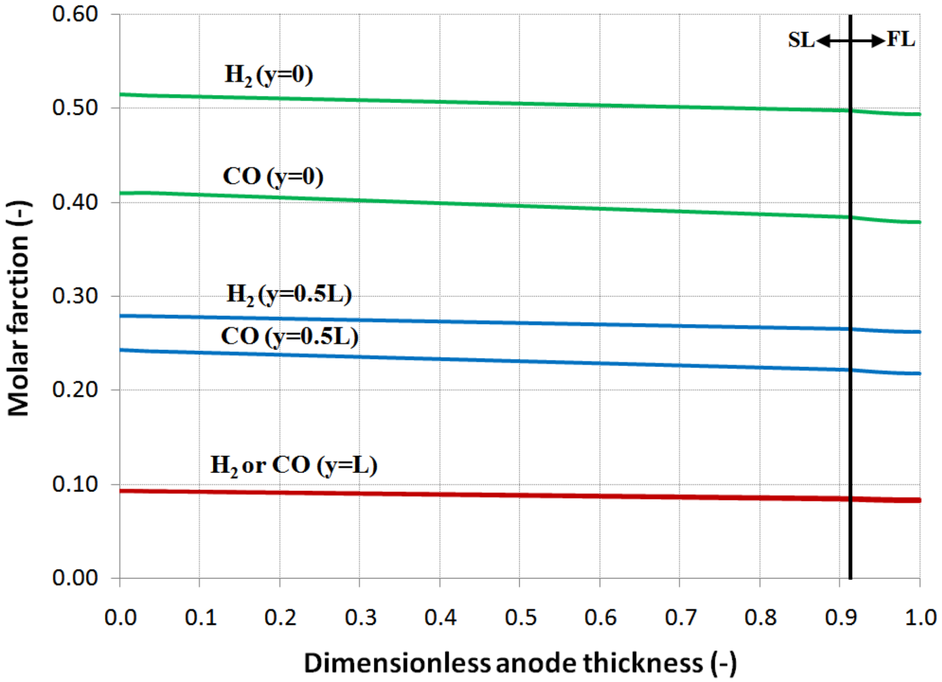

Figure 4.26: Distribution of the mole fraction of H_2 and CO along the thickness of the anode substrate (SL) and functional (FL) layers.

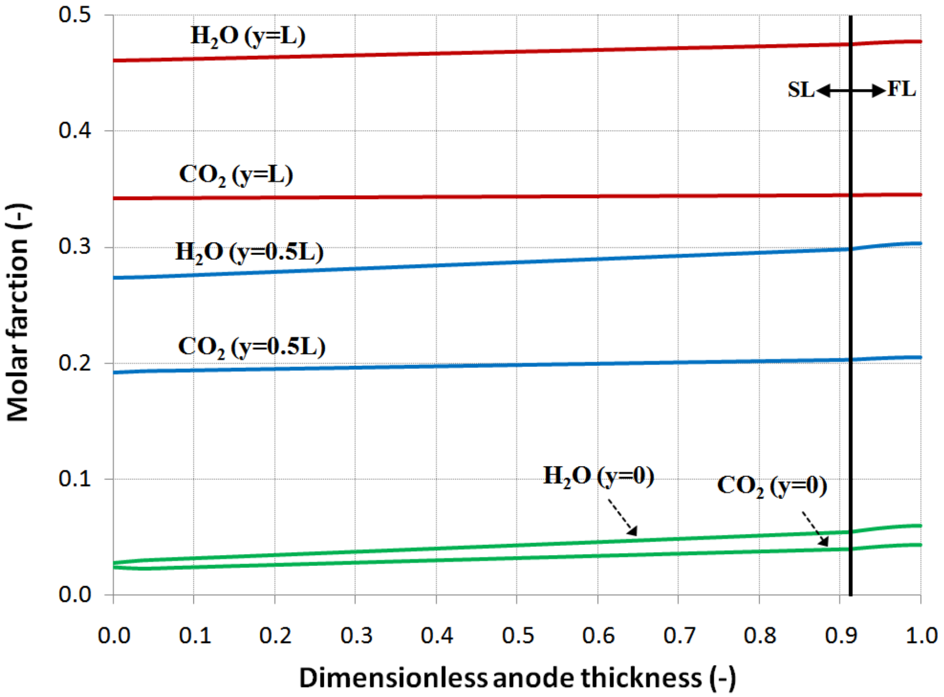

Figure 4.27: Distribution of the mole fraction of H_2O and CO_2 along the thickness of the anode substrate (SL) and functional (FL) layers.

4.4.2.5 Current Density in Anode

Figure 4.28 shows the distribution of the local current density along the thickness of the anode functional layer at the beginning, middle, and end of the cell length. The results indicate that the generation of electric current increases along the thickness of the anode functional layer. At the beginning of the cell length, more than 34% of the electric current is generated within 20% of the anode thickness near the interface of the anode and electrolyte. This means that more than 34% of the electroreduction reactions take place within 20% of the anode functional layer near the interface of the anode and electrolyte. Moreover, less than 13% of the electric current is generated within 20% of the thickness of the anode functional layer near the interface of the anode functional and substrate layers. At the end of the cell length, less than 28% and more than 15% of the electric current is generated within 20% of the anode thickness near the interfaces of the anode and electrolyte and the substrate and functional layers, respectively.

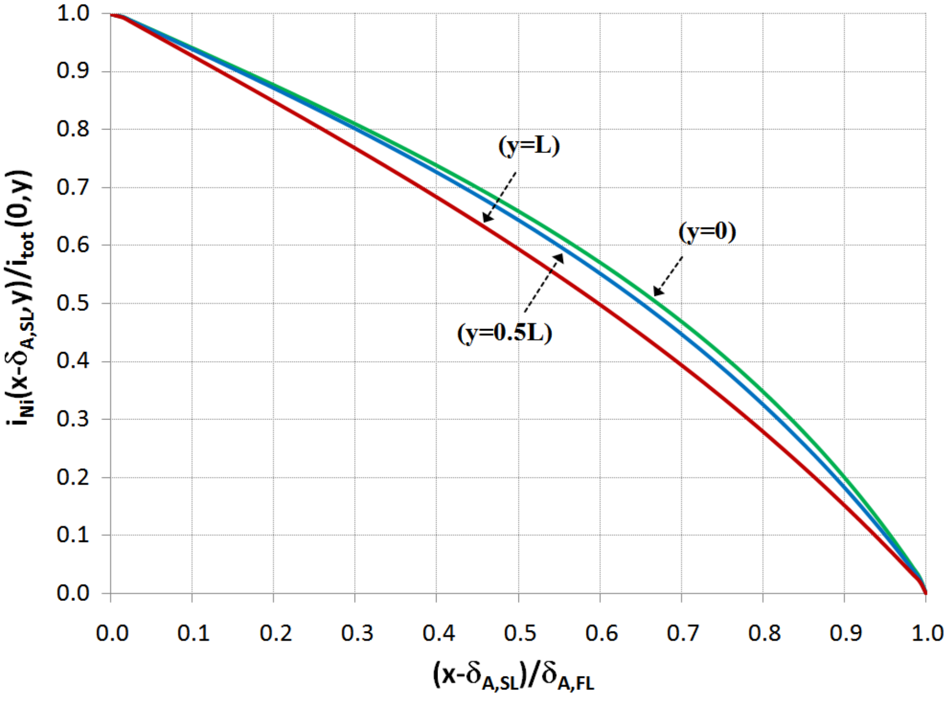

Figure 4.28: Distribution of the current density along the thickness of the anode functional layer, ($\delta_{A,SL}<x<(\delta_{A,SL}+\delta_{A,FL})$).

4.4.2.6 Polarization in Anode

Figure 4.29 shows the distribution of the polarization along the thickness of the anode functional layer at the beginning, middle, and end of the cell length. The local anode polarization increases along the thickness of the functional layer. The increase in the local polarization is negligible at the interface of the anode substrate and functional layers, and reaches the maximum value at the interface of the anode and electrolyte. This is due to the fact that the maximum electric current is generated at the interface of the anode and electrolyte where the transport length of ionic charges approaches zero.

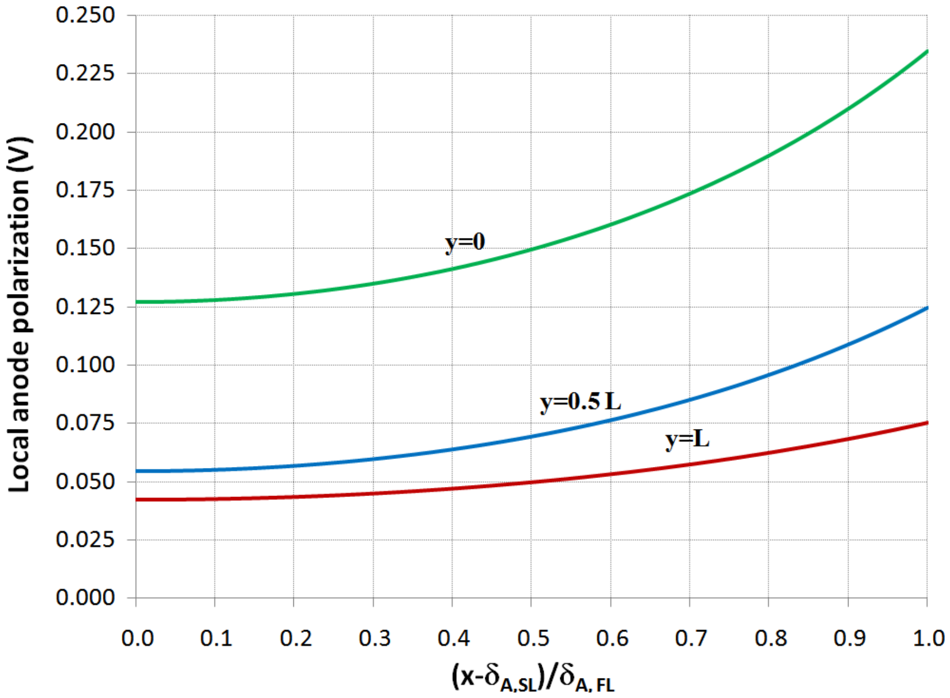

Figure 4.29: Distribution of the anode polarization along the thickness of the anode functional layer, ($\delta_{A,SL}<x<(\delta_{A,SL}+\delta_{A,FL})$).

4.4.3 Effect of the Microstructure of Porous Composite Electrodes on the Cell Performance

The microstructure of porous composite electrodes significantly affects the activation polarization due to the change of the active sites for electrochemical reactions, the ohmic polarization due to the change of the effective electronic and ionic resistivities, and the concentration polarization due to the change of the electrode pore size. Therefore, the cell performance is strongly dependent on the design of the microstructure of these electrodes. To study the effect of the microstructure of porous composite electrodes on the cell performance, several anode-supported co-flow planar cells with various microstructures of electrodes were simulated on the basis of the cell combined micro- and macro-model. Table 4.4 was used as a reference for the design and operating parameters of the cells studied. The gas obtained from processing biogas by the AGR method at temperature of 1073.15 K and pressure of 1 atm was also used as the inlet fuel to the cells studied. The composition of this gas is listed in Table 4.3.

4.4.3.1 Polarization Resistances

The mean total polarization resistance and the mean polarization resistances corresponding to the anode, cathode, electrolyte, and interconnect may change significantly by varying the microstructure of electrodes. The effect of the microstructural variables of the porous composite electrodes on these mean polarization resistances is studied in this section.

4.4.3.1.1 Ni Volume Fraction and Particle Size Ratio in the Anode Functional Layer

The effect of the Ni volume fraction in the anode functional layer on the mean total polarization resistance is shown in Figure 4.30. As seen in this figure, with an increase in the Ni volume fraction from its percolation threshold, the mean total polarization resistance decreases to a certain value and then increases. Therefore, there is an optimum Ni volume fraction in the anode functional layer at which the mean total polarization resistance is minimized. Our studies confirm that there is always such an optimum Ni volume fraction that minimizes the mean total polarization resistance. The effect of the particle size ratio of the anode functional layer is also shown in Figure 4.30. Among the optimum Ni volume fractions obtained at different particle size ratios, the one associated with the particle size ratio of unity provides the lowest mean total polarization resistance. This can be generalized to any anode microstructure and operating conditions. Indeed, for an anode functional layer with an optimum Ni volume fraction the optimum particle size ratio is always equal to 1. At the particle size ratio of unity, the mean total polarization resistance of the cell studied is minimized at the Ni volume fraction of ≈0.44.

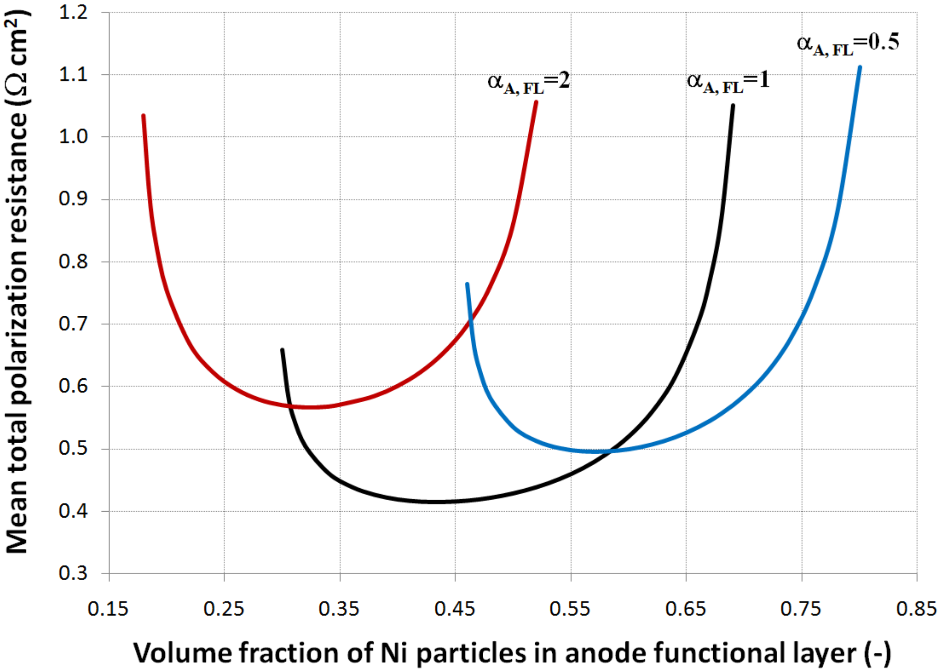

Figure 4.30: Effect of the Ni volume fraction in the anode functional layer at the particle size ratios of 0.5, 1 and 2 on the mean total polarization resistance.

The effect of the Ni volume fraction in the anode functional layer at the particle size ratio of unity on the mean polarization resistances of the anode, cathode, electrolyte, and interconnect is shown in Figure 4.31. With an increase in the volume fraction of Ni from its percolation threshold, the anode mean polarization resistance decreases to a certain value and then increases. Therefore, there is an optimum Ni volume fraction at which the anode mean polarization resistance is minimized. This optimum value for the cell studied at the particle size ratio of unity is predicted to be ≈0.44. For the particle size ratios greater than unity, this optimum Ni volume fraction is not in the range of $[(3.38\alpha_{A,FL}+2.4)/(2.4\alpha^2_{A,FL}+6.76\alpha_{A,FL}+2.4),\ 1/(\alpha_{A,FL}\ /2.4+1)]$. This occurs because the increase in the Ni volume fraction in this range decreases the electrochemical active area and pore size and increases the effective resistivity of YSZ. Consequently, all three activation, concentration, and ohmic polarizations in the anode functional layer increase. This would be valid for particle size ratios of less than unity if the pore size is not too small to inhibit the fuel species transport from the bulk to the active sites of the anode.

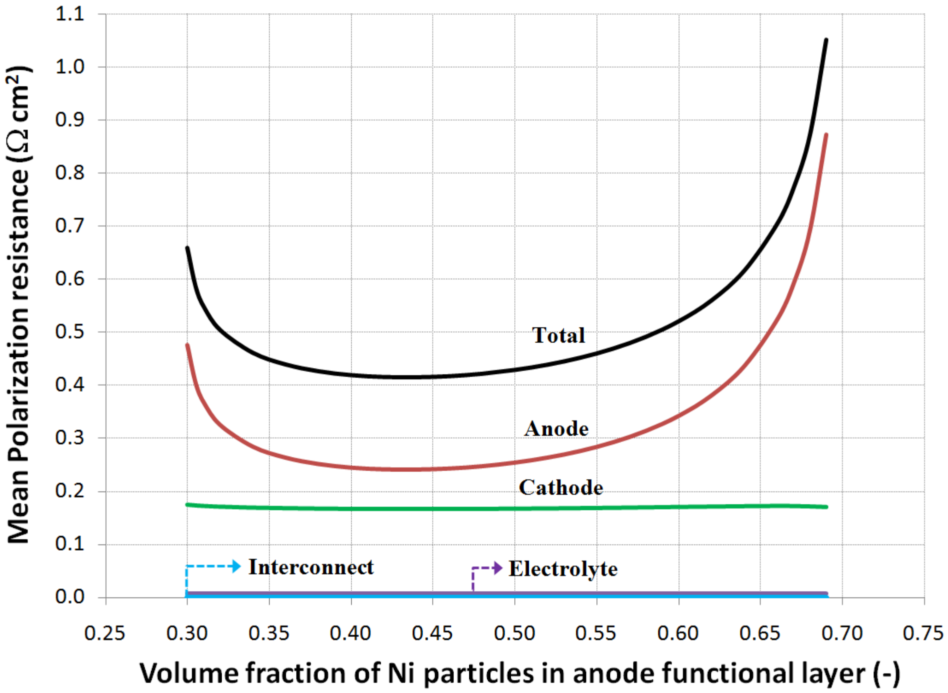

Figure 4.31: Effect of the Ni volume fraction in the anode functional layer at particle size ratio of unity on the mean total polarization resistance and mean polarization resistances of the anode, cathode, electrolyte, and interconnect.

At the particle size ratio of unity, varying the Ni volume fraction in the anode functional layer of the cell studied from 0.3 to 0.69 can affect the mean total polarization resistance up to 0.636 Ω cm^2 and the mean polarization resistances of the anode and cathode up to 0.633 Ω cm^2 and 0.01 Ω cm^2, respectively. Therefore, the cathode mean polarization resistance is a weak function of the Ni volume fraction in the anode functional layer. The change in the mean polarization resistances of the electrolyte and interconnect is negligible.

4.4.3.1.2 Size of Ni Particles in the Anode Functional Layer

The effect of the size of the Ni particles in the anode functional layer on the mean total polarization resistance and the mean polarization resistances of the anode, cathode, electrolyte, and interconnect is shown in Figure 4.32. In the range of the Ni particles sizes investigated, the mean total and anode polarization resistances decrease with a decrease in the size of Ni particles. However, because the contribution of the anode concentration polarization may become significant for particles smaller than 0.1 µm in diameter, the mean total and anode polarization resistances may increase by reducing the size of particles to less than 0.1 μm. Therefore, there may be an optimum size for the Ni particles in the anode functional layer at which the total and anode mean polarization resistances are minimized. However, using Ni particles in the range of 0.1 μm may decrease these mean polarization resistances because the anode may be vulnerable to degradation due to an extensive grain growth of particles during the sintering process and the operation of the cell [127]. The grain growth significantly reduces the electrochemical active area and leads to a decrease in the power density. This may necessitate the optimum size of the Ni particles to be selected by durability analysis rather than the combined micro- and macro model.

The studies point out that varying the size of Ni particles in the anode functional layer of the cell studied from 0.1 μm to 5 μm can affect the mean total polarization resistance up to 0.547 Ω cm^2 and the mean polarization resistances of the anode and cathode up to 0.524 Ω cm^2 and 0.025 Ω cm^2, respectively. Therefore, the cathode mean polarization resistance is a weak function of the size of Ni particles in the anode functional layer. The change in the mean polarization resistances of the electrolyte and interconnect is also predicted to be negligible.

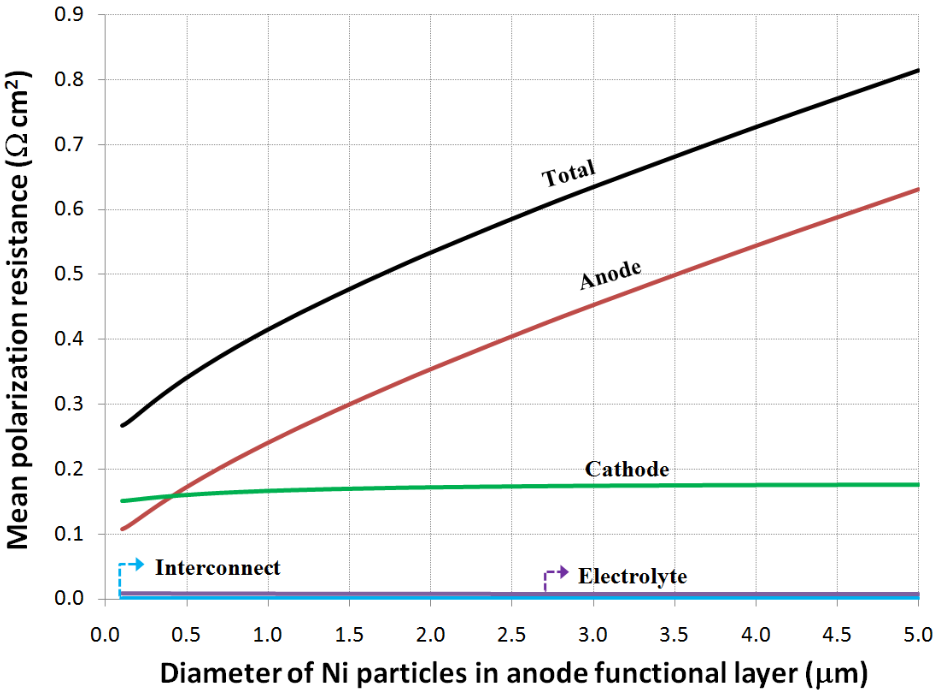

Figure 4.32: Effect of the size of Ni particles in the anode functional layer on the mean total polarization resistance and mean polarization resistances of the anode, cathode, electrolyte, and interconnect.

4.4.3.1.3 Thickness of the Anode Functional Layer

The effect of the thickness of the anode functional layer on the mean total polarization resistance and mean polarization resistances of the anode, cathode, electrolyte, and interconnect is shown in Figure 4.33. With an increase in the thickness of the anode functional layer, the mean total and anode polarization resistances decrease to a certain value and then increase linearly with a slight slope. Therefore, there is an optimum value for the thickness of the anode functional layer at which the mean total and anode polarization resistances are minimized. This optimum thickness for the cell studied is predicted to be ≈85 μm; however, the increase in these polarization resistances is negligible if the thickness decreases to even around 45 μm. This trend makes sense because for thin anode functional layers the activation polarization significantly increases due to the insufficient active sites for the H_2 and CO electrooxidation reactions. For thick functional layers, the contribution of ohmic and concentration polarizations becomes significant due to the increase in the mass and charge transport lengths.

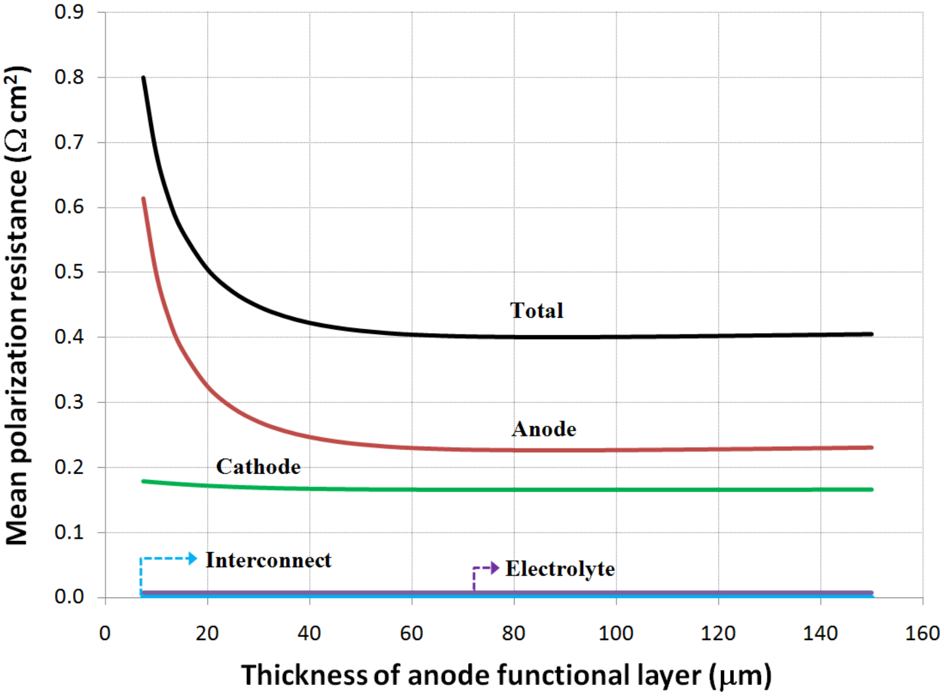

Figure 4.33: Effect of the thickness of the anode functional layer on the mean total polarization resistance and mean polarization resistances of the anode, cathode, electrolyte, and interconnect.

The studies show that varying the thickness of the anode functional layer of the cell studied from 5 μm to 150 μm can affect the mean total polarization resistance up to 0.625 Ω cm^2 and the mean polarization resistances of the anode and cathode up to 0.611 Ω cm^2 and 0.015 Ω cm^2, respectively. Therefore, the cathode mean polarization resistance is a weak function of the thickness of the anode functional layer. The change in the mean polarization resistances of the electrolyte and interconnect is also negligible.

4.4.3.1.4 Porosity of the Anode Functional Layer

The effect of the porosity of the anode functional layer on the mean total polarization resistance and mean polarization resistances of the anode, cathode, electrolyte, and interconnect is shown in Figure 4.34. With a decrease in the porosity of the anode functional layer, the mean total and anode polarization resistances decrease to a certain value due to the decrease in the anode activation and ohmic polarizations, and then they increase due to a significant increase in the anode concentration polarization. Therefore, there is an optimum porosity at which the mean total and anode polarization resistances are minimized. The optimum porosity for the cell studied is predicted to be ≈0.19. For a random-packing of spherical particles with a given size, the porosity cannot be less than a certain value if the average contact angle between the particles is not increased during the sintering process. In such a situation, if the low porosity of 0.19 is not achievable, the minimum possible porosity can be selected for the anode functional layer.

The studies indicate that varying the porosity of the anode functional layer of the cell studied from 0.13 to 0.6 can affect the mean total polarization resistance up to 0.201 Ω cm^2 and the mean polarization resistances of the anode and cathode up to 0.194 Ω cm^2 and 0.007 Ω cm^2, respectively. Therefore, the mean polarization resistance of the cathode is a weak function of the porosity of the anode functional layer. The change in the mean polarization resistances of the electrolyte and interconnect is also negligible.

4.4.3.1.5 Size of Ni Particles in the Anode Substrate Layer

The effect of the size of Ni particles in the anode substrate layer on the mean total polarization resistance and mean polarization resistances of the anode, cathode, electrolyte, and interconnect is shown in Figure 4.35. In the range of Ni particles sizes investigated, the mean total and anode polarization resistances decrease with an increase in the size of Ni particles. However, the value of the decrease in these polarization resistances is negligible for Ni particles larger than 1.5 μm in diameter. For the particles smaller than 0.5 μm, the anode concentration polarization becomes significant; therefore, the minimum size of 0.5 μm is suggested for Ni particles in the anode substrate layer.

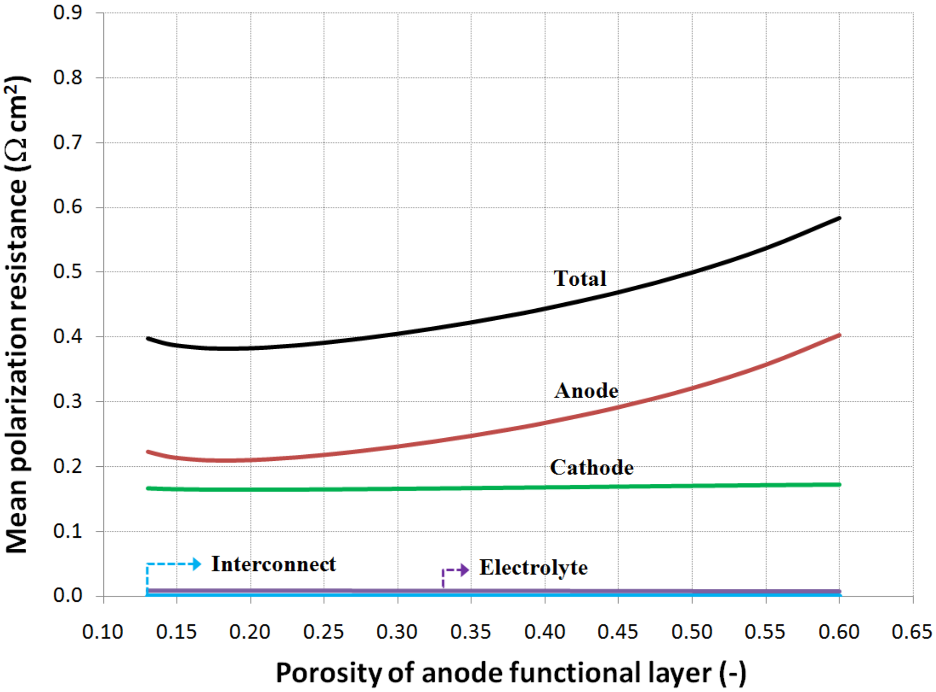

Figure 4.34: Effect of the porosity of the anode functional layer on the mean total polarization resistance and mean polarization resistances of the anode, cathode, electrolyte, and interconnect.

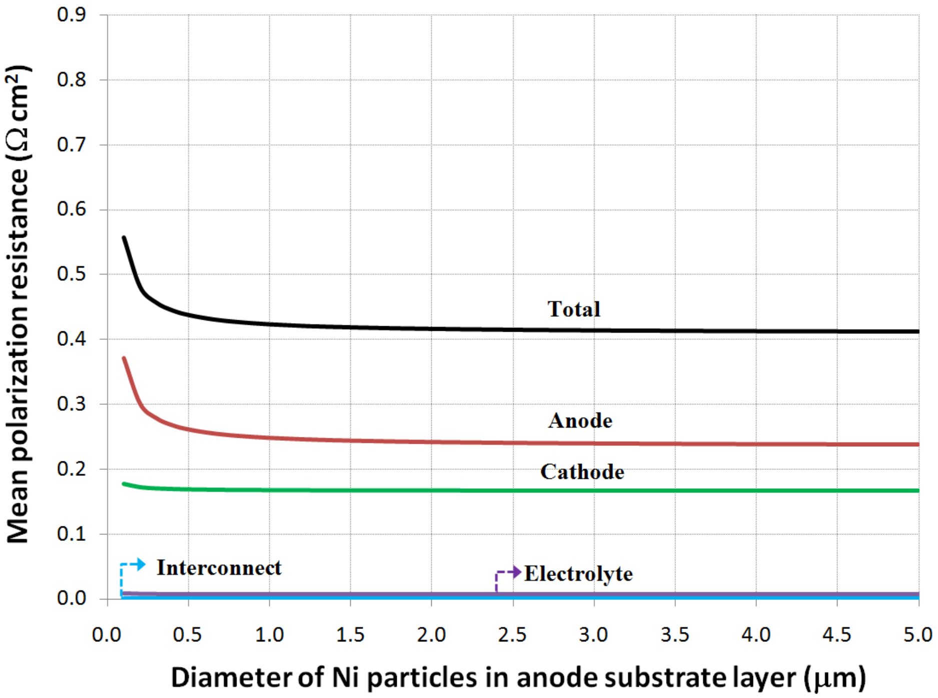

Figure 4.35: Effect of the size of Ni particles in the anode substrate layer on the mean total polarization resistance and mean polarization resistances of the anode, cathode, electrolyte, and interconnect.

An increase in the size of Ni particles in the anode substrate layer of the cell studied from 0.1 μm to 5 μm leads to a decrease of up to 0.144 Ω cm^2 in the mean total polarization resistance and 0.133 Ω cm^2 and 0.012 Ω cm^2 in the mean polarization resistances of the anode and cathode, respectively. Therefore, the cathode mean polarization resistance is a weak function of the size of Ni particles in the anode substrate layer. The change in the mean polarization resistances of the electrolyte and interconnect is also negligible.

4.4.3.1.6 Thickness of the Anode Substrate Layer

The effect of the thickness of the anode substrate layer on the mean total polarization resistance and mean polarization resistances of the anode, cathode, electrolyte, and interconnect is shown in Figure 4.36. In the range of the thicknesses investigated, with an increase in the thickness of the anode substrate layer, the mean total and anode polarization resistances increase linearly with a slight slope. An increase of from 50 μm to 1500 μm in this thickness increases the mean total polarization resistance up to ≈0.044 Ω cm^2 and the mean polarization resistances of the anode and cathode up to ≈0.038 Ω cm^2 and 0.004 Ω cm^2, respectively. Nevertheless, the minimum thickness required for the mechanical strength of the cell is suggested to be selected for the anode substrate layer. The effect of the thickness of the anode substrate layer on the mean polarization resistances of the electrolyte and interconnect is also negligible.

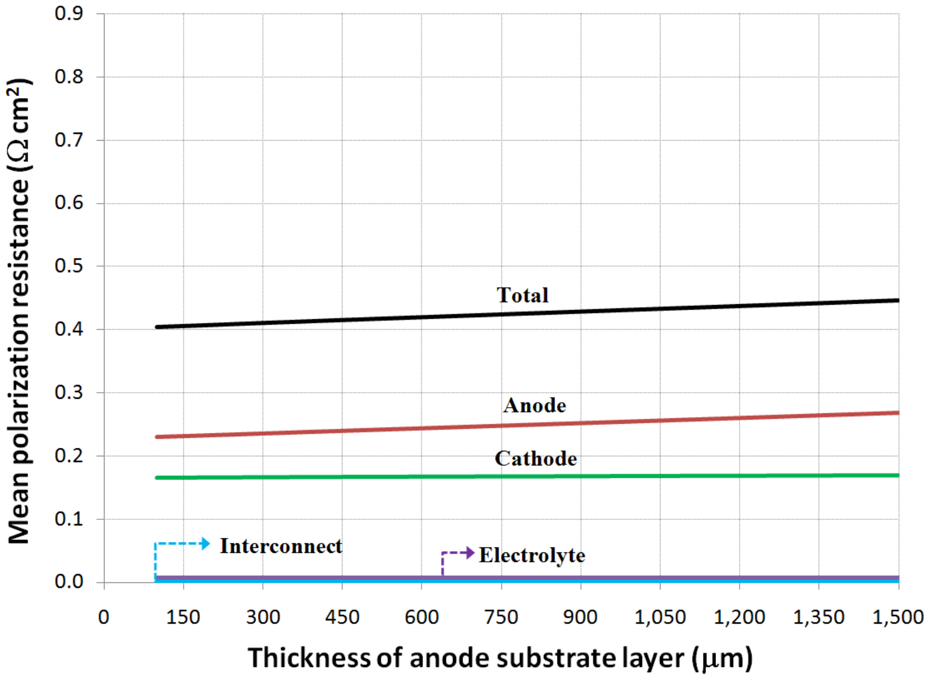

Figure 4.36: Effect of the thickness of the anode substrate layer on the mean total polarization resistance and mean polarization resistances of the anode, cathode, electrolyte, and interconnect.

4.4.3.1.7 Porosity of the Anode Substrate Layer

The effect of the porosity of the anode substrate layer on the mean total polarization resistance and mean polarization resistances of the anode, cathode, electrolyte, and interconnect is shown in Figure 4.37. In the range of the porosities investigated, the mean total and anode polarization resistances decrease with an increase in the porosity of the anode substrate layer; however, the value of this decrease is negligible for porosities greater than ≈0.5. For the porosities of less than ≈0.25, the decrease in the porosity leads to a significant increase in the mean total and anode polarization resistances due to the significant increase in the anode concentration polarization. An increase in this porosity from 0.13 to 0.6 leads to a decrease in the mean total polarization resistance of up to 0.477 Ω cm^2 and the mean polarization resistances of the anode and cathode up to 0.448 Ω cm^2 and 0.028 Ω cm^2, respectively. Therefore, the mean polarization resistance of the cathode is a weak function of the porosity of the anode substrate layer. The change in the mean polarization resistances of the electrolyte and interconnect is also negligible.

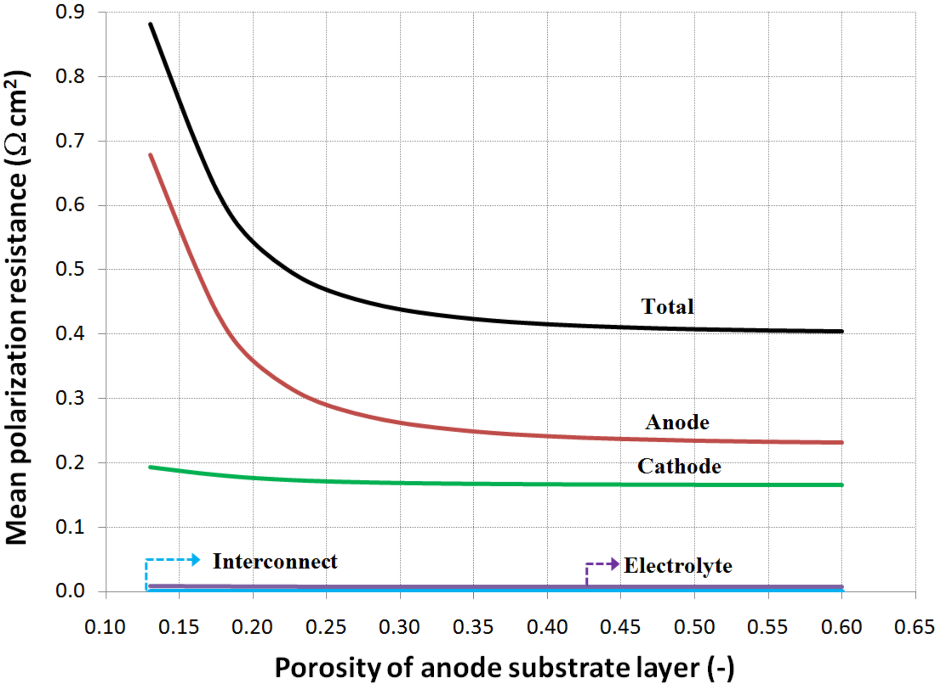

Figure 4.37: Effect of the porosity of the anode substrate layer on the mean total polarization resistance and mean polarization resistances of the anode, cathode, electrolyte, and interconnect.

4.4.3.1.8 LSM Volume Fraction and Particle Size Ratio of the Cathode

The effect of the LSM volume fraction in the cathode on the mean total polarization resistance is shown in Figure 4.38. As seen in this figure, with an increase in the volume fraction of LSM from its percolation threshold, the mean total polarization resistance decreases to a certain value and then increases. Therefore, there is an optimum LSM volume fraction in the cathode at which the mean total polarization resistance is minimized. The studies confirm that there is always such an optimum LSM volume fraction that minimizes the mean total polarization resistance.

The effect of the particle size ratio of the cathode is also shown in Figure 4.38. Among the optimum LSM volume fractions obtained at different particle size ratios, the one associated with the particle size ratio of unity provides the lowest mean total polarization resistance. The studies confirm that this can be generalized for any cathode microstructure and operating conditions of the cell. Indeed, for a cathode with an optimum LSM volume fraction, the optimum particle size ratio is always equal to 1. At the particle size ratio of unity, the mean total polarization resistance of the cell studied is minimized at the LSM volume fraction of ≈0.42.

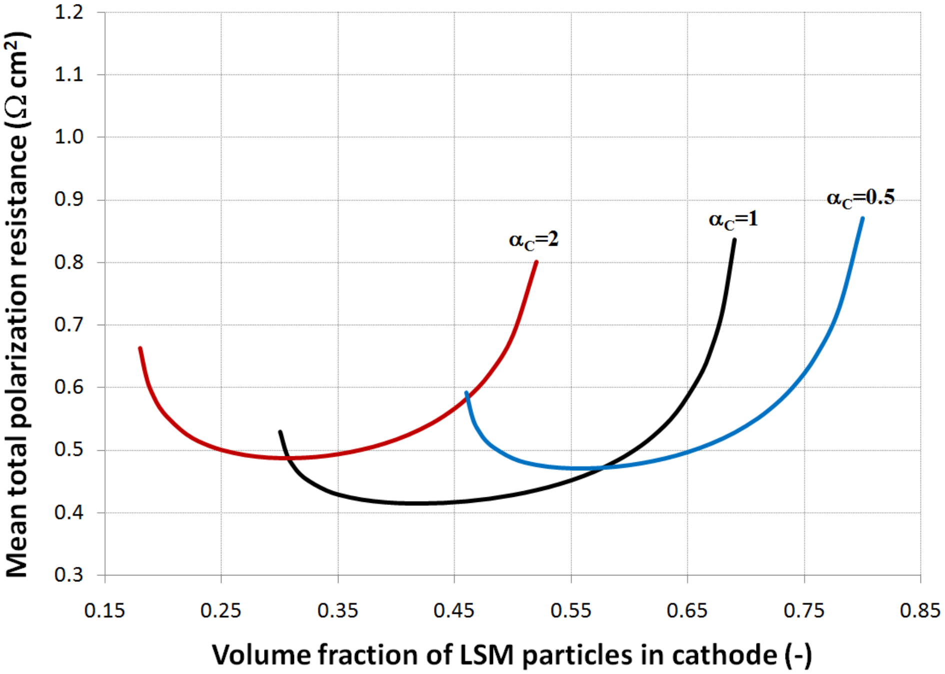

Figure 4.38: Effect of the volume fraction of LSM in the cathode at particle size ratios of 0.5, 1, and 2 on the mean total polarization resistance.

Figure 4.39 shows the effect of the LSM volume fraction in the cathode at the particle size ratio of unity on the mean polarization resistances of the anode, cathode, electrolyte, and interconnect. With an increase in the volume fraction of LSM, the cathode mean polarization resistance decreases to a certain value and then increases. Therefore, there is an optimum LSM volume fraction at which the mean polarization resistance of the cathode is minimized. This optimum value for the cell studied at the particle size ratio of unity is predicted to be ≈0.42. For particle size ratios greater than unity, this optimum volume fraction is not in the range of $[(3.38\alpha_C+2.4)/(2.4\alpha_C^2+6.76\alpha_C+2.4),\ 1/(\alpha_C/2.4+1)]$, because with an increase in the volume fraction of LSM in this range, the electrochemical active area and pore size decrease and the effective resistivity of YSZ increases. Consequently, all three activation, concentration, and ohmic polarizations in the cathode increase. This would be valid for particle size ratios less than unity if the cathode pore size is not too small to inhibit the oxygen transport from the bulk to the active sites of the cathode.

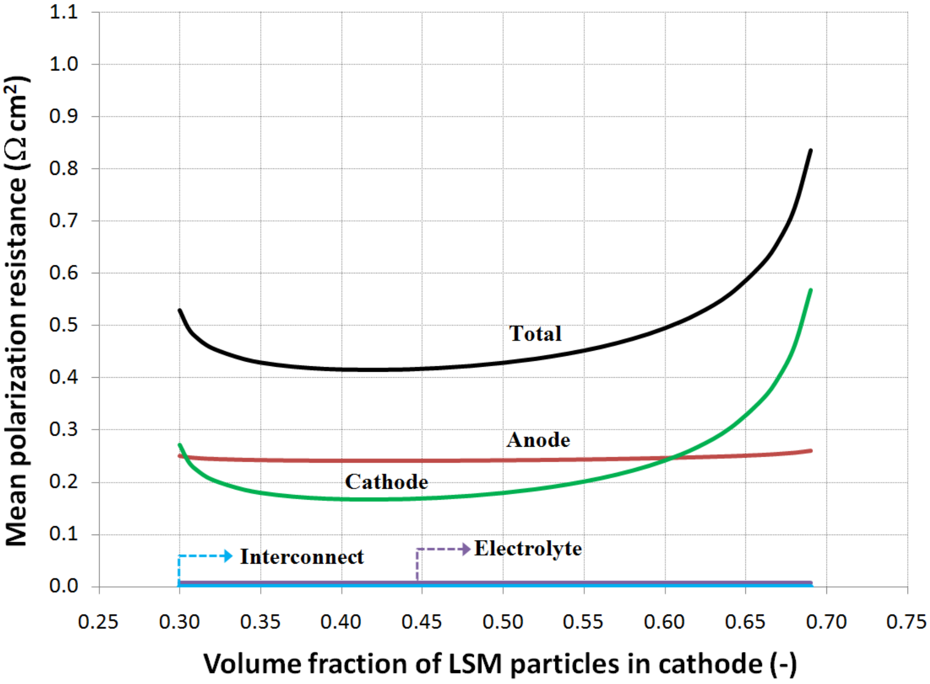

Figure 4.39: Effect of the volume fraction of LSM in the cathode at the particle size ratio of unity on the mean total polarization resistance and the mean polarization resistances of the anode, cathode, electrolyte, and interconnect.

The studies show that at the particle size ratio of unity, varying the LSM volume fraction in the cathode of the cell studied from 0.3 to 0.69 can affect the mean total polarization resistance up to 0.421 Ω cm^2 and the mean polarization resistances of the anode and cathode up to 0.019 Ω cm^2 and 0.403 Ω cm^2, respectively. Therefore, the anode mean polarization resistance is a weak function of the LSM volume fraction in the cathode. The change in the mean polarization resistances of the electrolyte and interconnect is also predicted to be negligible.

4.4.3.1.9 Size of LSM Particles in the Cathode

The effect of the size of LSM particles in the cathode on the mean total polarization resistance and mean polarization resistances of the anode, cathode, electrolyte, and interconnect is illustrated in Figure 4.40. As seen in this figure, with a decrease in the size of the LSM particles, the mean total and cathode polarization resistances decrease to a certain value and then increase. Therefore, there is an optimum size for the LSM particles at which the mean total and cathode polarization resistances are minimized. It is noted that for the LSM particles size ratio of unity, with a decrease in the size of particles, the cathode activation polarization decreases due to the increase in the cathode electrochemical active area. Additionally, the cathode concentration polarization increases due to the decrease in the cathode average pore size, and the ohmic polarization remains constant because the effective resistivity of the LSM and YSZ are not a function of the size of particles. For the LSM particles larger than the optimum size, the contribution of the cathode activation polarization in the cathode mean polarization resistance is greater than that of the cathode concentration polarization. Therefore, the mean polarization resistance of the cathode decreases with a decrease in the size of the LSM particles. For LSM particles smaller than the optimum size, the contribution of the cathode concentration polarization becomes more significant than that of the activation polarization; thus, the mean polarization resistance of the cathode increases with a decrease in the size of LSM particles. The optimum size of LSM particles for the cell studied is predicted to be ≈0.2 μm. Of course, employing the particles in this range may lead to an increase in the cathode mean polarization resistance due to the grain growth of the particles during the sintering process or the cell operation. Therefore, larger LSM particles may be selected for the cathode.

The studies point out that varying the size of LSM particles in the cathode of the cell studied from 0.1 μm to 5 μm can affect the mean total polarization resistance up to 0.254 Ω cm^2 and the mean polarization resistances of the anode and cathode up to 0.02 Ω cm^2 and 0.234 Ω cm^2, respectively. Therefore, the mean polarization resistance of the anode is a weak function of the size of LSM particles in the cathode. The change in the mean polarization resistances of the electrolyte and interconnect is also predicted to be negligible.

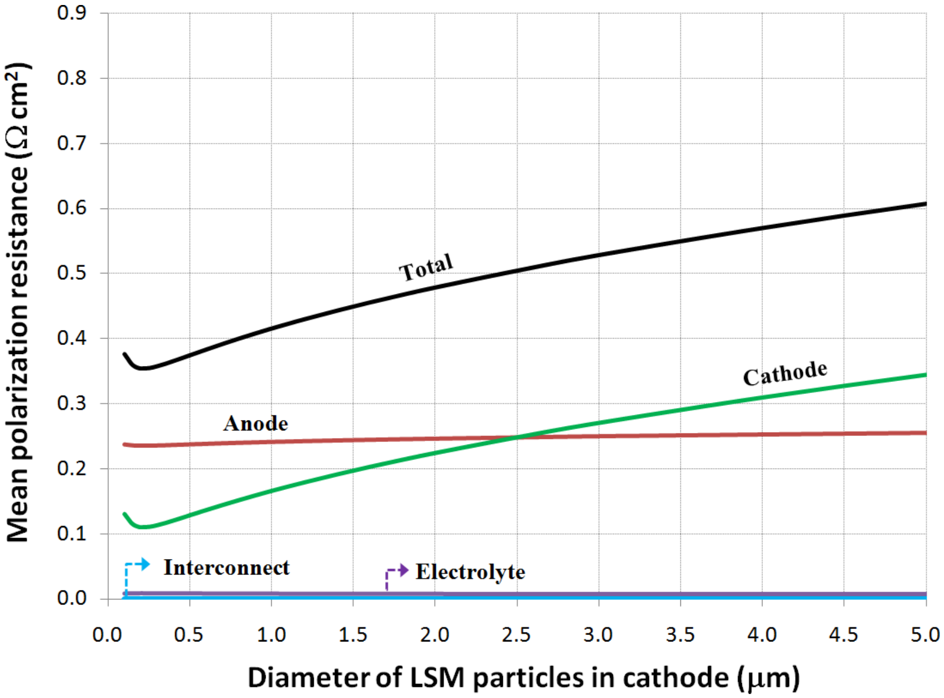

Figure 4.40: Effect of the size of LSM particles in the cathode on the mean total polarization resistance and mean polarization resistances of the anode, cathode, electrolyte, and interconnect.

4.4.3.1.10 Thickness of the Cathode

The effect of the cathode thickness on the mean total polarization resistance and mean polarization resistances of the anode, cathode, electrolyte, and interconnect is shown in Figure 4.41. With an increase in the cathode thickness, the mean total and cathode polarization resistances decrease to a certain value and then increase linearly with a slight slope. Therefore, there is an optimum value for the cathode thickness at which the mean total and cathode polarization resistances are minimized. This trend makes sense because for thin cathodes the cathode activation polarization significantly increases due to the insufficient active sites for the oxygen electroreduction reaction. For thick cathodes, the contribution of the cathode ohmic and concentration polarizations becomes significant due to the increase in the mass and charge transport lengths. The optimum cathode thickness for the cell studied is predicted to be ≈70 µm; however, the mean total and cathode polarization resistances increase negligibly if the thickness decreases to even around 45 µm.

Varying the cathode thickness of the cell studied from 5 µm to 150 µm can affect the mean total polarization resistance up to 0.274 Ω cm^2 and the mean polarization resistances of the anode and cathode up to 0.028 Ω cm^2 and 0.245 Ω cm^2, respectively. Therefore, the anode mean polarization resistance is a weak function of the cathode thickness. The change in the mean polarization resistances of the electrolyte and interconnect is also predicted to be negligible.

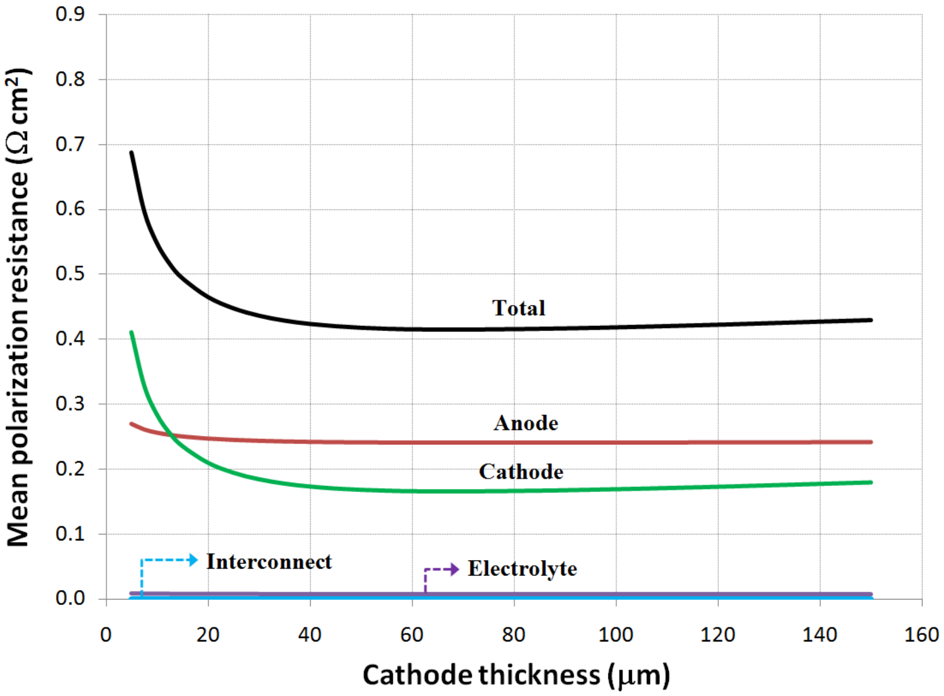

Figure 4.41: Effect of the cathode thickness on the mean total polarization resistance and mean polarization resistances of the anode, cathode, electrolyte, and interconnect.

4.4.3.1.11 Porosity of the Cathode

The effect of the cathode porosity on the mean total polarization resistance and mean polarization resistances of the anode, cathode, electrolyte, and interconnect is shown in Figure 4.42. With a decrease in the cathode porosity, the mean total and cathode polarization resistances decrease to a certain value due to the decrease in the cathode activation and ohmic polarizations, and then they increase due to a significant increase in the cathode concentration polarization. Therefore, there is a porosity at which the mean total and cathode polarization resistances are minimized. For the cell studied, the optimum cathode porosity is predicted to be ≈0.21. If this low porosity cannot be achieved, the minimum possible porosity should be selected for the cathode.

The studies indicate that varying the cathode porosity of the cell studied from 0.13 to 0.6 can affect the mean total polarization resistance up to 0.142 Ω cm^2 and the mean polarization resistances of the anode and cathode up to 0.009 Ω cm^2 and 0.134 Ω cm^2, respectively. Therefore, the anode mean polarization resistance is a weak function of the cathode porosity. The change in the mean polarization resistances of the electrolyte and interconnect is also predicted to be negligible.

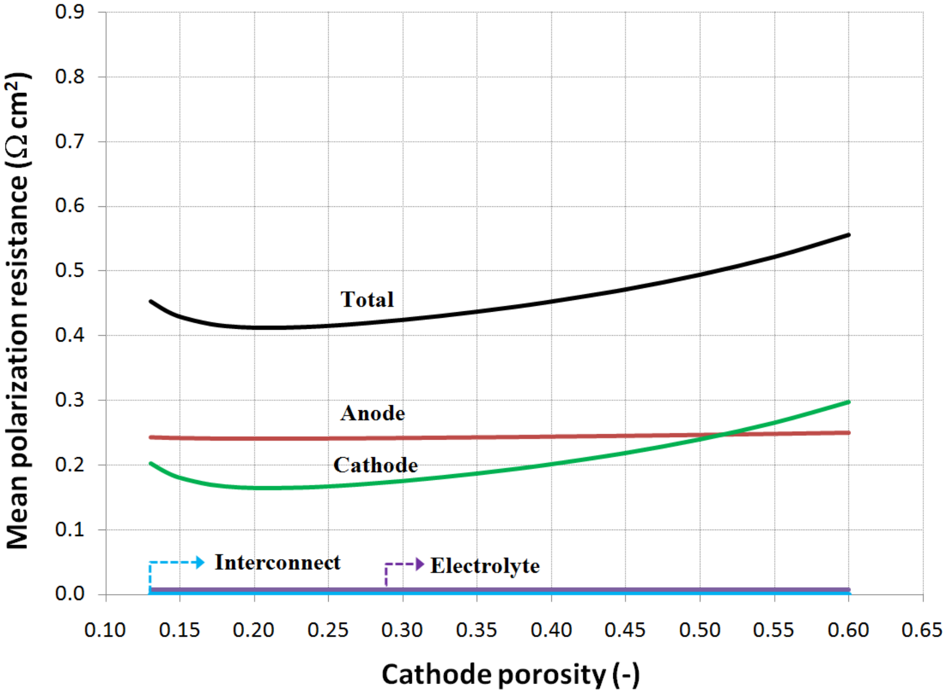

Figure 4.42: Effect of the cathode porosity on the mean total polarization resistance and mean polarization resistances of the anode, cathode, electrolyte, and interconnect.

The effects of the microstructural variables of the porous composite electrodes of the cell studied on the mean total polarization resistance and the mean polarization resistances of the anode and cathode are summarized in Table 4.6.

Table 4.6: Summary of the effect of the microstructure of porous composite electrodes on the mean total polarization resistances.

Microstructural Variable			**Mean Polarization Resistance (Ω cm^2)**					
			Total		**Anode**		**Cathode**	
Variable	Range of investigation	Optimum value	Interval of changes	Magnitude of changes	Interval of changes	Magnitude of changes	Interval of changes	Magnitude of changes
Volume fraction of Ni in the anode functional layer at various particle size ratios	$0.46 \leq \varphi_{Ni,A,FL} \leq 0.8$ $\alpha_{A,FL}=0.5$	0.58	[0.496,1.112]	0.616	[0.318,0.935]	0.617	[0.170,0.176]	0.006
	$0.3 \leq \varphi_{Ni,A,FL} \leq 0.69$ $\alpha_{A,FL}=1$	0.44	[0.416,1.052]	0.636	[0.241,0.874]	0.633	[0.166,0.176]	0.010
	$0.18 \leq \varphi_{Ni,A,FL} \leq 0.52$ $\alpha_{A,FL}=2$	0.32	[0.566,1.057]	0.491	[0.385,0.878]	0.493	[0.172,0.178]	0.006
Volume fraction of LSM in the cathode at various particle size ratios	$0.46 \leq \varphi_{LSM,C} \leq 0.80$ $\alpha_C=0.5$	0.56	[0.471,0.871]	0.400	[0.245,0.260]	0.015	[0.218,0.603]	0.385
	$0.3 \leq \varphi_{LSM,C} \leq 0.69$ $\alpha_C=1$	0.42	[0.416,0.837]	0.421	[0.241,0.260]	0.019	[0.167,0.569]	0.403
	$0.18 \leq \varphi_{LSM,C} \leq 0.52$ $\alpha_C=2$	0.30	[0.488,0.801]	0.313	[0.247,0.259]	0.012	[0.233,0.534]	0.301
Diameter of electron-conducting particles (μm)	$0.1 \leq d_{Ni,A,FL} \leq 5.0$	<0.1	[0.267,0.814]	0.547	[0.107,0.631]	0.524	[0.151,0.176]	0.025
	$0.1 \leq d_{LSM,C} \leq 5.0$	0.2	[0.354,0.608]	0.254	[0.235,0.255]	0.020	[0.111,0.345]	0.234
	$0.1 \leq d_{Ni,A,SL} \leq 5.0$	as high as possible	[0.413,0.557]	0.144	[0.238,0.371]	0.133	[0.166,0.178]	0.012
Thickness (μm)	$5 \leq \delta_{A,FL} \leq 150$	85	[0.401,1.026]	0.625	[0.227,0.838]	0.611	[0.165,0.180]	0.015
	$5 \leq \delta_C \leq 150$	70	[0.415,0.689]	0.274	[0.241,0.269]	0.028	[0.166,0.411]	0.245
	$50 \leq \delta_{A,SL} \leq 1500$	as low as possible	[0.402,0.446]	0.044	[0.230,0.268]	0.038	[0.165,0.169]	0.004
Porosity	$0.13 \leq \varepsilon_{A,FL} \leq 0.60$	0.19	[0.383,0.584]	0.201	[0.210,0.404]	0.194	[0.165,0.172]	0.007
	$0.13 \leq \varepsilon_C \leq 0.60$	0.21	[0.413,0.555]	0.142	[0.241,0.250]	0.009	[0.164,0.298]	0.134
	$0.13 \leq \varepsilon_{A,SL} \leq 0.60$	as high as possible	[0.404,0.881]	0.477	[0.231,0.679]	0.448	[0.166,0.194]	0.028

4.4.3.2 Electric Power Generation

The total power density and the power densities generated due to H_2 and CO electrochemical reactions may change significantly by varying the microstructure of electrodes. The effect of the microstructural variables of the porous composite electrodes on the mean value of these power densities is studied in this section.

4.4.3.2.1 Ni Volume Fraction and Particle Size Ratio in the Anode Functional Layer

The effect of the Ni volume fraction in the anode functional layer on the mean total power density and mean power densities due to H_2 and CO electrochemical reactions is shown in Figure 4.43. As seen in this figure, with an increase in the volume fraction of Ni particles from its percolation threshold, the mean total power density and mean power densities due to H_2 and CO electrochemical reactions increase to a certain value and then decrease. Therefore, there is an optimum Ni volume fraction in the anode functional layer at which these mean power densities are maximized. The effect of the particle size ratio of the anode functional layer is also shown in Figure 4.43. Among the optimum Ni volume fractions obtained at different particle size ratios, the one associated with the particle size ratio of unity provides the highest mean power densities. Indeed, for an anode functional layer with an optimum Ni volume fraction the optimum particle size ratio is always equal to 1.

At the particle size ratio of unity, the mean power density is maximized at the Ni volume fraction of ≈ 0.44 in the anode functional layer of the cell studied. The studies also indicate that at the particle size ratio of unity, varying the volume fraction of Ni in the anode functional layer from 0.3 to 0.69 can affect the mean total power density up to 0.238 W/cm^2 and the mean power densities due to H_2 and CO electrochemical reactions up to 0.172 W/cm^2 and 0.065 W/cm^2, respectively.

4.4.3.2.2 Size of Ni Particles in the Anode Functional Layer

Figure 4.44 shows the effect of the size of Ni particles in the anode functional layer on the mean total power density and mean power densities due to H_2 and CO electrochemical reactions. In the range of the Ni particle sizes investigated, the mean total power density and mean power densities due to H_2 and CO electrochemical reactions increase with a decrease in the size of Ni particles. However, because the contribution of the anode concentration polarization may become significant for fine-size particles and limit the power density, the mean power densities may decrease with the reduction of the size of Ni particles to less than 0.1 μm. Therefore, there may be an optimum size for the Ni particles of the anode functional layer at which these mean power densities are maximized. Although using Ni particles in the range of 0.1 μm may increase these mean power densities, the anode may be vulnerable to degradation due to an extensive grain growth of particles during the sintering process and operation of the cell [127]. This may necessitate that the size of Ni particles is selected by durability analysis rather than the electrical performance analysis through the combined micro- and macro model. The studies point out that varying the size of Ni particles in the anode functional layer from 0.1 μm to 5 μm can affect the mean total power density up to 0.41 W/cm^2 and mean power densities due to H_2 and CO electrochemical reactions up to 0.298 W/cm^2 and 0.113 W/cm^2, respectively.

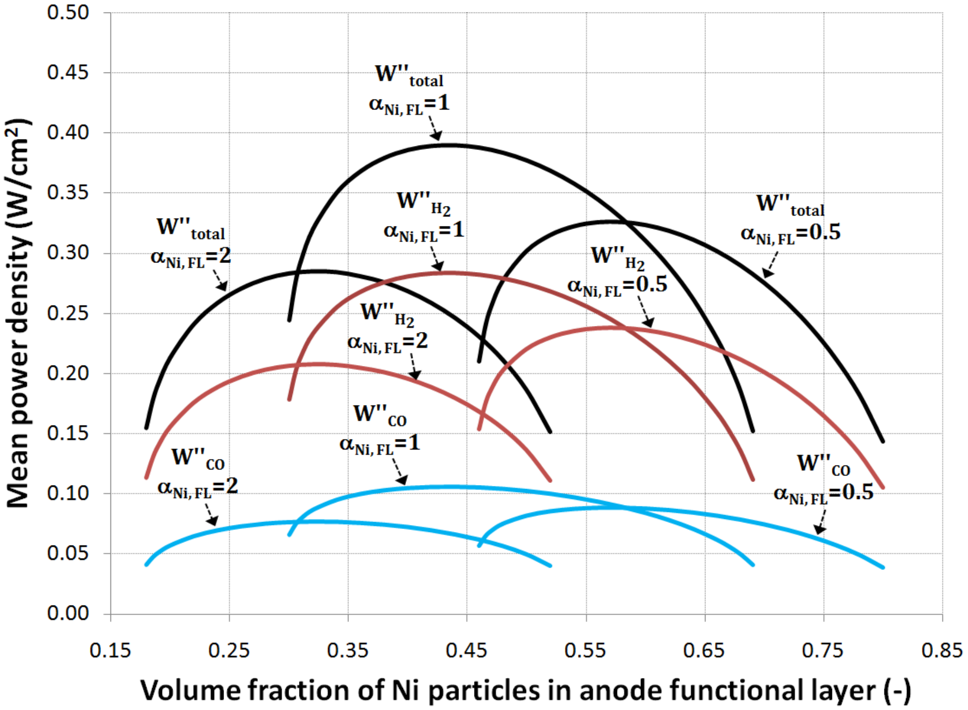

Figure 4.43: Effect of the Ni volume fraction in the anode functional layer at particle size ratios of 0.5, 1, and 2 on the cell mean total power density and mean power densities due to H_2 and CO electrochemical reactions.

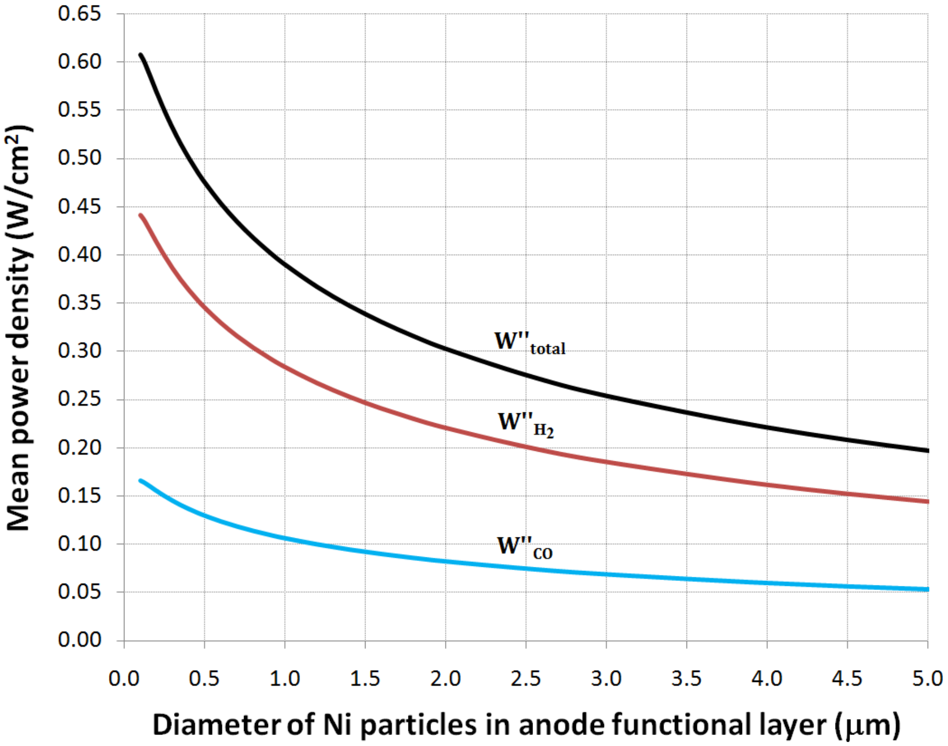

Figure 4.44: Effect of the size of Ni particles in the anode functional layer on the cell mean total power density and mean power densities due to H_2 and CO electrochemical reactions.

4.4.3.2.3 Thickness of the Anode Functional Layer

Figure 4.45 shows the effect of the thickness of the anode functional layer on the mean total power density and mean power densities due to H_2 and CO electrochemical reactions. As seen in this figure, with an increase in the thickness of the anode functional layer the mean total power density and mean power densities due to H_2 and CO electrochemical reactions increase to a certain value and then decrease linearly with a slight slope. Therefore, there is an optimum value for the thickness of the anode functional layer at which these power densities are maximized. This trend makes sense because for thin anode functional layers the anode activation polarization increases significantly due to insufficient active sites for the H_2 and CO electrooxidation reactions. For thick functional layers, the contribution of the anode ohmic and concentration polarizations becomes significant due to the increase in the mass and charge transport lengths. For the cells studied, the optimum thickness of the anode functional layer is predicted to be ≈85 µm; however, decreases in the mean power densities are negligible if the thickness decreases to even around 45 µm.

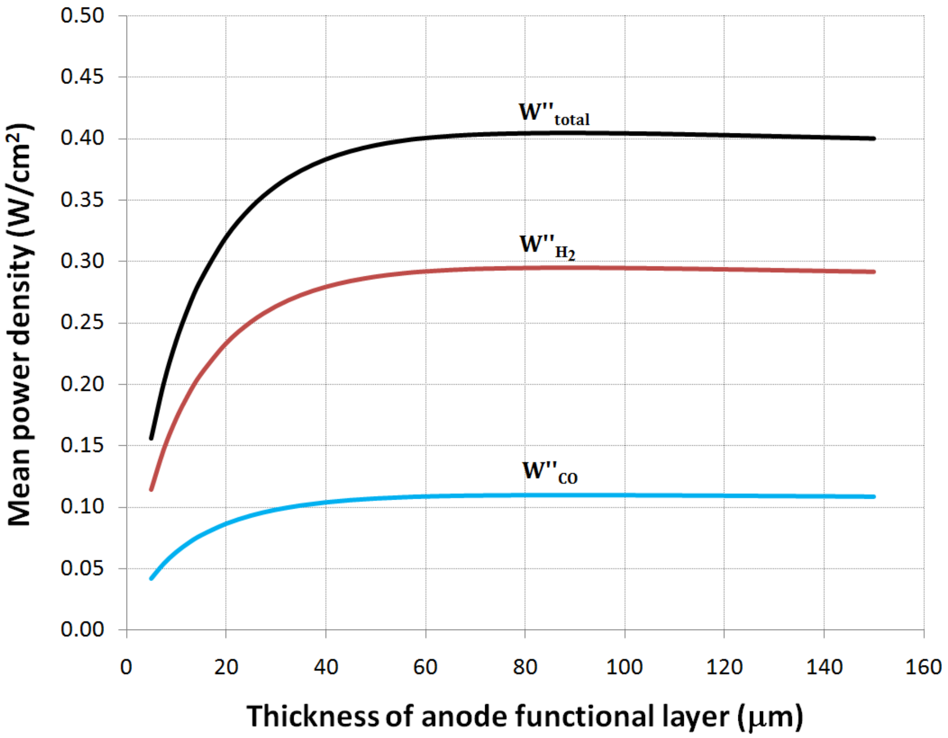

Figure 4.45: Effect of the thickness of the anode functional layer on the cell mean total power density and mean power densities due to H_2 and CO electrochemical reactions.

The studies show that varying the thickness of the anode functional layer from 5 μm to 150 μm can affect the mean total power density up to 0.249 W/cm^2 and the mean power densities due to H_2 and CO electrochemical reactions up to 0.181 W/cm^2 and 0.068 W/cm^2, respectively.

4.4.3.2.4 Porosity of the Anode Functional Layer

Figure 4.46 shows the effects of the porosity of the anode functional layer on the mean total power density and mean power densities due to H_2 and CO electrochemical reactions. With a decrease in the porosity, the mean total power density and the mean power densities due to H_2 and CO electrochemical reactions increase to a certain value due to the decrease in the anode activation and ohmic polarizations. They then decrease suddenly due to a significant increase in the anode concentration polarization. Therefore, there is a porosity at which these mean power densities are maximized. For the cell studied, the optimum porosity of the anode functional layer is predicted to be ≈0.19. For a random-packing of spherical particles with a given size, the porosity cannot be less than a certain value if the average contact angle between the particles is not increased during the sintering process. In such a situation, if the low porosity of 0.19 is not achievable, the minimum possible porosity can be selected for the anode functional layer. The studies also indicate that varying the porosity of the anode functional layer from 0.13 to 0.6 can affect the mean total power density up to 0.147 W/cm^2 and the mean power densities due to H_2 and CO electrochemical reactions up to 0.107 W/cm^2 and 0.04 W/cm^2, respectively.

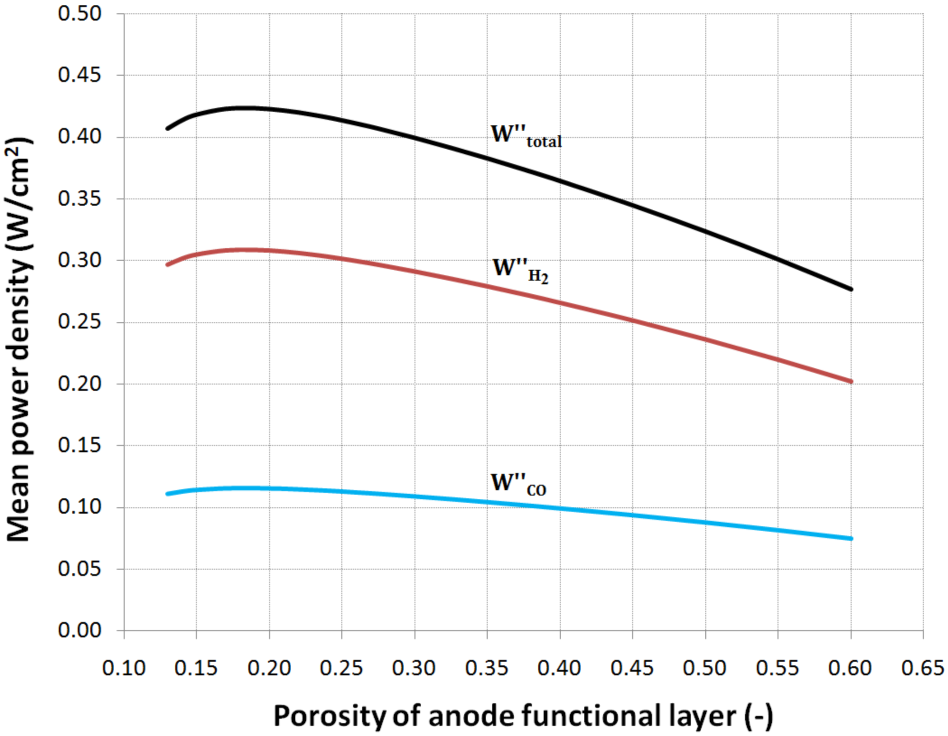

Figure 4.46: Effect of the porosity of the anode functional layer on the cell mean total power density and mean power densities due to H_2 and CO electrochemical reactions.

4.4.3.2.5 Size of Ni Particles in the Anode Substrate Layer

Figure 4.47 shows the effect of the size of Ni particles in the anode substrate layer on the mean total power density and mean power densities due to H_2 and CO electrochemical reactions. In the range of the Ni particle sizes investigated, the mean total power density and mean power densities due to H_2 and CO electrochemical reactions increase with an increase in the size of Ni particles. However, the increase in these power densities is negligible for Ni particles with diameters of greater than 1.5 μm. For particles smaller than 0.5 μm, the anode concentration polarization becomes significant and limits the power densities. Therefore, the minimum size of 0.5 μm is suggested for the size of Ni particles in the anode substrate layer. The studies indicate that an increase in the size of Ni particles in the anode substrate layer from 0.1 μm to 5 μm leads to an increase equal to 0.103 W/cm^2 in the mean total power density and 0.075 W/cm^2 and 0.026 W/cm^2 in the mean power densities due to H_2 and CO electrochemical reactions, respectively.

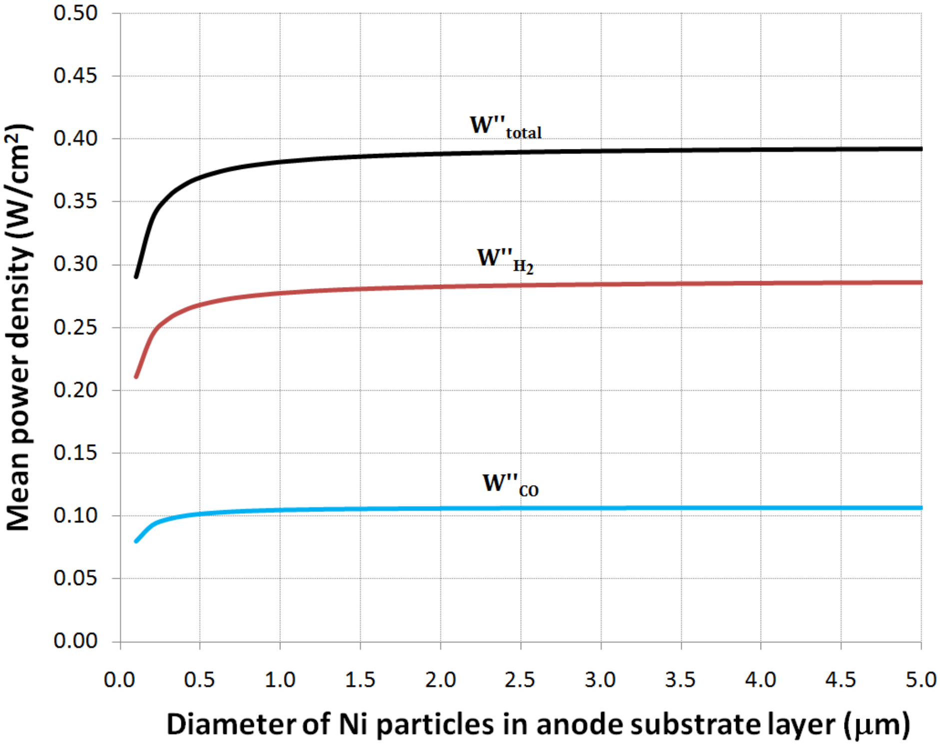

Figure 4.47: Effect of the size of Ni particles in the anode substrate layer on the cell mean total power density and mean power densities due to H_2 and CO electrochemical reactions.

4.4.3.2.6 Thickness of the Anode Substrate Layer

Figure 4.48 shows the effect of the thickness of the anode substrate layer on the mean total power density and mean power densities due to H_2 and CO electrochemical reactions. In the range of the thicknesses investigated, with an increase in the thickness of the anode substrate layer the mean total power density and mean power densities due to H_2 and CO electrochemical reactions decrease linearly with a slight slope. An increase in the thickness of the anode substrate layer from 50 μm to 1500 μm decreases the mean total power density only about 0.033 W/cm^2. The mean power densities due to H_2 and CO electrochemical reactions also decrease only around 0.024 W/cm^2 and 0.009 W/cm^2, respectively. The minimum thickness required for the mechanical strength of the cell is suggested to be selected for the anode substrate layer.

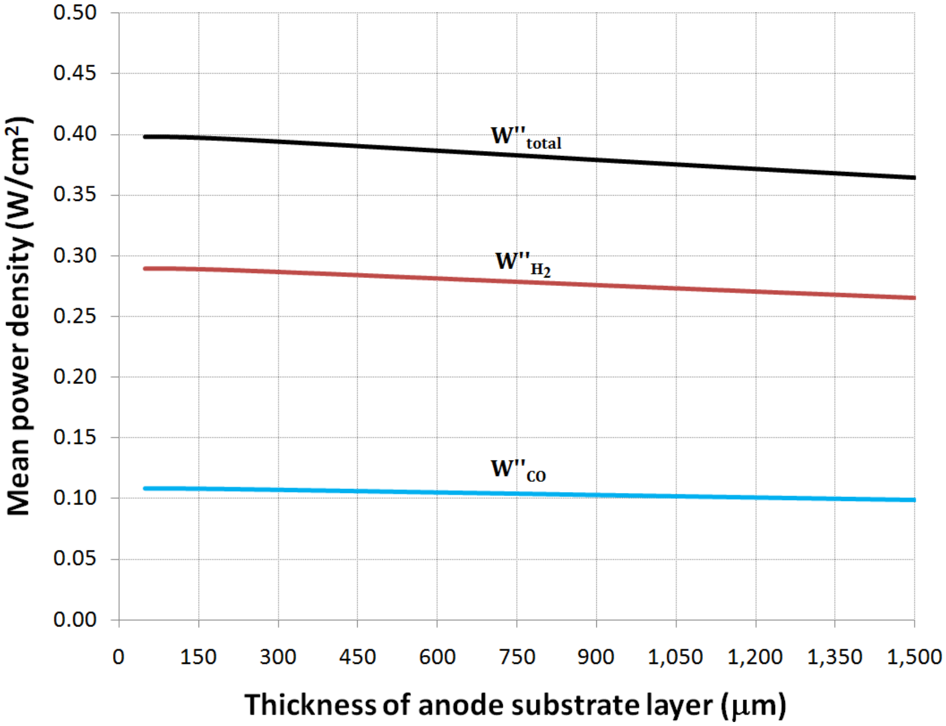

Figure 4.48: Effect of the thickness of the anode substrate layer on the cell mean total power density and mean power densities due to H_2 and CO electrochemical reactions.

4.4.3.2.7 Porosity of the Anode Substrate Layer

Figure 4.49 shows the effects of the porosity of the anode substrate layer on the mean total power density and the mean power densities due to H_2 and CO electrochemical reactions. In the range of the porosities investigated, the mean total power density and mean power densities due to H_2 and CO electrochemical reactions increase with an increase in the porosity of the anode substrate layer. However, this increase is negligible for porosities greater than 0.5. This trend makes sense because with an increase in the porosity of the anode substrate layer, the anode concentration polarization decreases and, consequently, for a given cell voltage the power density increases. The studies point out that an increase in the porosity of the anode substrate layer from 0.13 to 0.6 leads to an increase in the mean total power density up to 0.239 W/cm^2, and the mean power densities due to H_2 and CO electrochemical reactions up to 0.173 W/cm^2 and 0.065 W/cm^2, respectively.

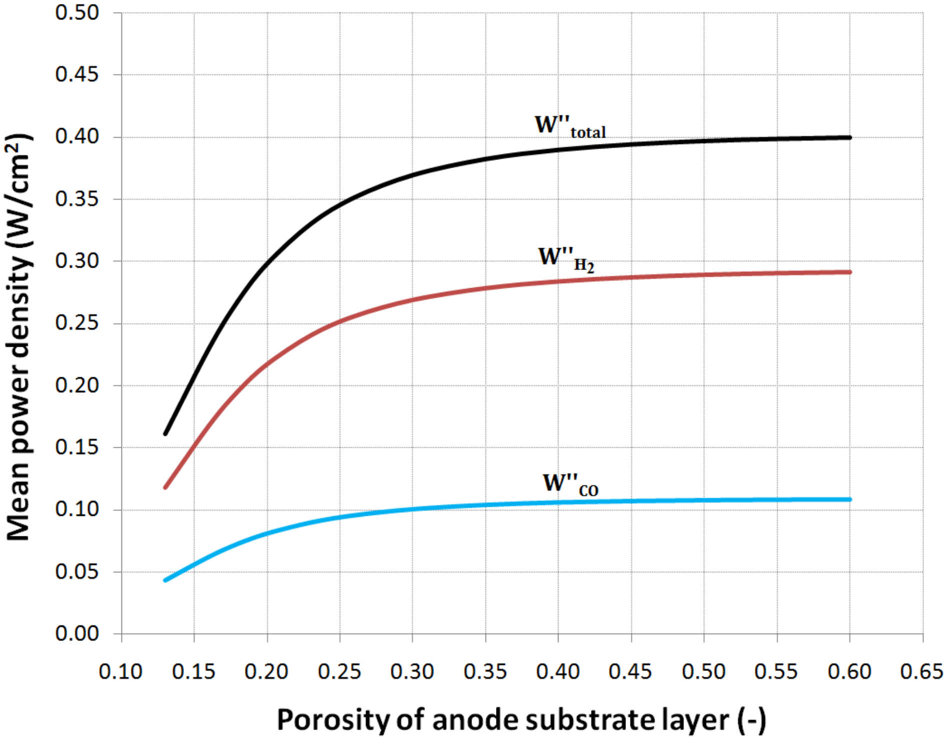

Figure 4.49: Effect of the porosity of the anode substrate layer on the cell mean total power density and mean power densities due to H_2 and CO electrochemical reactions.

4.4.3.2.8 LSM Volume Fraction and Particle Size Ratio of the Cathode

Figure 4.50 shows the effects of the LSM volume fraction in the cathode at various particle size ratios on the mean total power density and the mean power densities due to H_2 and CO electrochemical reactions. With an increase in the volume fraction of LSM from its percolation threshold, the mean total power density and the mean power densities due to H_2 and CO electrochemical reactions increase to a certain value and then decrease. Thus, there is an optimum LSM volume fraction at which these power densities are maximized. The studies confirm that for a cathode with any microstructural variables operated at any conditions, there is always such an optimum LSM volume fraction that maximizes these mean power densities. Similar to the anode, among the optimum LSM volume fractions obtained at various particle size ratios, the one associated with the particle size ratio of unity provides the highest mean power densities. Indeed, for a cathode microstructure with the optimum LSM volume fraction, the optimum particle size ratio is equal to 1. At the particle size ratio of unity, the mean power densities of the cell studied are maximized at the LSM volume fraction of ≈0.42 in the cathode.

The studies also indicate that at the particle size ratio of unity, varying the volume fraction of LSM in the cathode from 0.3 to 0.69 can affect the mean total power density up to 0.198 W/cm^2, and the mean power densities due to H_2 and CO electrochemical reactions up to 0.143 W/cm^2 and 0.054 W/cm^2, respectively.

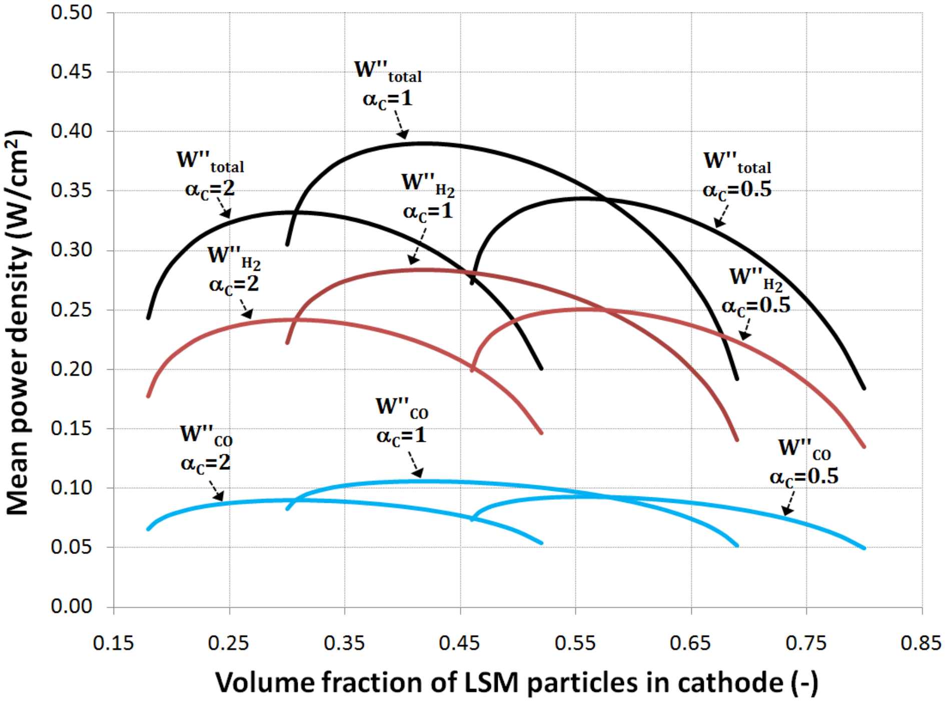

Figure 4.50: Effect of the volume fraction of LSM in the cathode at particle size ratios of 0.5, 1, and 2 on the cell mean total power density and mean power densities due to H_2 and CO electrochemical reactions.

4.4.3.2.9 Size of LSM Particles in the Cathode

Figure 4.51 shows the effects of the LSM particle size in the cathode on the mean total power density and the mean power densities due to H_2 and CO electrochemical reactions. With a decrease in the LSM particle size, the mean total power density and mean power densities due to H_2 and CO electrochemical reactions increase to a certain value and then decrease sharply. Therefore, there is an optimum size for the LSM particles at which these mean power densities are maximized. It is noted that for the LSM particle size ratio of unity, with a decrease in the size of the particle, the cathode activation polarization decreases due to the increase in the cathode electrochemical active area. Other effects are increases in the cathode concentration polarization due to the decrease in the cathode average pore size; and the ohmic polarization remaining constant because the effective resistivity of the LSM and YSZ are not a function of the size of particles. Since the contribution of the cathode activation polarization in these mean power densities is greater than that of the concentration polarization for the LSM particles larger than the optimum size, these mean power densities increase with a decrease in the LSM particles size. For LSM particles smaller than the optimum size, the contribution of the cathode concentration polarization is greater than that of the activation polarization; hence, the mean power densities decrease with a decrease in the size of LSM particles. The optimum size of LSM particles for the cell studied is predicted to be ≈0.2 μm. Of course, using the particles in this range may lead to a decrease in the mean power densities due to the grain growth of the particles during the sintering process or the cell operation. Therefore, larger LSM particles may be selected for the cathode to increase the cell durability.

The studies point out that varying the size of LSM particles in the cathode from 0.1 μm to 5 μm can affect the mean total power density up to 0.192 W/cm^2 and the mean power densities due to H_2 and CO electrochemical reactions up to 0.139 W/cm^2 and 0.053 W/cm^2, respectively.

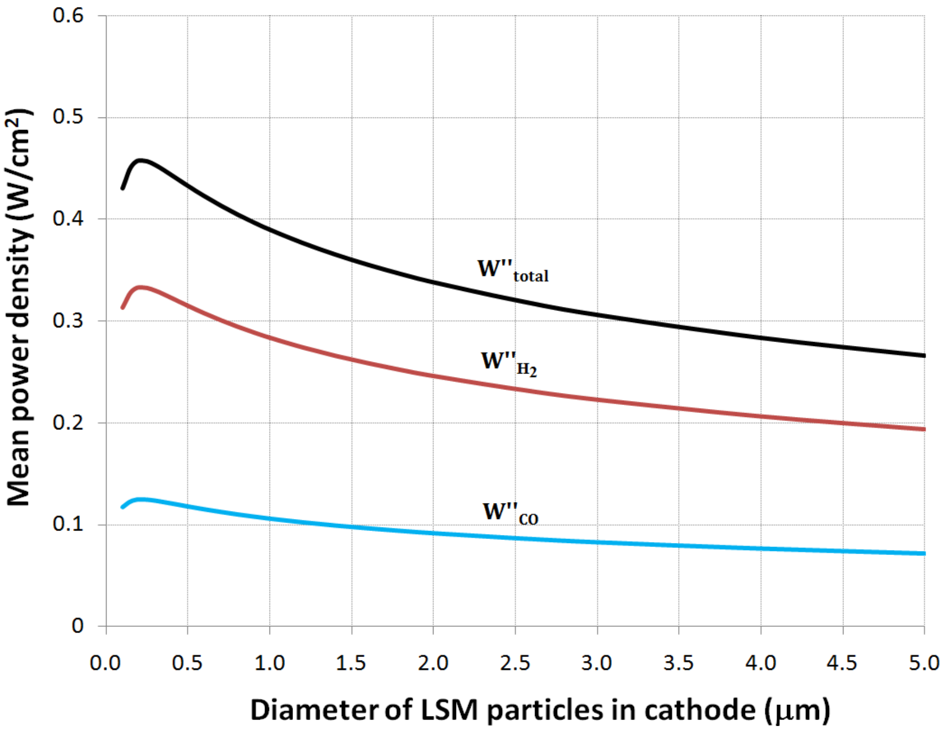

Figure 4.51: Effect of the size of LSM particles in the cathode on the cell mean total power density and mean power densities due to H_2 and CO electrochemical reactions.

4.4.3.2.10 Thickness of the Cathode

Figure 4.52 shows the effects of the cathode thickness on the mean total power density and mean power densities due to H_2 and CO electrochemical reactions. With an increase in the cathode thickness, the mean total power density and mean power densities due to H_2 and CO electrochemical reactions increase to a certain value and then decrease linearly with a slight slope. Therefore, there is an optimum value for the cathode thickness at which these mean power densities are maximized. This trend makes sense because for thin cathodes the cathode activation polarization increases significantly due to insufficient active sites for the oxygen electroreduction reaction. For thick cathodes, the contribution of the cathode ohmic and concentration polarizations becomes significant due to the increase in the mass and charge transport lengths. For the cell studied, the optimum thickness of the cathode is predicted to be ≈70 μm; however, these mean power densities reduce negligibly if the thickness decreases to even around 45 μm.

The studies also indicate that varying the thickness of the cathode from 5 μm to 150 μm can affect the mean total power density up to 0.156 W/cm^2 and the mean power densities due to H_2 and CO electrochemical reactions up to 0.113 W/cm^2 and 0.043 W/cm^2, respectively.

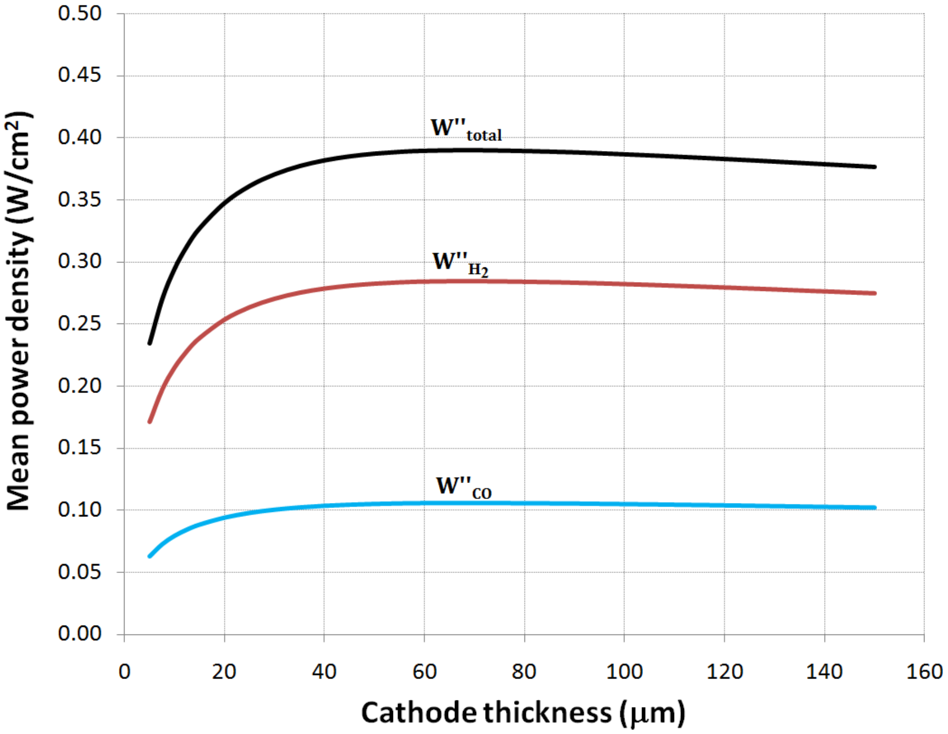

Figure 4.52: Effect of the cathode thickness on the cell mean total power density and mean power densities due to H_2 and CO electrochemical reactions.

4.4.3.2.11 Porosity of the Cathode

The effect of the porosity of the cathode on the mean total power density and the mean power densities due to H_2 and CO electrochemical reactions is shown in Figure 4.53. With a decrease in the porosity, the mean total power density and mean power densities due to H_2 and CO electrochemical reactions increase to a certain value due to the decrease in the cathode activation and ohmic polarizations. However, they then decrease suddenly due to a significant increase in the cathode concentration polarization. Therefore, there is a porosity at which these mean power densities are maximized. For the cell studied, the optimum cathode porosity is predicted to be ≈0.21. If this low porosity cannot be achieved for a random-packing of spherical particles with a given size, the minimum possible porosity should be selected for the cathode. The studies also reveal that varying the porosity of the cathode from 0.13 to 0.6 can affect the mean total power density up to 0.102 W/cm^2 and the mean power densities due to H_2 and CO electrochemical reactions up to 0.074 W/cm^2 and 0.028 W/cm^2, respectively.

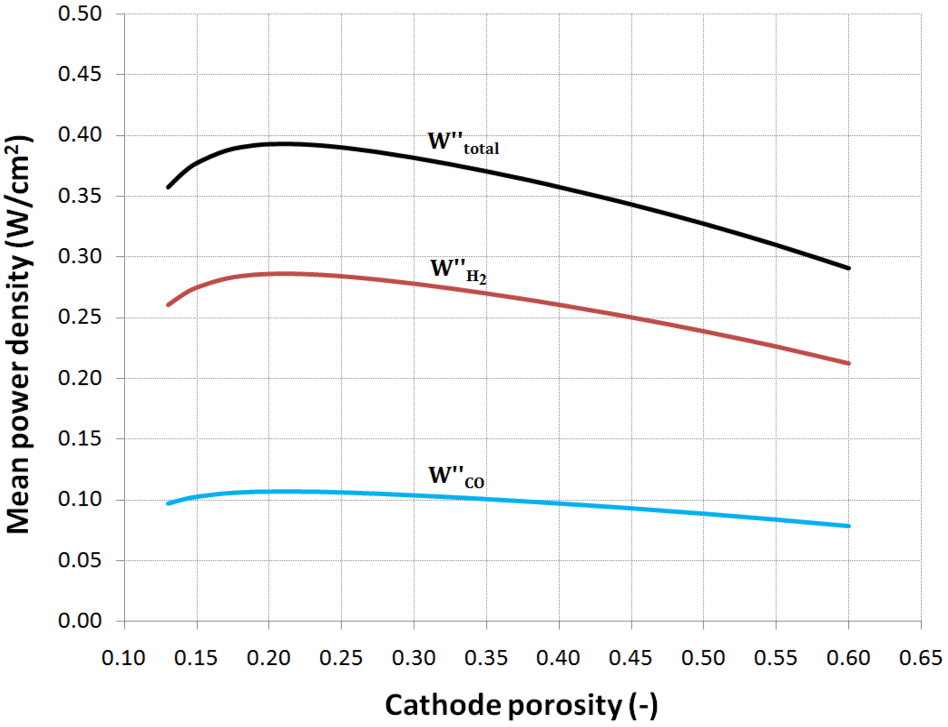

Figure 4.53: Effect of the cathode porosity on the mean total power density of the cell and mean power densities due to H_2 and CO electrochemical reactions.

A remarkable result, illustrated in Figures 4.43-4.53, is that the contribution of CO electrochemical reaction in the mean total power density is almost 27% and the rest of the power density is generated through H_2 electrochemical reaction. The microstructure of electrodes may change the contribution of the CO electrochemical reaction up to 1%-point.

The effect of the microstructural variables of the porous composite electrodes of the cell studied on the mean power densities is summarized in Table 4.7.

Table 4.7: Summary of the effect of the microstructure of porous composite electrodes on the mean total power densities.

Microstructural Variable			**Mean Power Density (W/cm^2)**					
			Total		**H_2 electrochemical reaction**		**CO electrochemical reaction**	
Variable	Range of investigation	Optimum value	Interval of changes	Magnitude of changes	Interval of changes	Magnitude of changes	Interval of changes	Magnitude of changes
Volume fraction of Ni in the anode functional layer at various particle size ratios	$0.46\leq\varphi_{Ni,A,FL}\leq0.8$ $\alpha_{A,FL}=0.5$	0.58	[0.144,0.326]	0.182	[0.105,0.238]	0.133	[0.038,0.088]	0.050
	$0.3\leq\varphi_{Ni,A,FL}\leq0.69$ $\alpha_{A,FL}=1$	0.44	[0.152,0.390]	0.238	[0.112,0.284]	0.172	[0.041,0.106]	0.065
	$0.18\leq\varphi_{Ni,A,FL}\leq0.52$ $\alpha_{A,FL}=2$	0.32	[0.151,0.285]	0.134	[0.111,0.208]	0.097	[0.041,0.077]	0.036
Volume fraction of LSM in the cathode at various particle size ratios	$0.46\leq\varphi_{LSM,C}\leq0.80$ $\alpha_{C}=0.5$	0.56	[0.184,0.344]	0.160	[0.135,0.250]	0.115	[0.049,0.093]	0.044
	$0.3\leq\varphi_{LSM,C}\leq0.69$ $\alpha_{C}=1$	0.42	[0.192,0.390]	0.198	[0.141,0.284]	0.143	[0.052,0.106]	0.054
	$0.18\leq\varphi_{LSM,C}\leq0.52$ $\alpha_{C}=2$	0.30	[0.201,0.332]	0.131	[0.147,0.242]	0.095	[0.054,0.090]	0.036
Diameter of electron-conducting particles (μm)	$0.1\leq d_{Ni,A,FL}\leq5.0$	<0.1	[0.197,0.607]	0.410	[0.144,0.442]	0.298	[0.053,0.166]	0.113
	$0.1\leq d_{LSM,C}\leq5.0$	0.2	[0.266,0.458]	0.192	[0.194,0.333]	0.139	[0.072,0.125]	0.053
	$0.1\leq d_{Ni,A,SL}\leq5.0$	as high as possible	[0.290,0.393]	0.103	[0.211,0.286]	0.075	[0.080,0.106]	0.026
Thickness (μm)	$5\leq\delta_{A,FL}\leq150$	85	[0.156,0.405]	0.249	[0.114,0.295]	0.181	[0.042,0.110]	0.068
	$5\leq\delta_{C}\leq150$	70	[0.234,0.390]	0.156	[0.171,0.284]	0.113	[0.063,0.106]	0.043
	$50\leq\delta_{A,SL}\leq1500$	as low as possible	[0.365,0.398]	0.033	[0.266,0.290]	0.024	[0.099,0.108]	0.009
Porosity	$0.13\leq\varepsilon_{A,FL}\leq0.60$	0.19	[0.277,0.424]	0.147	[0.202,0.309]	0.107	[0.075,0.115]	0.040
	$0.13\leq\varepsilon_{C}\leq0.60$	0.21	[0.291,0.393]	0.102	[0.212,0.286]	0.074	[0.079,0.107]	0.028
	$0.13\leq\varepsilon_{A,SL}\leq0.60$	as high as possible	[0.161,0.400]	0.239	[0.118,0.291]	0.173	[0.043,0.108]	0.065

4.4.3.3 Temperature of the Solid Structure of the Cell

The mean temperature, the temperature difference between the hottest and coldest spots, and the maximum temperature gradient in the solid structure, as three important parameters to design a durable cell, may change significantly by varying the microstructure of electrodes. The effect of the microstructural variables of the porous composite electrodes on these three parameters is studied in this section.

4.4.3.3.1 Volume Fraction of Electron-Conducting Particles and Particle Size Ratio

Figure 4.54 shows the effect of the Ni volume fraction in the anode functional layer and the LSM volume fraction in the cathode at various particle size ratios on the mean temperature, the temperature difference between the hottest and coldest spots, and the maximum temperature gradient in the solid structure. With an increase in the volume fraction of Ni in the anode functional layer or LSM in the cathode from their percolation thresholds, the mean temperature of the solid structure decreases to a certain value and then increases. Therefore, there is a value for the volume fraction of Ni in the anode functional layer and a value for the volume fraction of LSM in the cathode at which the mean temperature is minimized. The studies confirm that there are always such values for the Ni and LSM volume fractions that minimize the mean temperature of the solid structure. Among the values of the Ni and LSM volume fractions that minimize the mean temperature at various particle size ratios, the one associated with the particle size ratio of unity provides the lowest mean temperature. At the particle size ratio of unity, the mean temperature of the solid structure of the cell studied is minimized at the Ni volume fraction of ≈0.44 in the anode functional layer and the LSM volume fraction of ≈0.42 in the cathode. The studies also indicate that at the particle size ratio of unity, an increase in the volume fraction of Ni in the anode functional layer from 0.3 to 0.69 can affect the mean temperature of the solid structure up to 11.4 K. The effect of this increase in the volume fraction of LSM in the cathode can be up to 9.3 K.

In contrast to the mean temperature, with an increase in the volume fraction of Ni in the anode functional layer or the volume fraction of LSM in the cathode from their percolation thresholds, the temperature difference between the hottest and coldest spots in the solid structure increases to a certain value and then decreases. Therefore, there is a value for the volume fraction of Ni and a value for the volume fraction of LSM at which this temperature is maximized. Among the values of the Ni and LSM volume fractions that maximize this temperature at various particle size ratios, the one associated with the particle size ratio of unity always provides the highest temperature difference between the hottest and coldest spots in the solid structure. These statements are also valid for the maximum temperature gradient in the solid structure. At the particle size ratio of unity, the temperature difference between the hottest and coldest spots in the solid structure of the cell studied is maximized at the Ni volume fraction in the anode functional layer and the LSM volume fraction in the cathode of ≈0.46 and ≈0.44, respectively. The maximum temperature gradient also happens at the Ni and LSM volume fractions of ≈0.42. The studies also indicate that at the particle size ratio of unity, an increase in the volume fraction of Ni in the anode functional layer from 0.3 to 0.69 can affect the temperature difference between the hottest and coldest spots and the maximum temperature gradient in the solid structure up to 25.2 K and 2.5 K/cm, respectively. The effect of this increase in the volume fraction of LSM in the cathode on the temperature difference between the hottest and coldest spots and the maximum temperature gradient in the solid structure may be up to 20.2 K and 1.7 K/cm, respectively.

As a remarkable result, the effect of the volume fraction of Ni in the anode functional layer on the temperature distribution in the solid structure of the cell is more significant than the volume fraction of LSM in the cathode.

a

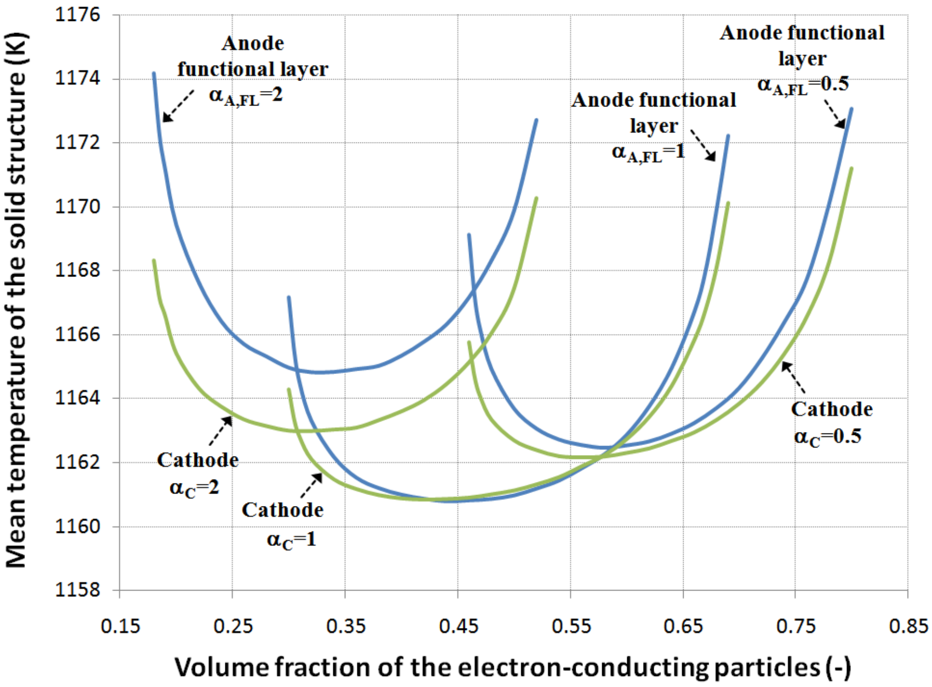

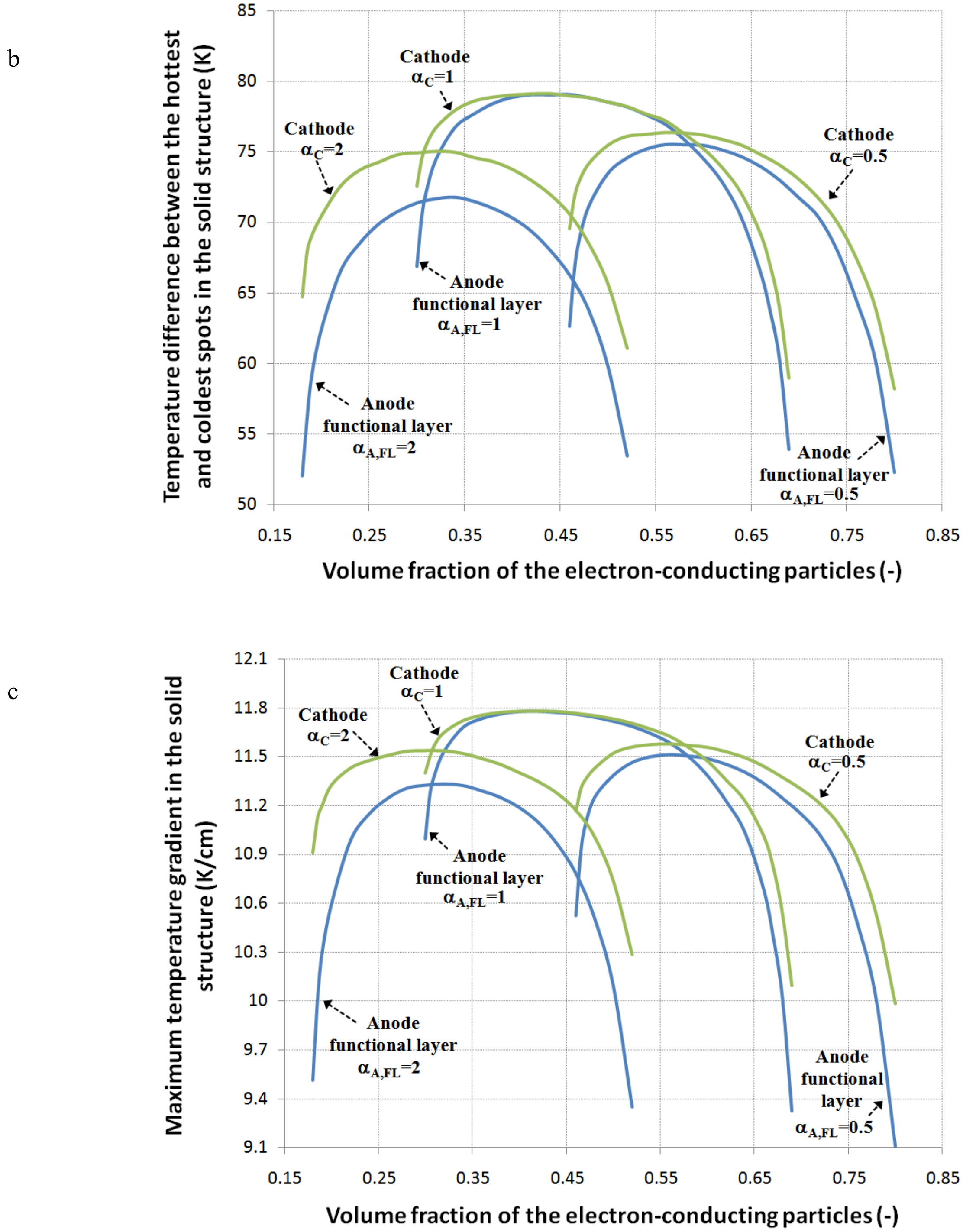

Figure 4.54: Effect of the volume fraction of electron-conducting particles in the anode functional layer and cathode at the particle size ratios of 0.5, 1 and 2 on the (a) mean temperature, (b) temperature difference between the hottest and coldest spots, and (c) maximum temperature gradient in the solid structure of the cell.

4.4.3.3.2 Size of Electron-Conducting Particles

Figure 4.55 shows the effects of the size of Ni particles in the anode functional and substrate layers and the size of LSM particles in the cathode on the mean temperature, the temperature difference between the hottest and coldest spots, and the maximum temperature gradient in the solid structure of the cell. With a decrease in the size of Ni particles in the anode functional layer or LSM particles in the cathode, the mean temperature of the solid structure decreases to a certain value and then increases. Therefore, there is a value for the size of the Ni particles in the anode functional layer and a value for the size of the LSM particles in the cathode at which the mean temperature is minimized. For the cell studied, the mean temperature of the solid structure of the cell is minimized at the size of ≈0.2 μm for Ni particles in the anode functional layer and the size of ≈0.3 μm for LSM particles in the cathode. The studies also indicate that an increase in the size of Ni particles in the anode functional layer from 0.1 μm to 5.0 μm can affect the mean temperature of the solid structure up to 11.1 K. The effect of this increase in the size of LSM particles in the cathode is predicted to be up to 6.8 K.

With an increase in the size of Ni particles in the anode substrate layer, the mean temperature of the solid structure decreases; however, the decrease in this temperature is negligible for Ni particle sizes greater than 1.5 μm. The studies also indicate that an increase in the size of Ni particles in the anode substrate layer from 0.1 μm to 5.0 μm can affect the mean temperature of the solid structure up to 5.9 K.

In contrast to the mean temperature, with a decrease in the size of Ni particles in the anode functional layer or LSM particles in the cathode, the temperature difference between the hottest and coldest spots in the solid structure increases to a certain value and then decreases; therefore, there is a value for the size of Ni particles and a value for the size of LSM particles at which this temperature is maximized. This statement is also valid for the maximum temperature gradient in the solid structure. For the cell studied, the temperature difference between the hottest and coldest spots in the solid structure of the cell is maximized at the size of ≈0.25 μm and ≈0.2 μm for the Ni particles in the anode functional layer and the LSM particles in the cathode, respectively. The maximum temperature gradient also happens at the size of the Ni and LSM particles of ≈0.12 μm and ≈0.25 μm, respectively. The studies also indicate that an increase in the size of Ni particles in the anode functional layer and LSM particles in the cathode from 0.1 μm to 5.0 μm can affect the temperature difference between the hottest and coldest spots up to 22.9 K and 13.3 K and the maximum temperature gradient in the solid structure up to 1.6 K/cm and 0.9 K/cm, respectively.

With an increase in the size of Ni particles in the anode substrate layer, the temperature difference between the hottest and coldest spots and the maximum temperature gradient in the solid structure increases; however, the increase in these temperatures is negligible for Ni particle sizes greater than ≈1.5 µm. The studies also indicate that an increase in the size of Ni particles in the anode substrate layer from 0.1 µm to 5.0 µm can affect the temperature difference between the hottest and coldest spots and the maximum temperature gradient in the solid structure up to 10.3 K and 0.3 K/cm, respectively.

As a remarkable result, among the sizes of the Ni particles in the anode substrate and functional layers and LSM particles in the cathode, the size of Ni particles in the anode functional layer has the highest effect on the temperature distribution in the solid structure of the cell, followed by the size of LSM particles in the cathode and the size of Ni particles in the anode substrate layer.

a

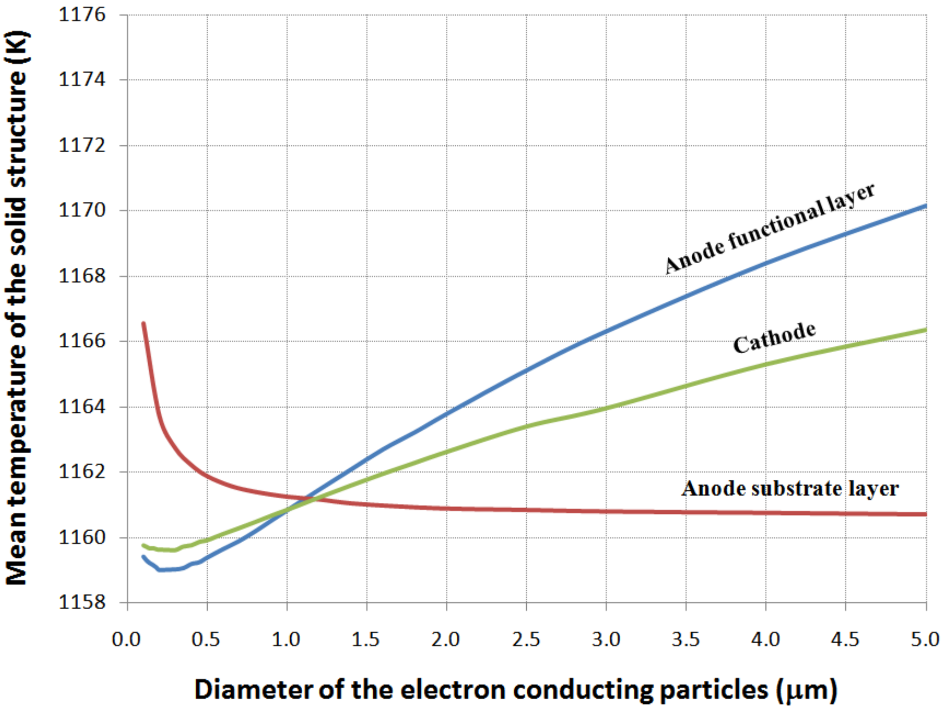

b

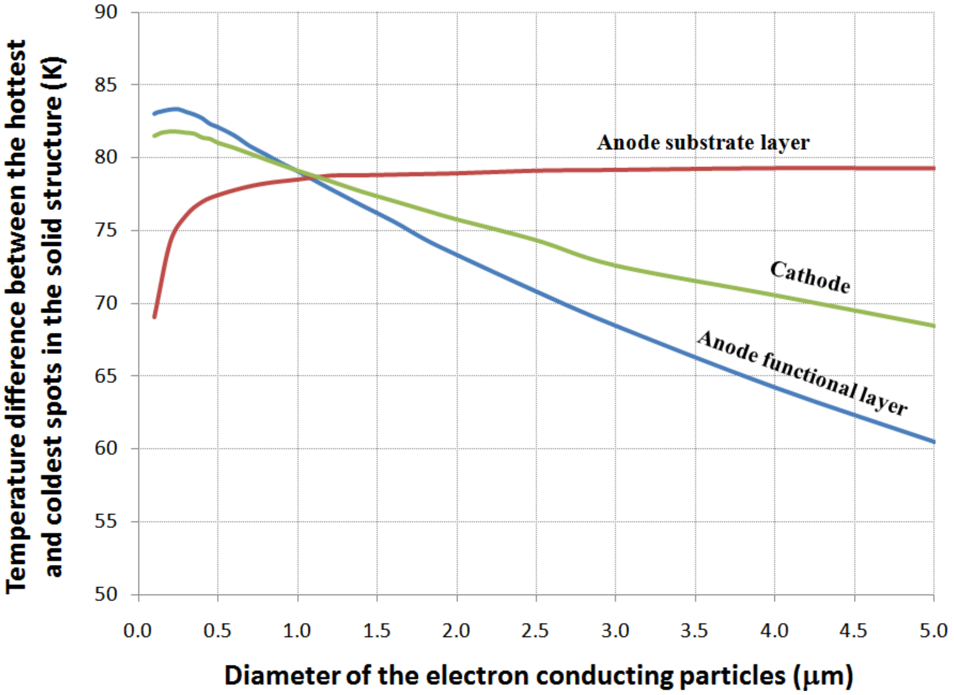

c

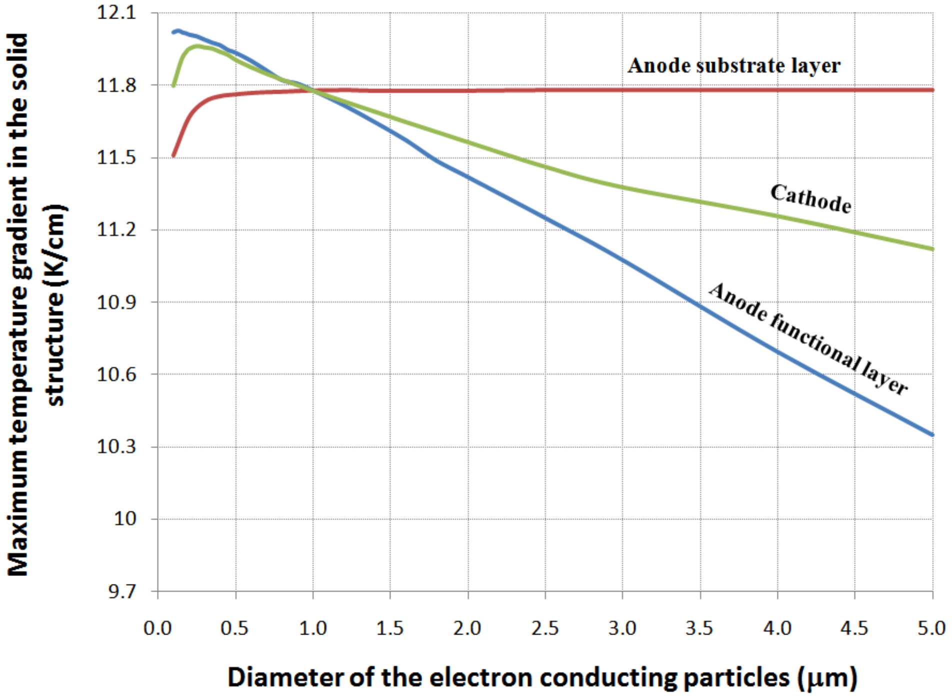

Figure 4.55: Effect of the size of Ni particles in the anode functional and substrate layers and the size of LSM particles in the cathode on the (a) mean temperature, (b) temperature difference between the hottest and coldest spots, and (c) maximum temperature gradient in the solid structure of the cell.

4.4.3.3.3 Thickness of Electrodes

Figure 4.56 shows the effects of the thickness of the anode functional and substrate layers and the thickness of the cathode on the mean temperature, the temperature difference between the hottest and coldest spots, and the maximum temperature gradient in the solid structure of the cell. As illustrated in Figure 4.56(a), with an increase in the thickness of the anode functional layer and cathode, the mean temperature of the solid structure decreases to a certain value and then increases. Therefore, there is a value for the thickness of the anode functional layer and a value for the thickness of the cathode at which the mean temperature is minimized. For the cell studied, the mean temperature of the solid structure of the cell is minimized at the thickness of the anode functional layer and cathode of ≈85 μm. Of course, the change in the mean temperature is negligible for thicknesses greater than 45 μm. The studies indicate that the increase in thicknesses of the anode functional layer and the cathode from 5 μm to 150 μm can affect the mean temperature of the solid structure up to 14.2 K and 9.2 K, respectively.

As shown in Figure 4.56(b), in contrast to the mean temperature, with an increase in the thickness of the anode functional layer and cathode, the temperature difference between the hottest and coldest spots in the solid structure increases to a certain value and then decreases with a slight slope; therefore, there is a value for the thickness of the anode functional layer and a value for the cathode thickness at which this temperature is maximized. For the cell studied, the temperature difference between the hottest and coldest spots in the solid structure of the cell is maximized at the anode functional layer and cathode thicknesses of ≈100 μm and ≈60 μm, respectively. The studies also indicate that the increase in thicknesses of the anode functional layer and cathode from 5 μm to 150 μm can affect this temperature difference up to ≈28.5 K and ≈17.4 K, respectively.

As shown in Figure 4.56(c), with an increase in the thickness of the anode functional layer, the maximum temperature gradient of the solid structure increases sharply if the thickness is less than ≈45 μm. The effect of the cathode thickness on the maximum temperature gradient becomes significant for cathodes thinner than ≈30 μm. The studies also reveal that an increase in thickness of the anode functional layer and cathode from 5 μm to 150 μm can affect the maximum temperature gradient in the solid structure up to 2.3 K/cm and 0.9 K/cm, respectively.

The mean temperature, the temperature difference between the hottest and coldest spots, and the maximum temperature gradient in the solid structure of the cell are weak functions of the thickness of the anode substrate layer. An increase in this thickness from 50 μm to 1500 μm can only affect the mean temperature, the temperature difference between the hottest and coldest spots, and the maximum temperature gradient in the solid structure around 1.3 K, 1.2 k, and 0.3 K/cm, respectively.

As a remarkable result, among the thicknesses of the cathode and the anode functional and substrate layers, the thickness of the anode functional layer has the highest effect on the temperature distribution in the solid structure, followed by the thicknesses of the cathode and anode substrate layer.

a

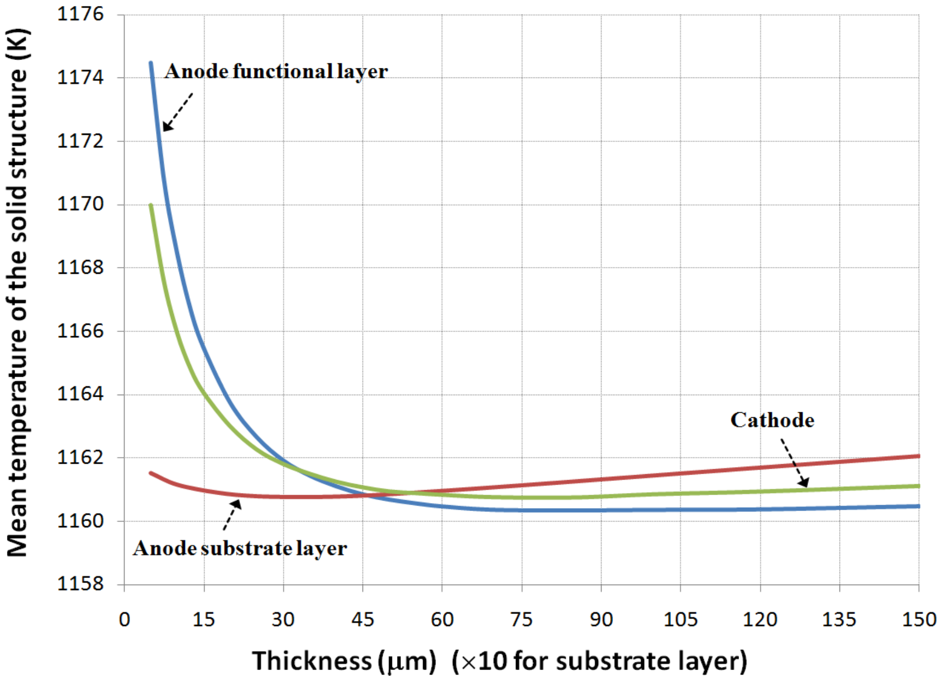

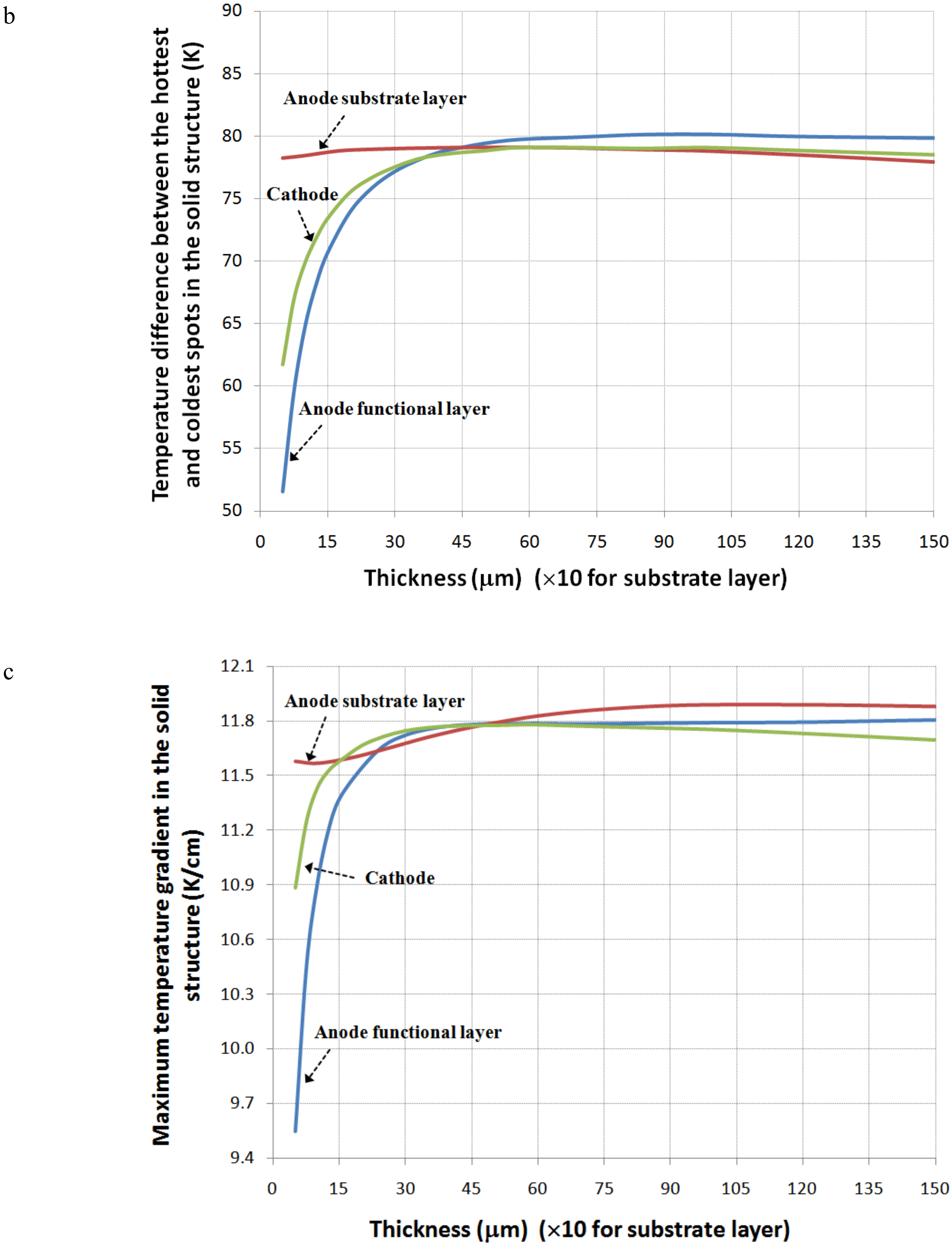

Figure 4.56: Effect of the thickness of the anode functional and substrate layers and the thickness of the cathode on the (a) mean temperature, (b) temperature difference between the hottest and coldest spots, and (c) maximum temperature gradient in the solid structure of the cell.

4.4.3.3.4 Porosity of Electrodes

Figure 4.57 shows the effects of the porosity of the anode functional and substrate layers and the porosity of the cathode on the mean temperature, the temperature difference between the hottest and coldest spots, and the maximum temperature gradient in the solid structure of the cell. With an increase in the porosity of the anode substrate layer, the mean temperature reduces and the temperature difference between the hottest and coldest spots in the solid temperature increases. Of course, for porosities greater than 0.5, these temperatures are weak functions of the porosity of the anode substrate layer. With an increase in the porosity of the anode substrate layer, the maximum temperature gradient in the solid structure increases to a certain value and then decreases; therefore, there is a value for the porosity of the anode substrate layer at which the maximum temperature gradient is maximized. The maximum temperature gradient in the solid structure of the cell is maximized at the porosity of ≈0.3 for the anode substrate layer. The studies indicate that an increase in the porosity of the anode substrate layer from 0.13 to 0.6 can affect the mean temperature, the temperature difference between the hottest and coldest spots, and the maximum temperature gradient in the solid structure up to 15.0 K, 28.3 K, and 1.5 K/cm, respectively.

With an increase in the porosity of the anode functional layer and cathode, the mean temperature of the solid structure decreases to a certain value and then increases; therefore, there is a value for the porosity of the anode functional layer and a value for the porosity of the cathode at which the mean temperature is minimized. For the cell studied, the mean temperature of the solid structure of the cell is minimized at the porosity of the anode functional layer and cathode of ≈0.21. The studies also indicate that an increase in the porosity of the anode functional layer and cathode from 0.13 to 0.6 can affect the mean temperature of the solid structure up to 4.0 K and 3.7 K, respectively.

In contrast to the mean temperature, with an increase in the porosity of the anode functional layer and cathode the temperature difference between the hottest and coldest spots in the solid structure increases to a certain value and then decreases; therefore, there is a value for the porosity of the anode functional layer and a value for the porosity of the cathode at which this temperature is maximized. This statement is also valid for the maximum temperature gradient in the solid structure. For the cell studied, the temperature difference between the hottest and coldest spots in the solid structure of the cell is maximized at the anode functional layer and cathode porosities of ≈0.21 and ≈0.19, respectively. The maximum temperature gradient also occurs at the anode functional layer and cathode porosities of ≈0.14 and ≈0.23, respectively. The studies indicate that an increase in the porosity of the anode functional layer and cathode from 0.13 to 0.6 can affect the temperature difference between the hottest and coldest spots up to 8.5 K and 7.1 K and the maximum temperature gradient in the solid structure up to 0.7 K/cm and 0.5 K/cm, respectively.

As a remarkable result, among the porosities of the cathode and the anode substrate and functional layers, the porosity of the anode substrate layer has the highest effect on the temperature distribution in the solid structure of the cell, followed by the porosities of the anode functional layer and cathode.

The effects of the microstructural variables of the porous composite electrodes of the cell studied on the mean temperature, the temperature difference between the hottest and coldest spots, and the maximum temperature gradient in the solid structure of the cell are summarized in Table 4.8.

a

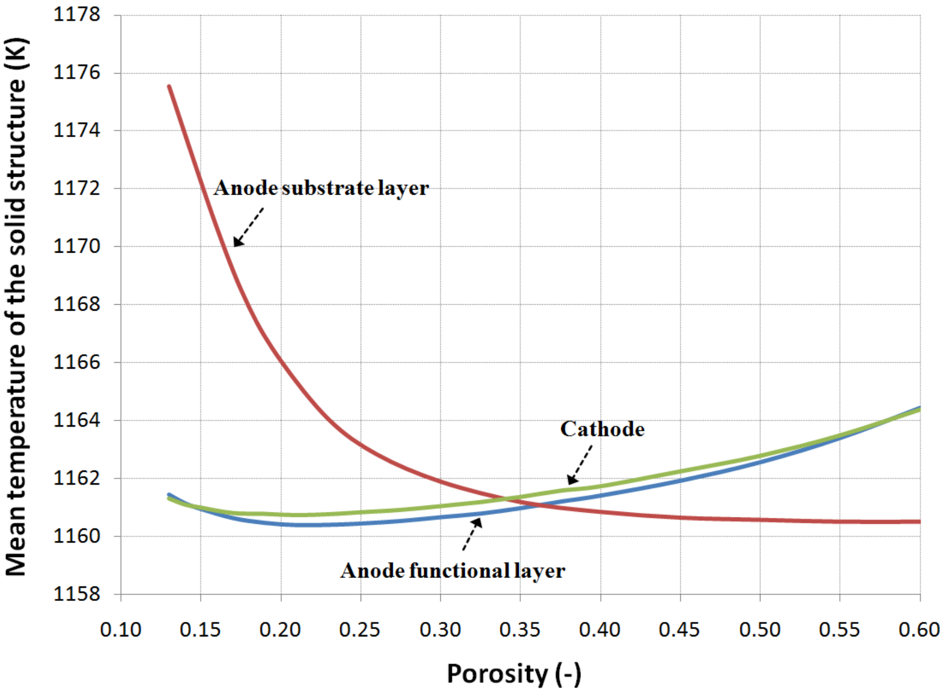

b

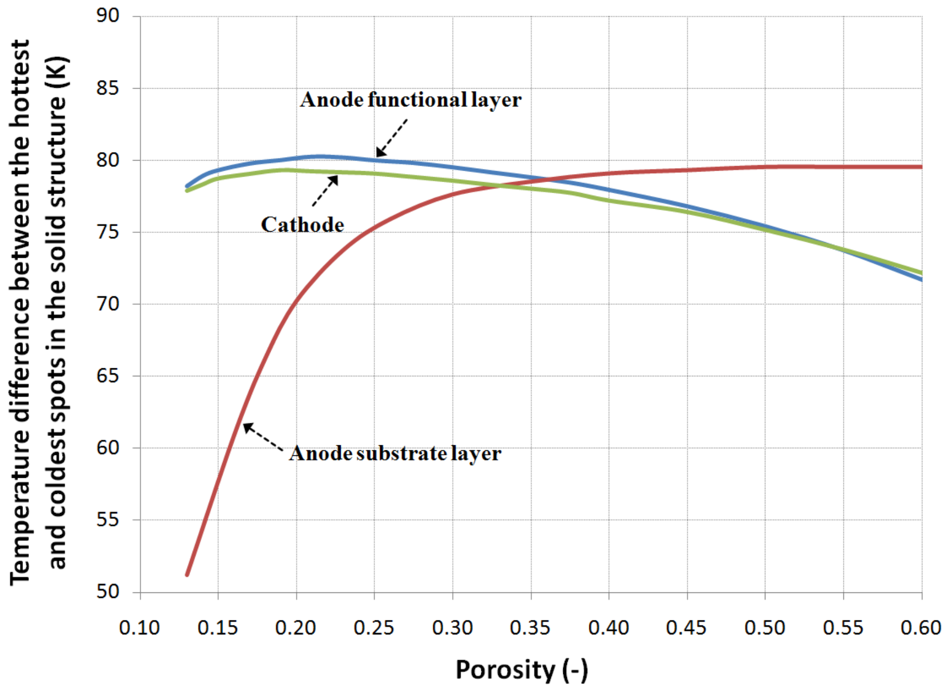

c

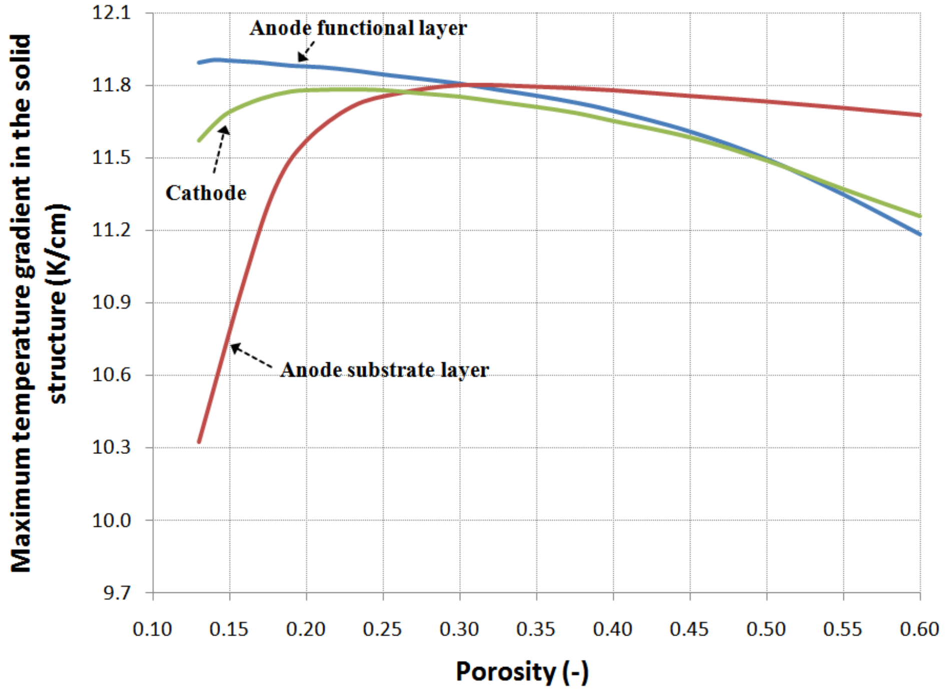

Figure 4.57: Effect of the porosity of the anode functional and substrate layers and the porosity of the cathode on the (a) mean temperature, (b) temperature difference between the hottest and coldest spots, and (c) maximum temperature gradient in the solid structure of the cell.

Table 4.8: Summary of the effect of the microstructure of porous composite electrodes on the mean temperature, the temperature difference between the hottest and coldest spots, and the maximum temperature gradient in the solid structure of the cell.

Microstructural variable		T_{mean} (K)		$T_{hottest}$-$T_{coldest}$ (K)		$(dT/dy)_{max}$ (K/cm)	
Variable	Range of investigation	Interval of changes	Magnitude of changes	Interval of changes	Magnitude of changes	Interval of changes	Magnitude of changes
Volume fraction of Ni in the anode functional layer at various particle size ratios	$0.46 \leq \varphi_{Ni,A,FL} \leq 0.8$ $\alpha_{A,FL}=0.5$	[1162.5,1173.1]	10.6	[52.3,75.5]	23.2	[9.1,11.5]	2.4
	$0.3 \leq \varphi_{Ni,A,FL} \leq 0.69$ $\alpha_{A,FL}=1$	[1160.8,1172.2]	11.4	[53.9,79.1]	25.2	[9.3,11.8]	2.5
	$0.18 \leq \varphi_{Ni,A,FL} \leq 0.52$ $\alpha_{A,FL}=2$	[1164.8,1174.2]	9.4	[52.0,71.8]	19.8	[9.4,11.3]	1.9
Volume fraction of LSM in the cathode at various particle size ratios	$0.46 \leq \varphi_{LSM,C} \leq 0.80$ $\alpha_{C}=0.5$	[1162.2,1171.2]	9.0	[58.2,76.4]	18.2	[10.0,11.6]	1.6
	$0.3 \leq \varphi_{LSM,C} \leq 0.69$ $\alpha_{C}=1$	[1160.8,1170.1]	9.3	[58.9,79.1]	20.2	[10.1,11.8]	1.7
	$0.18 \leq \varphi_{LSM,C} \leq 0.52$ $\alpha_{C}=2$	[1163.0,1170.3]	7.3	[61.1,75.1]	14.0	[10.3,11.5]	1.2
Diameter of electron-conducting particles (μm)	$0.1 \leq d_{Ni,A,FL} \leq 5.0$	[1159.0,1170.1]	11.1	[60.5,83.4]	22.9	[10.4,12.0]	1.6
	$0.1 \leq d_{LSM,C} \leq 5.0$	[1159.6,1166.4]	6.8	[68.5,81.8]	13.3	[11.1,12.0]	0.9
	$0.1 \leq d_{Ni,A,SL} \leq 5.0$	[1160.7,1166.6]	5.9	[69.0,79.3]	10.3	[11.5,11.8]	0.3
Thickness (μm)	$5 \leq \delta_{A,FL} \leq 150$	[1160.3,1174.5]	14.2	[51.6,80.1]	28.5	[9.5,11.8]	2.3
	$5 \leq \delta_{C} \leq 150$	[1160.8,1170.0]	9.2	[61.7,79.1]	17.4	[10.9,11.8]	0.9
	$50 \leq \delta_{A,SL} \leq 1500$	[1160.8,1162.1]	1.3	[77.9,79.1]	1.2	[11.6,11.9]	0.3
Porosity	$0.13 \leq \varepsilon_{A,FL} \leq 0.60$	[1160.4,1164.4]	4.0	[71.7,80.2]	8.5	[11.2,11.9]	0.7
	$0.13 \leq \varepsilon_{C} \leq 0.60$	[1160.7,1164.4]	3.7	[72.2,79.3]	7.1	[11.3,11.8]	0.5
	$0.13 \leq \varepsilon_{A,SL} \leq 0.60$	[1160.5,1175.5]	15.0	[51.2,79.5]	28.3	[10.3,11.8]	1.5

4.5 SOFC Systems

The performance of two SOFC systems proposed in chapter 3 was evaluated. First, the SOFC system I to generate heat and electric power in a WWTP and a residential dwelling was evaluated. Then, the SOFC system II for portable electric power generation was assessed.

4.5.1 Operation of the SOFC System I in a Wastewater Treatment Plant

The Robert O. Pickard Centre's WWTP in Ottawa, Ontario is selected as the plant to study the performance of the SOFC system I shown in Figure 4.58. This plant treats approximately 450,000 m^3/day domestic, commercial, and industrial wastewater in the city of Ottawa. Around 27,000 m^3/day biogas is produced through the anaerobic digestion process in this plant. In 1998, a conventional CHP system was installed in this plant. This system converts 32% of the chemical energy of the biogas produced into electric power and 48% into heat. The electric power generated is used for aeration blowers in the anaerobic digestion process. The heat generated is used to control the temperature of the digestion process and for the space heating. Of course, during periods of low heat demand, the heat generated is more than enough to meet the heat demand of the WWTP [19]. The average composition of the biogas produced in WWTPs in Ontario is adopted for the biogas produced in the Pickard plant. Three methods of the AGR, SR, and POX were considered for processing this gas. These three fuel processing methods suggest three different configurations for the SOFC system I (see Figure 4.58). The composition of the biogas processed by these methods is listed in Table 4.3. The SOFC stack employed in this system comprises ASC-3 cells produced by H.C. Starck Company. The insulation system I described in section 3.3 was also selected for insulating this stack. For the anode exchange current density of the ASC-3 cell, the value of γ_A, m_1, m_2, and $E_{act,A}$ in Equation (3.38) are 5×10^9, 1, -0.5, and 1.2×10^5, respectively [128]. For the cathode exchange current density of this cell, the value of 1.4×10^{10} (assumed), 0.25, and 1.4×10^5 [128] was used for γ_C, m_3, and $E_{act,C}$ in Equation (3.39), respectively. The input data for the computer simulation of this system is listed in Table 4.9.

The computer simulation results based on the cell, stack, and system input data in Table 4.9 is obtained and listed in Table 4.10. The results indicate that the electrical efficiency of all the configurations of the SOFC system I is higher than that of the conventional CHP system being operated in the Pickard Plant. Of course, the electrical efficiency of the configuration III with the POX fuel processor is only ≈1% higher than that of the existing system in the Pickard Plant. In contrast, configuration I with the AGR and configuration II with the SR fuel processor exhibit the electrical efficiency of ≈45.1% and ≈43.0%, respectively, which are significantly higher than the electrical efficiency of the existing CHP system in the Pickard Plant.

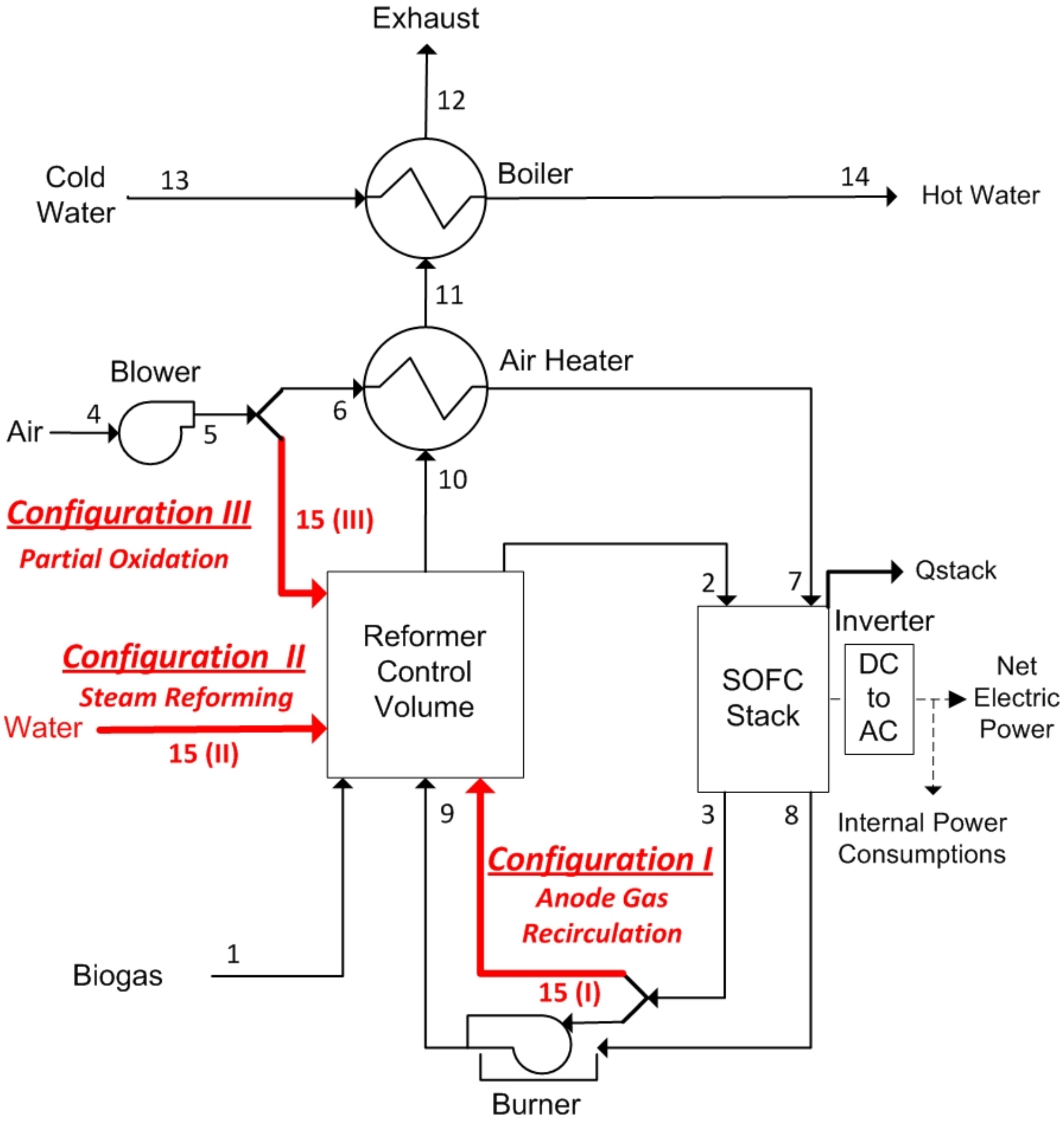

Figure 4.58: The SOFC system I with anode gas recirculation for configuration I, steam reforming for configuration II, and partial oxidation for configuration III.

Table 4.9: The design and operating parameters required for computer simulation of SOFC system I for operation in a WWTP.

Parameter		Value
Cell		
Operating voltage		0.7 V
Operating temperature		1073.15 K
Operating pressure		1 atm
Fuel utilization ratio		80%
Anode	thickness	518 μm
	porosity	0.33 (–)
	tortuosity	4 (–)
	pore size	0.66 μm
Cathode	thickness	45 μm
	porosity	0.33 (–)
	tortuosity	4 (–)
	pore size	0.66 μm
Electrical resistivity of anode		$\left(33557 exp(1392/T_s)\right)^{-1}$ Ω m
Electrical resistivity of cathode		$\left(12324.4 exp(-600/T_s)\right)^{-1}$ Ω m
Ionic resistivity of electrolyte		Equation (3.91)
Electrical resistivity of interconnect		$-6.25 \times 10^{-13} T_s^2 + 1.72 \times 10^{-9} T_s + 2.77 \times 10^{-8}$ Ω m
Electrolyte thickness		5 μm
Interconnect thickness		3 mm
Active length		10 cm
Active width		10 cm
Stack		
Solid insulation	thickness	50 mm
	thermal conductivity	0.025 W/m K
Emissivity of the outer metal surface		0.8 (–)
Temperatures of the inlet fuel and air		973.15 K
Temperatures of the outlet fuel and air		1173.15 K
Voltage drop due to stacking		2% of the voltage of each cell
Number of cells in parallel		1
System		
Flow rate of the inlet biogas		27,000 m^3/day
Temperature of the inlet biogas		30°C
Pressure drop		0.3 atm
Air blower efficiency		62.5%
Inlet cold water temperature		35°C
Outlet hot water temperature		95°C
Inverter efficiency		92%
Flue gas exhaust temperature		max($T_{dewPoint}$+50°C, $T_{W,Cold}$+20)

Table 4.10: The results of the computer simulation of the SOFC system I with three different configurations for operation in a WWTP.

Parameter	Configuration I	Configuration II	Configuration III
Net AC electric power generated (MW)	2.92	2.78	2.14
Heat generated (MW)	2.33	2.14	3.21
Electrical efficiency (%)	45.1	43.0	33.0
CHP efficiency (%)	84.1	78.6	86.8
Total exergy destruction of the system (MW)	3.61	3.78	4.28
Number of cells in the SOFC stack (–)	102,863	87,614	93,726
Flow rate of the hot water produced (kg/s)	10.10	9.23	13.89
Heat transfer from the SOFC stack (kW)	43.3	39.0	40.1
Reforming agent to the inlet biogas ratio (kg/kg)	0.93	0.38	1.38

In the case of operating the SOFC system I with configurations I and II, the electric power generated will be greater than the power required to operate the plant; and the extra electric power can be sold to the electrical grid. The results also indicate that the system with configuration III provides the highest CHP efficiency among the three configurations studied. Since the heat generated from the SOFC system with configurations I or II is enough for the WWTP, the high CHP efficiency of the configuration III may not be valuable for this application. The advantage of configuration II compared to the other configurations is the number of cells required for the SOFC stack. The number of cells for the SOFC system with configuration II is ≈17.4% less than that for the system with configuration I.

Overall, it seems that SOFC system I with configurations I and II are appropriate to be applied in the WWTP; however, a detailed economic analysis is required for selecting the best configuration.

4.5.1.1 Exergy Analysis

Figure 4.59 shows the share of each component of the SOFC system in the exergy destruction of the input biogas fuel to the system. The results indicate that the exergy destruction in the SOFC stack is not as significant as the exergy destruction in the air heater, reformer control volume, or boiler. In all three configurations of the system studied, the air heater has the largest share in the exergy destruction of the input biogas, followed by the boiler and burner for configuration I, the reformer control volume and burner for configuration II, and the boiler and reformer control volume for configuration III. There is a considerable potential to generate more electric power in all the configurations studied, especially in configuration III, if the SOFC system I is combined with other power generation systems and appropriately optimized.

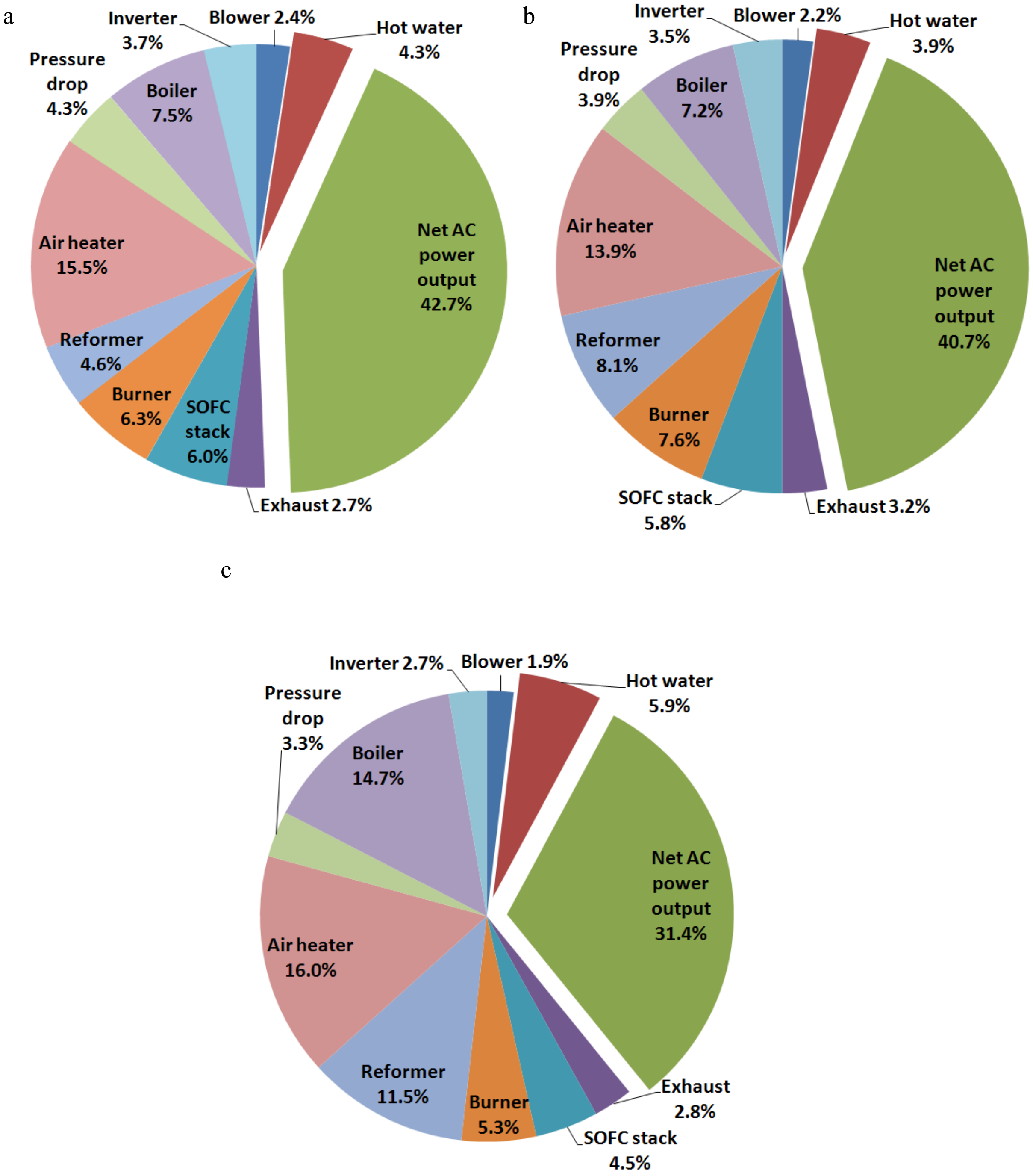

Figure 4.59: The exergy destruction of the input biogas fuel in each component of the SOFC system I with (a) configuration I, (b) configuration II, and (c) configuration III for operation in a WWTP.

4.5.2 Operation of the SOFC System I in Residential Dwellings

The performance of the SOFC system I was evaluated for operation in a residential dwelling. For this application, the TER generated in the SOFC system and the TER required for residential dwellings should be matched. The TER for residential dwellings can be determined based on space heating, space cooling, or domestic hot water demands and its magnitude is highly dependent on location, building type, design, usage pattern, time of day, and time of year [67]. The TER for hourly averaged annual domestic hot water for a 200 m^2 house can range from 0.7 to 1.0 [129]. The TER for space heating can be substantially higher (e.g. more than ten times) than that for domestic hot water in cold climates [67].

To evaluate the system, the average composition of the biogas produced in WWTPs in Ontario was adopted as the input fuel. Three methods of the AGR, SR, and POX were considered for the biogas processing. These three processing methods suggest three configurations for the SOFC system I (see Figure 4.58). The equilibrium composition of the biogas processed by these methods is listed in Table 4.3. The SOFC stack used in this system comprises 27 ESC-4 cells. The insulation system I described in section 3.3 was also selected for insulating this stack. For the anode exchange current density of the ESC-4 cell, the values of γ_A, m_1, m_2, and $E_{act,A}$ in Equation (3.38) are 1.4×10^{12}, 0.5, 0, and 1.294×10^{5}, respectively [130]. For the cathode exchange current density of this cell, the values of 2.9×10^{10} (assumed), 0.25, and 1.4×10^{5} [128] are used for γ_C, m_3, and $E_{act,C}$ in Equation (3.39), respectively. This system generates around 1 kW net AC electric power and the exhaust gases leave the systems at a temperature that is 50°C greater than the dew point temperature of the exhaust gases. The input data for the computer simulation of this system is listed in Table 4.11.

The computer simulation results based on the cell, stack, and system input data in Table 4.11 were obtained and are listed in Table 4.12. The minimum mass flow rate of the anode exit gas required for the reforming control volume of the system with configuration I depends on the fuel utilization ratio. The value of this flow rate is 0.63, 0.68, and 0.74 of the biogas mass flow rate at the entrance of the system at the fuel utilization ratios of 80%, 70%, and 60%, respectively. The minimum mass flow rate of the water and air required for the reforming control volume of the system with configurations II and III are predicted to be 0.29 and 1.08 of the biogas mass flow rate, respectively. These values are independent of the fuel utilization ratio. The results reveal that the mass flow rate of inlet biogas to the system with configurations I to III is ≈0.432 kg/hr, ≈0.436 kg/hr, and ≈0.536 kg/hr, respectively, at the fuel utilization ratio of 80%.

Table 4.11: The design and operating parameters required for computer simulation of the SOFC system I for operation in residential dwellings.

Parameter		Value
Cell		
Operating temperature		1123.15 K
Operating pressure		1 atm
Fuel utilization ratio		60%, 70%, or 80%
Anode and cathode	thickness	40 μm
	porosity	0.33 (–)
	tortuosity	4 (–)
	pore size	0.66 μm
Electrical resistivity of anode		1.25×10^{-5} Ω m [130]
Electrical resistivity of cathode		$\left(12324.4exp(-600/T_s)\right)^{-1}$ Ω m
Ionic resistivity of electrolyte		Equation (3.91)
Electrical resistivity of interconnect		$-6.25\times10^{-13}T_s^2+1.72\times10^{-9}T_s+2.77\times10^{-8}\Omega$ m
Electrolyte thickness		90 μm
Interconnect thickness		3 mm
Active length		10 cm
Active width		10 cm
Stack		
Solid insulation	thickness	50 mm
	thermal conductivity	0.025 W/m K
Emissivity of the outer metal surface		0.8 (–)
Temperatures of the inlet fuel and air		1023.15 K
Temperatures of the outlet fuel and air		1198.15 K
Number of ESC-4 cells		27
Number of cells in parallel		1
Voltage drop due to stacking		5% of the voltage of each cell
System		
Net AC electric power		≈ 1 kWe
Pressure drop		0.3 bar
Air blower efficiency		62.5%
Inlet cold water temperature		40°C
Outlet hot water temperature		90°C
Inverter efficiency		92%
Flue gas exhaust temperature		Max($T_{dewPoint}$+50°C, $T_{W,Cold}$+20)

The system with configuration I exhibits a net AC electrical efficiency of 42.4% at the fuel utilization ratio of 80%, followed by the system with configuration II with 41.7%, and the system with configuration III with 33.9%. The system with configuration III provides the highest CHP efficiency among the configurations studied, followed by the system with configurations I and II. At the fuel utilization ratio of 80%, the CHP efficiency of the system with configurations I to III is 76.9%, 72.9%, and 80.5%, respectively. The TER of the system with configurations I and II at the fuel utilization ratio of 70% and 80% is well-matched with the TER based on the domestic hot water demands for single-family detached dwellings [129]. The studies show that the TER of the system with configuration III is suitable for this application at the fuel utilization ratio of 90%. The excess air required for thermal management of the SOFC stack is lowest for the system with configuration II. Therefore, the size and initial investment cost for the blower, air heater, and burner is the lowest for this configuration. The voltage of the system with configuration II is the highest among the configurations studied. At the fuel utilization ratio of 80%, the voltage level reaches around 16.5 V for the system with configuration II and 16.3 V for the system with configurations I and III. The total exergy destructions in the system with configurations I and II are very close, especially at fuel utilization ratios greater than 80%, and are substantially less than that in the system with configuration III. The studies also indicate that depending on the fuel utilization ratio and the system configuration, 10%-16% of the electric power generated in the SOFC stack would be consumed in the air blower.

Table 4.12: The results of the computer simulation of the SOFC system I with three different configurations for operation in residential dwellings.

	Configuration I			Configuration II			Configuration III		
Fuel utilization ratio (%)	80	70	60	80	70	60	80	70	60
Reforming agent to biogas ratio (kg/kg)	0.63	0.68	0.74	0.29	0.29	0.29	1.08	1.08	1.08
Biogas mass flow rate (kg/hr)	0.432	0.443	0.475	0.436	0.454	0.508	0.536	0.59	0.662
Net AC electrical efficiency (%)	42.4	40.5	37.5	41.7	38.7	34.5	33.9	30.7	27.4
CHP efficiency (%)	77.5	78.4	80.3	72.9	75.1	77.6	80.5	82.5	84.5
TER (–)	0.81	0.94	1.15	0.75	0.94	1.25	1.38	1.68	2.09
Excess air (–)	5.2	4.2	3.3	4.9	3.9	3.1	5.1	4.2	3.4
Operating voltage of the system (V)	16.3	16.9	17.3	16.5	17.1	17.5	16.3	16.7	17.1
Total exergy destruction in the system (W)	1338	1401	1568	1369	1491	1751	1858	2122	2473
Blower input power (W)	156	132	119	141	118	105	158	145	132
Hot water produced (kg/hr)	13.5	15.2	18.5	12.2	15.0	19.8	22.6	27.6	34.3

4.5.2.1 Exergy Analysis

Figure 4.60 shows the share of each component of SOFC system I in the exergy destruction of the input biogas fuel to the system. The results indicate that the exergy destruction in the SOFC stack is not as significant as the exergy destruction in the air heater. In all the three configurations of the system studied, the air heater has the largest share in the exergy destruction of the input biogas, followed by the SOFC stack and burner/boiler for the system with configuration I, the SOFC stack and burner for the system with configuration II, and the boiler and SOFC stack for the system with configuration III. There is a considerable potential to generate more electric power in all the configurations studied, especially in configuration III, if the SOFC system I is combined with other power generation systems and appropriately optimized.

4.5.2.2 Sensitivity Analysis

Since the SOFC stack represents 30-50% of the initial investment cost of an SOFC system [131], the number of cells in the stack significantly contributes to economically optimize the SOFC system. Two key parameters that affect the number of cells are the cell voltage and fuel utilization ratio. In this section, the effect of the cell voltage at several fuel utilization ratios on the number of cells required for the SOFC stack to generate around 1 kW net AC electric power was studied through a sensitivity analysis. In addition to the number of cells, the cell voltage and fuel utilization ratio affect the TER, excess air, and electrical and CHP efficiencies of the system. Therefore, these parameters were also studied through the sensitivity analysis.

4.5.2.2.1 The Number of Cells and TER

Figure 4.61 shows the effects of the cell voltage at fuel utilization ratios of 60%, 70%, and 80% on the number of ESC-4 cells and TER of the SOFC system studied. In the range of the cell voltages investigated, the number of cells required for the SOFC stack to generate around 1 kW net AC electric power varies as a parabolic curve with the cell voltage. The cell voltages at which the minimum number of cells is obtained are listed in Table 4.13. At fuel utilization ratios between 60% and 80%, the cell voltage at which the minimum number of cells is obtained is between 0.55V and 0.62 V for the system with configuration I, 0.57V and 0.62 V for the system with configuration II, and 0.58 V and 0.61 V for the system with configuration III. At the fuel utilization ratio of 80%, the minimum number of cells is obtained 23, 23, and 24 cells for the system with configurations I to III, respectively.

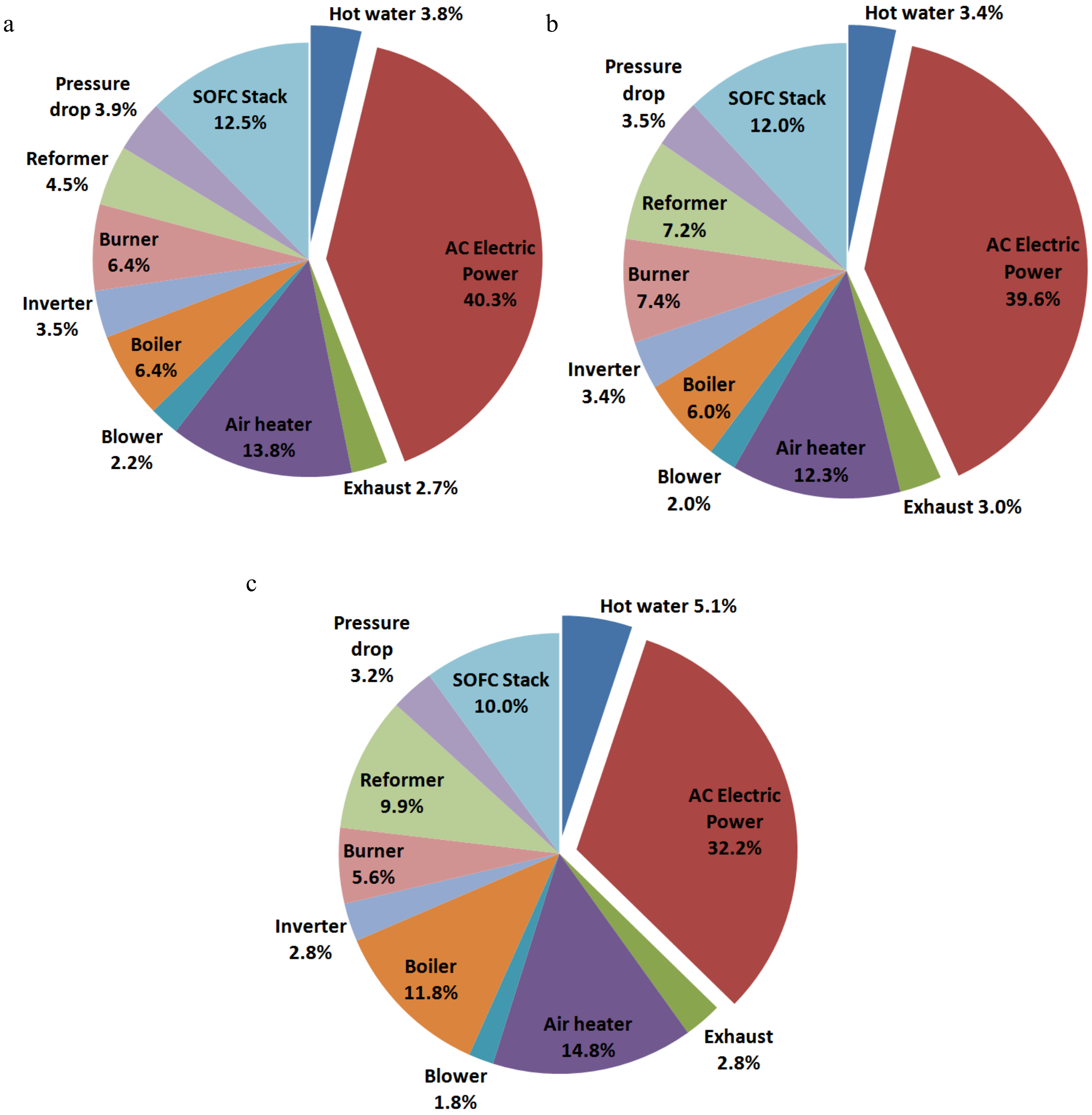

Figure 4.60: The exergy destruction of the input biogas fuel in each component of the SOFC system I with (a) configuration I, (b) configuration II, and (c) configuration III for operation in residential dwellings at the fuel utilization ratio of 80%.

a

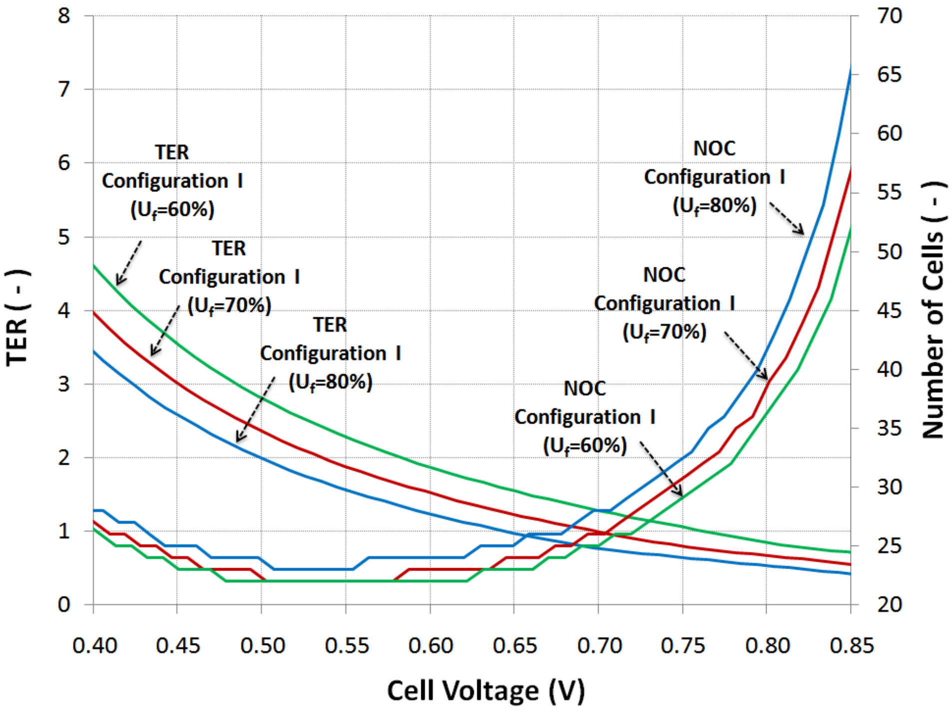

TER (-)
Number of Cells (-)
Cell Voltage (V)
0
1
2
3
4
5
6
7
8
20
25
30
35
40
45
50
55
60
65
70
0.40
0.45
0.50
0.55
0.60
0.65
0.70
0.75
0.80
0.85
TER
Configuration I
(U_f=60%)
TER
Configuration I
(U_f=70%)
TER
Configuration I
(U_f=80%)
NOC
Configuration I
(U_f=80%)
NOC
Configuration I
(U_f=70%)
NOC
Configuration I
(U_f=60%)

b

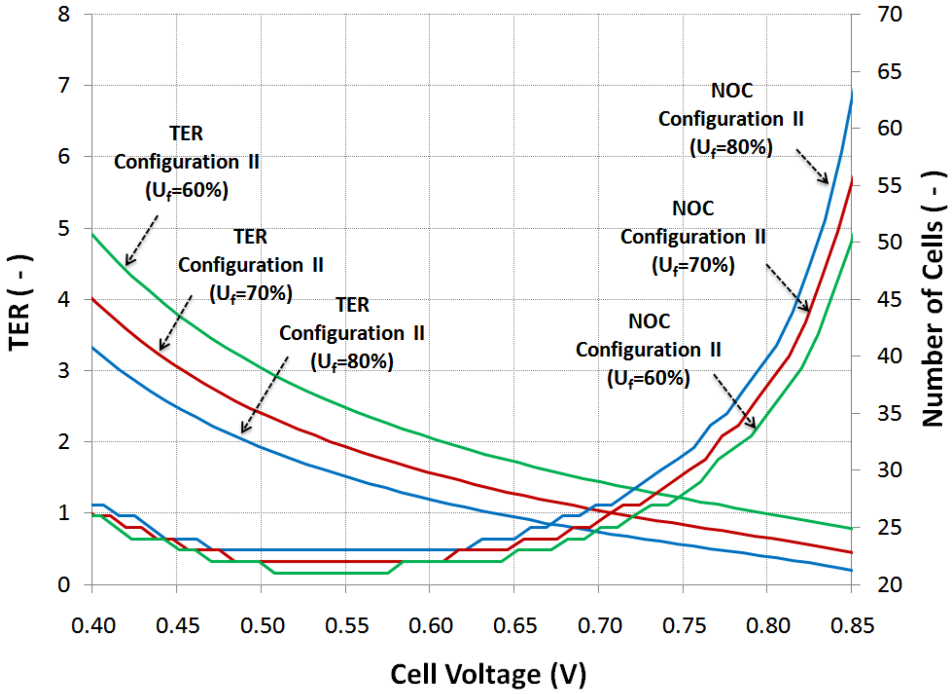

TER (-)
Number of Cells (-)
Cell Voltage (V)
0
1
2
3
4
5
6
7
8
20
25
30
35
40
45
50
55
60
65
70
0.40
0.45
0.50
0.55
0.60
0.65
0.70
0.75
0.80
0.85
TER
Configuration II
(U_f=60%)
TER
Configuration II
(U_f=70%)
TER
Configuration II
(U_f=80%)
NOC
Configuration II
(U_f=80%)
NOC
Configuration II
(U_f=70%)
NOC
Configuration II
(U_f=60%)

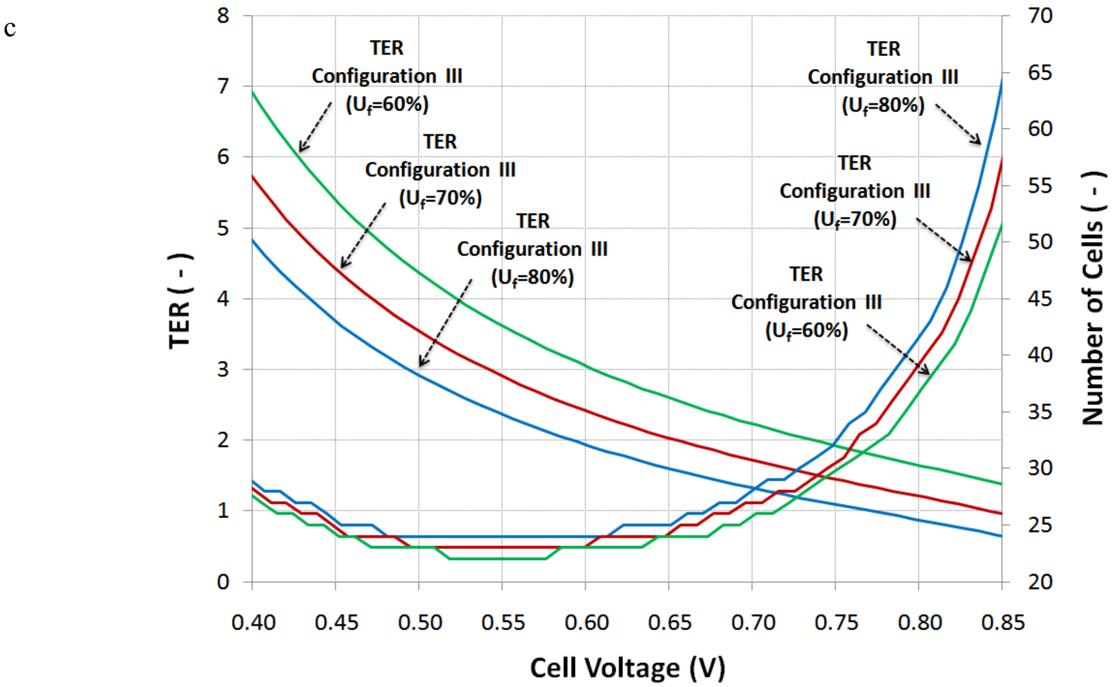

Figure 4.61: Effect of the cell voltage at fuel utilization ratios of 60%, 70%, and 80% on the number of cells and TER of the SOFC system with (a) configuration I, (b) configuration II, and (c) configuration III.

Table 4.13: The cell voltages at which the minimum number of cells is obtained for the Stack.

Variable	Configuration I			Configuration II			Configuration III		
Fuel utilization ratio (%)	60	70	80	60	70	80	60	70	80
Cell voltage (V)	0.62	0.58	0.55	0.57	0.61	0.62	0.58	0.60	0.61
Minimum number of cells	21	22	23	21	22	23	22	23	24

The cell voltages at which the minimum number of cells is obtained is important to economically optimize the SOFC system. Based on this voltage, the operating voltages of a cell can be divided into two groups. The voltages in group I are lower, and the voltages in group II are higher than the voltage at which the minimum number of cells is obtained. By decreasing the cell voltage, the number of cells required for the SOFC stack increases for group I and decreases for group II of the cell voltages. In the range of the fuel utilization ratios investigated, the number of cells decreases by decreasing the fuel utilization ratio for both groups of cell voltages.

The TER of the system with configurations studied increases progressively by decreasing the cell voltage. The TER also increases by decreasing the fuel utilization ratio. For group I of the cell voltages, the TER of all the configurations studied is greater than unity. It means that the heat produced in the system is more than the heat required for the domestic hot water demand for single-family detached dwellings.

4.5.2.2.2 Electrical and CHP Efficiencies

Figure 4.62 shows the effects of the cell voltage at fuel utilization ratios of 60%, 70%, and 80% on the electrical and CHP efficiencies of the SOFC system studied. In the range of the voltages investigated, an increase in the cell voltage leads to a linear increase in the net AC electrical efficiency of the system with configurations studied. In the range of the fuel utilization ratios investigated, the net AC electrical efficiency is higher at elevated fuel utilization ratios. The CHP efficiency of the system with configurations II and III decreases with an increase in the cell voltage. However, the CHP efficiency of the system with configuration I decreases to a certain value and then increases. For all the configurations studied, the variation in the CHP efficiency is not significant for group I of cell voltages. As a remarkable result, the electrical efficiency of the system for the cell voltages in group II is notably higher than that for the cell voltages in group I. For the system with configurations II and III, the CHP efficiency is slightly smaller for group II than group I of the cell voltages.

a

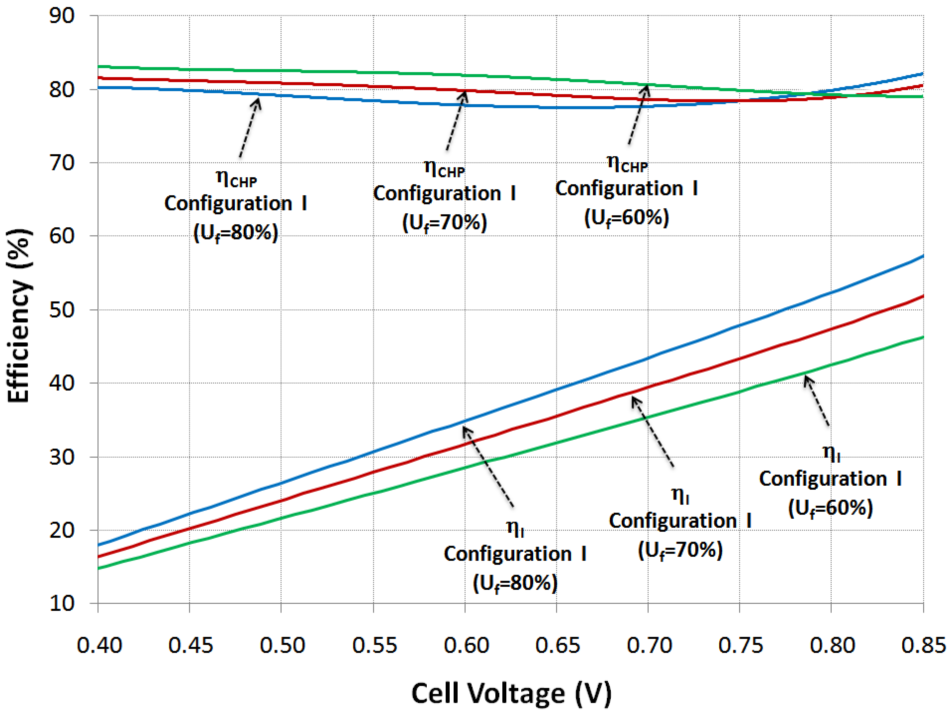

b

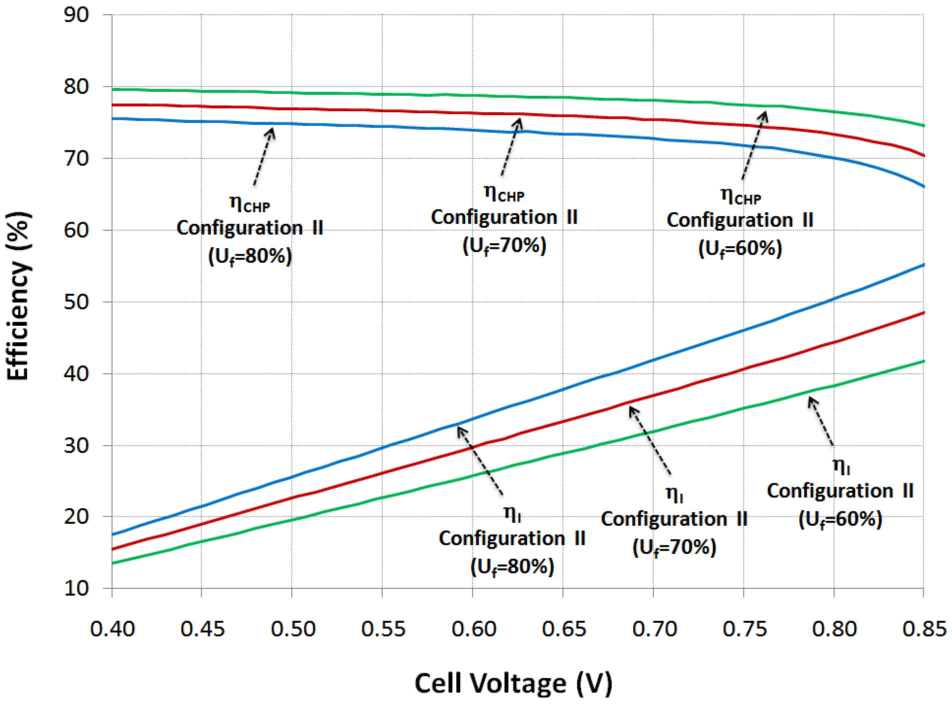

c

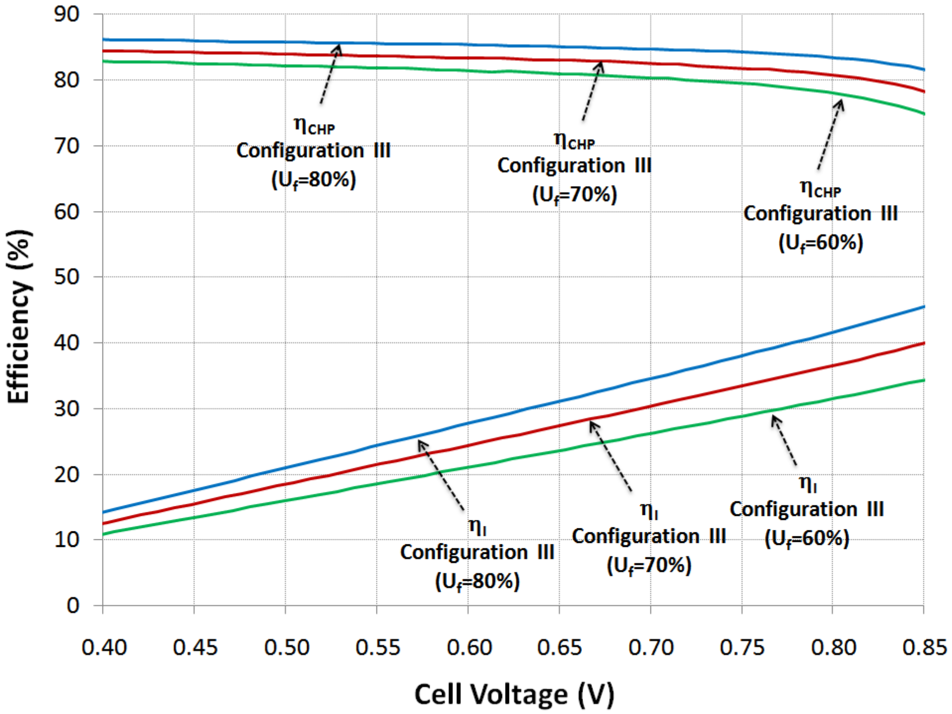

Figure 4.62: Effect of the cell voltage at fuel utilization ratios of 60%, 70%, and 80% on the net AC electrical and CHP efficiencies of the SOFC system with (a) configuration I, (b) configuration II, and (c) configuration III.

4.5.2.2.3 Biogas Fuel Consumption

The effect of the cell voltage at fuel utilization ratios of 60%, 70%, and 80% on the inlet biogas flow rate to the system is shown in Figure 4.63. As seen in this figure, by decreasing the cell voltage, the biogas mass flow rate increases progressively for all the configurations studied. The higher the fuel utilization ratio, the lower the biogas mass flow rate required for the SOFC system to generate around 1 kW AC electric power. If the amount of the biogas produced is limited to a certain value, this figure would be important to select an appropriate cell voltage and fuel utilization ratio for the system.

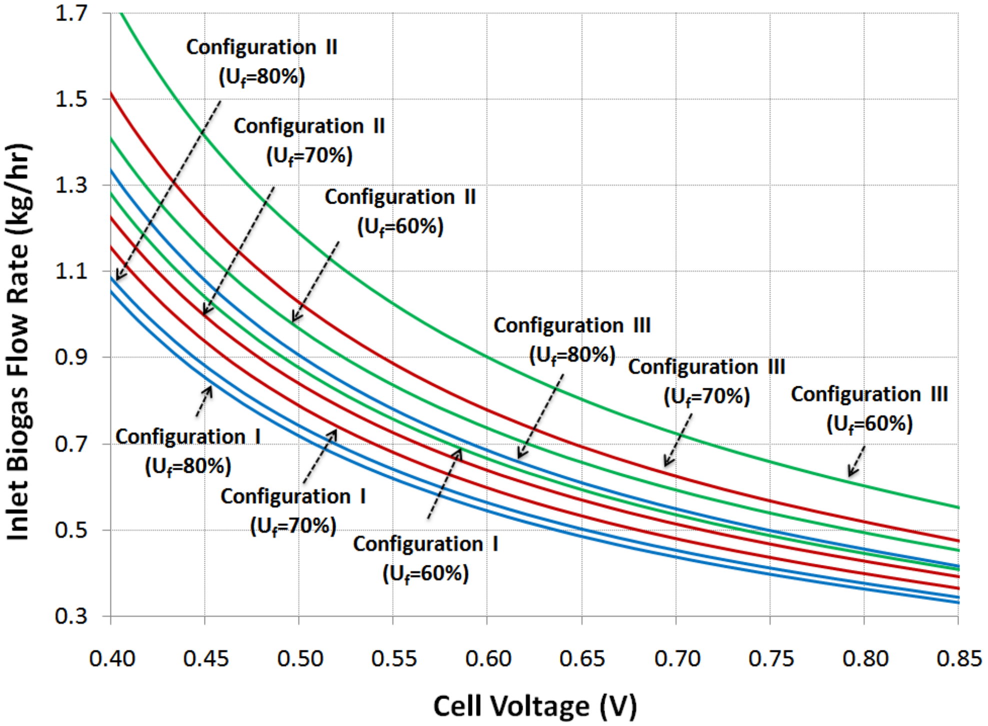

Figure 4.63: Effect of the cell voltage at fuel utilization ratios of 60%, 70%, and 80% on the inlet biogas flow rate to the SOFC system with configurations I to III.

4.5.2.2.4 Excess Air

The effect of the cell voltage at fuel utilization ratios of 60%, 70%, and 80% on the excess air required for thermal management of the SOFC stack for the system with configuration I is shown in Figure 4.64. An increase in the cell voltage leads to a decrease in the excess air; hence, the size and initial investment cost for the air heater, blower, and burner decreases with increasing the cell voltage. In the range of the fuel utilization ratios investigated, the excess air decreases by decreasing the fuel utilization ratio. These statements are also valid for the system with configurations II and III. Our studied show than the excess air for the system with configurations I and III is almost identical and a little greater than the excess air required for the system with configuration II.

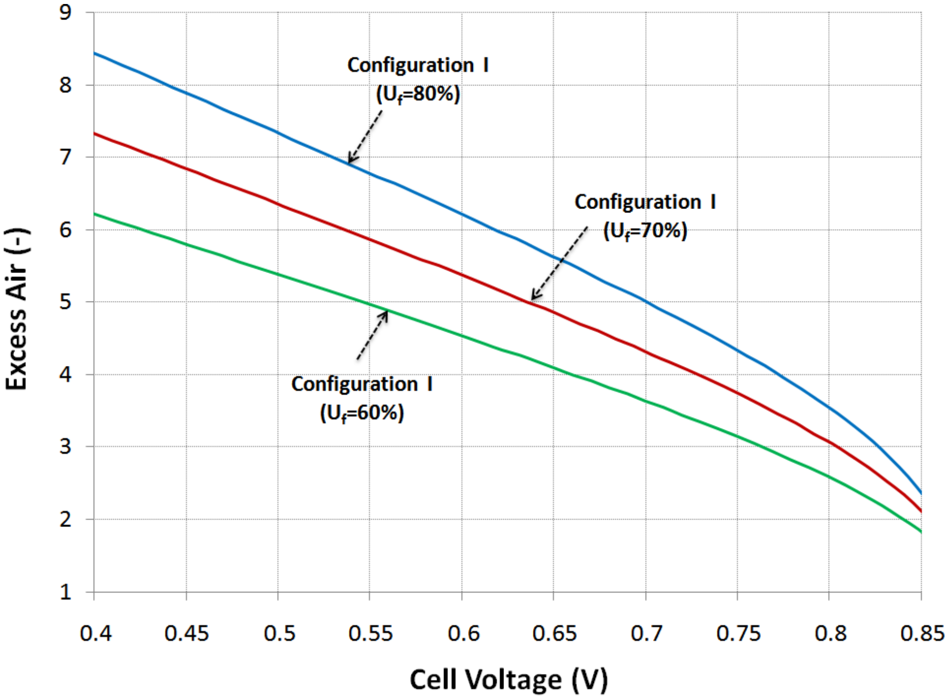

Figure 4.64: Effect of the cell voltage at fuel utilization ratios of 60%, 70%, and 80% on the excess air for the SOFC system with configuration I.

Overall, the results of the sensitivity analysis indicate that by decreasing the cell voltage in group I, the number of cells required for the SOFC stack and the excess air required for thermal management of the stack increase. Hence, the size and initial investment cost of the system increase. The decrease in the cell voltage in this group also leads to a decrease in the electrical efficiency and an increase in the biogas consumption; however, the CHP efficiency remains almost constant. The TER of the system also exceeds the TER required for the domestic hot water demands for single-family detached dwellings. Therefore, the optimum cell voltage is not in this group of cell voltages and should be searched in group II. It means that the lowest cell design voltage is limited to the cell voltage at which the minimum number of cells for the SOFC stack is obtained. In group II of the cell voltages, an increase in the cell voltage leads to an increase in the number of cells, but the biogas consumption and excess air decrease. Therefore, there is an optimum cell voltage in this group that should be determined by a detailed economic analysis.

4.5.3 SOFC System II for Portable Applications

The performance of the SOFC system II illustrated in Figure 3.14 was evaluated for portable electric power generation. The input fuel to this system is the liquid ammonia stored in a cylinder with a capacity of 0.8 liters. The SOFC stack employed in this system comprises ASC-3 cells to generate a net DC electric power of around 100 W. The vacuum layer described in section 3.3 is also selected as the thermal insulation system of the stack. The input data for the computer simulation of this system is listed in Table 4.14.

To evaluate this system, the cell voltage and fuel utilization ratio should be chosen. For this purpose, a sensitivity analysis was performed to determine the effects of these two parameters on key performance parameters of the system.

4.5.3.1 Sensitivity Analysis

The effects of the cell voltage and fuel utilization ratio on the number of cells required for the SOFC stack, first- and second-law efficiencies, system voltage, excess air, and duration of operation of the system were studied.

4.5.3.1.1 Number of Cells

The effect of the cell voltage at fuel utilization ratios of 60%, 70%, and 80% on the number of cells required in the SOFC stack to generate net DC electric power of around 100 W is shown in Figure 4.65. With an increase in the cell voltage, the number of cells varies as a concave upward parabolic curve. The minimum number of cells happens at the cell voltage of ≈0.57 V. In this voltage, the number of cells in the SOFC stack is 24, 23, and 22 at the fuel utilization ratios of 80%, 70%, and 60%, respectively. The cell voltage at which the minimum number of cells is obtained is important to select an appropriate cell voltage. Considering this voltage, the operating voltages of a cell can be divided into two groups. The operating voltages of group I are lower, and the operating voltages of group II are more than this voltage. These two groups are shown in Figure 4.65.

In group I of the cell voltages, a decrease in the voltage leads to a sharp increase in the number of cells. Accordingly, the size of the SOFC stack increases, which is not suitable for a portable system. In group II of the cell voltages, the number of cells and size of the SOFC stack decreases by decreasing the voltage. In this group, the number of cell also decreases by decreasing the fuel utilization ratio. At the cell voltage of 0.7 V, the number of cells reduces around 12% if the fuel utilization ratio is reduced from 80% to 60%.

Table 4.14: The design and operating parameters required for computer simulation of SOFC system II.

Parameter		Value
Cell		
Operating temperature		1073 K
Operating pressure		1 atm
Anode	thickness	518 μm
	porosity	0.33 (–)
	tortuosity	4 (–)
	pore size	0.66 μm
Cathode	thickness	45 μm
	porosity	0.33 (–)
	tortuosity	4 (–)
	pore size	0.66 μm
Electrical resistivity of anode		$\left(33557 exp(1392/T_s)\right)^{-1}$ Ω m
Electrical resistivity of cathode		$\left(12324.4 exp(-600/T_s)\right)^{-1}$ Ω m
Ionic resistivity of electrolyte		Equation (3.91)
Electrical resistivity of interconnect		$-6.25 \times 10^{-13} T_s^2 + 1.72 \times 10^{-9} T_s + 2.77 \times 10^{-8}$ Ω m
Electrolyte thickness		5 μm
Interconnect thickness		3 mm
Active length		3 cm
Active width		3 cm
Stack		
Emissivity of the vacuum layer [34]	Hot surface	0.03 (–)
	Cold surface	0.01 (–)
Emissivity of the outer metal surface		0.8 (–)
Temperatures of the inlet fuel and air		973 K
Temperatures of the outlet fuel and air		1173 K
Number of cells in parallel		1
Voltage drop due to stacking		5% of the voltage of each cell
System		
Net DC electric power generation		100 W
Estimated power for the control system		20 W
Pressure drop		0.3 bar
Air blower efficiency		55%
Capacity of the ammonia cylinder		0.8 litres
Capacity of the water cylinder		30 cc
Ammonia to water mixing ratio		19

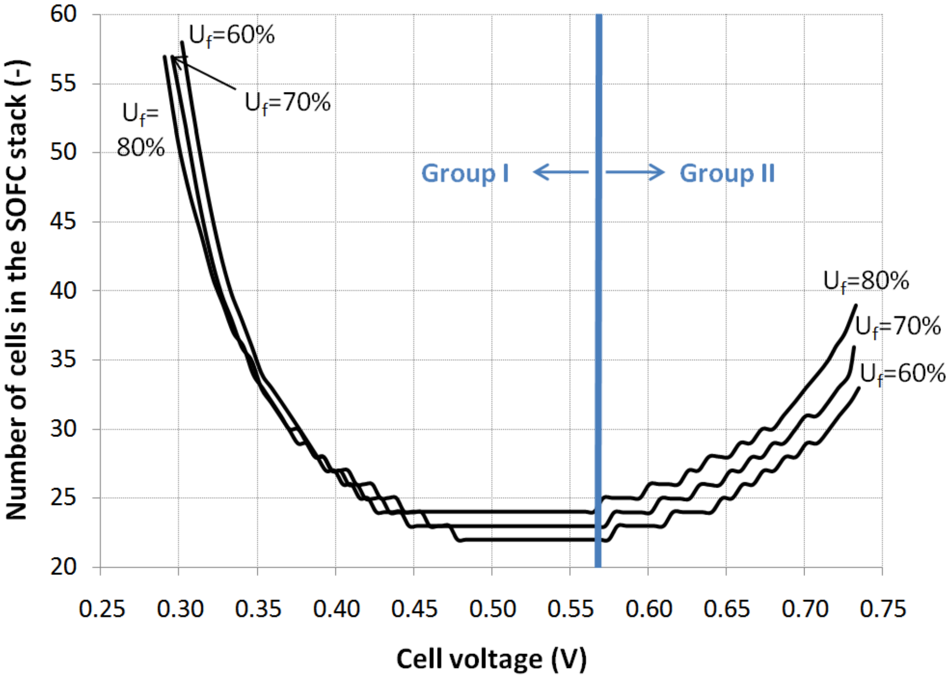

Figure 4.65: Effect of the cell voltage at fuel utilization ratios of 60%, 70%, and 80% on the number of cells in the SOFC stack of the SOFC system II.

4.5.3.1.2 First- and Second-law Efficiencies

The effects of the cell voltage at fuel utilization ratios of 60%, 70%, and 80% on the first- and second-law efficiencies of the system are shown in Figures 4.66 and 4.67. In the range of the cell voltages investigated, the first- and second-law efficiencies of the system increase linearly by increasing the cell voltage. In the range of the fuel utilization ratio that was investigated, the higher the fuel utilization ratio, the higher the first- and second-law efficiencies. The effect of the fuel utilization ratio on first- and second-law efficiencies is more significant at elevated cell voltages. The cell voltages in group II provide higher first- and second-law efficiencies of the system in comparison with the voltages in group I.

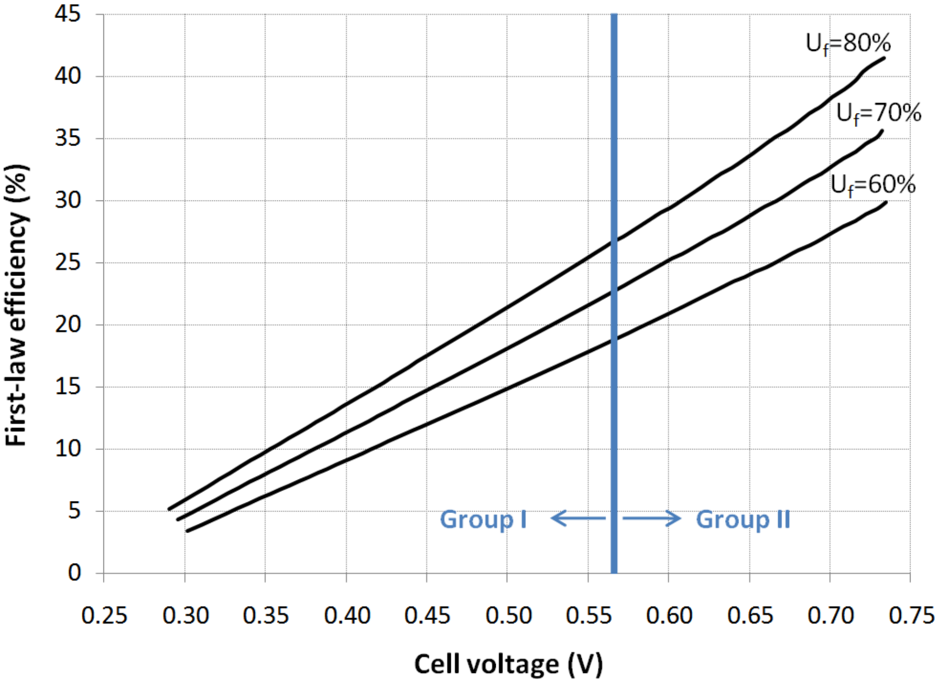

Figure 4.66: Effect of the cell voltage at fuel utilization ratios of 60%, 70%, and 80% on the first-law efficiency of the SOFC system II.

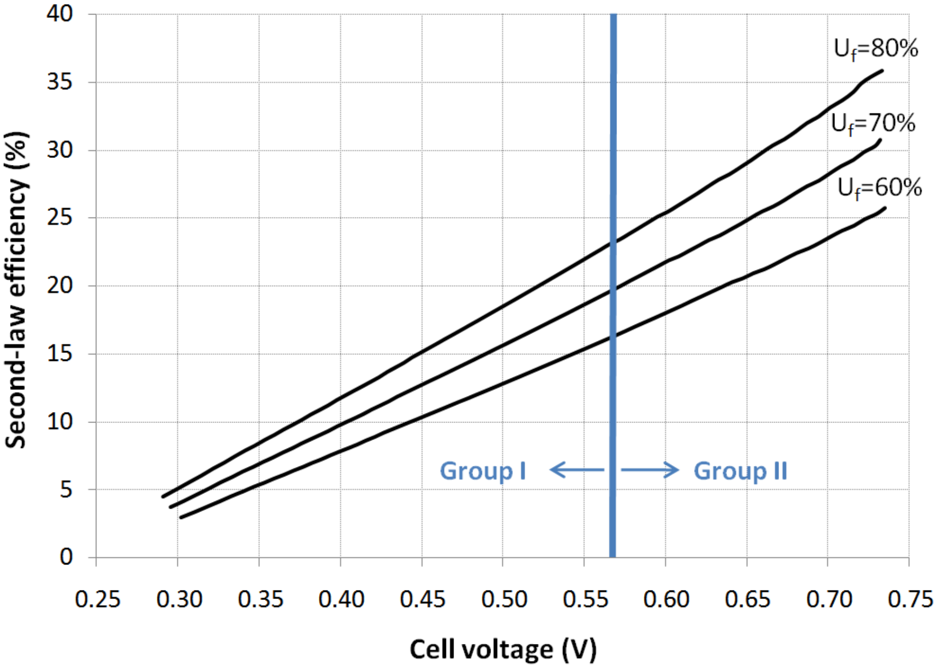

Figure 4.67: Effect of the cell voltage at fuel utilization ratios of 60%, 70%, and 80% on the second-law efficiency of the SOFC system II.

4.5.3.1.3 System Voltage

The effect of the cell voltage at fuel utilization ratios of 60%, 70%, and 80% on the operating voltage of the SOFC system II is shown in Figure 4.68. With an increase in the cell voltage, the voltage of the system decreases to a certain value and then increases. Since a high operating voltage for a portable power generation system is usually desirable, selecting a cell voltage from the cell voltages in group II may be preferred compared to the cell voltages in group I. In group II, the effect of the fuel utilization ratio on the system voltage is significant, especially at elevated cell voltages. At the cell voltage of 0.7 V, the system voltage increases around 12% if the fuel utilization ratio increases from 60% to 80%.

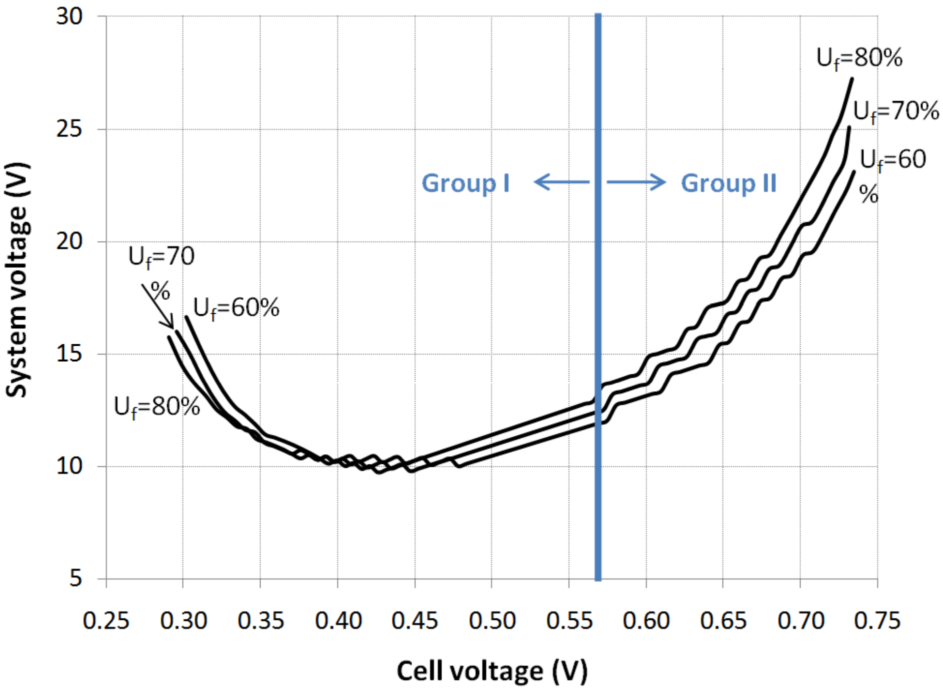

Figure 4.68: Effect of the cell voltage at fuel utilization ratios of 60%, 70%, and 80% on the operating voltage of the SOFC system II.

4.5.3.1.4 Excess Air

The effect of the cell voltage at fuel utilization ratios of 60%, 70%, and 80% on the excess air required to control the temperature of the SOFC stack is shown in Figure 4.69. The increase in the cell voltage leads to a decrease in the excess air and, accordingly, the size and cost of the heat exchanger, burner and air blower in the system decreases. The effect of the fuel utilization ratio on the excess air reduces at the elevated cell voltages. For the cell voltages less than 0.72 V, the higher the fuel utilization ratio the higher the excess air required for the SOFC stack.

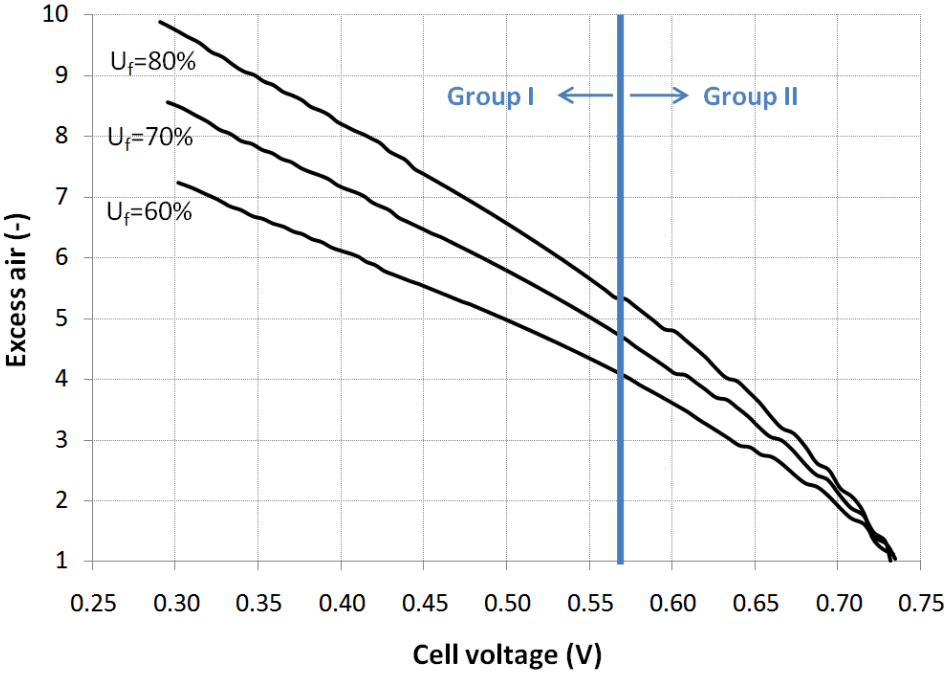

Figure 4.69: Effect of the cell voltage at fuel utilization ratios of 60%, 70%, and 80% on the excess air required to control the temperature of the SOFC stack in the SOFC system II.

4.5.3.1.5 Duration of Operation of the System

The effect of the cell voltage at fuel utilization ratios of 60%, 70%, and 80% on the duration of operation of the system with a full 0.8 liters ammonia cylinder is shown in Figure 4.70. The duration of system operation increases by increasing the cell voltage and fuel utilization ratio. The effect of the fuel utilization ratio on the duration of operation is more significant for group II of the cell voltages.

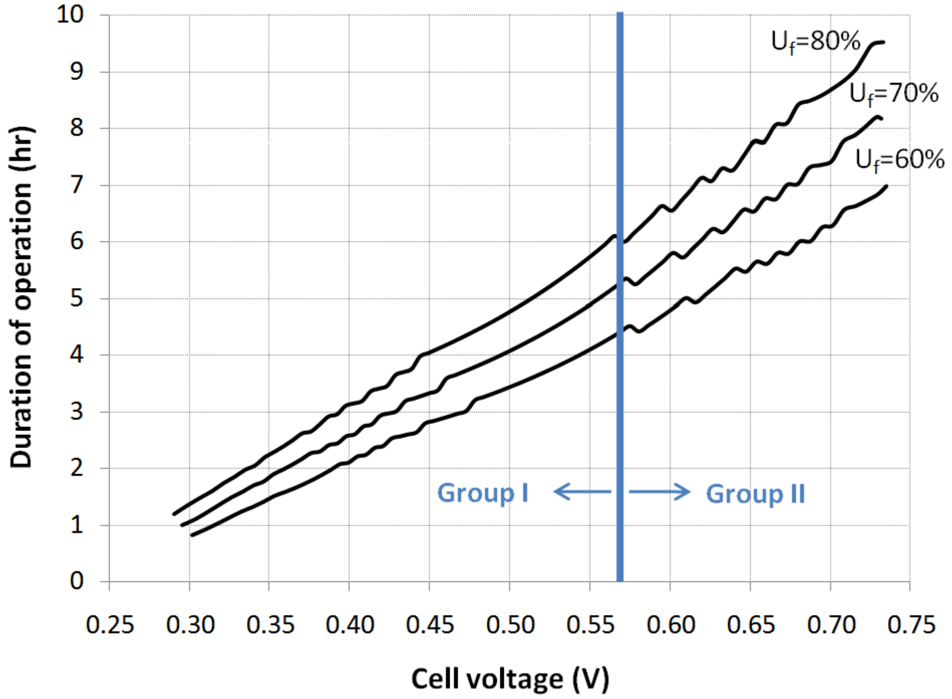

Figure 4.70: Effect of the cell voltage at fuel utilization ratios of 60%, 70%, and 80% on the duration of operating of the SOFC system II with a full 0.8 litres cylinder of ammonia.

Overall, in group I of the cell voltage, by decreasing the cell voltage, the number of cells and excess air required for the SOFC stack increases. Hence, the size and initial investment cost of the SOFC stack, heat exchanger, air blower, and burner increase. The decrease in the cell voltage in this group leads also to a decrease in the first- and second-law efficiencies and the duration of portable system operation. Therefore, the optimum cell voltage is not found in this group and should be searched in group II of the cell voltages. Indeed, the minimum cell voltage (mCV) that is logical to be selected to design the system is limited to the cell voltage at which the minimum number of cells in the SOFC stack is obtained. In group II of the cell voltages, by increasing the cell voltage, the number of cells increases; accordingly, the size and cost of the SOFC stack increases. By contrast, the increase in the cell voltage leads to a significant increase in the duration of operation and the operating voltage of the system, and a significant decrease in the size of the heat exchanger, air blower, and burner due to reduction in the excess air required for thermal management of the stack. Although a detailed economic analysis is required to determine the cell design voltage, we select the cell voltage of 0.73 V.

For the cell, stack, and system design and operating parameters listed in Table 4.14, the key performance parameters of the SOFC system II at the cell voltage of 0.73 V and mCV were obtained. These key performance parameters have been reported in Table 4.15. The results indicate that the number of cells for the SOFC stack increases five cells and the duration of operation of the portable system increases around three hours if the fuel utilization ratio increases from 60% to 80%.

At the cell voltage of 0.73 V, the first-law efficiency of the system is 41.1%, 35.1%, and 29.3% at the fuel utilization ratios of 80%, 70%, and 60%, respectively. At the fuel utilization ratio of 80%, the excess air required for thermal management of the SOFC stack and the system voltage is predicted to be 1.17 and 25.6 V, respectively. The electric power required for the air blower is also 6.7 W.

Table 4.15: The computer simulation results for a 100 W portable SOFC system, operated at the cell voltage of 0.73 V and mCV=0.57 V.

Parameter	Fuel utilization ratio (%)			Fuel utilization ratio (%)		
	80	70	60	80	70	60
Cell design voltage (V)	0.73	0.73	0.73	0.57	0.57	0.57
Number of cells in the SOFC stack (-)	37	34	32	24	23	22
1st law efficiency (%)	41.1	35.1	29.3	26.8	23.2	19.4
2nd law efficiency (%)	35.4	30.3	25.3	23.1	20.0	16.7
Excess air (-)	1.17	1.37	1.32	5.3	4.6	4.0
Duration of operation with a 0.8 l ammonia cylinder	9:34'	8:08'	6:47'	6:07'	5:21'	4:31'
System voltage (V)	25.6	23.6	22.2	12.9	12.5	12
Blower input power (W)	6.7	10.3	14	33.0	36.0	40.8

4.5.3.2 Exergy Analysis

The share of each component in the SOFC system II in the exergy destruction of the ammonia fuel at the cell voltage of 0.73 V and fuel utilization ratio of 80% is shown in Figure 4.71. Almost 35.4% of the ammonia’s exergy is converted to DC electric power in the system. Among the components of the system, the SOFC stack has the largest share in exergy destruction of the ammonia fuel with 26.6%, followed by the heat exchanger with 13.6% and burner with 9.6%. There is a potential to generate additional electric power if this system is combined with other power generation systems such as a thermoelectric device. However, the size and cost of the portable system may increase.

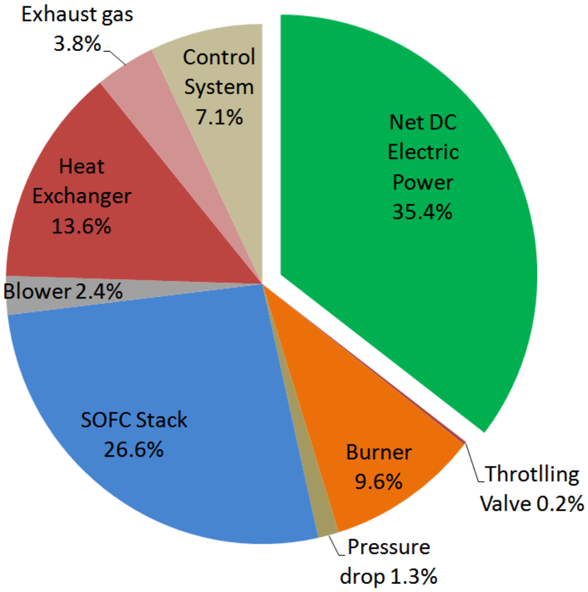

Figure 4.71: The share of each component in the SOFC system II in exergy destruction of the ammonia fuel at the cell voltage of 0.73 V and fuel utilization ratio of 80%.

4.6 Summary

The carbon deposition curves at several temperatures and pressure were obtained and demonstrated in the C-H-O ternary diagram. On the basis of these curves, the carbon deposition and safe regions in this diagram were introduced. It was shown that the location of biogas lies in the carbon deposition region. To transfer the location of the biogas to the safe region, three fuel processing methods of the AGR, SR, and POX were considered and the equilibrium compositions of the biogas processed by these three methods were determined.

The properties of microstructure of porous composite electrodes were studied at several volume fractions of the electron-conducting particles, particle size ratios, and sizes of the electron conducting particles. The results of this study showed that the electrochemical active area per unit volume is maximized at the average volume fraction of the electron- and ion-conducting particles at percolation thresholds. This area increases when the particle size ratio approaches unity or the size of the electron-conducting particles decreases. The maximum electrochemical active area can be obtained when the size and volume fraction of electron- and ion-conducting particles is identical. For the particle size ratio of unity, the average pore size remains constant throughout the entire range of the volume fraction of electron-conducting particles, and decreases linearly with a decrease in the size of the electron-conducting particles. The effective resistivity of YSZ is greater, by several orders of magnitude, than that of Ni or LSM. Hence, the effective resistivity of YSZ plays an important role in determining the optimum microstructure of the electrode rather than the effective resistivities of Ni or LSM. The effective resistivity of YSZ can be decreased with a decrease in the volume fraction of electron-conducting particles or an increase in the particle size ratio.

An anode-supported planar cell with given microstructures of the porous composite anode (Ni-YSZ) and cathode (LSM-YSZ) operated at a cell voltage of 0.7, fuel utilization ratio of 80%, and excess air of 10, was simulated on the basis of the combined micro- and macro model of the cell. The gas obtained from processing biogas by AGR method at a temperature of 1073 K and pressure of 1 atm was used as the inlet fuel to the cell studied. The results of the simulation indicated that the first and second law efficiencies of this cell are 41.7% and 91.3%, respectively. The mean total power density generated in the cell is 0.39 W/cm^2, 73% of which is contributed from H_2 and the remaining is from the CO electrochemical reaction. The distribution of the physical, chemical, and electrochemical variables along the cell length revealed that the Reynolds number of the air and fuel streams passing through the channels is less than 100; hence, the fuel and air streams are laminar. The Péclet numbers corresponding to the mass and energy transports in the air and fuel streams are substantially greater than unity; hence, the heat and mass diffusions in the air and fuel streams along the length of the cell are negligible. The temperature of the fuel stream approaches the temperature of the solid structure where $y \approx 0.1L$, and there is an overlap between the temperatures of the fuel stream and the solid structure in the rest of the cell length. The temperature of the air stream slowly approaches the temperature of the solid structure, and the overlap between the temperatures of the air stream and solid structure occurs at the end of the cell length. The highest local temperature of the solid structure is 1192.8 K, and the temperature difference between the hottest and coldest spots of the solid structure is 79.1 K. The maximum temperature gradient of the solid structure is also 11.8 K/cm. The mass flow rate of the air stream is ≈45 times higher than that of the fuel stream at the excess air of 10. This leads to a maximum pressure difference of 614 Pa between the fuel and air streams; thus, a change in the height of the air or fuel channels may be required. The mole fraction of CH_4 in the fuel stream approaches zero where $y \approx 0.2L$. Therefore, the steam reforming reaction occurs mainly at the entrance of the fuel channel where $y < 0.2L$. The ratio of the local power densities generated due to the H_2 and CO electrochemical reactions increases along the length of the cell. Indeed, the contribution of the H_2 electrochemical reaction in the local total power density reaches from 68% at the beginning to 76% at the end of the cell length. The anode have the highest contribution in the local total polarization resistance, followed by the cathode, electrolyte, and interconnect. The solid structure has the main contribution in the local total exergy destruction, followed by the air stream and fuel. The distribution of the physical, chemical, and electrochemical variables along the cell thickness also revealed that the consumption of electric current increases along the cathode thickness from the cathode and interconnect interface to the cathode and electrolyte interface. At the beginning of the cell length, more than 45% of the electric current is consumed within 20% of the cathode thickness near the cathode and electrolyte interface. Therefore, more than 45% of the oxygen electroreduction reaction takes place within 20% of the cathode near the cathode and electrolyte interface. Moreover, less than 10% of the electric current is consumed within 20% of the cathode thickness near the cathode and interconnect interface. The electric current generation increases along the thickness of the anode functional layer. At the beginning of the cell length, more than 34% of the electric current is generated within 20% of the anode thickness near the anode and electrolyte interface. Thus, more than 34% of the H_2 and CO electrooxidation reactions take place within 20% of the anode functional layer near the anode and electrolyte interface. Moreover, less than 13% of the electric current is generated within 20% of the thickness of the anode functional layer near the interface of the anode functional and substrate layers.

To study the effect of the microstructure of porous composite electrodes on the cell performance, several anode-supported co-flow planar cells with various microstructures of electrodes were simulated on the basis of the combined micro- and macro-model of the cell. The results of this study revealed that there is an optimum value for the Ni volume fraction at which the mean total polarization resistance is minimized. There is also an optimum value for this variable at which the cell mean power density is maximized. For an anode functional layer with an optimum Ni volume fraction, the optimum particle size ratio is always equal to 1. There is an optimum value for the variables of the thickness and porosity of the anode functional layer at which the mean total polarization resistance is minimized. There is also an optimum value for these variables at which the mean power density is maximized. With a decrease in the size of Ni particles to even 0.1 μm, the mean total polarization resistance decreases and the mean power density increases. In the range investigated for microstructure of the anode substrate layer, the mean total polarization resistance decreases and the mean power density increases with an increase in the size of Ni particles or porosity and with a decrease in the thickness of the anode substrate layer. The studies in the range of the cathode microstructural variables investigated indicated that there is an optimum LSM volume fraction at which the mean total polarization resistance will be minimized. An optimum value for the LSM volume fraction can be also found to maximize the mean power density. For a cathode with an optimum LSM volume fraction, the optimum particle size ratio is always equal to 1. There is an optimum value for the variables of the LSM particle size, thickness, and porosity of the cathode at which the mean total polarization resistance is minimized. There is also an optimum value for these variables at which the mean power density is maximized. The results of the simulation also revealed that there is a value for each microstructural variable of the anode functional layer and cathode at which the mean temperature of the solid structure is minimized. There is also a value for each microstructural variable of the anode functional layer and cathode at which the temperature difference between the hottest and coldest spots in the solid structure of the cell is maximized. The latter statement is also valid for the maximum temperature gradient in the solid structure, except the thickness of the anode functional layer. In the anode substrate layer, with an increase in the porosity and size of Ni particles, the mean temperature decreases and the temperature difference between the hottest and coldest spots in the solid structure increases. The higher the size of Ni particles, the higher the maximum temperature gradient in the solid structure. The mean temperature, the temperature difference between the hottest and coldest spots, and the maximum temperature gradient in the solid structure are weak functions of the thickness of the anode substrate layer.

The studies indicated that the effect of the Ni volume fraction in the anode functional layer on the mean total polarization resistance, the mean total power density, and the temperature distribution in the solid structure of the cell is more significant than the effect of the LSM volume fraction in the cathode. Among the size of the Ni particles in the anode substrate and functional layers and the LSM particles in the cathode, the size of Ni particles in the anode functional layer has the highest effect on the mean total polarization resistance, the mean total power density, and the temperature distribution in the solid structure of the cell, followed by the size of LSM particles in the cathode and the size of Ni particles in the anode substrate layer. Among the thicknesses of the cathode and anode substrate and functional layers, the thickness of the anode functional layer has the highest effect on the mean total polarization resistance, the mean total power density, and the temperature distribution in the solid structure of the cell, followed by the thickness of the cathode and the thickness of the anode substrate layer. Among the porosities of the anode substrate and functional layers and cathode, the porosity of the anode substrate layer has the highest effect on the mean total polarization resistance, the mean total power density, and the temperature distribution in the solid structure of the cell, followed by the porosities of the anode functional layer and cathode.

As a remarkable result, the cathode mean polarization resistance is a weak function of the microstructure of the anode functional and substrate layers. Similarly, the anode mean polarization resistance is a weak function of the cathode microstructure. The results also revealed that the contribution of CO and H_2 electrochemical reactions in the total mean power density are almost 27%, and 73%, respectively. The microstructure of electrodes may change the contribution of the CO and H_2 electrochemical reactions up to 1%-point.

The performance of two SOFC systems was studied. The performance of the first SOFC system that operates with biogas was evaluated for operation in a WWTP and residential dwellings. Three configurations for this system, different in the method of biogas processing, were considered in this evaluation. The SOFC stack employed in this system comprised ASC-3 cells for the system operated in the WWTP and ESC-4 cells for the system operated in residential dwellings.

The results of the operation of the first SOFC system in the WWTP indicated that the electrical efficiency of all the configurations of this system is higher than that of the conventional CHP system in the WWTP studied. Among the configurations of this system, configuration I with the AGR fuel processor exhibits a net AC electrical efficiency of 45.1%, followed by configurations II and III with an efficiency of 43% and 33%, respectively. The number of cells required for the SOFC stack is the lowest for the system with configuration II with SR fuel processor. The system with configuration III with POX fuel processor provides the highest CHP efficiency; however, the extra heat generated in the system with this configuration may not be suitable for this application. If the biogas produced in a WWTP is used in the system with configurations I and II, in addition to provide the electric power and heat required to operate the WWTP, extra electric power generated can be sold to the electrical grid.

The results of the operation of this SOFC system in single-family residential dwellings to generate ≈1 kW net AC electric power indicated that the for an SOFC stack with 27 ESC-4 cells operated at the fuel utilization ratio of 80%, the net AC electrical efficiency is 42.4%, 41.7%, and 33.9% for the system with configurations I, II, and III, respectively. In these conditions, the system with configuration III shows the highest CHP efficiency with 80.5%, followed by the system with configuration I with 76.9%, and configuration II with 72.9%. The excess air required for controlling the temperature of the SOFC stack is the lowest for the system with configuration II. The TER of the system with configurations I and II at the fuel utilization ratios of 70% and 80% and configuration III at the fuel utilization ratio of 90% is suitable to produce the electric power and hot water demands for a single-family detached dwelling. The sensitivity analysis in the range of the cell voltages and fuel utilization ratios investigated indicated that an increase in the cell voltage leads to a linear increase in the net AC electrical efficiency of the system. The net AC electrical efficiency also increases by increasing the fuel utilization ratio. The number of cells required in the SOFC stack to generate 1 kW net AC electric power in the system varies as a concave upward parabolic curve. The cell voltages at which the minimum number of cells is obtained is important to determine the optimum cell voltage. We found that the optimum cell voltage is greater than the cell voltage at which the minimum number of cells for the SOFC stack is obtained. The minimum number of cells at the fuel utilization ratio of 80% is obtained at the cell voltage of 0.55 V for the system with configuration I, 0.62 V for the system with configuration II, and 0.61 V for the system with configuration III.

Overall, the biogas, as a renewable and alternative source of fuel, is a suitable fuel for the first SOFC system for both the industrial and residential applications because the high amount of the mole fraction of CO_2 in this gas can reduce the amount of the reforming agent required to process biogas. This SOFC system also shows an appropriate performance to generate electric power. Of course, the exergy analysis showed that there is a considerable potential to generate additional electric power if this system is combined with a power generation system and appropriately optimized.

For the second SOFC system, the performance of this system that operates with liquid ammonia fuel was evaluated for portable electric power generation. This system has a simple layout and its size is small compared to the hydrocarbon-fuelled portable SOFC systems. The exhaust gas from this system contains only water vapour, oxygen, and nitrogen; hence, it contributes to reduction of greenhouse gas emissions. This system also shows an appropriate performance. The first-law efficiency of 41.1% and the system voltage of 25.6 V are predicted for this system if the ASC-3 cells operated at the voltage of 0.73 V, temperature of 1073 K, and fuel utilization ratio of 80% are employed in the SOFC stack of this system. In these conditions, a full 0.8 liters ammonia cylinder is sufficient for 9:34' full-load operation of a 100 W portable system. The sensitivity analysis in the range of the cell voltages and fuel utilization ratios investigated indicated that the first- and second-law efficiencies of the system increase linearly by increasing the cell voltage. These efficiencies also increase by increasing the fuel utilization ratio. There is a logical limitation for selecting a cell voltage at the design stage of this system. Indeed, the minimum cell design voltage is limited to the cell voltage at which the minimum number of cell for the SOFC stack is obtained. At the fuel utilization ratio of 80%, the minimum cell voltage of 0.57 V is obtained for this system.

Chapter 5

Conclusions and Recommendations

5.1 Conclusions

A new cell level model for SOFCs with porous composite electrodes was developed by a combination of the micro-model and the macro-model of the cell. In the micro-model, after modeling the microstructure of porous composite electrodes, the complex interdependency among the multi-component mass transport, electron and ion transports, and the electrochemical and chemical reactions within the microstructure of electrodes was taken into account. In the macro-model, the energy transport in the cell solid structure and the mass and energy transports in the fuel and air streams were considered. Using this new model, entitled the combined micro- and macro-model, the microstructure of porous composite electrodes could be linked to the cell performance.

Some of the significant results of modeling the microstructure of porous composite electrodes can be summarized as follows:

- The maximum electrochemical active area per unit volume of porous composite electrodes can be obtained if the size and volume fraction of electron- and ion-conducting particles is identical.
- For the particle-size ratio of unity, the average pore size remains constant throughout the entire range of the volume fraction of electron-conducting particles. The average pore size decreases linearly with a decrease in the size of electron-conducting particles.
- The effective resistivity of YSZ is greater, by several orders of magnitude, than that of Ni or LSM. The effective resistivity of YSZ decreases with a decrease in the volume fraction of electron-conducting particles or an increase in the particle-size ratio.

Some of the significant results of the combined micro- and macro-model of a typical anode-supported co-flow planar cell with specified microstructures of the porous composite Ni-YSZ anode and LSM-YSZ cathode can be summarized as follows:

- The Reynolds number of the air and fuel streams passing through the channels is less than 100; hence, the fuel and air streams are laminar.

- The Péclet numbers corresponding to the mass and energy transports in the air and fuel streams are substantially greater than unity; hence, the heat and mass diffusions in the air and fuel streams along the length of the cell can be ignored.
- The mole fraction of CH_4 in the fuel stream approaches zero where $y=0.2L_{Cell}$. Therefore, the steam reforming reaction occurs in the first 20% of the length of the cell.
- The contribution of the H_2 electrochemical reaction in the local total power density reaches from 68% at the beginning to 76% at the end of the cell length.
- The anode has the highest contribution in the local total polarization resistance, followed by the cathode, electrolyte, and interconnect.
- The solid structure has the main contribution in the local total exergy destruction, followed by the air and fuel streams.
- At the beginning of the cell length, more than 45% of the electric current is consumed within 20% of the cathode thickness near the cathode and electrolyte interface. Therefore, more than 45% of the oxygen electroreduction reaction takes place within 20% of the cathode thickness near the cathode and electrolyte interface. Moreover, less than 10% of the electric current is consumed within 20% of the cathode thickness near the cathode and interconnect interface.
- At the end of the cell length, less than 35% and more than 12% of the electric current is consumed within 20% of the cathode thickness near the interfaces of the cathode and electrolyte and the cathode and interconnect, respectively.
- At the beginning of the cell length, more than 34% of the electric current is generated within 20% of the anode thickness near the anode and electrolyte interface. Thus, more than 34% of the H_2 and CO electrooxidation reactions take place within 20% of the anode functional layer thickness near the anode and electrolyte interface. Moreover, less than 13% of the electric current is generated within 20% of the anode functional layer thickness near the interface of the anode functional and substrate layers.
- At the end of the cell length, less than 28% and more than 15% of the electric current is generated within 20% of the anode thickness near the interfaces of the anode and electrolyte and the substrate and functional layers, respectively.

Some of the important results of the combined micro- and macro-model of anode-supported co-flow planar cells with various microstructures of electrodes can be summarized as follows:

- There is an optimum value for the Ni volume fraction at which the mean total polarization resistance is minimized. There is also an optimum value for this microstructural variable at which the cell mean power density is maximized. For an anode functional layer with an optimum Ni volume fraction, the optimum particle size ratio is unity.
- There is an optimum value for the microstructural variables of the thickness and porosity of the anode functional layer at which the mean total polarization resistance is minimized. There is also an optimum value for these variables at which the mean power density is maximized.
- With a decrease in the size of Ni particles to even 0.1 μm, the mean total polarization resistance decreases and the mean power density increases.
- In the range investigated for microstructure of the anode substrate layer, the mean total polarization resistance decreases and the mean power density increases with an increase in the size of Ni particles or porosity or with a decrease in the thickness.
- There is an optimum LSM volume fraction in the cathode at which the mean total polarization resistance is minimized. An optimum value for the LSM volume fraction can also be found to maximize the mean power density. For a cathode with an optimum LSM volume fraction, the optimum particle size ratio is equal to 1.
- There is an optimum value for the microstructural variables of the LSM particle size, thickness, and porosity of the cathode at which the mean total polarization resistance is minimized. There is also an optimum value for these microstructural variables at which the mean power density is maximized.
- There is a value for each microstructural variable of the anode functional layer and cathode at which the mean temperature of the solid structure is minimized.
- There is a value for each microstructural variable of the anode functional layer and cathode at which the temperature difference between the hottest and coldest spots in the solid structure of the cell is maximized. This statement is also valid for the maximum temperature gradient in the solid structure, except the thickness of the anode functional layer.
- By increasing the porosity and size of Ni particles in the anode substrate layer, the mean temperature decreases and the temperature difference between the hottest and coldest spots in the solid structure increases.
- The mean temperature, the temperature difference between the hottest and coldest spots, and the maximum temperature gradient in the solid structure are weak functions of the thickness of the anode substrate layer.

- The effect of Ni volume fraction in the anode functional layer on the cell performance is more significant than the LSM volume fraction in the cathode.
- Among the size of the Ni particles in the anode substrate and functional layers and the LSM particles in the cathode, the size of Ni particles in the anode functional layer has the highest effect on the cell performance, followed by the size of LSM particles in the cathode, and the size of Ni particles in the anode substrate layer.
- Among the thicknesses of the cathode and anode substrate and functional layers, the thickness of the anode functional layer has the highest effect on the cell performance, followed by the thickness of the cathode and the thickness of the anode substrate layer.
- Among the porosities of the cathode and anode substrate and functional layers, the porosity of the anode substrate layer has the greatest effect on the cell performance, followed by the porosities of the anode functional layer and cathode.
- The mean polarization resistance of the cathode is a weak function of the microstructure of the anode functional and substrate layers.
- The mean polarization resistance of the anode is a weak function of the cathode microstructure.
- The contribution of CO and H_2 electrochemical reactions in the total mean power density of the cell are ≈27%, and ≈73%, respectively. The microstructure of the electrodes may affect these values up to ±1%-point.

To model SOFCs at the system level, the basic cell model was used to model SOFCs at the cell level, the repeated-cell stack model was used to model SOFCs at the stack level, and the thermodynamic model was used to model the BoP components of the system. In addition to these models, a carbon deposition model based on the thermodynamic equilibrium assumption was used. By employing the carbon deposition model, the carbon deposition curves at several temperatures and pressures were obtained and demonstrated in the C-H-O ternary diagram. On the basis of these curves, the carbon deposition and safe regions in the C-H-O ternary diagram were introduced. It was shown that the location of most of the hydrocarbon fuels may lie in the carbon deposition region. This means that the carbon deposition on the anode catalyst and the deactivation of the anode is possible if these fuels are fed directly to the anode channels. To transfer the location of these fuels in the C-H-O ternary diagram to the safe region, several fuel processing methods can be used. The minimum flow rate of reforming agent required to process these fuels and the equilibrium compositions of the fuels processed can be obtained using the carbon deposition model. Because the heat transfer from the SOFC stack can play an important role in performance prediction of SOFC systems, a model to predict the heat transfer from outer surfaces of the stack was developed. For this purpose, two different insulation systems for SOFC stacks were suggested and modeled.

Using the model developed at the system level, the performance of two SOFC systems was evaluated. The first system operates with biogas fuel and is suitable to generate heat and electric power for industrial and residential applications. Three configurations for this system, different in the method of fuel processing, were considered. The AGR, SR, and POX were the fuel processing methods considered for configurations I-III, respectively. The second system operates with liquid ammonia fuel and is suitable for portable power generation applications. This system has a simple layout and its size is small compared to the hydrocarbon-fuelled portable SOFC systems.

Some of the important results of the operation of the first SOFC system in a WWTP can be summarized as follows:

- Biogas is a suitable fuel for the SOFC system because the high amount of the mole fraction of CO_2 in this gas reduces the flow rate of reforming agent required to process the biogas.
- The electrical efficiency of all the configurations of the first SOFC system is higher than that of the conventional CHP system that already operates in the WWTP studied.
- For an SOFC stack with ASC-3 cells operated at the fuel utilization ratio of 80%, the system with configuration I exhibits a net AC electrical efficiency of 45.1%, followed by configurations II and III with an efficiency of 43% and 33%, respectively.
- The number of cells required for the SOFC stack is the lowest for the system with configuration II.
- The system with configuration III generates the highest CHP efficiency; however, the extra heat generated in the system with this configuration may not be required for the WWTP.
- If the biogas produced in the WWTP is used in the system with configurations I and II, it not only generates the electric power and heat required to operate the WWTP, but the extra electric power generated can also be sold to the electrical grid.

Some of the important results of the operation of the first SOFC system in single-family residential dwellings can be summarized as follows:

- For an SOFC stack with 27 ESC-4 cells operated at the fuel utilization ratio of 80%, the net AC electrical efficiency is 42.4%, 41.7%, and 33.9% for the system with configurations I, II, and III, respectively.
- The system with configuration III showed the highest CHP efficiency with 80.5%, followed by the system with configuration I with 76.9%, and the system with configuration II with 72.9%.
- The excess air required for thermal management of the SOFC stack is the lowest for the system with configuration II.
- The TER of the systems with configurations I and II at the fuel utilization ratios of 70% and 80% and configuration III at the fuel utilization ratio of 90% is suitable to produce the electric power and hot water demands for a single-family detached dwelling.
- By increasing the cell voltage, the number of cells required in the SOFC stack to generate 1 kW net AC electric power in the system varies as a concave upward parabolic curve. The optimum cell voltage is greater than the cell voltage at which the minimum number of cells for the SOFC stack is obtained.
- The minimum number of cells at the fuel utilization ratio of 80% is obtained at the cell voltage of 0.55 V for the system with configuration I, 0.62 V for the system with configuration II, and 0.61 V for the system with configuration III.

Some of the important results of the operation of the second SOFC system for portable electric power generation can be summarized as follows:

- The system can achieve the first-law efficiency of 41.1% and the voltage of 25.6 V if the ASC-3 cells operated at the voltage of 0.73 V, temperature of 1073 K, and fuel utilization ratio of 80% are employed in the SOFC stack.
- In these conditions, a full 0.8 liters liquid ammonia cylinder is sufficient for 9.5 hours full-load operation of a 100 W portable system.
- There is a logical limitation for selecting a cell voltage at the design stage of the system. Indeed, the minimum cell design voltage is limited to the cell voltage at which the minimum number of cells for the SOFC stack is obtained.
- At the fuel utilization ratio of 80%, the minimum cell voltage of 0.57 V is obtained for this system.

5.2 Recommendations

For the combined micro- and macro-model that was developed, the following items are recommended for future research:

- Improving the microstructure model of porous composite electrodes to consider the size distribution of particles and to improve the prediction of the effect of the sintering process on the microstructural properties of electrodes.
- Improving the combined micro- and macro-model by employing a detailed electrochemical reaction mechanism with a more precise determination of the rate determining steps.
- Expanding the combined micro- and macro-model for prediction of the effect of microstructure of porous composite electrodes on the thermal stresses in the solid structure of the cell.
- Expanding the combined micro- and macro-model to take account of the mixed ion-electron conductor materials, such as the lanthanum strontium cobalt iron oxide (LSCF) for cathodes or GDC for electrolytes.
- Employing the combined micro- and macro-model to optimize the microstructure of porous composite electrodes of an anode-supported co-flow planar cell to reach a desired cell performance with consideration of the cell fabrication and operational constraints.
- Developing a 2-D micro-model and comparing the results of the 1-D and 2-D micro-models.
- Employing the combined micro- and macro-model to study the effect of the microstructure of porous composite electrodes on the performance of counter-flow planar cells.
- Developing the combined micro- and macro-model for cross-flow planar cells. For this purpose, the heat transfer model in the solid structure of the cell should be modified from the 1-D model to a 2-D model and the mass and energy transports should be considered for fuel and air streams in all channels of the cell.

For the model developed for SOFCs at the system level the following items are recommended for future research:

- Employing the system level model for various fossil and renewable fuels to predict the effect of different fuel processors on the system performance.
- Improving the basic model of the cell to take account of the effect of the CO electrooxidation reaction at the interface of the anode and electrolyte.

- Improving the carbon deposition model to take account of the effect of the anode catalyst on the possibility or rate of carbon deposition.
- Improving the system level model to take account of the system at part load operations.
- Using an economic analysis model to predict the cost of the system at different design and operating conditions.

References

[1] Fuel cell handbook, EG&G Technical Services, Inc, U.S. Department of Energy, 7th edition, 2004.

[2] X. Li. Principles of Fuel Cells, Taylor & Francis, New York, NY 10016, 2006.

[3] S.C. Singhal, Solid oxide fuel cells-status, challenges and opportunities, *Finnish solid oxide fuel cell conference*, ESPOO, Finland, 2006.

[4] S.C. Singhal, and K. Kendall, High temperature solid oxide fuel cells, fundamentals, design and applications, Elsevier Ltd, 2004.

[5] B. Sunden, M. Faghri, Transport phenomena in fuel cells, WIT Press, 2005.

[6] www.thyssenkrupp-vdm.com/en/downloads/data-sheets.html, Accessed in January 2011.

[7] V.A.C. Haanappel, J. Mertens, D. Rutenbeck, C. Tropartz, W. Herzhof, D. Sebold, and F. Tietz, Optimisation of processing and microstructural parameters of LSM cathodes to improve the electrochemical performance of anode-supported SOFCs, *Journal of Power Sources*, 141, 216–226, 2005.

[8] D.L. King, J.J. Strohm, X. Wang, H. Roh, C. Wang, Y. Chin, Y. Wang, Y. Lin, R. Rozmiarek, and P. Singh, Effect of nickel microstructure on methane steam-reforming activity of Ni–YSZ cermet anode catalyst, *Journal of Catalysis*, 258, 356–365, 2008.

[9] C. Xia, and M. Liu, Microstructures, conductivities, and electrochemical properties of $Ce_{0.9}Gd_{0.1}O_2$ and GDC–Ni anodes for low-temperature SOFCs, *Solid State Ionics*, 152-153, 423– 430, 2002.

[10] A.K.N. Reddy, R.H. Williams, and T.B. Johansson, Energy After Rio: Prospects and Challenges, United Nations Development Program, New York, NY, 1997.

[11] Y. Yi, A.D. Rao, J. Brouwer, and G.S. Samuelsen, Fuel flexibility study of an integrated 25kW SOFC reformer system, *Journal of Power Sources*, 144, 67–76, 2005.

[12] C. Zamfirescu, and I. Dincer, Using ammonia as a sustainable fuel, *Journal of Power Sources*, 185, 459-465, 2008.

[13] J.J. Mackenzie, and W.H. Avery, Ammonia fuel: the key to hydrogen-based transportation, *Energy Conversion Engineering Conference*, Washington DC. 1996.

[14] S. Farhad, and F. Hamdullahpur, Developing fuel map to predict the effect of fuel composition on the maximum voltage of solid oxide fuel cells, *Journal of Power Sources*, 191(2), 407–416, 2009.

[15] S. Farhad, and F. Hamdullahpur, Developing fuel map to predict the effect of fuel composition on

the maximum efficiency of solid oxide fuel cells, *Journal of Power Sources*, 193(2), 632–638, 2009.

[16] A.S. Osered'ko, High-temperature corrosion of structural materials in gaseous ammonia, *Materials Science*, 15, 647–649, 1980.

[17] A. Wojcik, H. Middleton, I. Damopoulos, and J. Van herle, Ammonia as a fuel in solid oxide fuel cells, *Journal of Power Sources*, 118, 342–348, 2003.

[18] G.G.M. Fournier, I.W. Cumming, and K. Hellgardt, High performance direct ammonia solid oxide fuel cell, *Journal of Power Sources*, 162, 198–206, 2006.

[19] S. Farhad, Y. Yoo, and F. Hamdullahpur, Conceptual design of anaerobic digestion gas-fuelled SOFC systems to generate electricity and heat in wastewater treatment plants, *Proceedings of the 9th International Colloquium on Environmentally Preferred Advanced Power Generation (ICEPAG-2009)*, CA, USA, February, 2009.

[20] S. Farhad, Y. Yoo, and F. Hamdullahpur, Performance evaluation of different configurations of biogas-fuelled SOFC systems for residential applications, *European Fuel Cell Forum*, Lucerne, Switzerland, 2009.

[21] E.S. Hecht, G.K. Gupta, H. Zhu, A.M. Dean, R.J. Kee, L. Maier, and O. Deutschmann, Methane reforming kinetics within a Ni–YSZ SOFC anode support, *Applied Catalysis A: General*, 295, 40–51, 2005.

[22] E.J. Cairns, A.D. Tevebaugh, CHO gas phase compositions in equilibrium with carbon, and carbon deposition boundaries at one atmosphere, *Journal of Chemical Engineering Data*, 9 (3), 453–462, 1964.

[23] K. Sasaki, and Y. Teraoka, Equilibria in Fuel Cell Gases, I. Equilibrium Compositions and Reforming Conditions, *Journal of the Electrochemical Society*, 150 (7), A878-A884, 2003.

[24] G.H J. Broers, and B.W. Treijte, Carbon deposition boundaries and other constant parameter curves, in the triangular representation of C-H-O equilibria, with applications to fuel cells, *Advanced Energy Conversion*, 5, 365-382, 1965.

[25] S. Assabumrungrat, N. Laosiripojana, V. Pavarajarn, W. Sangtongkitcharoen, A. Tangjitmatee, and P. Praserthdam, Thermodynamic analysis of carbon formation in a solid oxide fuel cell with a direct internal reformer fuelled by methanol, *Journal of Power Sources*, 139, 55-60, 2005.

[26] D. Singh, E. Hernandez-Pacheco, P.N. Hutton, N. Patel, and M.D. Mann, Carbon deposition in an SOFC fueled by tar-laden biomass gas: a thermodynamic analysis, *Journal of Power Sources*, 142, 194–199, 2005.

[27] J.W. Kim, A.V. Virkar, K.Z. Fung, K. Mehta, and S.C. Singhal, Low temperature, high performance anode-supported solid oxide fuel cells, *Journal of the Electrochemical Society*, 146(1), 69–78, 1999.

[28] S.H. Chan, K.A. Khor, and Z.T. Xia, A complete polarization model of a solid oxide fuel cell and its sensitivity to the change of cell component thickness, *Journal of Power Sources*, 93, 130–140, 2001.

[29] S.H. Chan, C.F. Low, and O.L. Ding, Energy and exergy analysis of solid-oxide fuel-cell power systems, *Journal of Power Sources*, 103, 188-200, 2002.

[30] S.H. Chan, and O.L. Ding, Simulation of a solid oxide fuel cell power system fed by methane, *International Journal of Hydrogen Energy*, 30, 167-179, 2005.

[31] J.R. Ferguson, J.M. Fiard, R. Herbin, Three-dimensional numerical simulation for various geometries of solid oxide fuel cells, *Journal of Power Sources*, 58, 109-122, 1996.

[32] F. Calise, G. Ferruzzi , and L. Vanoli, Parametric exergy analysis of a tubular Solid Oxide Fuel Cell (SOFC) stack through finite-volume model, *Applied Energy*, 86, 2401–2410, 2009.

[33] S. Campanari, and P. Iora, Definition and sensitivity analysis of a finite volume SOFC model for a tubular cell geometry, *Journal of Power Sources*, 132, 113–126, 2004.

[34] C. Stiller, B. Thorud, S. Seljebø, Ø. Mathisen, H. Karoliussen, and O. Bolland, Finite-volume modeling and hybrid-cycle performance of planar and tubular solid oxide fuel cells, *Journal of Power Sources*, 141, 227–240, 2005.

[35] B. Zitouni, G.M. Andreadis, B.M. Hocine, A. Hafsia, H. Djamel, and Z. Mostefa, Two-dimensional numerical study of temperature field in an anode supported planar SOFC: Effect of the chemical reaction, *International Journal of Hydrogen Energy*, 36, 4228-4235, 2011.

[36] C. Baoa, N. Caib, and E. Croiset, An analytical model of view factors for radiation heat transfer in planar and tubular solid oxide fuel cells, *Journal of Power Sources*, 196, 3223–3232, 2011.

[37] N. Vivet, S. Chupin, E. Estrade, T. Piquero, P.L. Pommier, D. Rochais, and E. Bruneton, 3D Microstructural characterization of a solid oxide fuel cell anode reconstructed by focused ion beam tomography, *Journal of Power Sources*, 196, 7541– 7549, 2011.

[38] C.-K. Lin, T.-T. Chen, Y.-P. Chyoub, and L.-K. Chiang, Thermal stress analysis of a planar SOFC stack, *Journal of Power Sources*, 164, 238–251, 2007.

[39] H. Apfel, M. Rzepka, H. Tua, and U. Stimming, Thermal start-up behaviour and thermal management of SOFC's, *Journal of Power Sources*, 154, 370–378, 2006.

[40] L.-K. Chiang, H.-C. Liu, Y.-H. Shiu, C.-H. Lee, and R.-Y. Lee, Thermo-electrochemical and thermal

stress analysis for an anode-supported SOFC cell, Renewable Energy, 33, 2580– 2588, 2008.

[41] H. Yakabe, and T. Sakurai, 3D simulation on the current path in planar SOFCs, *Solid State Ionics*, 174, 295–302, 2004.

[42] K.P. Recknagle, R.E. Williford, L.A. Chick, D.R. Rector, M.A. Khaleel, Three-dimensional thermofluid electrochemical modelling of planar SOFC stacks, *Journal of Power Sources*, 113, 109-114, 2003.

[43] U. Pasaogullari and C.-Y. Wang, Computational fluid dynamics modeling of solid oxide fuel cells, Electrochemical Engine Center, *Proceedings of SOFC-VIII*, S.C. Singhal and M. Doliya, 1403-1412, 2003.

[44] S.B. Beale, Y. Li, S.V. Zhubrin, and W. Dong, Computer methods for performance prediction in fuel cells, *Journal of Power Sources*, 118, 79-85, 2003.

[45] E. Achenbach, Three-dimensional and time-dependent simulation of a planar solid oxide fuel cell stack, *Journal of Power Sources*, 49, 333-348, 1994.

[46] R. Krishna, J.A. Wesselingh, The Maxwell-Stefan approach to mass transfer, *Chemical Engineering Science*, 52, 861-911, 1997.

[47] P. Aguiar, C.S. Adjiman, and N.P. Brandon, Anode-supported intermediate temperature direct internal reforming solid oxide fuel cell. I: model-based steady-state performance, *Journal of Power Sources*, 138, 120-136, 2004.

[48] K. Nikooyeh, A.A. Jeje, and J.M. Hill, 3D modeling of anode-supported planar SOFC with internal reforming of methane, *Journal of Power Sources*, 171, 601–609, 2007.

[49] M. Suzuki, and T. Oshima, Estimation of the co-ordination number in a multi-component mixture of spheres, *Powder Technology*, 35, 166-159, 1983.

[50] M Suzuki, and T. Oshima, Estimation of the co-ordination number in a two-component mixture of cohesive spheres, *Powder Technology*, 36, 181–188, 1983.

[51] M. Suzuki, T. Oshima, Verification of a model for estimating the void fraction in a three-component randomly packed bed, *Powder Technology*, 43, 147-153, 1985.

[52] M. Suzuki, T. Oshima, Co-ordination number of a multi-component randomly packed bed of spheres with size distribution, *Powder Technology*, 44, 213-218, 1985.

[53] D. Bouvard, and F.F. Lange, Relation between percolation and particle coordination in binary powder mixtures, *Acta metal. Mater*. 39(12), 3083-3090, 1991.

[54] C.H. Kuo, P.K. Gupta, Rigidity and conductivity percolation thresholds in particulate composites.

Acta metall mater, 43(1), 397-403, 1995.

[55] P. Costamagna, P. Costa, and V. Antonucci, Micro-modelling of solid oxide fuel cell electrodes, *Electrochimica Acta*, 43, 375–394, 1998.

[56] C. Nicolella, A. Bertei, M. Viviani, and A. Barbucci, Morphology and electrochemical activity of SOFC composite cathodes: II. Mathematical modelling, *Journal of Applied Electrochemistry*, 39, 503–511, 2009.

[57] D.H. Jeon, J.H. Nam, and K. Charn-Jung, Microstructural optimization of anode-supported solid oxide fuel cells by a comprehensive microscale model, *Journal of the Electrochemical Society*, 153, A406–A417, 2006.

[58] B. Kenney, M. Valdmanis, C. Baker, J.G. Pharoah, and K. Karan, Computation of TPB length, surface area and pore size from numerical reconstruction of composite solid oxide fuel cell electrodes, *Journal of Power Sources*,189, 1051–1059, 2009.

[59] S.H. Chan, and Z.T. Xia, Anode micro-model of solid oxide fuel cell, *Journal of Electrochemical Society*, 148(4), A388-A394, 2001.

[60] Z.T Xia, S.H. Chan, and K.A. Khor, An improved anode micro model of SOFC, *Electrochemical and Solid-State Letters*, 7, A63-A65, 2004.

[61] S.H. Chan, X.J. Chen, K.A. Khor, Cathode micromodel of solid oxide fuel cell, *Journal of the Electrochemical Society*, 151(1), A164-A174, 2004.

[62] X.J. Chen, S.H. Chan, and K.A. Khor, Simulation of a composite cathode in solid oxide fuel cells, *Electrochimica Acta*, 49, 1851-1861, 2004.

[63] J.H. Nam, D.H. Jeon, A comprehensive micro-scale model for transport and reaction in intermediate temperature solid oxide fuel cells, *Electrochimica Acta*, 51, 3446–3460, 2006.

[64] M.M. Hussain, X. Li, and I. Dincer, Mathematical modeling of transport phenomena in porous SOFC anodes, *International Journal of Thermal Sciences*, 46, 48–56, 2007.

[65] M.M. Hussain, X. Li, and I. Dincer, A numerical investigation of modeling an SOFC electrode as two finite layers, *International Journal of Hydrogen Energy*, 34, 3134-3144, 2009.

[66] S.H. Chan, and O.L. Ding, Simulation of a solid oxide fuel cell power system fed by methane, *International Journal of Hydrogen Energy* 30, 167–179, 2005.

[67] R.J. Braun, S.A. Kleina, and D.T. Reindla, Evaluation of system configurations for solid oxide fuel cell-based micro-combined heat and power generators in residential applications, *Journal of Power Sources*, 158(2), 1290-1305, 2006.

[68] C.O. Colpan, F. Hamdullahpur, I. Dincer, and Y. Yoo, Effect of gasification agent on the performance of solid oxide fuel cell and biomass gasification systems, *International Journal of Hydrogen Energy*, 35, 5001-5009, 2010.

[69] B.E. Mai, T. Semper, T. Heller, and C. Wunderlich, SOFC stack testing at Staxera, *8th European SOFC Forum*, Switzerland, 2008.

[70] K. Lai, B.J. Koeppel, K.S. Choi, K.P. Recknagle, X. Sun, L.A. Chick, V. Korolev, and M. Khaleel, A quasi-two-dimensional electrochemistry modeling tool for planar solid oxide fuel cell stacks, *Journal of Power Sources*, 196, 3204–3222, 2011.

[71] S. Farhad, F. Hamdullahpur, Conceptual design of a novel ammonia–fuelled portable solid oxide fuel cell system, *Journal of Power Sources*, 195, 3084–3090, 2010.

[72] S. Farhad, Y. Yoo, F. Hamdullahpur, Effects of fuel processing methods on industrial scale biogas-fuelled solid oxide fuel cell system for operating in wastewater treatment plants, *Journal of Power Sources*, 195, 1446–1453, 2010.

[73] S. Farhad, F. Hamdullahpur, Y. Yoo, Performance evaluation of different configurations of biogas-fuelled SOFC micro-CHP systems for residential applications, *International Journal of Hydrogen Energy*, 35(8), 3758-3768, 2010.

[74] F.A. Al-Sulaiman, I. Dincer, and F. Hamdullahpur, Exergy analysis of an integrated solid oxide fuel cell and organic Rankine cycle, for cooling, heating and power production, *Journal of Power Sources*, 195, 2346–2354, 2010.

[75] F.A. Al-Sulaiman, I. Dincer, and F. Hamdullahpur, Energy analysis of a trigeneration plant based on solid oxide fuel cell and organic Rankine cycle, *International Journal of Hydrogen Energy*, 35, 5104–5113, 2010.

[76] M. Santin, A. Traverso, L. Magistri, and A. Massardo, Thermoeconomic analysis of SOFC-GT hybrid systems fed by liquid fuels, *Energy*, 35, 1077–1083, 2010.

[77] F. Calise, M.D. d'Accadia, A. Palombo, and L. Vanoli, Simulation and exergy analysis of a hybrid Solid Oxide Fuel Cell (SOFC)–Gas Turbine System, *Energy*, 31, 3278–3299, 2006.

[78] Y. Yi, A.D. Rao, J. Brouwer, G.S. Samuelsen, Analysis and optimization of a solid oxide fuel cell and intercooled gas turbine (SOFC–ICGT) hybrid cycle, *Journal of Power Sources*, 132, 77–85, 2004.

[79] M. Liu, P.V. Aravind, T. Woudstra, V.R.M. Cobas, and A.H.M. Verkooijen, Development of an integrated gasifier–solid oxide fuel cell test system: A detailed system study, *Journal of Power*

Sources, 196, 7277– 7289, 2011.

[80] M. Rokni, Thermodynamic analysis of an integrated solid oxide fuel cell cycle with a Rankine cycle, *Energy Conversion and Management*, 51, 2724–2732, 2010.

[81] Y. Komatsu, S. Kimijima, and J.S. Szmyd, Performance analysis for the part-load operation of a solid oxide fuel cell–micro gas turbine hybrid system, *Energy*, 35, 982–988, 2010.

[82] A. Arsalis, Thermoeconomic modeling and parametric study of hybrid SOFC–gas turbine–steam turbine power plants ranging from 1.5 to 10MWe, *Journal of Power Sources*, 181, 313–326, 2008.

[83] R. Kandepu, L. Imsland, B.A. Foss, C. Stiller, B. Thorud, and O. Bolland, Modeling and control of a SOFC-GT-based autonomous power system, *Energy*, 32, 406–417, 2007.

[84] F. Jurado, Power supply quality improvement with a SOFC plant by neural-network-based control, *Journal of Power Sources*, 117, 75–83, 2003.

[85] A. Franzoni, L. Magistri, A. Traverso, and A.F. Massardo, Thermoeconomic analysis of pressurized hybrid SOFC systems with CO_2 separation, *Energy*, 33, 311–320, 2008.

[86] P. Piroonlerkgul, N. Laosiripojana, A.A. Adesina, S. Assabumrungrat, Performance of biogas-fed solid oxide fuel cell systems integrated with membrane module for CO_2 removal, *Chemical Engineering and Processing*, 48, 672–682, 2009.

[87] G.F. Froment, Production of synthesis gas by steam- and CO_2 -reforming of natural gas, *Journal of Molecular Catalysis: Chemical*, 163, 147-156, 2000.

[88] K. Sasaki, and Y. Teraoka, Equilibria in fuel cell gases - II. The C-H-O ternary diagrams, *Journal of the Electrochemical Society*, 150(7), A885-A888, 2003.

[89] H. Zhu, and R.J. Kee, Thermodynamics of SOFC efficiency and fuel utilization as functions of fuel mixtures and operating conditions, *Journal of Power Sources*, 161, 957–964, 2006.

[90] B.J. McBride, M.J. Zehe, and S. Gordon, NASA Glenn coefficients for calculating thermodynamic properties of individual species, NASA/TP-2002-211556, Glenn Research Center, Cleveland, Ohio, 2002.

[91] R. Parsons, General equations for the kinetics of electrode process, *Transactions of the Faraday Society*, 47, 1332-1344, 1951.

[92] P. Costamagna, K. Honegger, Modelling of solid oxide heat exchanger integrated stacks and simulation at high fuel utilization, *Journal of Electrochemical Society*, 145(11), 3995-4007, 1999.

[93] E.N. Fuller, K. Ensley, and J.C. Giddings, Diffusion of halogenated hydrocarbons in helium. The effect of structure on collision cross sections, *Journal of physical chemistry*, 78, 3679-3685, 1969.

[94] B. Kenney, K. Karan, Engineering of microstructure and design of a planar porous composite SOFC cathode: a numerical analysis, *Solid State Ionics*, 178, 297–306, 2007.

[95] A.J. Bard, L.R. Faulkner, Electrochemical Methods: Fundamentals and Applications, 2nd edition, Wiley, New York, 2001.

[96] A.C. Co, S.J. Xia, and V.I. Birss, A kinetic study of the oxygen reduction reaction at LaSrMnO3 - YSZ composite, *Journal of the Electrochemical Society*, 152, A570–A576, 2005.

[97] E.A. Mason, Gas Transport in Porous Media: the Dusty-Gas Model, Elsevier, New York, 1983.

[98] R. Suwanwarangkul, E. Croiset, M.W. Fowler, P.L. Douglas, E. Entchev, and M.A. Douglas, Performance comparison of Fick's, dusty-gas and Stefan–Maxwell models to predict the concentration overpotential of a SOFC anode, *Journal of Power Sources*, 122, 9–18, 2003.

[99] B.E. Poling, J.M. Prausnitz, and J.P. O'Connell, The Properties of Gases and Liquids, McGraw-Hill, 5th edition, 2000.

[100] B. Habibzadeh, Understanding the CO oxidation in solid oxide fuel cells using nickel patterned anode, PhD thesis, University of Maryland, 2007.

[101] K. Ahmed, and K. Foger, Kinetics of internal steam reforming of methane on Ni/YSZ-based anodes for solid oxide fuel cells, *Catalysis Today*, 63, 479–487, 2000.

[102] R. Peters, R. Dahl, U. Kluttgen, C. Palm, and D. Stolen, Internal reforming of methane in solid oxide fuel cell systems, *Journal of Power Sources*, 106, 238–244,2002.

[103] A.L. Dicks, K.D. Pointon, and A. Siddle, Intrinsic reaction kinetics of methane steam reforming on a nickel/zirconia anode , *Journal of Power Sources*, 86, 523–530, 2000.

[104] R. Ǿdegard, E. Johnsen, H. Karoliussen, Methane reforming on Ni/Zirconia SOFC anodes, *Proceeding of the 4th international Symposium on Solid Oxide Fuel Cells*, 1995, Yokohama, Japan.

[105] W.M. Rohsenow, J.P. Hartnett, Y.I. Cho, Handbook of Heat Transfer, Chapter 5, 3rd edition, McGraw Hill, New York, 1995.

[106] B. Todd, and J.B.Young, Thermodynamic and transport properties of gases for use in solid oxide fuel cell modeling, *Journal of Power Sources*, 110, 186-200, 2002.

[107] F.P. Incropera, D.P. DeWitt, T.L. Bergman, and A.S. Lavine, Introduction to Heat Transfer, 4th edition. John Wiley & Sons, New York, 2002.

[108] A. Bejan, and A.D. Kraus, Heat Transfer Handbook, John Wiley & Sons, Inc., New Jersey, 2003.

[109] I. Wheeldon, C. Caners, K. Karan, B. Peppley, Utilization of biogas generated from Ontario wastewater treatment plants in solid oxide fuel cell systems: a process modeling study, *International Journal of Green Energy*, 4, 221-231, 2007.

[110] J. Szargut, D.R. Morris, and F.R. Steward, Exergy Analysis of Thermal, Chemical, and Metallurgical Processes, Hemisphere Publishing Corporation, 1988.

[111] W. Arabczyk, D. Moszyński, U. Narkiewicz, R. Pelka, and M. Podsiadły, Poisoning of iron catalyst by sulfur, *Catalysis Today*, 124, 43-48, 2007.

[112] M. Ni, D.Y.C. Leung, and M.K.H. Leung, Thermodynamic analysis of ammonia fed solid oxide fuel cells: Comparison between proton-conducting electrolyte and oxygen ion-conducting electrolyte, *Journal of Power Sources*, 183, 682-686, 2008.

[113] Q. Ma, J. Ma, S. Zhou, R. Yan, J. Gao, and G. Meng, A high-performance ammonia-fueled SOFC based on a YSZ thin-film electrolyte, *Journal of Power Sources*, 164, 86-89, 2007.

[114] N. Maffei, L. Pelletier, and A. McFarlan, A high performance direct ammonia fuel cell using a mixed ionic and electronic conducting anode, *Journal of Power Sources*, 175, 221-225, 2008.

[115] J.P. Collins, and J.D. Way, Catalytic decomposition of ammonia in a membrane reactor, *Journal of Membrane Science*, 96, 259–274, 1994.

[116] L. Li, and J.A. Hurley, Ammonia-based hydrogen source for fuel cell applications, *International Journal of Hydrogen Energy*, 32, 6–10, 2007.

[117] S.F. Yin, B.Q. Xu, X.P. Zhou, and C.T. Au, A mini-review on ammonia decomposition catalysts for on-site generation of hydrogen for fuel cell applications, Applied *Catalysis A: General*, 277, 1–9, 2004.

[118] Q. Ma, R.R. Peng, L. Tian, and G. Meng, Direct utilization of ammonia in intermediate-temperature solid oxide fuel cells, *Electrochemistry Communications*, 8, 1791-1795, 2006.

[119] H.C. Strack Company, www.hcstarck-ceramics.com/, Accessed in April 2009.

[120] P.h. Hofmann, A. Schweiger, L. Fryda, K.D. Panopoulos, U. Hohenwarter, J.D. Bentzen, J.P. Ouweltjes, J. Ahrenfeldt, U. Henriksen, E. Kakaras, High temperature electrolyte supported Ni-GDC/YSZ/LSM SOFC operation on two-stage Viking gasifier product gas, *Journal of Power Sources*, 173, 357–366, 2007.

[121] J.-D. Kim, G.-D. Kim, J.-W. Moon, H.-W. Lee, K.-T. Lee, C.-E. Kim, The effect of percolation on electrochemical performance, *Solid State Ionics*, 133, 67–77, 2000.

[122] J.-D. Kim, G.-D. Kim, J.-W. Moon, Y.-I, Park, W.-H. Lee, K. Kobayashi, M. Nagai, and C.-E. Kim, Characterization of LSM–YSZ composite electrode by ac impedance spectroscopy, *Solid State Ionics*,143, 379-389, 2001.

[123] J.R. Smith, A. Chen, D. Gostovic, D. Hickey, D. Kundinger, K.L. Duncan, R.T. DeHoff, K.S. Jones, and E.D. Wachsman, Evaluation of the relationship between cathode microstructure and

electrochemical behaviour for SOFCs, *Solid State Ionics*, 180, 90–98, 2009.

[124] A. Barbucci, M.P. Carpanese, M. Viviani, N. Vatistas, C. Nicolella, Morphology and electrochemical activity of SOFC composite cathodes: I. experimental analysis, *Journal of Applied Electrochemistry*, 39, 513–521, 2009.

[125] M. Brown, S. Primdahl, and M. Mogensen, Structure/performance relations for Ni/yttria-stabilized zirconia anodes for solid oxide fuel cells, *Journal of the Electrochemical Society*, 147, 475–485, 2000.

[126] Y. Matsuzaki, and I. Yasuda, Electrochemical oxidation of H_2 and CO in a H_2–H2O–CO–CO_2 system at the interface of a Ni–YSZ cermet electrode and YSZ electrolyte, *Journal of the Electrochemical Society*, 147, 1630–1635, 2000.

[127] H.S. Song, S. Lee, S.H. Hyun, J. Kim, and J. Moon, Compositional influence of LSM-YSZ composite cathodes on improved performance and durability of solid oxide fuel cells, *Journal of Power Sources*, 187, 25–31, 2009.

[128] M. Suzuki, N. Shikazono, K. Fukagata, and N. Kasagi, Numerical analysis of heat/mass transfer and electrochemical reaction in an anode supported flat-tube solid oxide fuel cell, *4th international conference on fuel cell science*, engineering and technology, Irvine, California, United States, 2006.

[129] R.J. Braun, S.A. Klein, and D.T. Reindl, Considerations in the design and application of solid oxide fuel cell energy systems in residential markets, *ASHRAE Transactions*, 110(1), 14-24, 2004.

[130] R.J. Leah, N.P. Brandon, and P. Aguiar, Modelling of cells, stacks and systems based around metal-supported planar IT-SOFC cells with CGO electrolytes operating at 500-600°C, *Journal of Power Sources*, 145, 336-352, 2005.

[131] T. Nietsch, J. Clark, Market oriented design studies for SOFC based systems, ETSU report F/0.1/00129/REP; 1999.

[132] P.W. Li, M.K. Chyu, Electrochemical and transport phenomena in solid oxide fuel cells, *Transaction of ASME*, 127, 1344-1362, 2005.